

QUASIFERROMAGNETISM

By

THIERRY DUBROCA

A DISSERTATION PRESENTED TO THE GRADUATE SCHOOL
OF THE UNIVERSITY OF FLORIDA IN PARTIAL FULFILLMENT
OF THE REQUIREMENTS FOR THE DEGREE OF
DOCTOR OF PHILOSOPHY

UNIVERSITY OF FLORIDA

2007

© 2007 Thierry Dubroca

To Jonathan Hack

ACKNOWLEDGMENTS

I must confess that I was pretty naïve when I chose the topic of my dissertation. My decision to study the magnetic properties of semiconductor materials came very quickly after attending a seminar on spintronics, a related field. I felt passionate about semiconductor magnetic properties right away. Professor Rolf Hummel, who has been my advisor during the full length of my graduate studies, has fully supported my decision for the topic. It was only after a couple years of studying this subject that I deeply understood the real difficulties of choosing one's own topic. Then, during the most difficult times, when a critical equipment of my work caught on fire and was destroyed, he reassured me by giving me his full support a second time. Without him, I most probably would have not completed my doctorate work. This is why my deepest appreciation goes to Professor Hummel. He has been the best advisor a student could ever dream of.

In addition, I am very grateful to Dr. Alexander Angerhofer for his generosity. Dr. Angerhofer has not only given me a lot of his time to teach me how to use the EPR system, he also amply advised me throughout my doctoral work. The main experiments of this dissertation could not have been conducted without his supervision.

Our laboratory was not equipped with the magnetometer required to develop my work. Dr. Arthur Hebard has been very kind in letting me use his SQUID magnetometer for many years and I am very thankful to him for it.

I would also like to thank Dr. William Vernetson for letting us use the nuclear reactor in order to prepare the neutron irradiated silicon samples.

I feel very lucky to have studied here in the Materials Science department at the University of Florida, where I found very supportive and caring professors. In particular, I would like to

thank my committee members from this department, Dr. Paul Holloway, Dr. David Norton and Dr. Wolfgang Sigmund for their continuing support.

Jonathan Hack discovered the magnetic hysteresis of spark processed silicon at UF several years before I became a graduate student. Jonathan was very helpful and spent countless hours discussing my experimental results and ideas. Jonathan will always hold a special place in my heart and will never be forgotten. His sudden death came to all of us as a shock.

I am also very grateful to my colleagues and friends, Kwanghoon Kim, Anna Fuller, Julien Gratier and Max Lemaitre who had to put up with my incisiveness during our weekly group meetings. Their pertinent remarks have grown in me a way of thinking which, I am sure, will help me all through my life.

I would like to express my gratitude to my long time friends, Anne Charneau and Fabien Gerard for their unconditional support, express my sincere appreciation to my friend Courtney Allen for her patience and thank Orlando Rios for his support and help in preparing a magnetic standard.

I will conclude my acknowledgement by thanking my parents, Michel and Christiane Dubroca who deserve my deepest love for the support they have given me all along my schooling and in particular during my doctoral work.

TABLE OF CONTENTS

	<u>page</u>
ACKNOWLEDGMENTS	4
LIST OF TABLES	9
LIST OF FIGURES	10
ABSTRACT.....	16
CHAPTER	
1 WHY STUDY QUASIFERROMAGNETISM?	18
1.1 Definition of Quasiferromagnetism.....	18
1.2 Motivation for Studying Quasiferromagnetism.....	20
1.3 Could Quasiferromagnetics Be Used in Spintronics?	21
1.4 Understanding the Fundamental Physics of Quasiferromagnetism.....	21
2 WHERE DOES QUASIFERROMAGNETISM STAND WITHIN CLASSICAL MAGNETISM?	23
2.1 Diamagnetism.....	23
2.2 Paramagnetism.....	24
2.3 Ferromagnetism.....	27
2.4 Unclassified Magnetic Materials	32
2.5 Summary.....	38
3 MANUFACTURING, MACROSCOPIC CHARACTERIZATION AND EXPERIMENTAL RESULTS OF QUASIFERROMAGNETIC MATERIALS	40
3.1 Room Temperature Study of Spark-Processed Silicon	40
3.1.1 Production of Spark-Processed Silicon for Magnetic Studies.....	40
3.1.2 Magnetic Characterization Process Parameter Influence	42
3.2 Magnetic Characterization of Spark-Processed Silicon at High Temperature	46
3.2.1 Magnetic Characterization Method at High Temperatures	47
3.2.2 Verification of the Modified Magnetometer	55
3.2.3 High Temperature Spark-Processed Silicon Magnetization.....	58
3.2.4 Annealing Effect on the Magnetization.....	62
3.3 Low Temperature Magnetization	64
3.3.1 Magnetic Reference Material HgCo(SNC) ₄ for the 2-100K Temperature Range	65
3.3.2 Aluminum Reference for the 50-300 K Temperature Range	65
3.3.3 Oxygen Effect at Low Temperature	66
3.3.4 Spark-Processed Silicon Low Temperature Magnetization	67
3.4 Summary.....	71

4	INTERPRETATION OF QUASIFERROMAGNETISM IN SPARK PROCESSED SILICON.....	72
4.1	Model Concerning the Distribution of Paramagnetic Centers.....	72
4.2	Electron Paramagnetic Resonance (EPR) Concepts.....	74
4.3	Characterization of Continuous Wave Electron Paramagnetic Resonance Spectra	75
4.4	Electron Paramagnetic Resonance Parameter versus Temperature.....	87
4.4.1	Low Temperature 5 to 300K	88
4.4.2	High Temperature 300 to 800K.....	92
4.5	Characterization of Pulsed Electron Paramagnetic Resonance	99
4.6	Relaxation Rates	99
4.6.1	Spin-Lattice Relaxation Rate.....	99
4.6.2	Spin-Spin Relaxation Rate	101
4.7	Separation of Rates to Identify Paramagnetic Centers	104
4.8	Spin Density.....	106
4.9	Summary.....	111
5	FURTHER CONSIDERATIONS	112
5.1	Annealing of Spark Processed Silicon.....	112
5.2	Ion Implanted Silicon	115
5.2.1	Magnetic Response of Ion Implanted Silicon	115
5.2.2	Electron Paramagnetic Resonance of Ion Implanted Silicon	117
5.3	Neutron Irradiated Silicon	119
5.4	Highly Oriented Pyrolytic Graphite	120
5.4.1	Magnetization Response of Highly Oriented Pyrolytic Graphite	121
5.4.2	Electron Paramagnetic Response of Highly Oriented Pyrolytic Graphite	121
5.5	Summary.....	123
6	CONCLUSION.....	124
6.1	Macroscopic Magnetic Behavior of Spark-Processed Silicon.....	124
6.2	Electron Paramagnetic Resonance of Spark-Processed Silicon	124
6.3	Quasiferromagnetic Model for Spark-Processed Silicon	125
6.4	Other Quasiferromagnetic Materials	126
6.5	Future Work.....	126
APPENDIX		
A	SPARK PROCESS POWER SUPPLY	129
A.1	Power Supply Principles of Operation.....	129
A.2	Power Supply Inner Components	131
B	HgCo(SCN) ₄ MAGNETIC REFERENCE.....	134
B.1	SQUID Magnetometer Verification.....	134
B.2	Model Weighting	138

B.3 Temperature Independent Susceptibility	145
B.4 Zero Field Splitting and Exchange Interaction	148
B.5 Conclusions.....	150
C ALUMINUM MAGNETIC REFERENCE FOR TEMPERATURE RANGE 50 – 300 K .	151
D OXYGEN CONTAMINATION AT LOW TEMPERATURES.....	154
E ELECTRON PARAMAGNETIC RESONANCE SYSTEM OVEN APPARATUS	158
LIST OF REFERENCES.....	161
BIOGRAPHICAL SKETCH	165

LIST OF TABLES

<u>Table</u>	<u>page</u>
4-1 Characteristic values of echo detected field sweep and amplitude of exponential decay as a function of magnetic field.	106
B-1 Constants from susceptibility model.....	137
B-2 Magnetic susceptibility [10^{-6} g^{-1}] as function of temperature of $\text{HgCo}(\text{SNC})_4$ of our data set and O'Connor's data set.	139
B-3 Data example.	140
B-4 Fitting parameters.	140
B-5 Comparison of the direct and classic method of O'Connor data set. For the classic method the diamagnetic constant is set and equal to the value found through the direct method.	144
B-6 Comparison of the direct and classic method with O'Connor data set. For the classic method the diamagnetic constant is set and equal to the value proposed by O'Connor.	145
B-7 Diamagnetic correction per mol.....	146
C-1 Comparison of model constants for aluminum.	152

LIST OF FIGURES

<u>Figure</u>	<u>page</u>
2-1 Magnetization of silicon as a function of magnetic field (own measurements).	24
2-2 Magnetization as a function of magnetic field for a paramagnetic material.....	25
2-3 Magnetic susceptibility versus temperature for a paramagnetic material.....	26
2-4 Electronic configuration of Aluminum.	26
2-5 Magnetization as function of magnetic field for ferromagnetic materials.....	28
2-6 Magnetization as a function of temperature at 1000 Oe for a nickel thin film on a silicon substrate.....	29
2-7 Magnetization process.	30
2-8 Magnetic phases as a function of particle diameter.	31
3-1 Spark-processing of silicon.....	40
3-2 Scanning electron micrograph of spark-processed silicon. A) large top view. B) zoom-in view.	41
3-3 Magnetization as a function of magnetic field strength measured at room temperature for spark-processed silicon (sparking time = 6 hours, frequency = 22.5 kHz).	43
3-4 Secondary ion mass spectrum of spark-processed silicon. The largest peaks have been labeled accordingly. See also 3-5.	44
3-5 Secondary ion mass spectrum of spark-processed silicon zoomed in around the iron atomic number. An arrow marks the position of where the iron isotope with an atomic mass of 54 should be if it was present in the sample.	45
3-6 Spark-processed silicon magnetization at 0 Oe (i.e. remanence) and 1000 Oe as a function of the spark frequency (sparking time was set at 12 hours for all samples).....	46
3-7 Spark-processed silicon magnetization at 0 Oe (i.e. remanence,) 1000 Oe and hysteresis area as a function of the sparking time (spark frequency was set at 16 kHz for all samples).....	47
3-8 Super quantum interference device magnetometer with oven insert and sample holder.	49
3-9 Simulated detector voltage (a.u.) as a function of the position.....	51

3-10	Simulated detector voltage (a.u.) as a function of the position (blue diamonds) zoomed in around the sample located 7 cm away from the end of the holder. The computer model is plotted in solid orange.....	52
3-11	Simulated detector voltage (a.u.) as a function of the position.....	53
3-12	Simulated detector voltage (a.u.) as a function of the position (blue diamonds) zoomed in around the sample located 3.5 cm away from the end of the holder. The computer model is plotted in solid orange.....	54
3-13	Magnetization of pure nickel as function of temperature at 1000 Oe. A Curie temperature of 625 K is found as indicated by the arrow.....	55
3-14	Magnetization versus magnetic field for a silicon sample weighting 10.3 mg, measured at 300K.	56
3-15	Magnetization versus temperature (grey dots) for a 10.3 mg silicon wafer measured at 10,000 Oe. The plotted magnetization is divided by 10, equivalent to magnetization at 1000 Oe. The average (solid line) is -2.8×10^{-6} emu.....	57
3-16	Magnetization as a function of temperature upon heating (blue diamonds) at 1000 Oe for spark-processed silicon (sparking time = 6 hours, frequency = 22.5 kHz) and the field cooled magnetization (red square).....	58
3-17	Magnetization as a function of the magnetic field strength before (blue curve) and after field cooling (red curve) measured at room temperature for spark-processed silicon (sparking time = 6 hours and frequency = 22.5 kHz).	59
3-18	Normalized magnetization as a function of temperature for spark-processed silicon measured at 1000 Oe represented by red diamonds.....	60
3-19	Normalized magnetization as a function of temperature for spark-processed silicon measured at 500 Oe represented by red diamonds.....	61
3-20	Remanent magnetization of spark-processed silicon (sparking time = 6 hours, frequency = 22.5 kHz) measured as a function of temperature upon heating (blue dots) and cooling (red dots).	62
3-21	Magnetization as function of magnetic field for a spark-processed silicon sample (sparking time = 6 hours and frequency = 22.5 kHz) at room temperature after each heating cycle (heating up to 800 K and cooling down to 300 K in a 1000 Oe field).	63
3-22	Magnetization at 1000 Oe (blue diamonds) and 0 Oe (red squares) versus annealing time for spark-processed silicon (sparking time = 6 hours and frequency = 22.5 kHz).	64
3-23	Magnetization versus field at 70 K and 35 K of spark-processed silicon (square and round points, respectively).....	68

3-24	Magnetization versus temperature for spark-processed silicon at 1000 Oe (red triangle) and 0 Oe (bleu squares).....	69
3-25	Magnetization adjusted for diamagnetism and remanence as a function of inverse temperature.....	70
4-1	Proposed paramagnetic centers distribution.....	73
4-2	Energy levels of an electron at the resonance field.....	73
4-3	Lorentzian distribution and 1 st derivative of electron microwave absorbance as a function of the magnetic field. A) one type of paramagnetic center. B) two different types of paramagnetic centers (red curves) and their deconvolution (blue and green curves).....	75
4-4	Electron paramagnetic resonance spectrum of spark-processed silicon (back line) at room temperature with its double Lorentzian 1 st derivative model (red).....	77
4-5	Electron paramagnetic spectra of spark-processed silicon along with DPPH reference standard (black line).....	78
4-6	Nature of spark-processed silicon paramagnetic centers.....	79
4-7	Amplitude of D paramagnetic centers as a function of microwave power.....	80
4-8	Amplitude of D paramagnetic centers as a function of the square root of the microwave power (dots). A linear trend is fitted for the lowest power data points ($R^2=0.995$).....	81
4-9	Amplitude of E' paramagnetic centers as a function of microwave power.....	82
4-10	Amplitude of E' paramagnetic center as function of the square root of the microwave power (dots). A linear trend is fitted for the lowest power data points ($R^2=0.995$).....	83
4-11	Saturation effect observed for the two paramagnetic centers in spark-processed silicon.....	84
4-12	Line width as a function of Log (power) for spark-processed silicon.....	85
4-13	Amplitude of D paramagnetic centers as a function of microwave power (dots). Two saturation models are fitted to the data (solid lines).....	85
4-14	Amplitude of E' paramagnetic centers as a function of microwave power for sp-Si (dots). Two saturation models have been fitted to the data (solid lines).....	86
4-15	Electron paramagnetic resonance spectra of spark-processed silicon at 4.2K (black line) and two possible models:.....	86

4-16	Amplitude of D centers versus temperature. The data points above 40K have been divided by 10 to account for the change in gain setting. The gain is changed to keep the signal in the linear regime.	87
4-17	Amplitude of D centers versus inverse temperature (dots). The data points below 0.025K^{-1} have been divided by 10 to account for the increased gain. A linear trend is fitted to the data (solid line).	88
4-18	Amplitude of E' centers versus temperature. The data points above 40K have been divided by 10 to account for the increased gain.	89
4-19	Amplitude of E' centers versus inverse temperature (dots). The data points below 0.025K^{-1} have been divided by 10 to account for the increased gain. A linear trend is fitted to the data (solid line).	90
4-20	Line width of the two paramagnetic centers present in spark-processed silicon versus temperature in the low temperature range. Line width 1 corresponds to the D centers and line width 2 corresponds to the E' centers.	91
4-21	Spark-processed silicon paramagnetic centers g-factor (uncalibrated) versus temperature. The g-factor 1 corresponds to the D centers while the g-factor 2 corresponds to the E' centers.	92
4-22	Spark-processed silicon paramagnetic centers g-factor versus temperature.	93
4-23	EPR line width of the two paramagnetic centers present in spark-processed silicon versus temperature in the high temperature range.	95
4-24	Amplitude of D (blue) and E' (red) centers versus temperature for spark-processed silicon in the high temperature range.	96
4-25	Amplitude of D centers (blue dots) and Magnetization at 1000 Oe (green dots) versus temperature for spark-processed silicon in the high temperature range.	97
4-26	Intensity versus time for a spin-lattice relaxation rate experiment of spark-processed silicon (black line), one-exponential decay model (green line) and bi-exponential decays (red line).	100
4-27	Spin-lattice relaxation rates versus temperature for spark-processed silicon.	101
4-28	Intensity versus time for a spin-spin relaxation rate experiment on spark-processed silicon (black line), one-exponential decay model (green line) and bi-exponential decays (red line).	102
4-29	Spin-spin relaxation rates versus temperature for spark-processed silicon.	103
4-30	Field sweep pulsed electron paramagnetic resonance of spark-processed silicon (black curve).	104

4-31	Amplitude of exponential decays in spin-spin relaxation rate experiments versus field for spark-processed silicon (dots).....	105
4-32	Phase memory time for each paramagnetic center measured as a function of the input power of spark-processed silicon.....	107
4-33	Inverse phase memory time ($1/T_m'$) versus $\sin^2(\pi/2 \times (\text{power}/\text{power}_0)^{1/2})$ of spark-processed silicon (dots).....	108
4-34	Density of paramagnetic centers as a function of the spark frequency for spark-processed silicon.	110
5-1	Magnetization at 0 and 1000 Oe of spark processed silicon as a function of cumulative isochronal (30 min) annealing temperature.....	113
5-2	Electron paramagnetic resonance peak to peak spectra line of spark processed silicon as a function of cumulative isochronal (30 min) annealing temperature.....	114
5-3	Magnetization as a function of the magnetic field strength at 300 K for silicon implanted with argon ions.....	116
5-4	Magnetization as a function of magnetic field strength at 300 K for silicon implanted with silicon ions.	116
5-5	Electron paramagnetic resonance spectra of argon implanted into silicon at a dose of $2 \times 10^{16} \text{ cm}^{-2}$ (blue squares) and its Lorentzian model (solid red).....	117
5-6	Electron paramagnetic resonance spectra of silicon implanted into silicon at a dose of 10^{16} cm^{-2} (blue squares) and its two-Lorentzian model (solid red).	118
5-7	Magnetization versus magnetic field strength of neutron irradiated silicon at a dose of $4 \times 10^{16} \text{ cm}^{-2}$	120
5-8	Magnetization as a function of magnetic field strength of HOPG graphite.	121
5-9	Electron paramagnetic resonance spectra of HOPG graphite (blue squares) and its Dysonian line model (solid red).....	122
A-1	Power supply schematic.....	130
A-2	Typical waveform observed at the read out (E) on the screen of an oscilloscope.....	131
A-3	Power supply without its top cover.....	132
A-4	Front side of the spark machine. The labels A – G designate the same control as in the schematic (A-1).....	133
B-1	Magnetization versus field at room temperature for $\text{HgCo}(\text{SNC})_4$ (square). A linear curve has been fitted to the data points (solid line).	135

B-2	Magnetization versus temperature at 1000Oe for HgCo(SNC) ₄	136
B-3	Magnetization adjusted for diamagnetism as a function of the inverse temperature (squares).....	137
B-4	Example of the Curie law model. A) M-T plot and its model. B) M-1/T plot and its model.....	141
B-5	Magnetic susceptibility of HgCo(SNC) ₄ and its model using the direct method.	142
B-6	Inverse magnetic susceptibility of HgCo(SNC) ₄ adjusted for diamagnetism versus temperature and its model using the classic method.....	143
B-7	Three dimensional representation of HgCo(SNC) ₄ . X,Y,Z are the fractional coordinates.....	147
B-8	Magnetic susceptibility of HgCo(SNC) ₄ as function of magnetic field at 2 K (square) and its model (solid line).....	149
C-1	Magnetization versus field at room temperature of 99.999% pure aluminum (squares).....	151
C-2	Magnetization versus temperature at 1000 Oe for 99.999% pure aluminum.	152
C-3	Magnetization as function of temperature square at 1000Oe for 99.999% pure aluminum (diamonds). A linear trend is fitted to the data (solid line).....	153
D-1	Magnetization versus temperature for a piece of plastic straw at 500Oe.	154
D-2	Magnetization at 1000 Oe of a piece of straw as a function of temperature for several different purges.....	155
D-3	Oxygen magnetization peak height versus number of purges (diamonds).....	156
E-1	Picture and schematic cross section of the oven apparatus for the electron paramagnetic resonance system.....	159

Abstract of Dissertation Presented to the Graduate School
of the University of Florida in Partial Fulfillment of the
Requirements for the Degree of Doctor of Philosophy

QUASIFERROMAGNETISM

By

Thierry Dubroca

December 2007

Chair: Rolf E. Hummel

Major: Materials Science and Engineering

During the 20th century, the understanding of magnetic phenomena had a big breakthrough thanks to quantum physics. However, there are still many unanswered questions. The research work presented here attempts to answer the following question: where does the magnetic hysteresis come from in semiconductors not containing magnetic elements, such as iron, nickel, cobalt or rare earth elements?

We have found that materials composed of light elements, such as silicon, oxygen, or nitrogen possess a magnetic hysteresis in contradiction to classical theory. In order to avoid confusion between ferromagnets and those materials, a new name was coined to describe them: quasiferromagnets. In our investigation we used two techniques, namely electron paramagnetic resonance, and magnetometric measurements. We found a Curie temperature of 765 K for spark-processed silicon. Further, we identified two paramagnetic centers called D and E' in spark-processed silicon. We measured a density of $1.4 \times 10^{19} \text{ cm}^{-3}$ for the D centers and $0.5 \times 10^{19} \text{ cm}^{-3}$ for the E' centers leading to an average inter-spin distance of 3.7 nm. In addition, we present the magnetic properties including magnetic hysteresis of spark-processed silicon, argon implanted silicon as well as neutron irradiated silicon and highly oriented pyrolytic graphite.

We propose a model to explain quasiferromagnetism based on the inhomogeneous distribution of paramagnetic defects. Our distribution model is based on the inhomogeneous structure of the materials. Spark-processed silicon is known to have silicon nanoclusters embedded into a silicon dioxide matrix. The clustering of paramagnetic centers allows positive exchange interactions between them. We suggest that this clustering explains the observed macroscopic magnetic behavior in particular the magnetic hysteresis at room temperature.

CHAPTER 1 WHY STUDY QUASIFERROMAGNETISM?

Magnetism has been a topic of interest since the discovery of ferromagnetism by the ancient Greeks from the city of Magnesia several thousands of years ago. Much later, the compass was invented using the properties of a magnetized iron needle which orients itself toward the north direction. The first theories of magnetism were developed in the 19th century, a magnetic field created by a current in a wire by Oersted and Ampere. Since, Weiss, Curie and Langevin, to name a few, developed theories to explain other magnetic phenomena such as antiferromagnetism, diamagnetism or paramagnetism. This was the beginning of what we know today as the “theory of magnetism.” Our study expands this theory with a new branch, which should be tentatively called quasiferromagnetism.

1.1 Definition of Quasiferromagnetism

A “crystal” defines a material that can be sorted according to its crystallographic signature. Bravais, in 1845, mathematically defined the maximum number of possible crystallographic arrangements (lattices) to be 14. Therefore, for half a century, crystals were mathematically defined and there was no room for other type of periodic arrangements of atoms which did not correspond to the Bravais networks. Later, between 1970 and 1980, a researcher (D. Shechtman) measured what seemed to be periodic lattices that were outside the Bravais networks. Because the word crystal was so closely attached to the concept of the Bravais networks, newly discovered pseudo-periodic lattices could not be named crystals, even though from a logical point of view, they were like crystals. The very close similarities with the classical Bravais networks, these periodic lattices were then named quasi-crystals! A few years later, the scientists (among them D. Shechtman) who discovered the quasi-crystals received numerous awards for their intensive work in this field.

A few years ago, I was telling this story to a dear friend, the late Jonathan Hack, after brainstorming magnetic properties of semiconductors. He told me about his first time presenting a magnetic hysteresis loop obtained on spark-processed silicon at a conference: the participants did not agree to let him call what he was presenting “ferromagnetism.” At that time, in the mid-nineties, almost no one believed that one could observe ferromagnetic behavior in materials not containing d or f shell electrons. Right after this conversation, there was no doubt that what we were studying should not continue to be called ferromagnetism, in order to avoid further semantic opposition and confusion. Thus, we decided to name our research topic “quasiferromagnetism” which occurred naturally to us after discussing the origin of the word “quasi-crystals.”

Moreover, it should be noted, that a group of scientists working on ferromagnetic semiconductors (Si containing ferromagnetic trace elements) ran into a similar problem. They could not use the word “ferromagnetism” by itself to describe their work because it was not within the exact framework of classical ferromagnetism. Therefore to avoid their new results being rejected from the strict ferromagnetism label they came up with the word “dilute magnetic semiconductors” (DMS). We discuss (Chapter 2) the differences between DMS and quasiferromagnetics.

Quasiferromagnetics define materials displaying a behavior similar to classical ferromagnetic materials, but without containing d or f shell electrons. The difference in the type of electrons involved leads to large differences in observed magnetic behavior. For example, quasiferromagnetics exhibit a magnetic hysteresis at room temperature, despite the fact that they essentially do not contain domain walls in the commonly used sense.

This work is the continuation of what Jonathan Hack started 10 years ago when he discovered the magnetic hysteresis of spark-processed silicon. This was discovered in our lab, and back then, Dr. Hummel, suggested studying the magnetic properties of this material. He was expecting to find that the magnetic susceptibility would go to minus one, characteristic of superconductors. It turned out that sp-Si was not a superconductor but rather exhibited a new effect which we call today: quasiferromagnetism. My doctoral work focuses mostly on explaining the origin of this effect.

1.2 Motivation for Studying Quasiferromagnetism

At first, we thought we would be able to use these materials, so that we could assemble them into a spintronic transistor. Spintronics are devices that use the spin of electrons rather than their charge to store and transfer information. These devices are thought to be much faster than the classical electronic devices and therefore would further the improvement of the computer industry. However, as we advanced our studies for explaining quasiferromagnetism, we understood that implementing quasiferromagnetic materials into Spintronics devices would very likely be a difficult task, at least before we fully understand how they behave. Therefore, we decided to limit the scope of this work to make experiments which would allow us to explain where quasiferromagnetism originates from.

Consequently, our motivation shifted. Our passion pushed us toward understanding the fundamental physics behind this newly discovered magnetic property. In addition, by broadening of our research scope, we hope to promote the understanding of physics by changing the way we saw magnetism as a whole. This is our goal and challenge.

In short, quasiferromagnets arise from unpaired bonds produced during processing of materials. For example, silicon or (carbon,) which are ion implanted, neutron irradiated, plasma

sprayed or spark processed yield a high density of unpaired bonds leading to quasiferromagnetism.

1.3 Could Quasiferromagnetics Be Used in Spintronics?

Spintronics as a new branch of physics and engineering has a handful of applications. The most commonly known application is the read head of hard drives in personal computers. But spintronics is mostly a research discipline in which engineers and physicists try to understand how they can control and transport the spin of electrons in semiconductors.

Early on, we thought that the materials we studied were part of the “spintronic world,” in particular the diluted magnetic semiconductors, but as we will show throughout this dissertation, this is not the case. They share a common semiconductor host, as well as similar magnetic hysteresis. Spintronics use classical ferromagnetic elements, such as Fe, Ni, Co, Gd, etc., all containing d and/or f shell electrons which are at the origin of the observed magnetic behavior. On the other hand, quasiferromagnetics are only composed of p and s shell electrons; therefore, they have a very different origin for explaining their magnetic behavior. It is to be noted, as we will see in detail through Chapter 2, that quasiferromagnetism is not a subpart of ferromagnetism, paramagnetism, diamagnetism or other classical subfields of magnetism.

As a consequence, the significant differences between spintronics and quasiferromagnetism lead us to the introduction of a new category of magnetic materials: the quasiferromagnets. A new field of study in physics of magnetism is born.

1.4 Understanding the Fundamental Physics of Quasiferromagnetism

As a field of physics, quasiferromagnetism aims at describing the fundamental behavior of electrons to explain macroscopic physical observation. Our goal is to develop a comprehensive model of electron spin behavior which explains the magnetic behavior of quasiferromagnetics.

For example, we could try to describe the macroscopic hysteresis loop observed at room temperature by using our understanding on how electron spins interact at the atomic scale.

CHAPTER 2

WHERE DOES QUASIFERROMAGNETISM STAND WITHIN CLASSICAL MAGNETISM?

Magnetism can be classified either through its response to a magnetic field or through its electronic interactions. In the first case, we can distinguish several classes: diamagnetism, paramagnetism, ferromagnetism, anti-ferromagnetism, ferrimagnetism. On the other hand, the classification using electron behavior also separates the different classes of magnetic materials according to their exchange interactions which can be direct or indirect, such as double exchange, super exchange, anisotropic exchange or itinerant exchange. In this chapter we develop most of the concepts which lead to the classification of quasiferromagnetism within classical magnetism.

2.1 Diamagnetism

Diamagnetic materials have a negative response to an applied external magnetic field. The magnetic moment (M) induced from an external applied magnetic field is opposed to the applied field. Furthermore, the magnetic moment of diamagnetic materials is linearly proportional to the applied magnetic field, where the coefficient of linearity, called the susceptibility, is negative. For example, silicon (Si) shows a diamagnetic behavior (Figure 2-1). Its susceptibility (χ) is -0.32×10^{-6} (unitless in the cgs system). In addition, the susceptibility as a function of temperature is another way to characterize the magnetic behavior and classify materials accordingly. In the case of diamagnetism, the susceptibility does not change as a function of temperature.

Diamagnetism is commonly explained by postulating the motion of electrons orbiting around the nucleus within an atom. According to Ampere, the motion of an electron around its nucleus creates a current within a loop (the orbit). This current, in a loop, creates an orbital magnetic moment. In addition, each electron possesses a spin. The spin is a concept originating from the relativistic quantum theory. Hence, each electron has a magnetic moment stemming

from its spin and its orbital motion. Each atom (except hydrogen) is composed of several electrons. To compute the magnetic moment per atom, one sums the contribution of each electron spin. When the net sum of the spin magnetic moment is zero and only orbital magnetic moment is left we have a diamagnetic material^{1,2}.

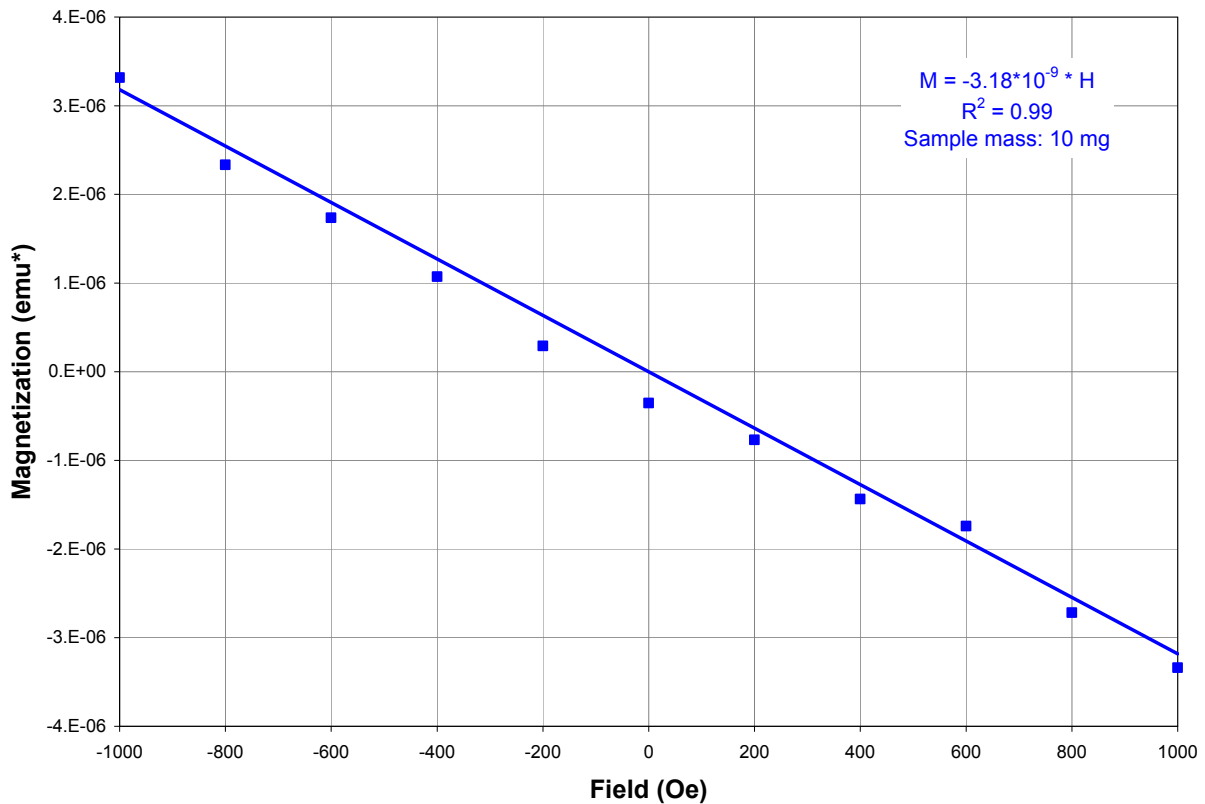


Figure 2-1. Magnetization of silicon as a function of magnetic field (own measurements).

2.2 Paramagnetism

In the case of paramagnetism, the magnetization is proportional to the applied external magnetic field, but the response is positive as shown in Figure 2-2. For example, Aluminum is a paramagnet and its susceptibility is $+1.65 \times 10^{-6}$ (unitless in the cgs system) at room temperature. In addition, the susceptibility is a function of temperature and can be used to classify materials into the paramagnetic behavior: the phenomenon can be seen in Figure 2-3. The susceptibility (χ)

*emu: electro-magnetic unit, measure of the magnetization in the centimeter-gram-second (CGS) system.

follows the Curie law; it is inversely proportional to the temperature: $\chi = C / T$, where C is a constant depending on each materials and T is the temperature in Kelvin.

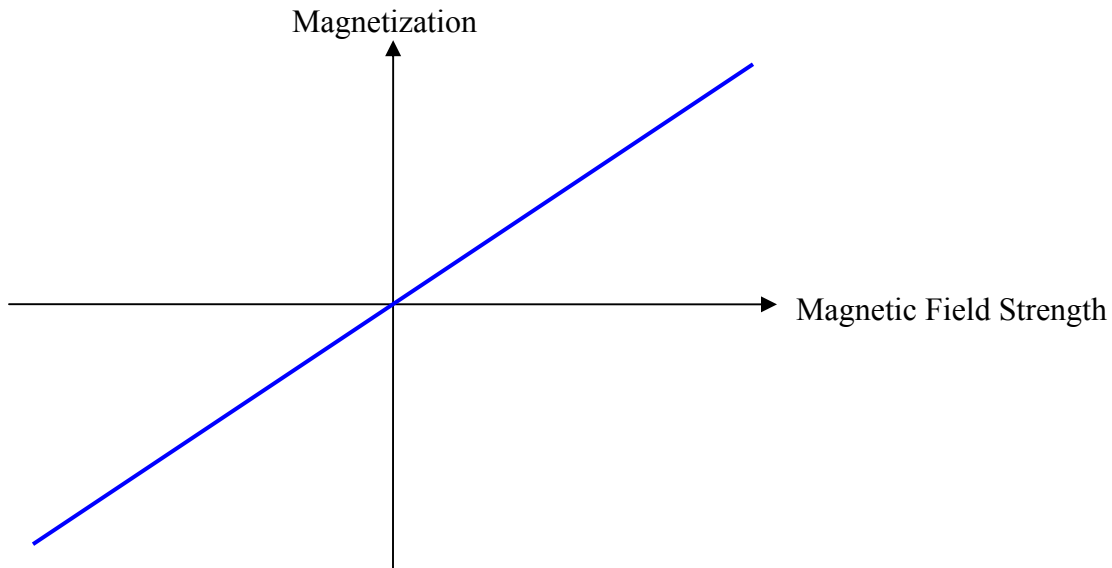


Figure 2-2. Magnetization as a function of magnetic field for a paramagnetic material.

Langevin explains the origin of paramagnetism. We present the essence of his theory, without going into the details of the quantum mechanical equations. We will continue with the example of Aluminum (Al). Figure 2-4 displays the electronic structure of Al. The electrons which compose the Al atom have different energy levels and spins. The possible energy levels are: 1s, 2s, 2p, 3s and 3p whereby the possible spins are up or down. Electron energies and spins can only take specific values, as displayed in Figure 2-4. For example, there are two electrons in the 2s energy levels with opposite spins. Their magnetic moments cancel one another. This is true for all paired electrons. Al has one unpaired electron in the 3p energy level, which contributes to a positive atomic moment. It is oriented in the direction of the external magnetic field and therefore explains the positive susceptibility.

It is to be noted that the magnetic moments of unpaired electrons do not interact with one another in the case of Al.

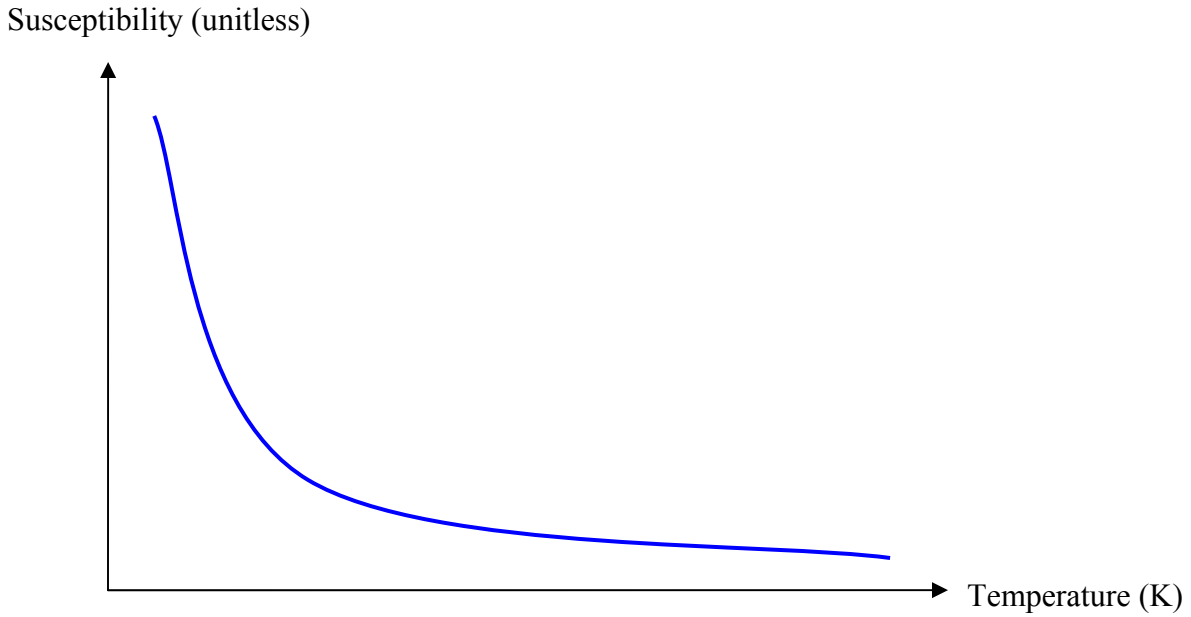


Figure 2-3. Magnetic susceptibility versus temperature for a paramagnetic material.

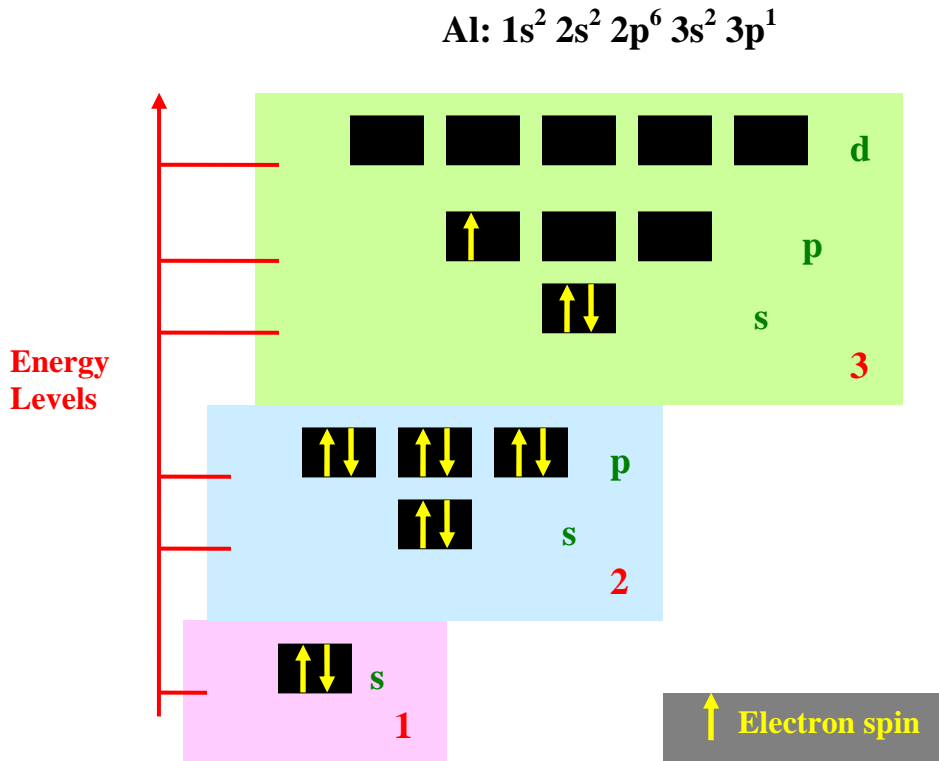


Figure 2-4. Electronic configuration of Aluminum.

Why is the susceptibility temperature dependant? For example, at room temperature and at zero field, Al atomic moments are randomly distributed due to thermal energy and therefore the net magnetic moment is zero. When one applies an external magnetic field, the Al atomic moments tend to orient in the direction of the field. Thermal fluctuations are strong and tend to randomize the atomic moments. As the temperature is lowered, the thermal fluctuation decreases leading to a larger magnetic moment, which increases the susceptibility. Similarly, when the temperature is increased the thermal fluctuation increases and the susceptibility decreases. For a full description through equations of the relationship between the paramagnetic susceptibility and the temperature see Cullity¹ or Hummel².

2.3 Ferromagnetism

In the previous section we introduced the Curie-Weiss law. This law stems from the Weiss molecular field theory. In order to explain ferromagnetism, we will start with this theory which explains the macroscopic magnetic behavior. Then, we will discuss how this theory is deepened by quantum mechanics and gives an explanation for the magnetic behavior at the electronic level.

Weiss introduced a new field in his theory. This field (H_m) is a local field “seen” by electrons which is added to the external applied field (H_e). This local field is postulated to be proportional to the magnetization of the material ($H_m = \gamma \times M$), where γ is a proportionality factor. Hence, the material under magnetic characterization is excited by the total field (H_t) equal to H_m plus H_e . When there is no external magnetic field ($H_e = 0$) the material still experiences the internal field which aligns the electron spins. This alignment of spins without external field creates a remanent magnetization; therefore, when an external field is applied the magnetization changes. A typical magnetization response is shown in Figure 2-5.

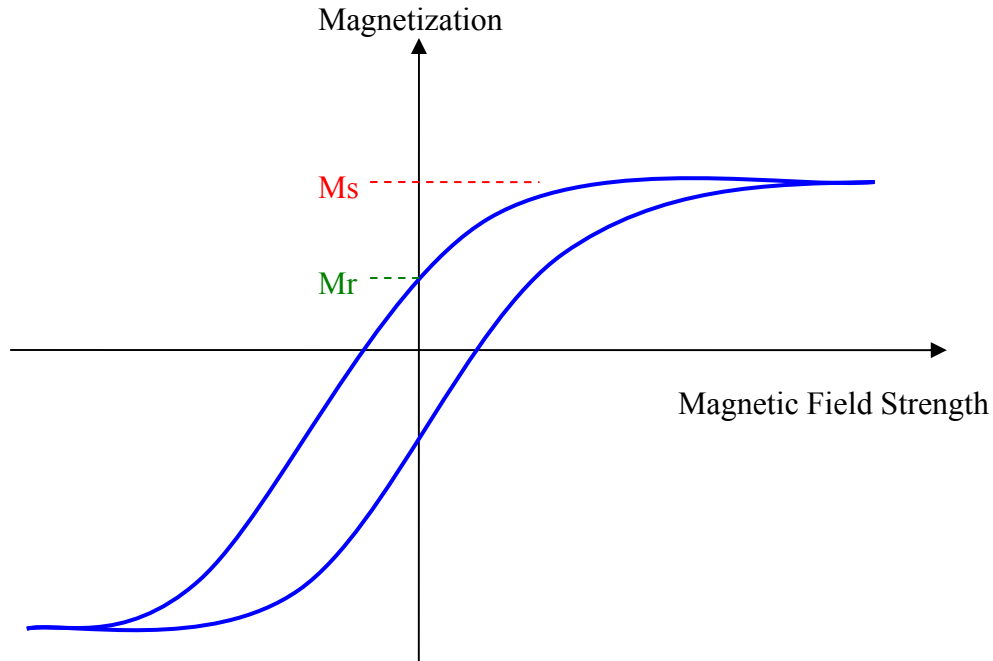


Figure 2-5. Magnetization as function of magnetic field for ferromagnetic materials. The saturation magnetization (M_s) as well as the remanent magnetization (M_r) are shown.

Using the molecular field theory, we can better explain the Curie-Weiss law starting with the Curie law ($\chi = C / T$) and the definition of the susceptibility ($\chi = M / H$), $C / T = M / H$. When replacing H by H_t ($H_m + H_e$) we obtain: $C / T = M / (H_m + H_e)$. Since $H_m = \gamma \times M$, the previous equation becomes: $C / T = M / (H_e + \gamma \times M)$. This expression can be derived and expressed as such: $M / H_e = C / (T - \gamma \times C)$. Using the definition of the susceptibility, we finally get the Curie-Weiss law: $\chi = C / (T - \theta)$, where $\theta = \gamma \times C$. In the case of ferromagnets, the temperature term θ is positive and is essentially identical with the Curie temperature, T_c . Below this temperature the material is ferromagnetic while above the Curie temperature it is paramagnetic. For example, Figure 2-6 displays the magnetization measured as a function of temperature for a thin film of nickel on a silicon wafer. The measured Curie temperature is 625K for nickel, which is within 1% lower than previously published data². Below 625K, Ni is

ferromagnetic, that is, the electron spins are interacting together such that they align in the same direction within a domain. While above 625K, Ni is paramagnetic, the temperature is such that the thermal agitation randomizes the electron spin orientations more than the exchange interaction aligns them.

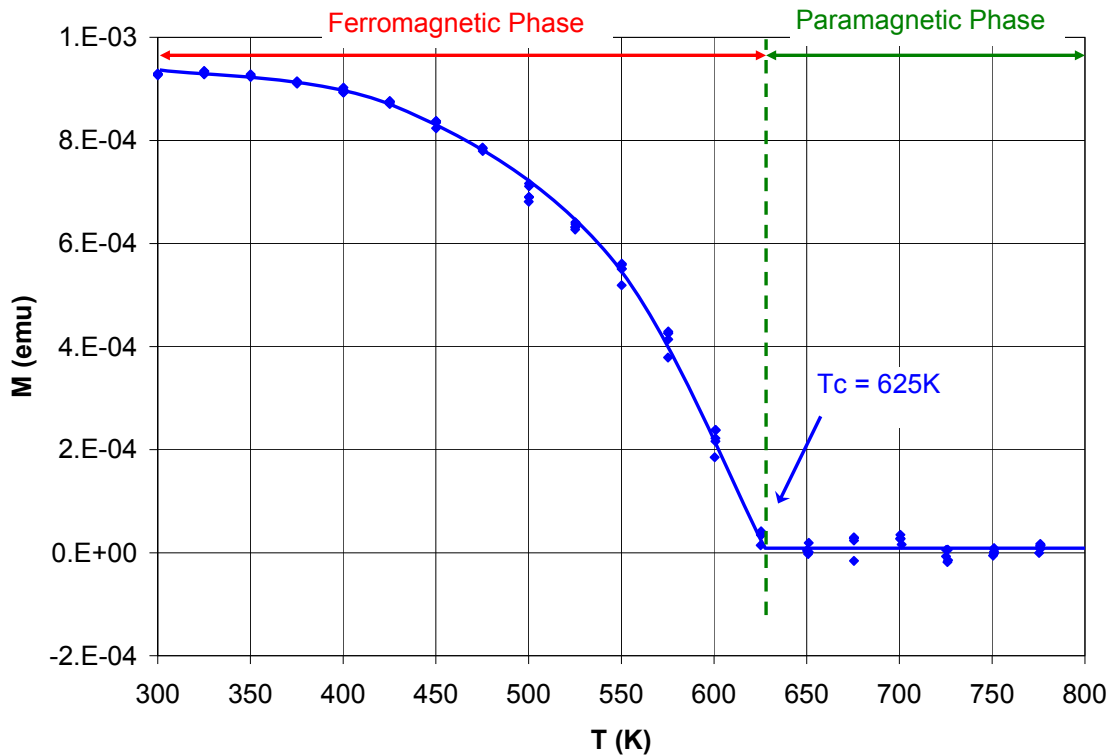


Figure 2-6. Magnetization as a function of temperature at 1000 Oe for a nickel thin film on a silicon substrate. The measured Curie temperature is 625K. Below the Curie temperature nickel is ferromagnetic and above it, nickel is paramagnetic (own measurements).

It should be noted in passing that the silicon wafer's magnetization is 2 orders of magnitude smaller than the Ni film and therefore is not taken into account into our analysis.

The magnetization can be zero at zero external field in the following cases: if the material has never been exposed to a magnetic field (then it is called a virgin material) or if the material is de-gaussed (use of an alternating field to randomize the spins) or by heating the sample above its Curie temperature for example.

In order to explain how the magnetization can be zero in a ferromagnet Weiss introduced the concept of domains. Each domain contains only electrons having magnetic moments oriented in the same direction. Figure 2-7 schematically represents the different magnetic orientations which can be taken while exposed to an external magnetic field.

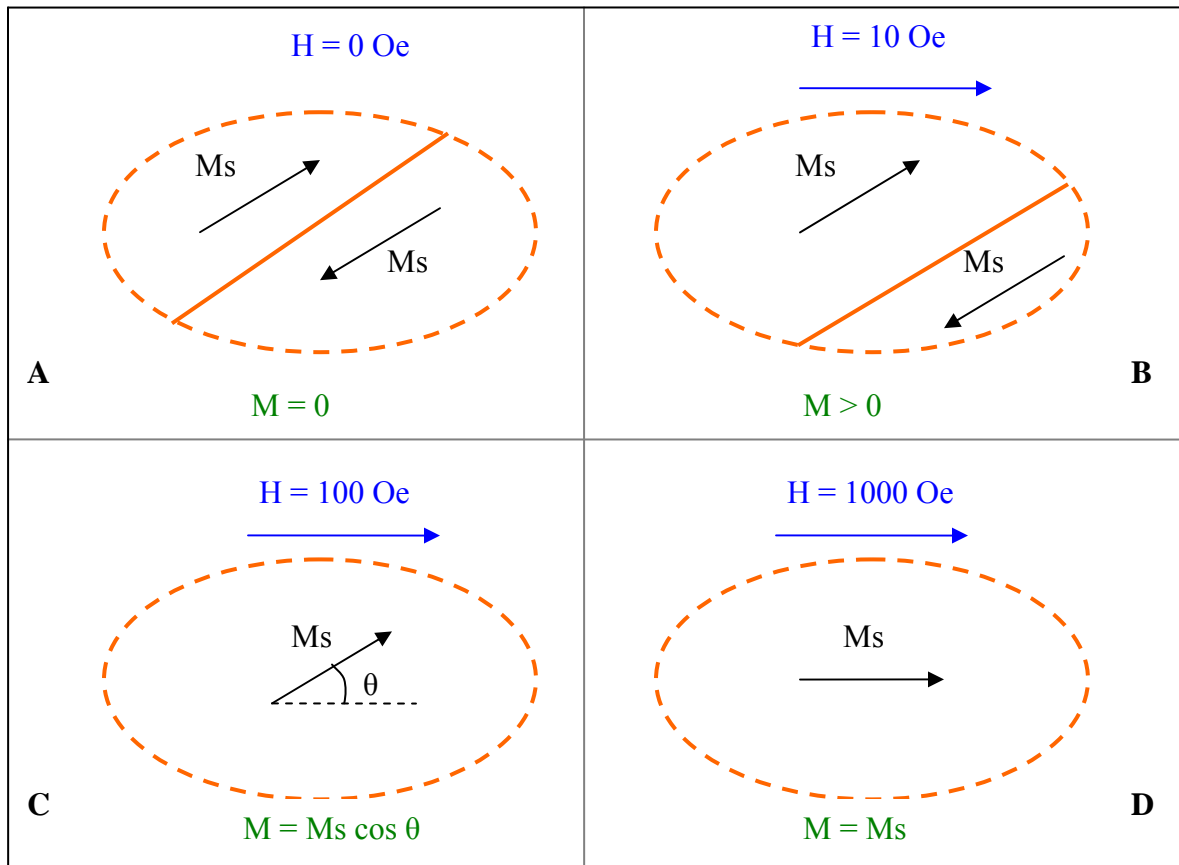


Figure 2-7. Magnetization process. A) the magnetic field is zero and the magnetizations from each domain cancel each other. B) under a small magnetic field the domain wall moves and increases the magnetic moment of a domain while decreasing the other one, the net magnetization is not zero. C) at a higher field there is only one domain left and the total magnetization depends on the angle between the magnetic field and the domain magnetic moment. D) at the saturation field the magnetization is maximum.

In the example of Figure 2-7, at zero field the two domains have opposite magnetic moment leading to a total magnetic moment of zero. Once we apply an external field, the magnetic domain which is oriented the closest to the direction of the field increases in size. Once

the magnetic field is high enough there is only one domain left. Then as we continue to increase the external magnetic field the domain magnetic moment orients itself toward the field until it is completely aligned. At this point the total magnetization is equal to the saturation magnetization.

The notion of magnetic domains is essential in order to understand a limiting phenomenon in ferromagnetic materials. This phenomenon is called superparamagnetism. It appears when the theoretical domain size is larger than the particle of a given material. To explain this important phenomenon, we will use the simple case where a material is formed of spherical, identical and independent particles (no magnetic coupling). At a critical size, the thermal agitation randomly orients the magnetic moment of the entire particle. Within the particle, the electron magnetic moments stay coupled such that they all align in the same direction. Figure 2-8 shows the different magnetic states as a function of the size.

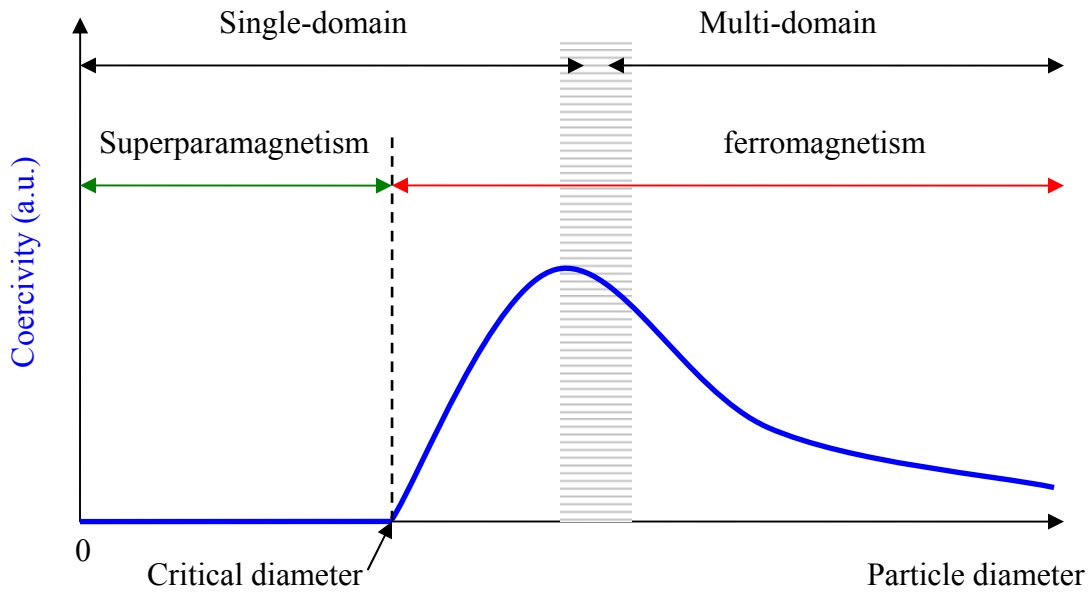


Figure 2-8. Magnetic phases as a function of particle diameter.

For example, the critical particle diameter for Cobalt is 2 nm¹ (measured at 76K) which equates to 380 atoms of cobalt. Above 2 nm cobalt particles behaves as ferromagnets while for

particles smaller than 2 nm it behaves like a paramagnet. From this definition, we now understand why superparamagnetism is different from quasiferromagnetism.

In conclusion, ferromagnetism is originating from the positive exchange interaction from the electron's spins. It requires a minimum amount of unpaired spins grouped together in order to prevent going into the superparamagnetic state.

What we have described so far is classical magnetism. Now, we are going to present recent results on magnetic phenomena which have not been forecasted by the classical theory of magnetism and in particular the theory of ferromagnetism.

2.4 Unclassified Magnetic Materials

Our group has been active in magnetic material research since the mid-nineties. In 1995 Hack³ discovered that spark-processed silicon had a magnetic hysteresis loop at room temperature and demonstrated that the magnetic behavior was not due to ferromagnetic impurities. He suggested that the magnetic behavior was due to defects present in the processed material. Later, our group investigated silicon irradiated by Si, Ar and neutrons⁴. We found that these Silicon-based materials have a high number of defects as well as similar magnetic behavior as spark-processed Si. More details about the process and the characterization of these materials will be given in the following chapters.

We can distinguish three main groups of materials which could not be classified according to the previous definitions of diamagnets, paramagnets, ferromagnets, or other classical magnetic materials. These materials are not predicted by the classical theory of magnetism.

The first group of materials is based on carbon. Carbon in the form of graphite or diamond is diamagnetic, but carbon can be made paramagnetic or ferromagnetic-like using specific processes. For example, Esquinazi⁵ showed in 2002 that highly oriented pyrolytic graphite (HOPG) has a magnetic hysteresis at room temperature stemming from defects in carbon rather

than from magnetic impurities such as Iron (Fe) or Nickel (Ni). They postulated that it is not a ferromagnet because the observed hysteresis does not originate from partially filled d or f shells like in Fe, Ni, Co or rare earth elements. In addition, HOPG graphite has topological defects such as grain boundaries and edge states. It is understood that these defects are of the “dangling bonds” type which provide unpaired spins. It is believed that these unpaired spins, when correlated, give rise to the hysteresis behavior. The magnetization under a magnetic field only changes by 10% with temperature ranging from 300 to 500K. This is characteristic of a high Curie temperature. Also, it is to be noted that the HOPG graphite has a paramagnetic behavior at low temperatures. HOPG graphite has two magnetic components, one which is strongly temperature dependant at low temperatures, characteristic of dangling bond defects and one which is weakly temperature dependant at high temperatures (well below the Curie Temperature). It is associated with the hysteresis loop at room temperature which is characteristic of ferromagnetism. HOPG graphite cannot be classified as a ferrromagnet since no domains could be shown. Furthermore, Esquinazi⁶ and Spemann⁷ use proton irradiation (i.e. ionized hydrogen) to increase the magnetization of the HOPG graphite leading to magnetic domains. They present magnetic force microscopic images (MFM) and scans where magnetic domains can be seen in or around the irradiated spot. Final judgment on their interpretations needs to await further experimental results. Specifically, it is noted that they do not show magnetic domains in non irradiated HOPG even though it has a magnetic remanence. Also, proton irradiation of carbon changes the surface morphology and therefore affects the quality of the MFM images. It is possible that the magnetic domains presented could be artifacts due to the radiation damages. In addition, Spemann⁷ hypothesizes that magnetic ordering in HOPG is due to defects (i.e. “dangling bonds”) and the implanted hydrogen. Finally, no mechanism is

proposed to explain the exchange interaction between the unpaired spins (i.e. “dangling bonds”). Esquinazi’s group has published many papers on this topic⁸⁻¹².

Carbon nanofoam also has unusual magnetic properties. This material is produced using laser ablation/evaporation of carbon from an ultra high purity target onto a glass substrate. Rode¹³⁻¹⁵ in 2004-2006 presents evidence of ferromagnetism in carbon nanofoam below 90K. Above this temperature the nanofoam behaves as a paramagnet. It is well demonstrated that ferromagnetism is not due to impurities such as Ni or Fe and that the paramagnetic behavior is not due to Oxygen. They observe a decrease in the magnetization over time. We call this behavior room temperature annealing. It is another evidence of lack of impurities in the nanofoam since impurities do not disappear or self anneal at room temperature. In particular it is shown that carbon nanofoam has a coercive field of 420 Gauss at 1.8K. This is evidence of ferromagnetism-like behavior. The authors explain that the nanofoam has a large number of unpaired spins attributed to defects and they believe that it is at the origin of the observed magnetic behavior. Furthermore, they speculate that the nanofoam is formed of metallic carbon clusters separated by non conduction carbon walls, which would explain its overall magnetic and electrical response. The nanofoam is a semiconductor (explained by the behavior of non conducting walls) and has ferromagnetic-like clusters due to itinerant electrons which are responsible for the positive exchange interaction between the unpaired spins.

The Carbon nanofoam as well as the HOPG graphite are not true ferromagnetic materials. In addition, since the origin of the magnetic hysteresis and high Curie temperature is attributed to defects we classify these materials as quasiferromagnets.

Several research groups modeled the magnetic properties of carbon structures. Orellana¹⁶ demonstrated, through ab-initio calculations, that carbon nanotubes with a monovacancies

exhibits ferromagnetic ordering, while the same carbon nanotube with divacancies does not exhibit ferromagnetic character. Orellana used defects in carbon nanotubes to introduce undercoordinated carbon atoms. Furthermore, no mechanism is proposed to explain the positive exchange interaction between unpaired spins and the unusually high Curie temperature of such carbon structures. Similarly, Park¹⁷ calculated the stability of T-shaped carbon nanotube structures which demonstrates the possibility of unpaired spins on carbon atoms specifically located at the junction of carbon nanotubes. Park showed that curved graphite sheets modify the electronic structure of certain carbon atoms leading to unpaired spins. We believe that these unpaired spins have a similar role as dangling bonds. They are most probably at the origin of the magnetic hysteresis behavior. No mechanism was proposed by these authors to explain the exchange interaction between the unpaired spins.

All authors (experimentalist or theorist) who have studied the carbon based ferromagnetic-like materials agree that it stems from defects allowing for unpaired spins. They disagree as to where these unpaired spins come from. For some, it is due to dangling bonds while for others it is due to a modified electronic structure of carbon atoms (curved sheets). None of these authors propose a mechanism to explain the exchange interaction between the unpaired spins. Similar work has been done on silicon-based materials. We review here the work of the main-stream authors in this area.

In 1993, Laiho¹⁸ prepared porous silicon using anodic etching. The porous Si which he manufactured presented a magnetic hysteresis response as well as a Curie temperature of 570K. Porous Si is only composed of Si with a surface oxide (SiO_2). Laiho investigated the Si dangling bonds present in the material using Electron Paramagnetic Resonance (EPR). The EPR technique

showed direct evidence of dangling bonds. The dangling bonds create unpaired spins which are believed to be at the origin of the magnetic hysteresis loop observed.

Another technique is used by Khokhlov¹⁹ in 1967 to prepare silicon samples with a high number of paramagnetic defects (i.e. dangling bonds). Ion implantation using Neon and Argon is used at high doses (up to $3 \times 10^{17} \text{ cm}^{-2}$) to create large amount of defects. EPR is also used to investigate the paramagnetic centers. It is shown that the intensity of the absorption of microwaves, which is directly related to the susceptibility, does not follow a Curie law as it is always the case for paramagnetic materials. This is why Khokhlov suggests that such a material has a ferromagnetic phase. He measures a magnetic transition temperature of 150K using EPR. It is to be noted that no hysteresis curve is shown in his work. Our research furthers this work. It will be presented in Chapter 5 chapter.

Spintronics is the study and use of electron spins in electronic devices. Since it is a very recent field of study, the boundaries of this field are not well defined. Spintronics regroup giant magnetic resistance materials (metal alloys), semiconductors doped with magnetic ions, such as Mn, Co, Gd... Authors utilizing magnetic carbon also claim to be part of this field. In order to be precise and clear, we will define the spintronics materials as containing magnetic elements, d-shell or f-shell magnetic ions, like Gd, Mn, Co, Ni, with a ferromagnetic behavior and a potential to be used as magnetically driven devices. Therefore, our definition excludes carbon-based materials and other materials not containing magnetic ions.

More recently (2006) Bolduc²⁰ investigated the structural properties of ferromagnetic Mn implanted Si. It is classified as a spintronics material. Mn is implanted at doses ranging from 10^{15} cm^{-2} to 10^{16} cm^{-2} corresponding to peak concentration of 0.1 to 0.8 at. %. Hysteresis loops at room temperature are presented before and after annealing. A 5 min annealing at 800°C

increases the area of the hysteresis. Bolduc suggests that the Mn implanted Si magnetic behavior is due to carrier mediated interactions. In other words, the Mn electron spins interact together through the mediation of itinerant electrons.

Even if we do not agree with the conclusions of Bolduc and the origin of ferromagnetism we do not dispute the facts presented in his paper. More arguments will be given in the discussion part of this dissertation as to why we disagree with Bolduc on the origin of the magnetic hysteresis.

Another interesting material for its magnetic properties is CaB_6 . Lofland²¹ measured, in 2003, the magnetic response of CaB_6 as a function of temperature and demonstrated that the magnetic response varies with the environmental condition (gas employed during the annealing). He explained these differences by an increased number of defects due to gas-sample's surface interaction and subsequently that the ferromagnetic-like behavior in CaB_6 was due to dangling bonds.

Finally in 2005, Coey²²⁻²⁴ proposed several mechanisms to explain the magnetic behavior of the different carbon polymorphs, CaB_6 as well as the diluted magnetic semiconductors (DMS). DMS are semiconductors such as Si, GaN, GaAs or ZnO doped with magnetic ions such as Mn, Cr, Co, Ni or Gd. DMS are spintronic materials. First, Coey showed that the DMS behavior cannot be explained by the magnetic responses of the diluted ions within the material. For example, magnetization of ferromagnetic doped ZnO films decay with time²⁴. When magnetization is measured several times over a period of weeks, a clear decrease is observed due to self annealing (it is to be noted that this phenomenon is unrelated with superparamagnetism). These observations are not compatible with the classical explanation given for DMS, i.e. that the magnetic behavior is due to the interaction between itinerant electrons and electrons in the d or f-

shell of the magnetic ions. In addition Coey explained that DMS have a high number of crystal defects. Therefore, similarly to ferromagnetic-like carbon, he suggested that the origin of the magnetic hysteresis as well as the high Curie temperature is defects related. Even though Coey conceptualized the field of ferromagnetic-like materials and spintronics, he did not demonstrate which model or mechanism explains the observed phenomena.

In this dissertation we explore the origin of the magnetic hysteresis as well as the high Curie temperature associated with it in the case of materials for which explanations are incomplete or none existing.

Quasiferromagnetism is characterized by a magnetic hysteresis stemming from defects rather than from magnetic ions. Usually, quasiferromagnets have high Curie temperatures. In conclusion, all the unclassified materials which are believe to have their magnetic behavior defects related are quasiferromagnetic. This includes HOPG and nanofoam carbon, spark processed silicon, ion implanted silicon and to some extend ZnO doped with Mn where it is demonstrated that defects rather than Mn ions are responsible for the magnetic behavior.

2.5 Summary

There are several classes of magnetism:

- Diamagnetism stems from the electrons orbital moment. It is opposite to the field which created it.
- Paramagnetism originates from the spin of independent unpaired electrons. The magnetization is in the same direction as the field which created it. It is proportional to the inverse of the temperature.
- Ferromagnetism is characterized by its remanence and its Curie temperature. The remanence is due to the interaction of electron unpaired spins. The Curie temperature is a critical parameter as it is related to the strengths of that interaction.

- Superparamagnetism is a limiting case of ferromagnetism. It is observed when the thermal agitation randomizes the domain magnetization in small particles.
- A new class of magnetic material is proposed as a way of labeling materials in order to better explain their non classical magnetic behavior. Quasiferromagnetism appears in materials, such as s-Si, with a high density of defects, i.e. dangling bonds. It is postulated that the observed remanence is stemming from the interaction between the unpaired spins. A Curie temperature similarly to ferromagnetism is observed.

CHAPTER 3
MANUFACTURING, MACROSCOPIC CHARACTERIZATION AND EXPERIMENTAL
RESULTS OF QUASIFERROMAGNETIC MATERIALS

3.1 Room Temperature Study of Spark-Processed Silicon

3.1.1 Production of Spark-Processed Silicon for Magnetic Studies

The manufacturing of spark-processed silicon (sp-Si) was first developed by Hummel²⁵ with the intent of using the optical properties (specifically luminescence) of this newly created material. This method consists of applying a high voltage (several thousand volts) at a high frequency (several tens of kilo-hertz) between a substrate and a counter electrode, typically made of tungsten. I made several modifications to the original process in order to manufacture quasiferromagnetic sp-Si. These modifications include a change in the position of the substrate with respect to the stage and the use of a laboratory made power supply with slightly different voltage and frequency ranges. A complete description of the power supply which I designed and assembled is available in Appendix A. Figure 3-1 illustrates how sp-Si is produced: a silicon substrate is glued on an aluminum stage with silver paint.

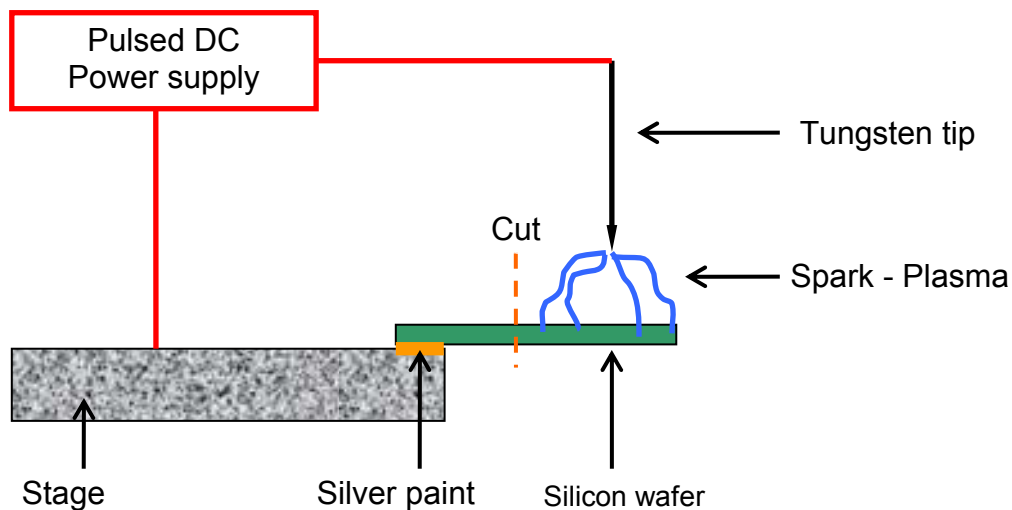


Figure 3-1. Spark-processing of silicon. A power supply provides several kilo-volts between the electrode and the substrate. The substrate is “hanging” from the stage and glued with silver paint. The end of the substrate (i.e. the sparked area) is subsequently cut at the mark to avoid any possible contamination of the sample.

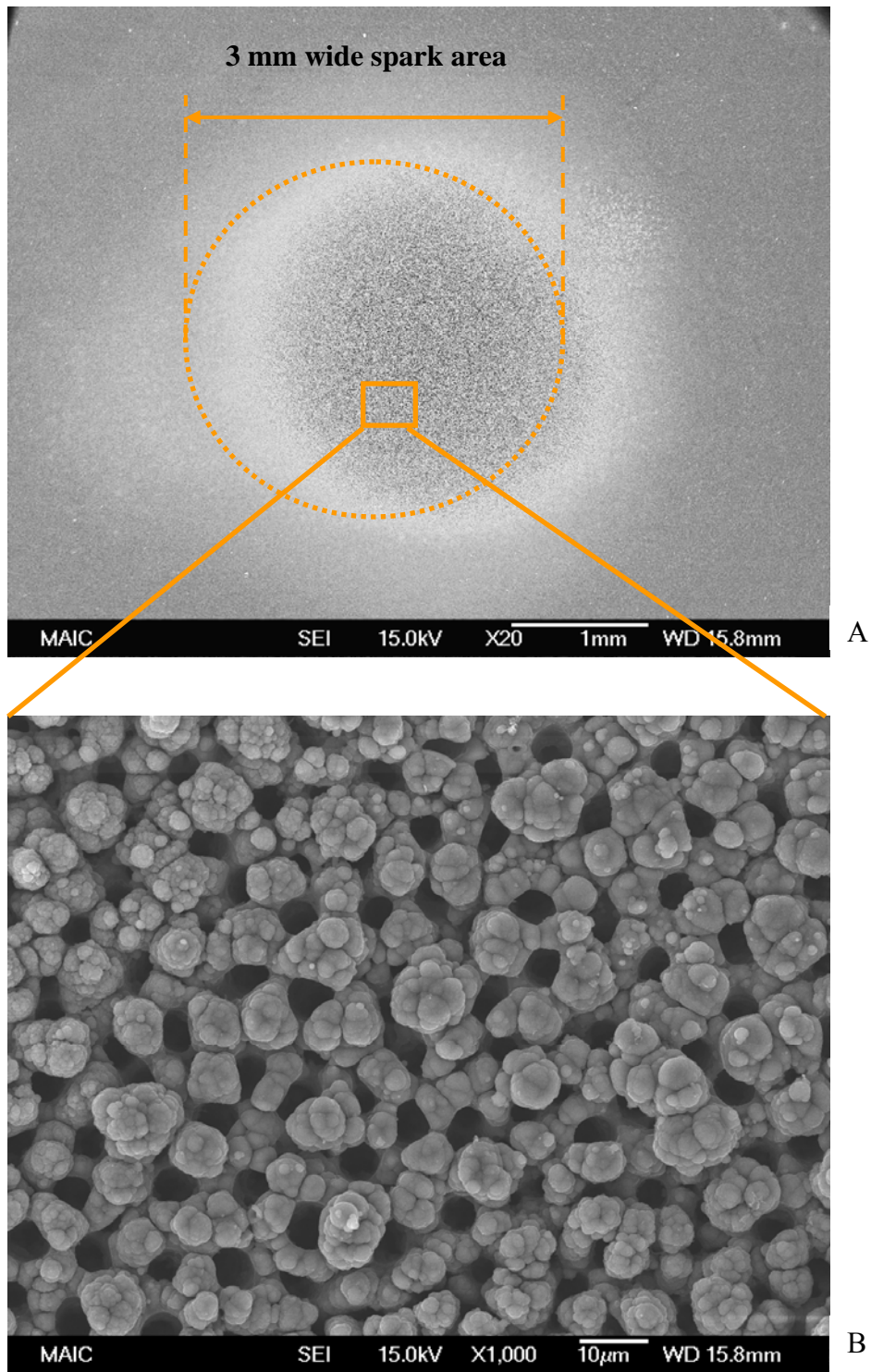


Figure 3-2. Scanning electron micrograph of spark-processed silicon. A) large top view. B) zoom-in view.

The silver paint provides the necessary conductivity for the current to flow from the substrate to the stage. The substrate hangs from the stage in order to prevent contamination through diffusion (or sparking) between the stage and the substrate. Once the silicon is spark-processed the substrate is cut as shown in Figure 3-1, to separate the potentially contaminated part (in contact with the stage) from the sample. The sample can be made to sizes ranging from 2mm x 5mm to 5mm x 10mm. The size of the sample is an important parameter in the characterization process since each equipment has a different size requirement.

To manufacture the samples, the voltage, current, duty cycle and tip to substrate distance are set while the frequency and the sparking time are varied with the laboratory made power supply.

Scanning electron microscope (SEM) micrographs of sp-Si were taken to show how our material looks like after being manufactured. Figure 3-2A is a large scale top view while Figure 3-2B is a zoomed-in picture of a small area of sp-Si. A large round sparked area is visible. It is composed of silicon, oxygen and up to 5% nitrogen, as previously shown elsewhere²⁶. The close look at the surface reveals large porous, and sphere-like particles.

Note: I published a study on sp-Si²⁷ in which I found a volume porosity of 43%.

Now that we have described the spark process technique, we can look how the process parameters influence the magnetic response.

3.1.2 Magnetic Characterization Process Parameter Influence

Several samples of sp-Si were prepared under various processing conditions and their magnetizations were observed as a function of an external magnetic field at room temperature, i.e. 300 K. In this section, we will present the results of these experiments.

Figure 3-3 is a typical magnetization curve as a function of the magnetic field for sp-Si. We used a commercial super quantum interference device magnetometer (SQUID) to conduct

the experiment. A hysteresis loop is observed at room temperature. The sample was spark-processed for 6 hours.

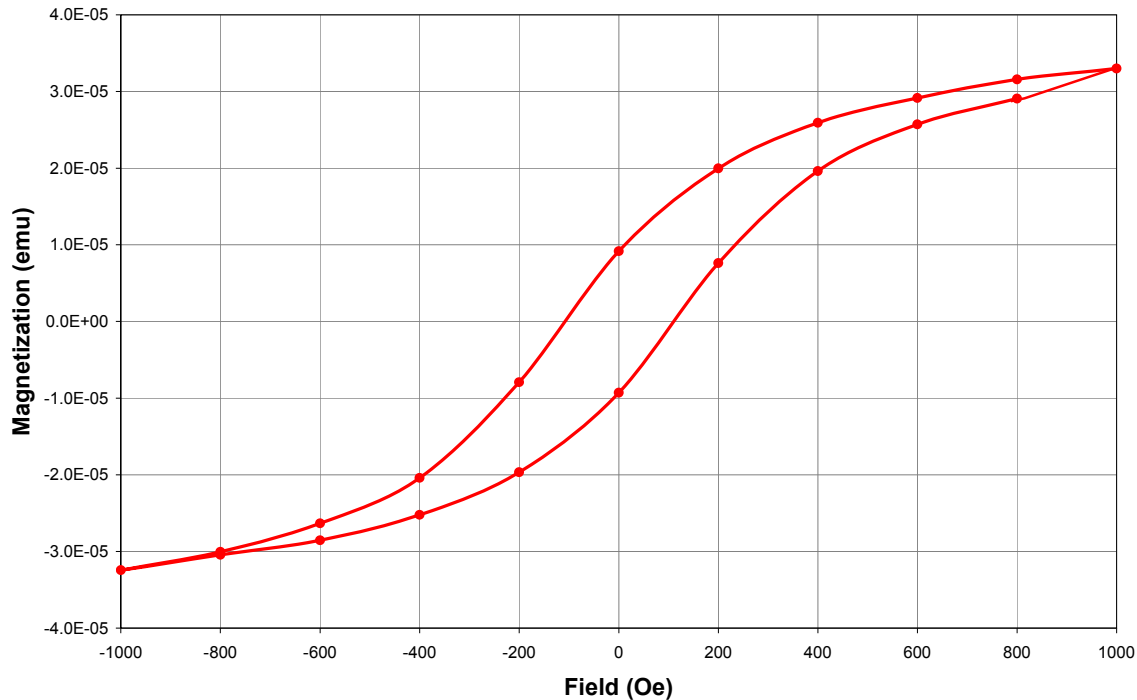


Figure 3-3. Magnetization as a function of magnetic field strength measured at room temperature for spark-processed silicon (sparking time = 6 hours, frequency = 22.5 kHz).

It could be argued that the hysteresis loop is due to ferromagnetic impurities such as iron, nickel or cobalt. In order to investigate this Secondary Ion Mass Spectroscopy technique (SIMS) has been applied down to the resolution limit of the instrument. For example, SIMS maximum resolution for iron in silicon is 5×10^{13} at.cm⁻³. Figure 3-4 displays the mass spectrum of sp-Si. For clarity a zoom in around the area where the iron isotope with a mass of 54 amu should be, is displayed Figure 3-5. As observed it iron is not detected. It should be concluded that ferromagnetic impurities cannot explain the observed magnetic hysteresis of sp-Si.

It should be noted in passing that surface passivation with hydrogen did not change the size or shape of the observed hysteresis.

We use two parameters to characterize the magnetic response: the remanence and the magnetization at 1000 Oe. The remanence is define as the magnetization at zero field after the sample has been exposed to an external field equal to or greater than the saturation magnetization, taken to be 1000 Oe for sp-Si. Figure 3-6 displays the remanence (M_r) and the magnetization at 1000 Oe (M_s) as a function of the processing frequency. Both, M_r and M_s increase as a function of frequency up to 22.5 kHz then decrease down to 25 kHz. Stora²⁸ observe a similar behavior with the photoluminescence of sp-Si. The photoluminescence intensity increases as a function of the frequency up to 10 kHz for the UV/blue band and 15 kHz for the green band and then decrease for high frequencies. It is to be noted that below 8 kHz there is no sparking. The frequency is too low to initiate a spark through the air between the tip and the substrate.

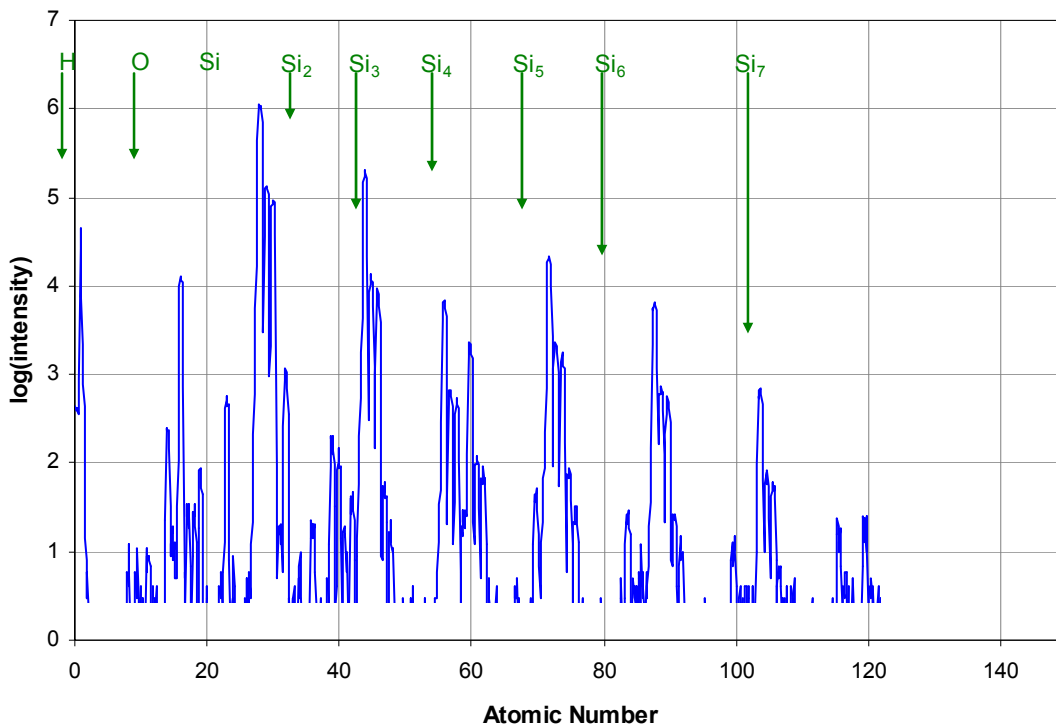


Figure 3-4. Secondary ion mass spectrum of spark-processed silicon. The largest peaks have been labeled accordingly. See also Figure 3-5.

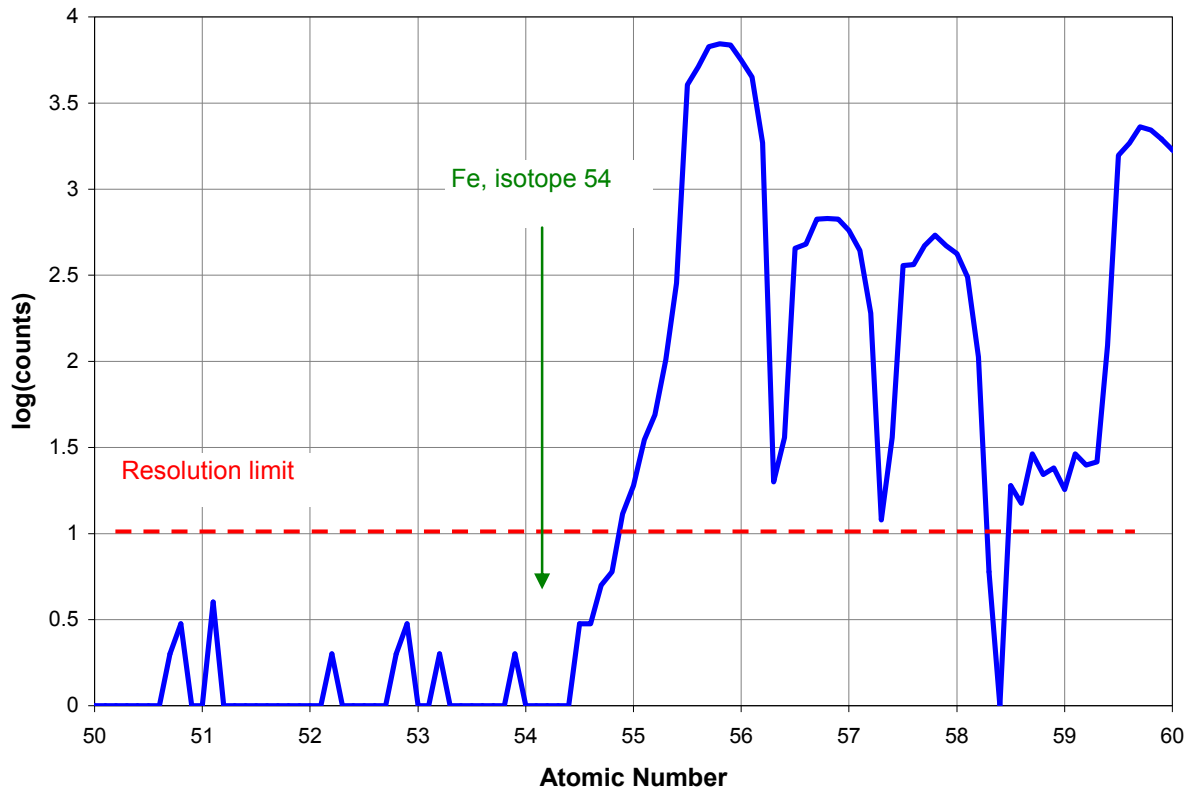


Figure 3-5. Secondary ion mass spectrum of spark-processed silicon zoomed in around the iron atomic number. An arrow marks the position of where the iron isotope with an atomic mass of 54 should be if it was present in the sample.

Figure 3-7 displays the remanence and magnetization at 1000 Oe as function of sparking time. The longer the substrate is processed the larger the magnetization. Stora²⁸ published a similar conclusion when studying the intensity of the photoluminescence of sp-Si as a function of the sparking time.

Even though knowing the influence of the process parameters are important information, more crucial information can be obtained by studying the magnetization as a function of temperature. Since we know that the samples prepared at a frequency of 22.5 kHz exhibit the strongest remanence (Figure 3-6), the next section will focus on studying sp-Si magnetization at high temperature (300 – 800 K) with samples prepared at this frequency.

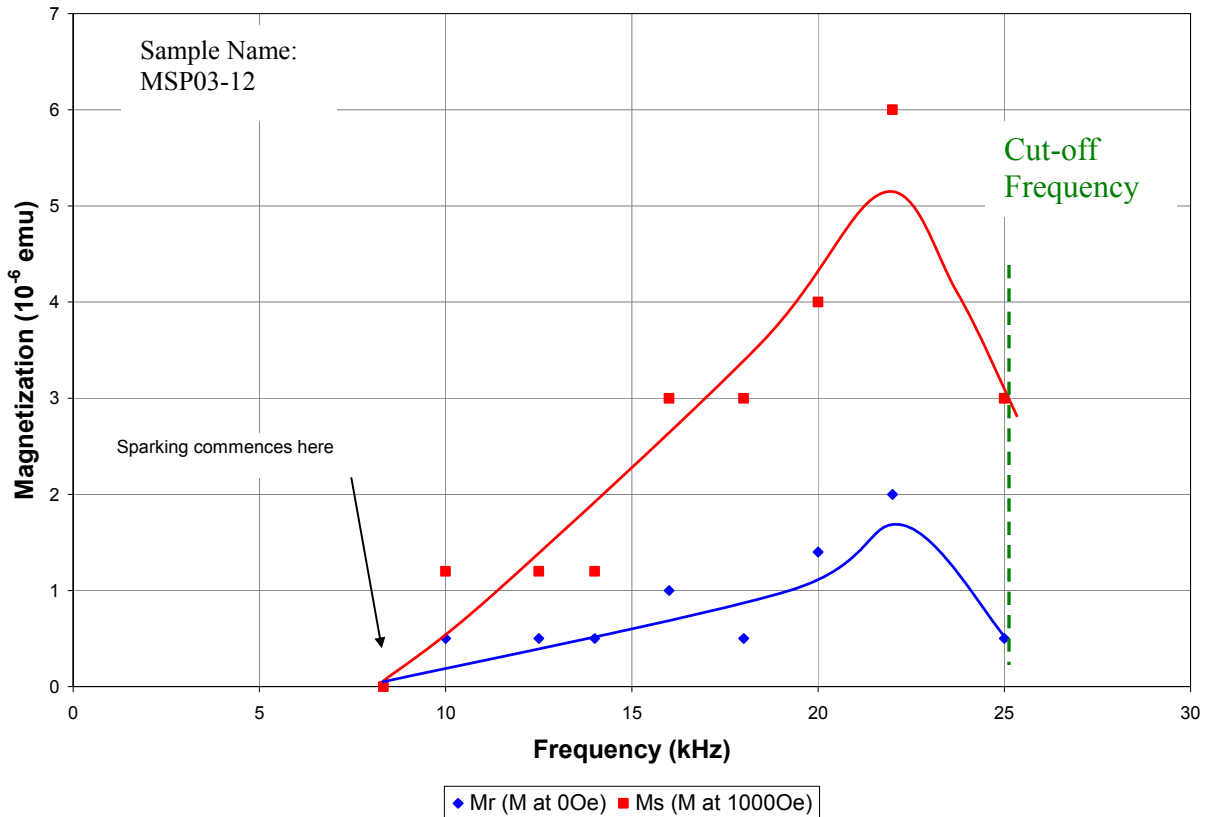


Figure 3-6. Spark-processed silicon magnetization at 0 Oe (i.e. remanence) and 1000 Oe as a function of the spark frequency (sparking time was set at 12 hours for all samples).

3.2 Magnetic Characterization of Spark-Processed Silicon at High Temperature

In this section, we describe the temperature dependence of the magnetic properties of sp-Si. Measuring the high temperature dependence in a SQUID magnetometer is by no means a trivial task for small signals as it is the case for spark-processed silicon. Therefore, we first describe a new measurement procedure to overcome the limitation of the SQUID magnetometer for temperature ranging from 300 to 800 K.

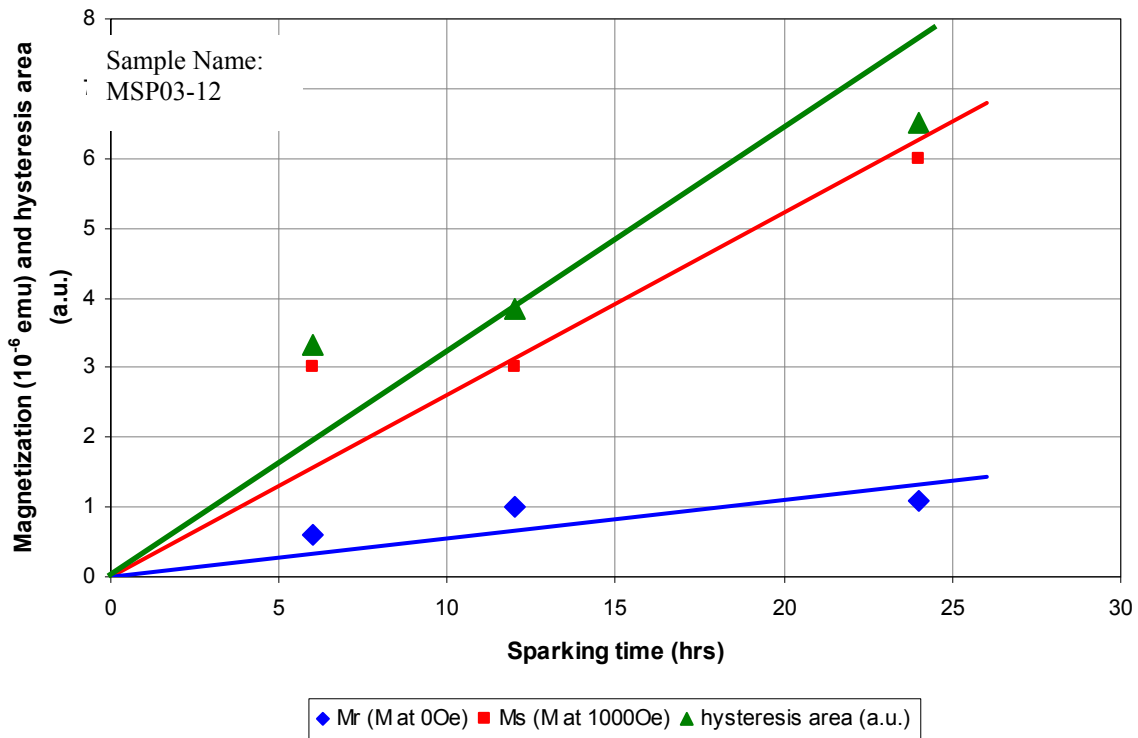


Figure 3-7. Spark-processed silicon magnetization at 0 Oe (i.e. remanence,) 1000 Oe and hysteresis area as a function of the sparking time (spark frequency was set at 16 kHz for all samples).

3.2.1 Magnetic Characterization Method at High Temperatures

All of our high temperature magnetization experiments were conducted in a commercial SQUID with an oven option. This oven insert allows us to measure magnetization as a function of temperature in the range 300 – 800 K. The commercial software sold with the SQUID is designed to measure the magnetization with a maximum resolution of 10^{-7} emu without the oven insert and 10^{-5} emu with the oven insert while controlling the temperature with great accuracy (0.01 K). But the resolution limit of 10^{-5} emu was not acceptable for our purpose since our samples have typical magnetization in the 10^{-6} emu range. Therefore, I modified the measurement procedure in order to restore the magnetization resolution back to its 10^{-7} emu value. The drop in maximum resolution is due to the heating system within the oven. Figure 3-8

shows a schematic representation of the oven apparatus installed in the SQUID magnetometer. It is important to notice that the oven is inserted in the detector loop. When the computer software controls the temperature of the oven, it continuously adjusts the current in the heating element which causes the detector to acquire an additional unwanted signal. This unwanted signal decreases the resolution from 10^{-7} emu to 10^{-5} emu. In order to avoid this unwanted signal the temperature controller is turned off during the measurement. The measurement takes about 4 min and during this time the temperature drifts. The maximum drift is about 1 K at the highest temperature (800 K). This is down from the 0.01 K accuracy when the temperature controller is on but it is acceptable for our purpose. To summarize, the new measurement procedure is:

- the temperature is set while the temperature controller is on,
- the temperature controller is turned off when the temperature is stable,
- the magnetization is measured,
- the temperature controller is turned back on.

This improvement allows us to measure the magnetization as a function of the temperature of the samples with an acceptable loss of temperature accuracy.

Other procedures were suggested by the manufacturer of the SQUID magnetometer but implementing them revealed to be extremely difficult. To our knowledge, no one else has ever used this new procedure to measure small magnetization with the oven insert. It should be noted in passing that this procedure has been validated by the manufacturer before it was implemented to prevent any damages to our equipment. In addition to improvements in the computer software, a new sample holder was constructed. Indeed, the two types of sample holders proposed by the SQUID manufacturer were not intended to work at such high resolution with the oven insert. The first type of holder is made of copper wires and has a limited resolution of about 10^{-4} emu (measurement not shown) due to magnetic impurities in the copper.

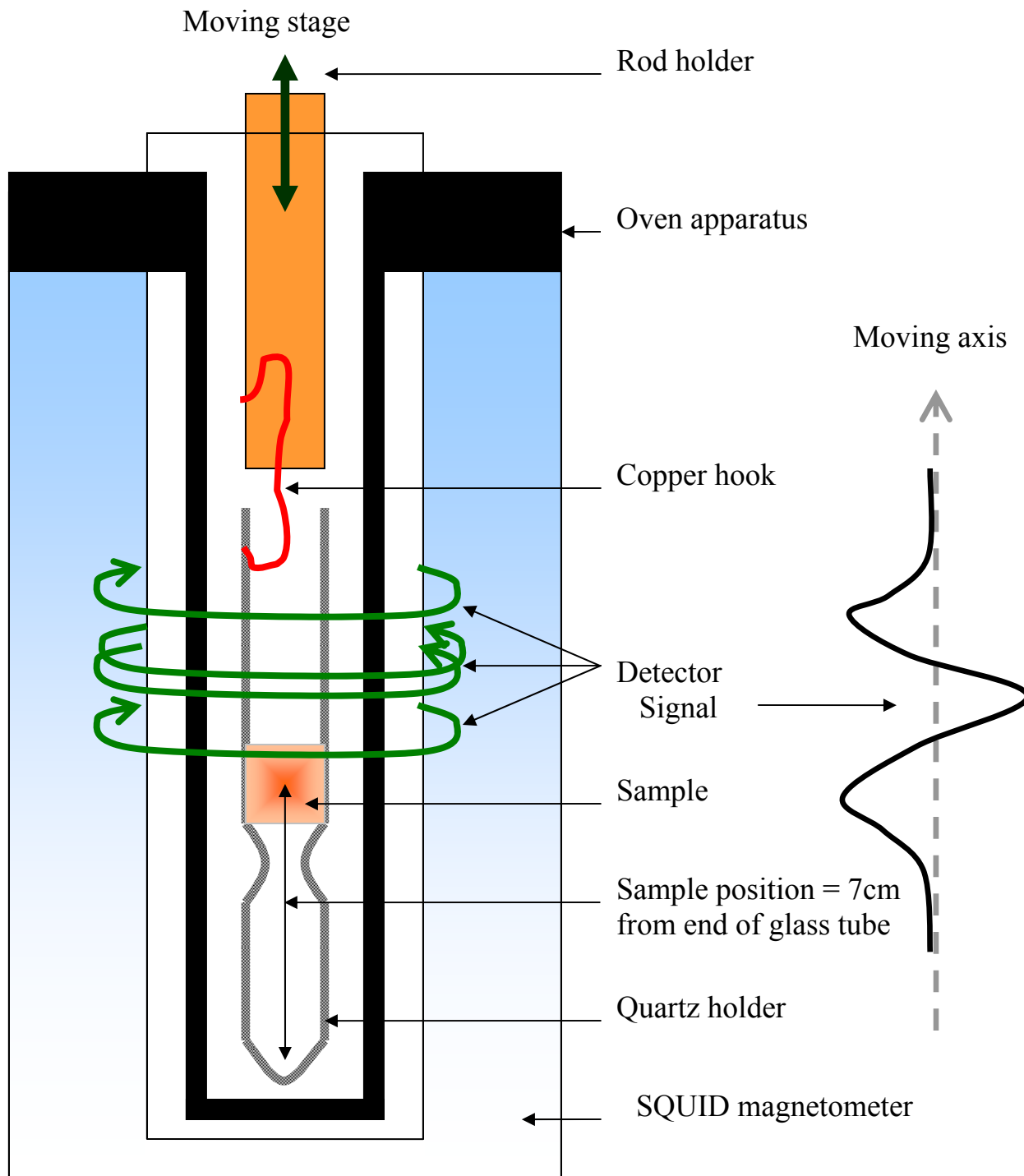


Figure 3-8. Super quantum interference device magnetometer with oven insert and sample holder.

The second type made of quartz had to be modified to reduce the diamagnetic response added to the sample signal. We re-designed the quartz holder proposed by Lewis²⁹. Lewis proposed a quartz sample holder composed of an outer quartz tube with two inner quartz rods fitted inside. In this case, the sample is being positioned between the two quartz rods. These two rods have a diamagnetic response which is superimposed to the signal coming from the sample. Such a holder reduces the accuracy of the magnetization measurement.

Our new design includes a thinner outer tube with a wall of 0.4 mm (instead of 0.6 mm for Lewis design) leading to a 30% decrease in mass, allowing accommodation of larger samples (2.2 mm up from 1.8 mm). In addition, the rods were removed while a notch in the quartz tube was added to hold the sample in place as shown Figure 3-8. These two modifications improved the magnetization signal coming from the sample while decreasing the influence of the signal generated by the holder.

In addition to the general design of the sample holder, the position of the sample with respect to the end of the holder is a critical parameter. It has been found³⁰ that the end of the quartz holder creates an artifact in the measurement. Also, it has been shown how to position the sample with respect to the end of the holder to prevent this artifact from interfering with the sample signal. Similarly, with our new designed holder we came to the same conclusion. In order to understand how to remove the artifact stemming from the end of the sample holder we now describe how the SQUID magnetometer calculates the magnetization from the detector voltage output signal.

In a SQUID magnetometer the sample is moved up and down along the vertical axis (Figure 3-8). When the sample moves, the detector measures the change in the magnetic flux as a function of z (the sample position). Then, the detector outputs a voltage, proportional to the

magnetic flux, which is plotted against z . Then, this curve is modeled by the computer to calculate the magnetization in emu units. The model, $f(z)$, used by the software is defined as followed: $f(z) = 2[R^2 + z^2]^{-3/2} - [R^2 + (z + L)^2]^{-3/2} - [R^2 + (z - L)^2]^{-3/2}$, where R and L are instrument constants. The computer only uses data spanning over a 4 cm range to calculate the magnetization.

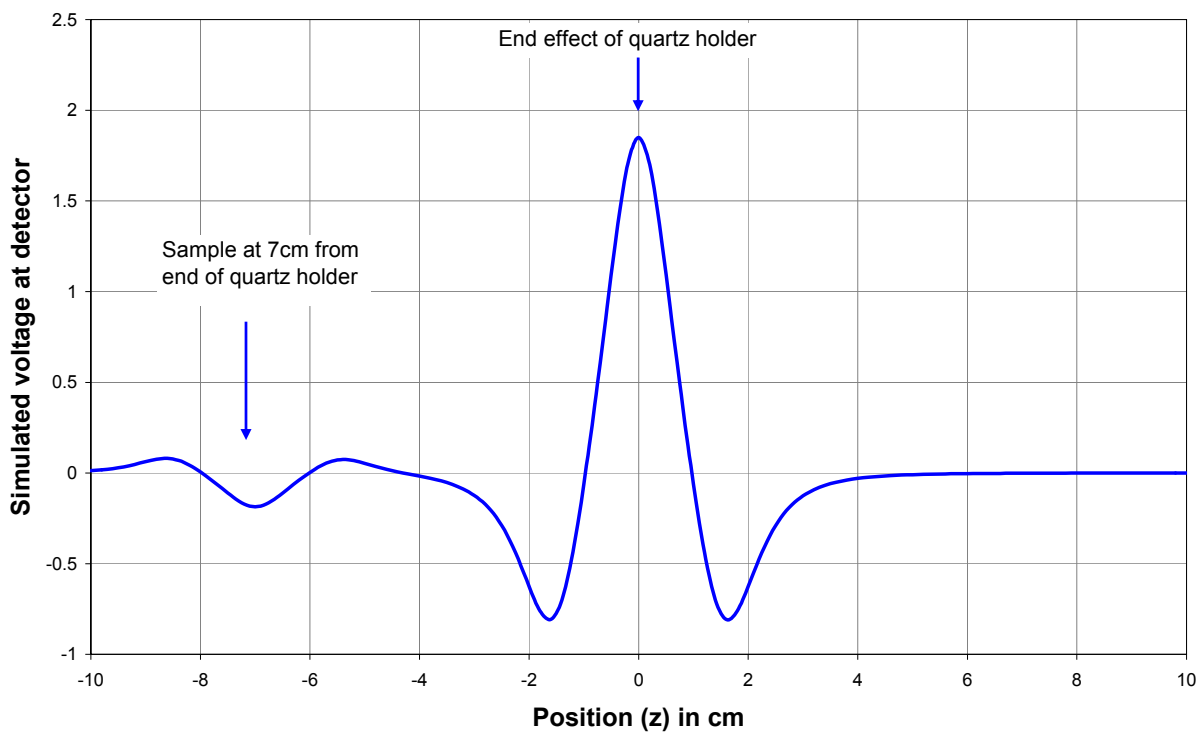


Figure 3-9. Simulated detector voltage (a.u.) as a function of the position. The simulated function is defined as: $f(z) - 0.1 \times f(z + 7)$.

In order to understand the artifact due to the end effect, we show on Figure 3-9 the simulated output voltage from the detector including both signals from the sample and the end of the holder. The simulated function is: $f(z) + 0.1 \times f(z + 7)$, where $f(z)$ is the signal coming from the end of the quartz holder while the second term $0.1 \times f(z + 7)$, simulates the sample signal. Usually, the sample signal is one order of magnitude smaller than the artifact signal and

positioned 7 cm away from the end of the holder. Figure 3-10 shows the simulated function centered at 7 cm (the sample position) with a range of 4 cm along with the modeled curve from the software.

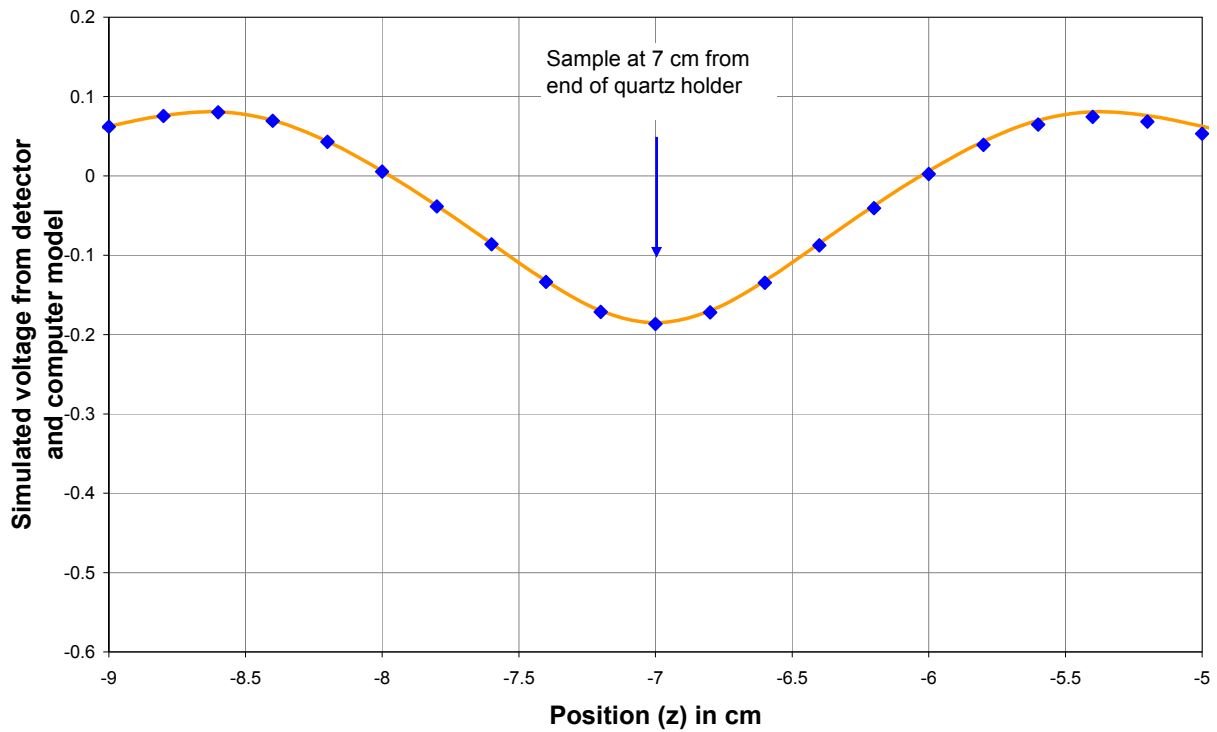


Figure 3-10. Simulated detector voltage (a.u.) as a function of the position (blue diamonds) zoomed in around the sample located 7 cm away from the end of the holder. The computer model is plotted in solid orange.

When the sample is placed at 7 cm from the end of the holder the modeled curve is very close to the simulated one (the correlation coefficient is greater than 0.9) and therefore the calculated magnetization is the correct value. On the other hand, when we position the sample at only 3.5 cm from the end of the holder the modeled curve does not fit with the detector voltage (the correlation coefficient is only 0.4). Therefore the calculated magnetization is an incorrect value. To illustrate this effect, Figure 3-11 shows the simulated curve when the sample is 3.5 cm

from the end of the holder. We observe that the signal from the sample and the one from the end of the holder overlap.

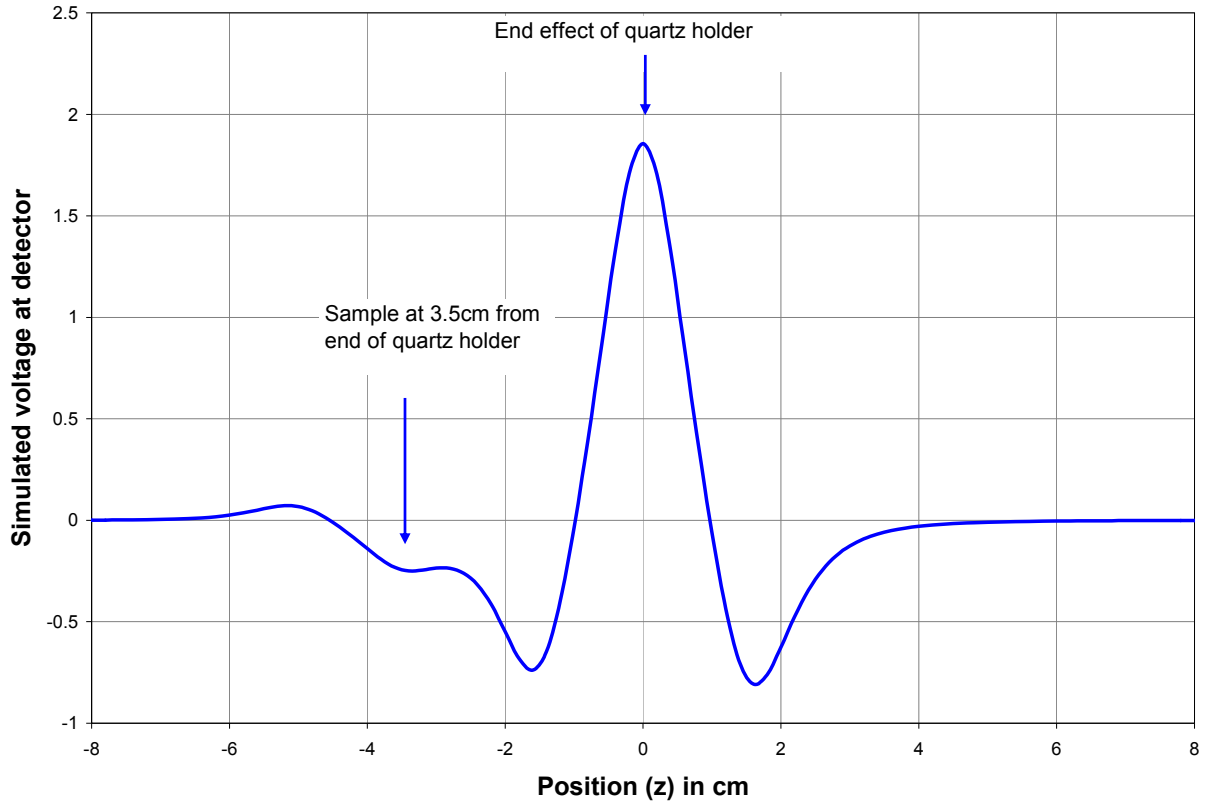


Figure 3-11. Simulated detector voltage (a.u.) as a function of the position. The simulated function is defined as: $f(z) - 0.1 \times f(z + 3.5)$.

Upon zooming on the 4 cm range around the sample, as shown in Figure 3-12 we clearly notice the large discrepancy between the model curve used to calculate the magnetization and the simulated detector voltage curve which causes an incorrect measurement.

Now, it becomes clear that the further the sample is located from the end of the quartz holder the more accurate the measurement. Unfortunately, the oven itself limits the length of the holder and therefore the maximum practical distance is 7 cm. With this design and proper sample position, the measurement accuracy is more than sufficient for our purpose.

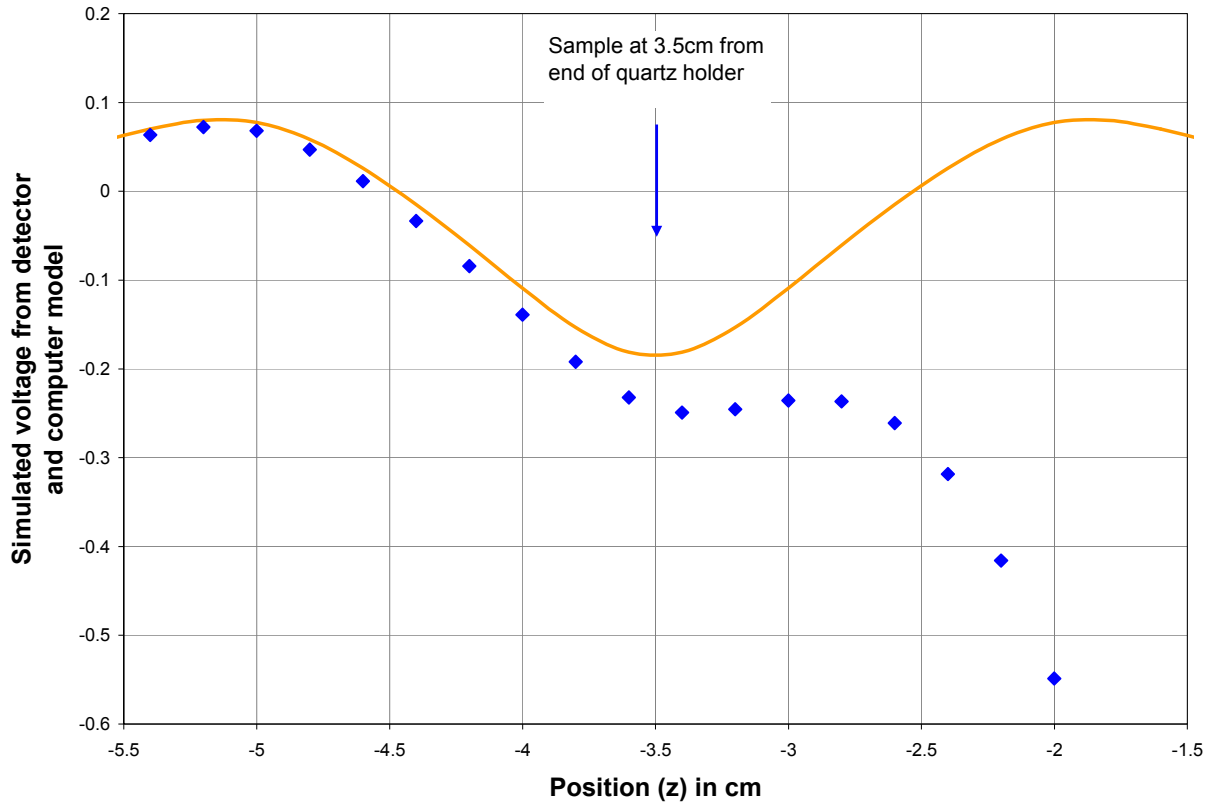


Figure 3-12. Simulated detector voltage (a.u.) as a function of the position (blue diamonds) zoomed in around the sample located 3.5 cm away from the end of the holder. The computer model is plotted in solid orange.

To summarize, here are the modifications done to the SQUID in order to measure the magnetization in the temperature range 300 to 800 K:

- Add the oven insert,
- Use an ultra thin tube for the holder,
- Use a notch in the holder rather than inner rods for sample support,
- Position the sample with respect to the end of the tube as far as possible,
- Turn off the temperature controller during each measurement,
- Turn back on the temperature controller and go to the next data point.

3.2.2 Verification of the Modified Magnetometer

In order to validate the SQUID modifications and before measuring the magnetization of sp-Si, three experiments were made.

First, the magnetization as function of temperature at 1000 Oe of a pure nickel sample was measured; the data is presented in Figure 3-13. We observe a Curie temperature of 625 K to be compared with published value² of 631 K. This is a very good agreement and corresponds to a discrepancy of less than 1%.

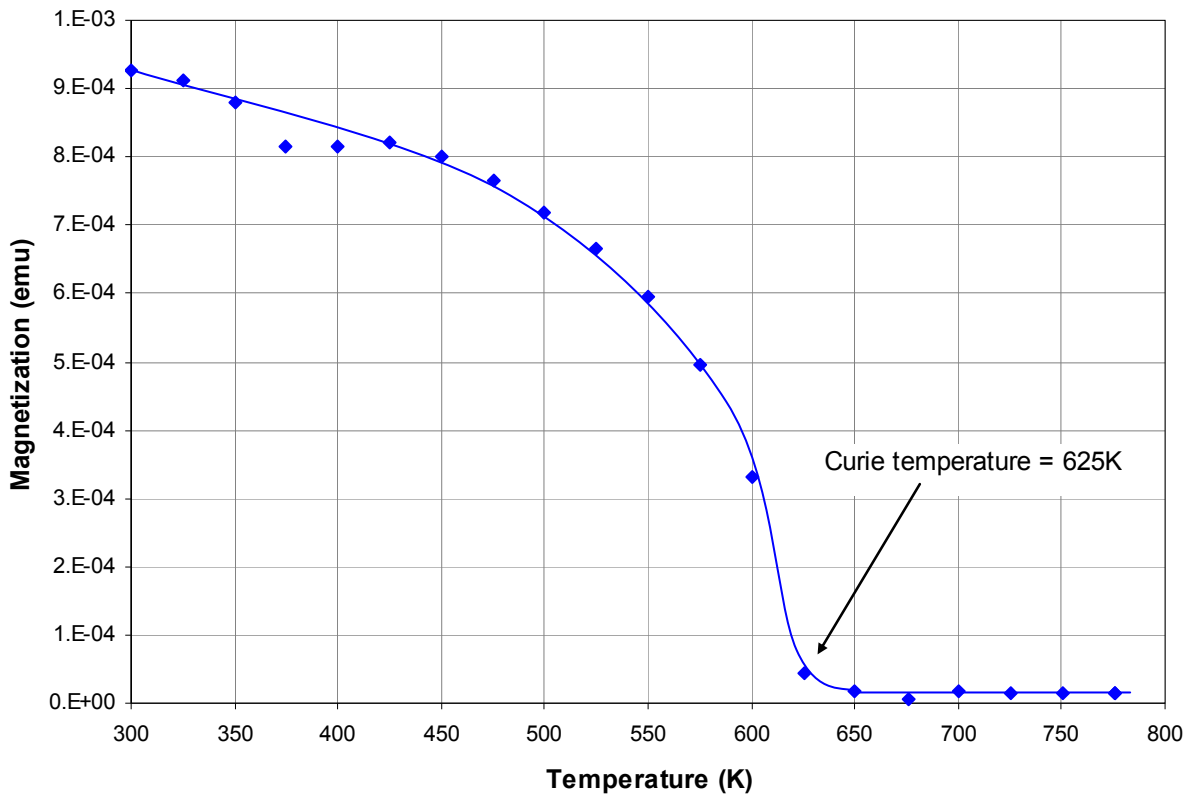


Figure 3-13. Magnetization of pure nickel as function of temperature at 1000 Oe. A Curie temperature of 625 K is found as indicated by the arrow.

Secondly, we measured the magnetization at room temperature of a piece of silicon wafer as function of the field. We used the newly designed sample holder without the oven. The result is plotted Figure 3-14. The very well known diamagnetic response of silicon is observed. In

addition, the susceptibility (0.318×10^{-6}) measured is less than 3% different from the published value². This is acceptable and further validates the modification of the sample holder. In other words, our sample holder does not interfere with the magnetization measurements.

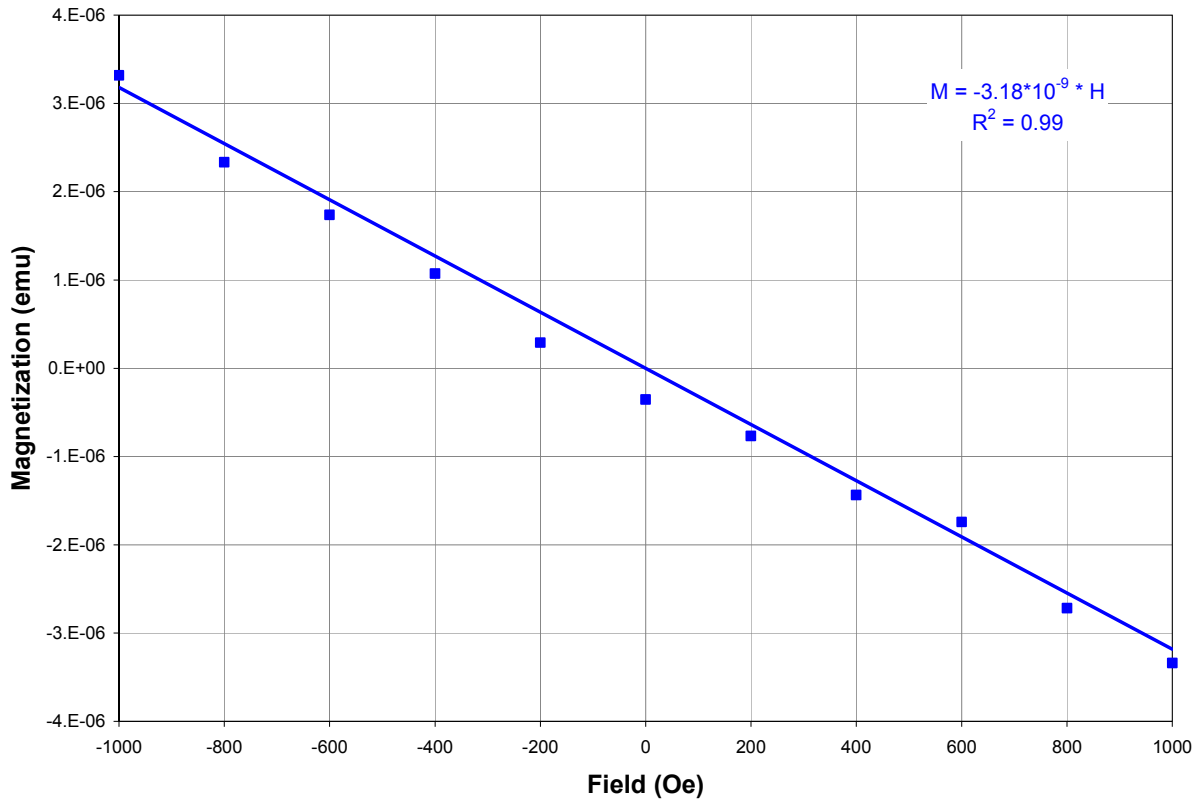


Figure 3-14. Magnetization versus magnetic field for a silicon sample weighting 10.3 mg, measured at 300K.

Finally, we measured the magnetization of the same piece of silicon wafer as a function of the temperature at 10,000 Oe. The resulting data is plotted on Figure 3-15. It is to be noted that we measured the magnetization of the silicon sample at 10,000 Oe and then divided the measured value by ten. This was done in order to compare directly with the magnetization as function of temperature curves for sp-Si which we will present in the next section. The magnetization is independent of the temperature over the entire range (300-800 K) as expected for silicon. From the average magnetization we derive the susceptibility; it is about 15% smaller

than the susceptibility we obtained at room temperature without the oven insert. Since we use the same holder in both measurements we attribute the discrepancy to the oven itself. The design of the SQUID requires the oven to be inserted between the detector and the sample; therefore it induces a perturbation during measurements. It seems that 15% is a large discrepancy, but this is still better than what we initially observed before the modifications.

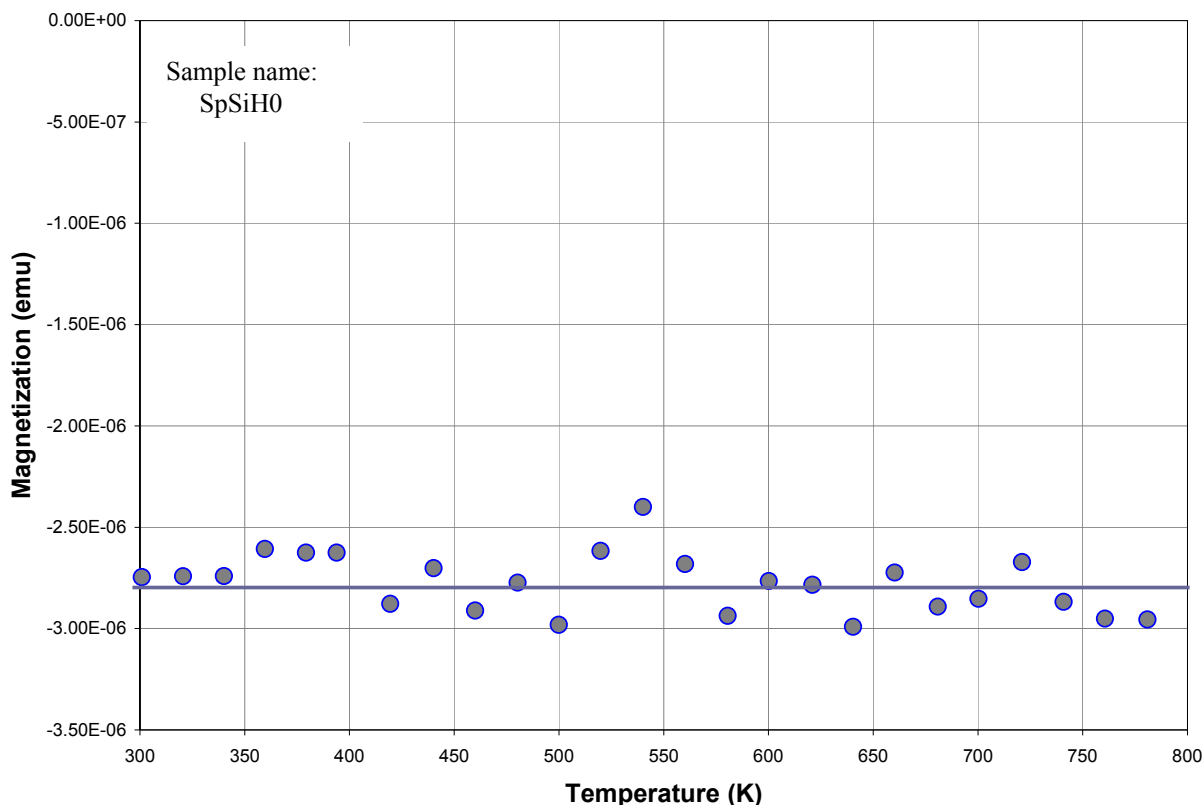


Figure 3-15. Magnetization versus temperature (grey dots) for a 10.3 mg silicon wafer measured at 10,000 Oe. The plotted magnetization is divided by 10, equivalent to magnetization at 1000 Oe. The average (solid line) is -2.8×10^{-6} emu.

The magnetization versus temperature of nickel and silicon are satisfactory and provide us with validation standards for our method of measurement.

3.2.3 High Temperature Spark-Processed Silicon Magnetization

Using the improved high temperature SQUID oven, we measure the magnetization as function of temperature for sp-Si spark-processed for 6 hrs at a frequency of 22 kHz. Figure 3-16 displays the resulting curve upon heating and cooling in an external magnetic field of 1000 Oe. We observe that the magnetization decreases as the temperature increases and increases as the temperature decreases. In addition, the magnetization at room temperature is larger (by 35%) after cooling in the field than before going through the heating cycle. Cooling of a ferromagnetic material in a magnetic field (field cooling) is known to cause additional alignment of spins. This causes an increase in the remanence.

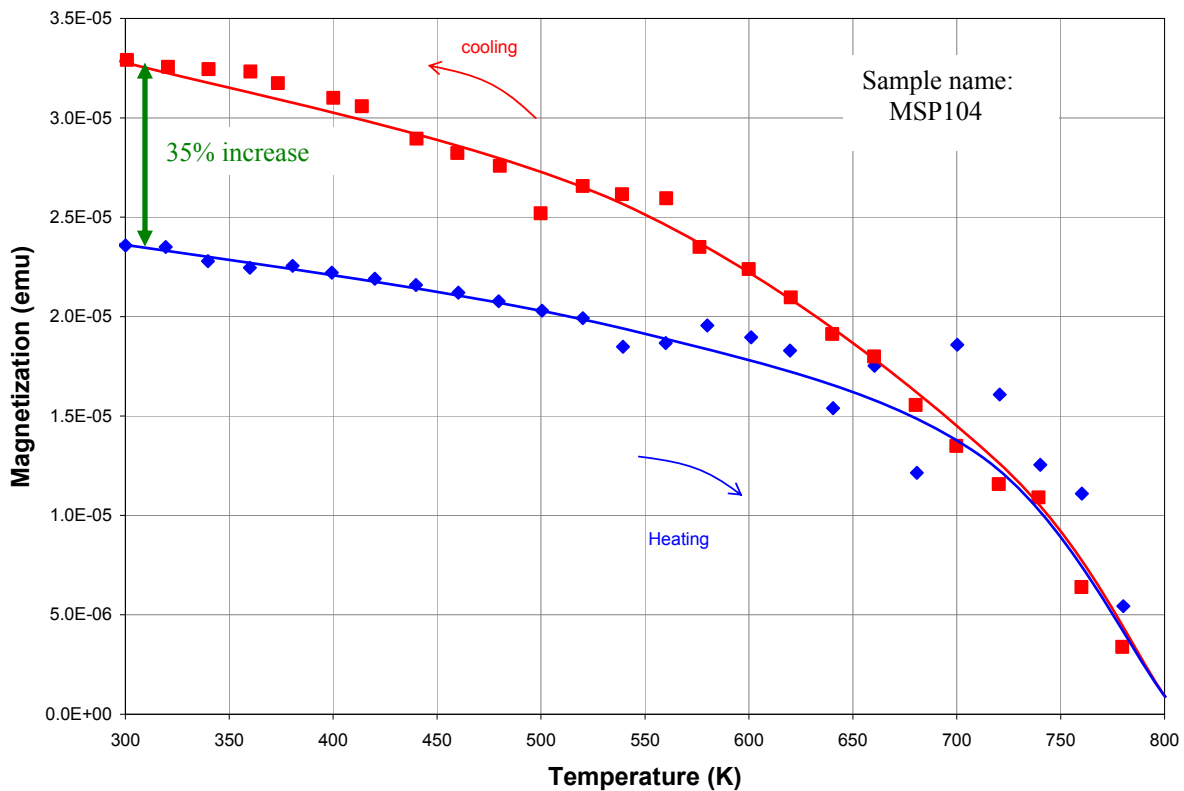


Figure 3-16. Magnetization as a function of temperature upon heating (blue diamonds) at 1000 Oe for spark-processed silicon (sparking time = 6 hours, frequency = 22.5 kHz) and the field cooled magnetization (red square).

The effect of field cooling is better seen in Figure 3-17 where we plot the magnetization as a function of the field at room temperature before and after field cooling. After field cooling, the hysteresis loop is much larger than before.

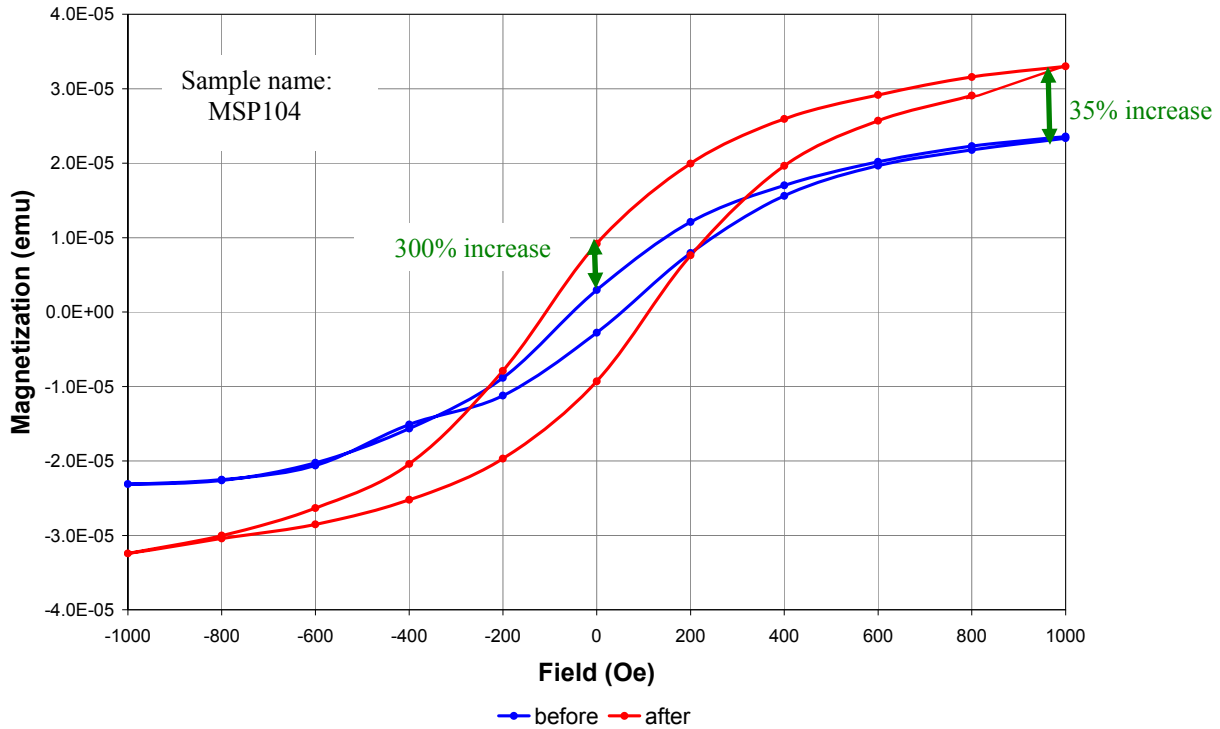


Figure 3-17. Magnetization as a function of the magnetic field strength before (blue curve) and after field cooling (red curve) measured at room temperature for spark-processed silicon (sparking time = 6 hours and frequency = 22.5 kHz).

Using the Weiss model¹ define as: $\frac{M}{M_0} = \tanh \left(\frac{\frac{M}{M_0}}{\frac{T}{T_c}} \right)$, where M is the magnetization at a

given temperature, M_0 is the magnetization at zero Kelvin and T_c is the Curie temperature, we find a very good agreement between the Weiss molecular field theory and our sp-Si data. Figure 3-18 and 3-19 display two measured samples along with their Weiss models. For the first sample (spark time = 12 hours, frequency = 22.5 kHz) the Weiss model leads to a Curie temperature of 770 K while for the second sample (spark time = 6 hours, frequency = 22.5 kHz) the model leads

to a Curie temperature of 760 K. The correlation coefficient between the model and the measured data are very good, that is 0.983 for sample 1 and 0.988 for sample 2. The temperature dependence of the magnetization shows a strong similarity between sp-Si and ferromagnetic behavior.

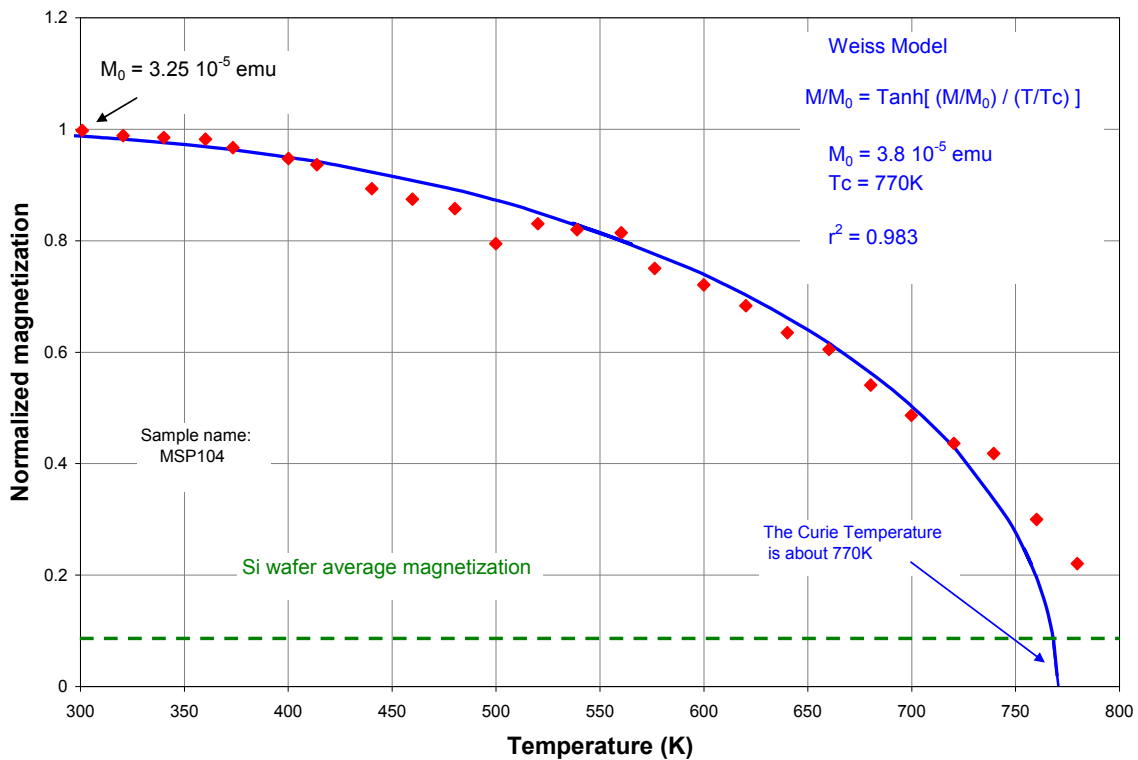


Figure 3-18. Normalized magnetization as a function of temperature for spark-processed silicon measured at 1000 Oe represented by red diamonds. The sample was processed for 12 hours at a frequency of 22.5 kHz. The blue line represents the Weiss model with a Curie temperature of 770 K. The average magnetization of a piece of silicon wafer comparable in size to the measured sp-Si sample is plotted for comparison (green dash line).

The sample was processed for 6 hours at a frequency of 22.5 kHz. The blue line represents the Weiss model with a Curie temperature of 760 K. The average magnetization of a piece of silicon wafer comparable in size to the measured sp-Si sample is plotted for comparison (green dash line).

The two most important parameters for describing the macroscopic magnetic behavior of a material are the remanence and the saturation magnetization. In our study, we use the magnetization at 1000 Oe as saturation point. In the previous section we presented the temperature dependence of the saturation magnetization.

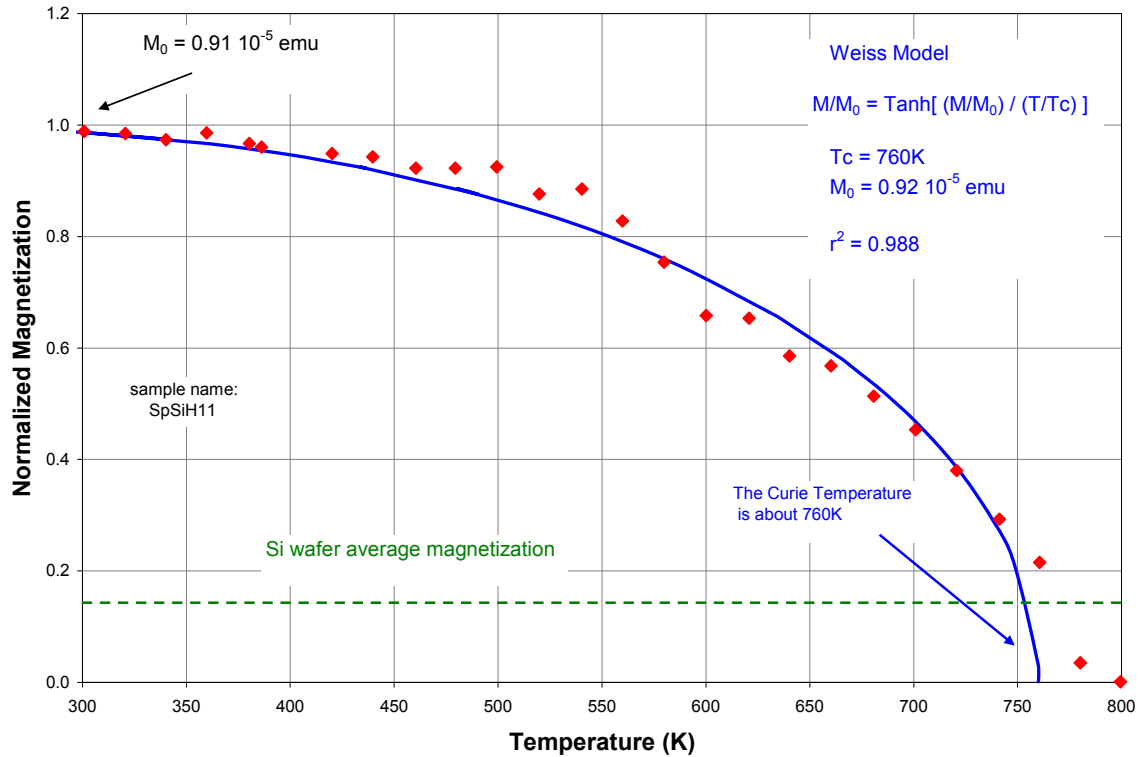


Figure 3-19. Normalized magnetization as a function of temperature for spark-processed silicon measured at 500 Oe represented by red diamonds.

In the next section we briefly describe the effect of temperature on the remanence. Figure 3-20 displays the remanence of sp-Si (sparking time = 6 hrs and frequency = 22.5 kHz) as a function of temperature. We observe a decrease in the remanence as the temperature increases and an increase as the temperature decreases, but the heating and cooling curve are not superimposed on one another (the cooling magnetization is smaller than the magnetization upon

heating). Heating up at the Curie temperature randomizes the spins. Upon cooling a small but discernable spontaneous magnetization is observed.

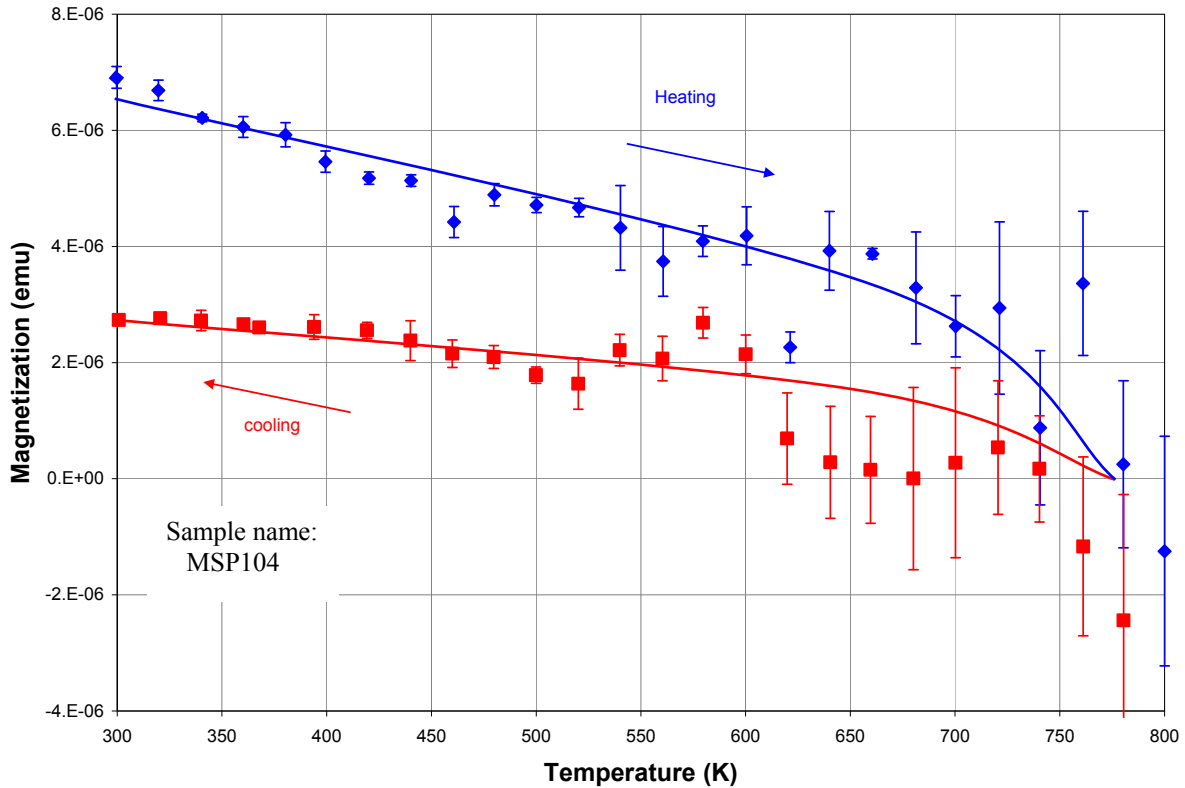


Figure 3-20. Remanent magnetization of spark-processed silicon (sparking time = 6 hours, frequency = 22.5 kHz) measured as a function of temperature upon heating (blue dots) and cooling (red dots). The large error bars at high temperatures are caused by a lower sensitivity of the instrument in such temperatures. Note that these measurements were made at 0 Oe whereas in Figure 3-16 they were made at 1000 Oe.

In this section, we presented the magnetization as a function of the temperature and concluded that the magnetic behavior of sp-Si is very similar to ferromagnetic materials. Now we investigate the effect of annealing on the magnetization.

3.2.4 Annealing Effect on the Magnetization

The magnetization as a function of the field was measured after a number of heating and cooling cycle. A cycle included heating the sample at 800 K and cooling it down to room

temperature at a field of 1000 Oe. A cycle takes 7 hours. The resulting curves are plotted in figure 3-21. The area within the hysteresis loops, measured at room temperature, is observed to become smaller as the number of cycle increases.

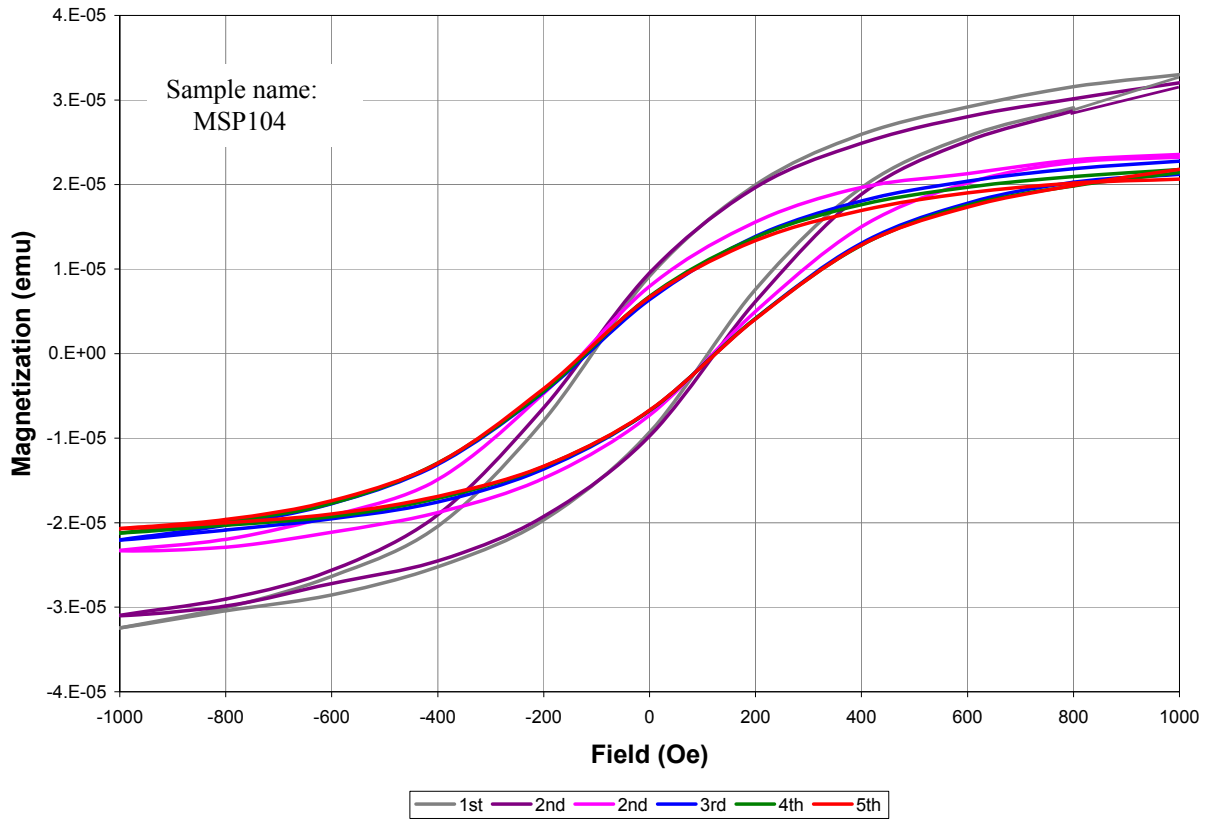


Figure 3-21. Magnetization as function of magnetic field for a spark-processed silicon sample (sparking time = 6 hours and frequency = 22.5 kHz) at room temperature after each heating cycle (heating up to 800 K and cooling down to 300 K in a 1000 Oe field). The first two (grey and purple) were measured on the same day, while the others were measured at a later time.

The relevant data, remanence and magnetization at 1000 Oe as a function of annealing time, can be better seen in the next graph, figure 3-22. The remanence as well as the magnetization at 1000 Oe decrease slowly in a linear manner with annealing time. The magnetization at 1000 Oe decreases by about 15% over an annealing time range of 35 hrs. This is only a 3% decrease per heating cycle. The previously presented data of magnetization as a

function of temperature is only marginally affected. Therefore, our conclusions on the magnetic behavior of sp-Si at high temperatures are unchanged.

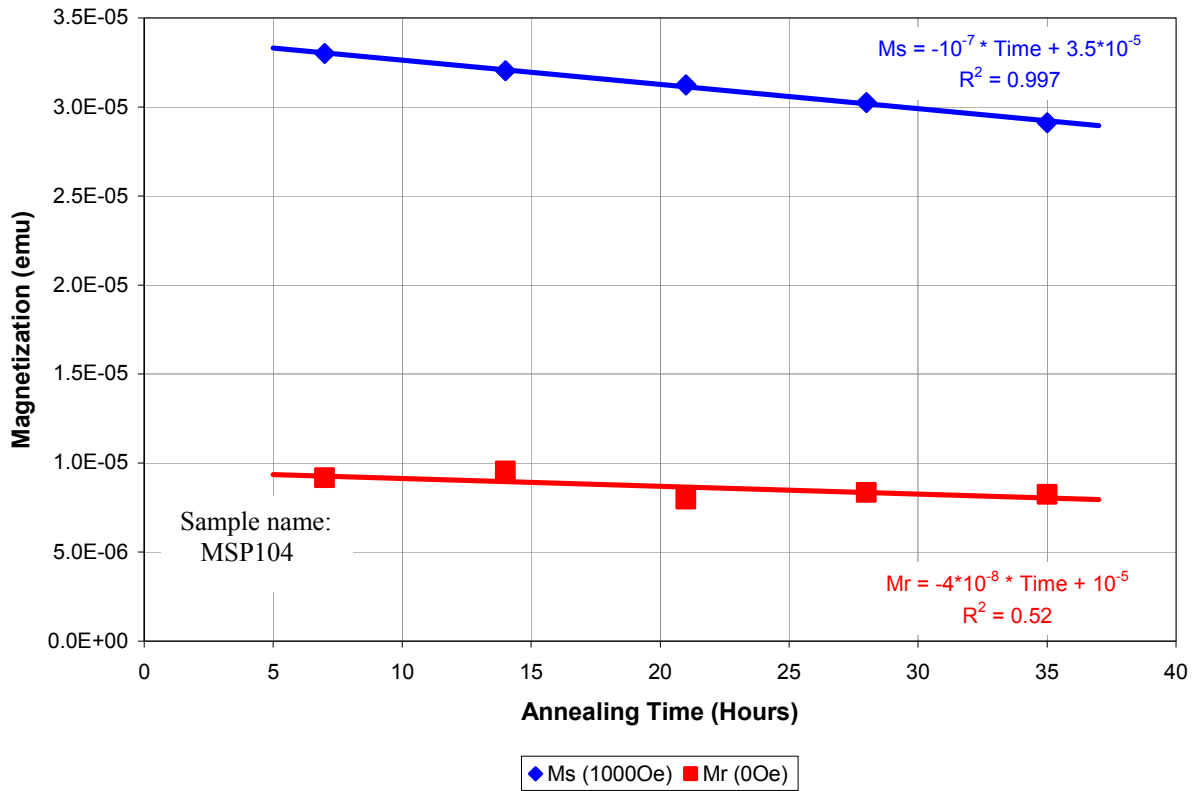


Figure 3-22. Magnetization at 1000 Oe (blue diamonds) and 0 Oe (red squares) versus annealing time for spark-processed silicon (sparking time = 6 hours and frequency = 22.5 kHz). Linear models are plotted as solid lines. The annealing was performed during heating at 800 K and cooling back to 300 K in a 1000 Oe field over a 7 hours heating-cooling cycle.

3.3 Low Temperature Magnetization

In this section we present and analyze the magnetization as function of temperature of spark-processed silicon at low temperatures. But, similarly to high temperatures, proper control measurements need to be performed before doing experiments on unknown material such as sp-Si. Therefore, we will use HgCo(SNC)₄ and aluminum as low temperature references. Also, we will discuss observed artifact caused by oxygen in the sample chamber.

3.3.1 Magnetic Reference Material HgCo(SNC)₄ for the 2-100K Temperature Range

This reference material is used to make sure that the SQUID magnetometer measurements are reliable. Several references can be used to validate magnetization measurements with the SQUID magnetometer at very low temperature (2-100K). The cobalt mercury cyanide is a widely used reference for this range and was readily available to us. This material comes in a powder form and special handling is required due to its toxicity and potential to contaminate the magnetometer. A special sample holder was designed to prevent loss or scattering of the material during the measurement process. A description of the holder design can be found in the Appendix B.

To evaluate the reliability of the SQUID magnetic measurements, we look at the correlation between the magnetic susceptibility of HgCo(SNC)₄ as a function of temperature of our own data and the one published by O'Connor³². We find an excellent match with a correlation coefficient of 0.9999. Our results are also consistent with the values published by Bunzli³³.

We concluded that HgCo(SNC)₄ is a good choice of standard for very low temperature magnetic measurements and that our SQUID magnetometer gives reliable magnetic measurements in the 2 to 100K range since we had a very good correlation between our data and previously published ones. This work is fully detailed in the Appendix B.

3.3.2 Aluminum Reference for the 50-300 K Temperature Range

Aluminum has been well studied in the 50-300K temperature range and is a better suited magnetic standard than HgCo(SNC)₄ in this range due to its large temperature coefficient.

First, we measured a magnetic susceptibility at room temperature of 3.377×10^{-8} emu for the aluminum sample. Using the measured weight of the sample (53.4 ± 0.1 mg) we calculated a

sample volume of $0.0198 \pm 0.00004 \text{ cm}^{-3}$ leading to a volume susceptibility of $1.70 \pm 0.03 \times 10^{-6} \text{ cm}^{-3}$. This value is very close to the published value² of $1.65 \times 10^{-6} \text{ cm}^{-3}$.

Next, we measured the susceptibility as function of temperature. The aluminum susceptibility is linearly dependant on the square of temperature according to Hedgcock³⁴. This dependence can be expressed by the following equation: $\chi = \chi_{dia} + \chi_{para}^0 + B \times T^2$ where χ_{dia} is diamagnetic susceptibility, χ_{para}^0 is the temperature independent paramagnetic susceptibility and where B is a constant characteristic of aluminum. We found a correlation coefficient of 0.997 between our data and this proposed model.

The results from $\text{HgCo}(\text{SNC})_4$ and Aluminum reference lead us to conclude that our the magnetization measurements at low temperatures with our SQUID magnetometer are reliable. In addition, to proper calibration, oxygen contamination could be an issue with high resolution magnetization at low temperature. In the next section, we will discuss the oxygen contamination.

3.3.3 Oxygen Effect at Low Temperature

Oxygen contamination is a known problem with low temperature measurements with a SQUID magnetometer but not very publicized. I have published on this topic³⁵ and found out that it was known to Quantum Design Inc., the manufacturer of our SQUID magnetometer but an application note has never been written to help users properly interpret their measurements. Therefore some clarifications are needed.

Oxygen is paramagnetic in its gas and liquid phases, becomes antiferromagnetic when solid below 54.3 K, and changes its crystal structure^{36,37} (β to γ at 43.8 K). The magnetic transitions of oxygen at 54.3 K and 43.8 K generate a noticeable change in the measured magnetic susceptibility of a sample while some gaseous oxygen is left in the sample chamber.

Typically a large peak around 50 K is observed in addition to the magnetization of the characterized sample.

In our SQUID magnetometer, a sample is normally measured in a Helium gas. Following the sample loading, the load lock (or the entire chamber) is purged with Helium gas. But due to pumping and Helium quality there is still oxygen left in the chamber. When no purge is performed a large peak is observed as expected since we leave a large amount of oxygen gas from air in the chamber. But, even when we purged 3 times the oxygen peak is still visible. This small trace of oxygen could be explained by the limiting pumping capability of the mechanical pump and the presence of trace oxygen within the helium gas use to cool down the sample. See Appendix D for more details.

Finally, this “oxygen” effect is only visible in samples with magnetization in the 10^{-5} or 10^{-6} emu range. Therefore we recommend, in addition to multi-purging, using samples as large as possible to decrease the relative effect due to oxygen magnetic transition.

Now that we have shown that our SQUID magnetometer works properly over the entire temperature working range and that we have discussed the problem associated with the oxygen, we can focus on spark-processed silicon.

3.3.4 Spark-Processed Silicon Low Temperature Magnetization

We have previously shown that spark-processed silicon had a magnetic hysteresis at room temperature. Upon cooling, this magnetic hysteresis loop remains present as seen in Figure 3-23. The magnetization versus field was measured at 35 and 70 K. The remanence is the same for both temperature but the magnetization at non zero field increases as the temperature is cooled down. The magnetization increases by 30% at 1000 Oe. Further, the hysteresis loop rotates counterclockwise as the temperature is lowered. This can be explained using a complete model of the magnetization for spark-processed silicon.

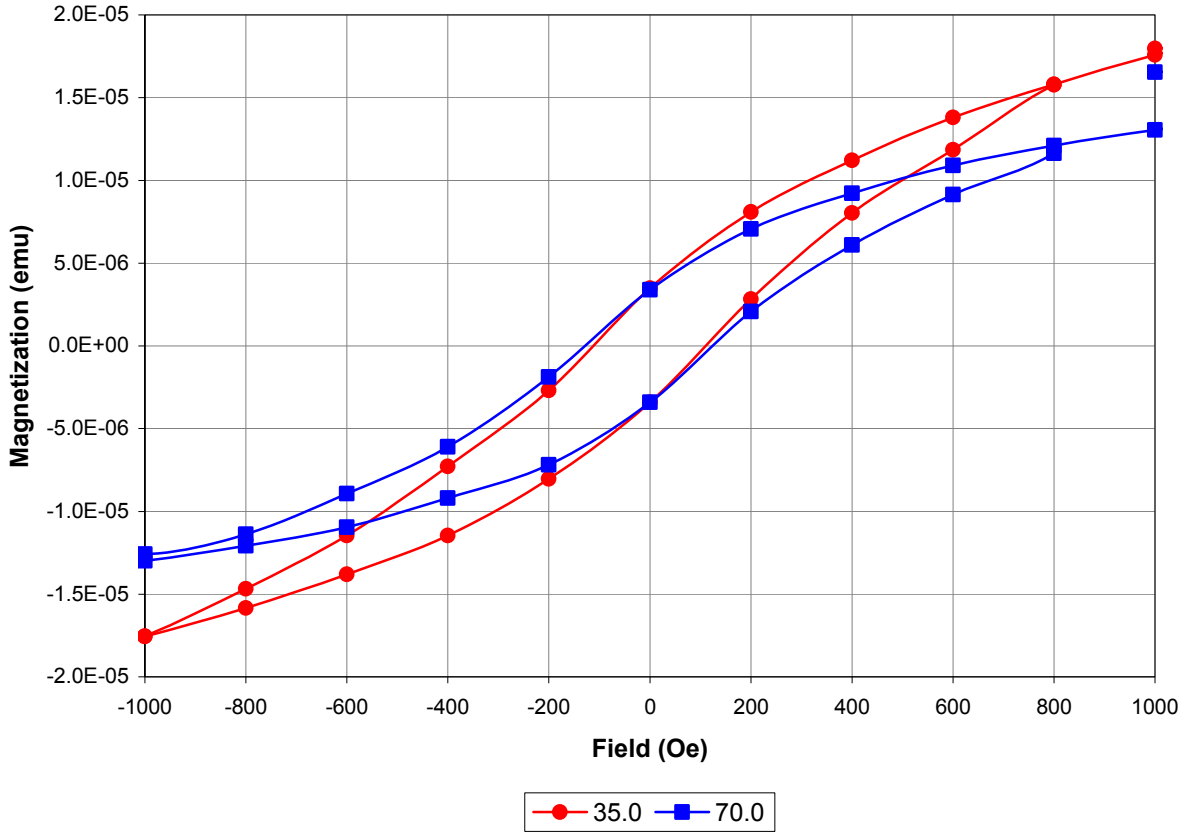


Figure 3-23. Magnetization versus field at 70 K and 35 K of spark-processed silicon (square and round points, respectively).

We model the magnetization as followed:

$$M_{sp-Si} = [\chi_{dia}^0 + \chi_{para}^0 + \chi_{para}(T)] \times H + M_{Hysteresis}(T, H), \text{ where } \chi_{dia}^0 \text{ is the diamagnetic}$$

susceptibility, χ_{para}^0 is the temperature independent paramagnetic susceptibility, $\chi_{para}(T) = \frac{C}{T - \theta}$

is the Curie-Weiss susceptibility and $M_{Hysteresis}(T, H)$ is the Weiss magnetization presented in

Section 3.2.3. The Weiss magnetization is only temperature dependent near the Curie

temperature. At temperatures well below the Curie temperature (760 K for sp-Si), the Weiss

magnetization is almost temperature independent. For example, using the Weiss model, we

evaluated a magnetization decrease of 1.3% between 10 and 300 K using a Curie temperature of

760 K. On the other hand, the Curie-Weiss susceptibility is strongly temperature dependent at low temperature. The rotation of the hysteresis loop at low temperature is therefore interpreted to be due to paramagnetic centers which follow the Curie-Weiss law.

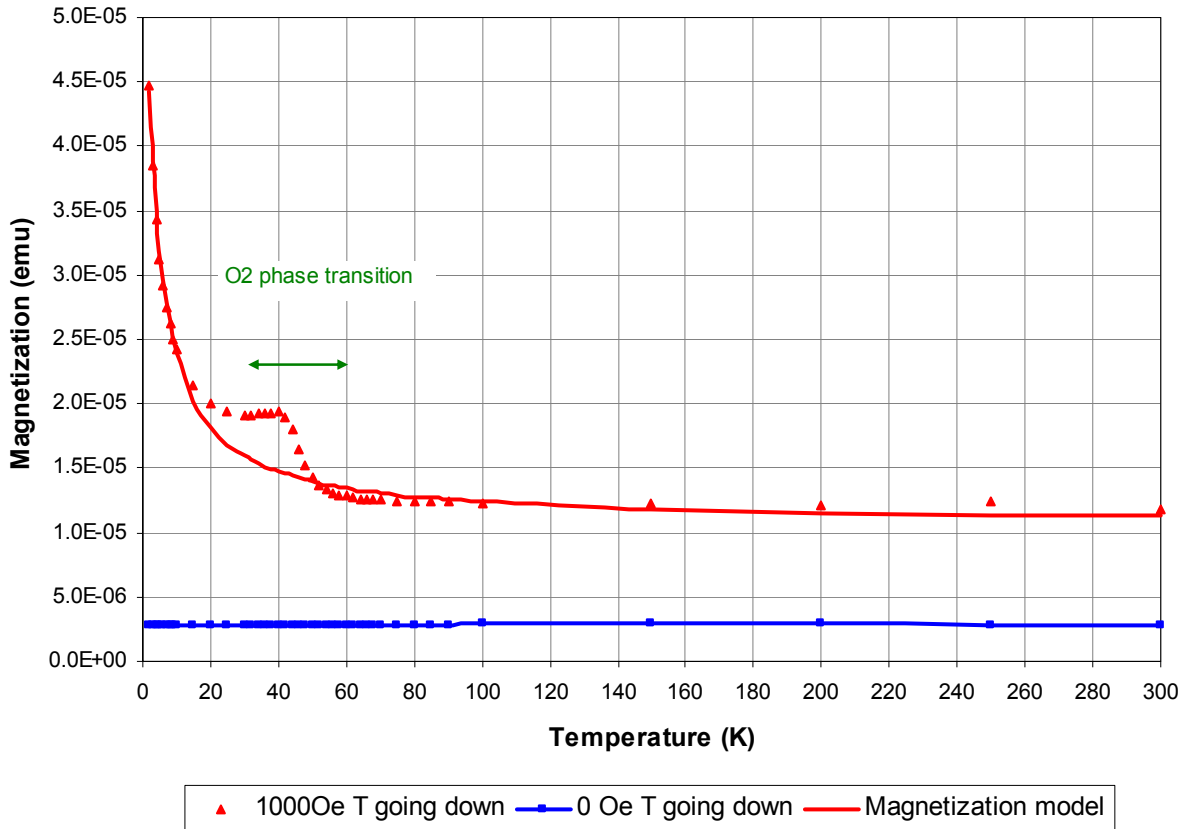


Figure 3-24. Magnetization versus temperature for spark-processed silicon at 1000 Oe (red triangle) and 0 Oe (bleu squares). A model is fitted to the 1000 Oe magnetization curve in solid red. The bump in magnetization near 40 K is an artifact caused by a phase change of oxygen contamination in the measured chamber (see Appendix D).

If we set the magnetic field and consider the Weiss magnetization to be temperature

independent we can simplify our magnetization model to: $M_{sp-Si} = M_0 + \frac{C'}{T - \theta}$, where

$$M_0 = [\chi_{dia}^0 + \chi_{para}^0] \times H + M_{Hysteresis}(H) \text{ and } C' = C \times H .$$

Using this model on our magnetization

versus temperature data for sp-Si presented in Figure 3-24, we obtain the following fitting

parameters: $M_0 = 1.07 \times 10^{-5}$ emu, $C' = 1.73 \times 10^{-4}$ emu. Oe and $\theta = -3.16$ K with a correlation

coefficient of 0.995. (Since oxygen has an influence on the data in the temperature range 20 to 60 K, we only use the data points outside this temperature range to fit our model). In addition, Figure 3-24 also contains the remanence versus temperature of sp-Si. It should be noted that the remanence does not change with temperature over the whole range, therefore validating the temperature independence assumption from the Weiss model.

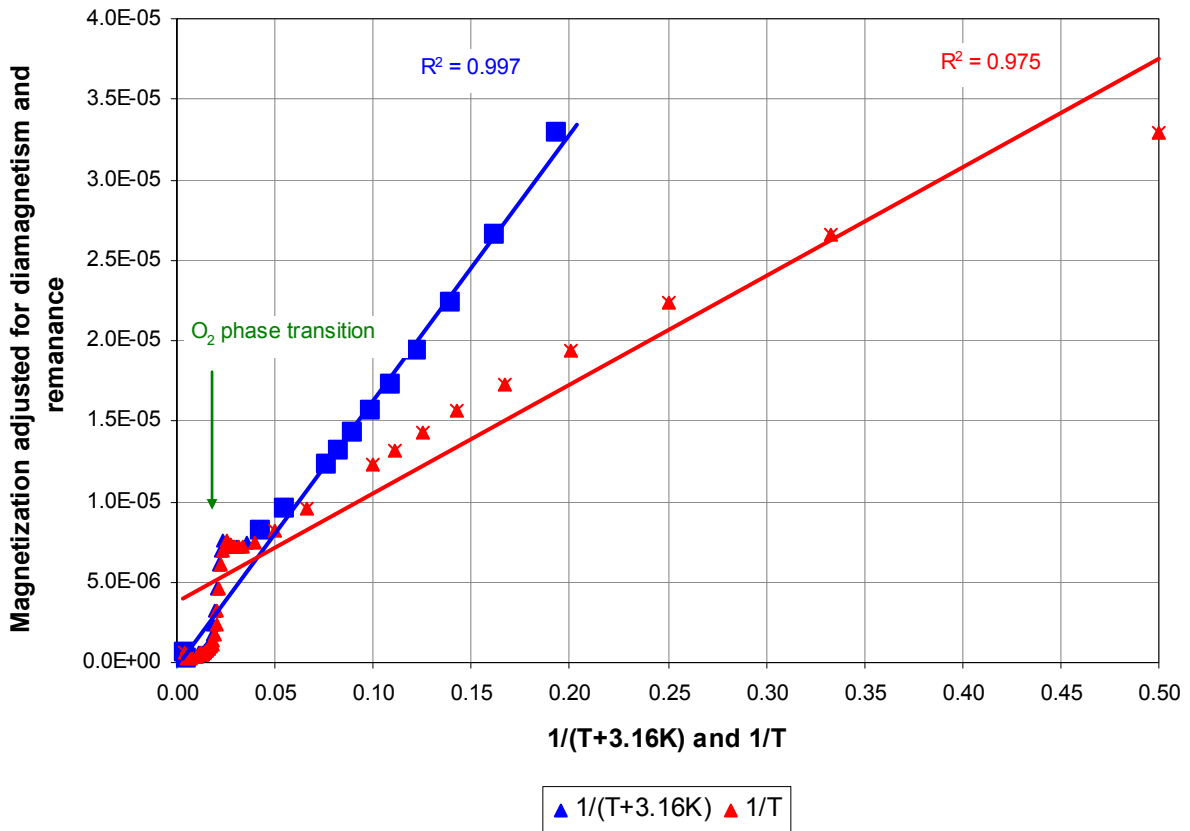


Figure 3-25. Magnetization adjusted for diamagnetism and remanence as a function of inverse temperature. The temperature has been shifted by 3.16 K to account for low temperature exchange interactions. A linear trend is fitted to the low temperature data (solid line). A green arrow marks the oxygen phase transition.

Since it is difficult to visualize the good correlation between our data and our proposed model in Figure 3-24, another presentation of the data is proposed Figure 3-25. In Figure 3-25, the magnetization at 1000 Oe is plotted as a function of $\frac{1}{T+\theta}$ [K⁻¹]. This method emphasizes

more the data points below 20 K and allows for a good visual correlation between our proposed model and our data. For comparison the magnetization is also plotted as function of $\frac{1}{T} [K^{-1}]$. It is observe that in this case the model does not fit well the data.

3.4 Summary

From my research we learn the following:

- Sp-Si displays a magnetic hysteresis loop at room temperature under certain processing conditions.
- A specific method was developed to measure the magnetization of sp-Si at high temperature. From this method it was found that sp-Si magnetization as a function of temperature follows the Weiss equation.
- A Curie temperature of 765 K as been evaluated from the Weiss equation applied to the high temperature magnetic measurements for sp-Si.
- Annealing of sp-Si up to 800 K decreases the magnetization at 1000 Oe and the remanence weakly.
- At low temperatures, sp-Si exhibits a large magnetization inversely proportional to the temperature which is characteristic of paramagnets.

CHAPTER 4 INTERPRETATION OF QUASIFERROMAGNETISM IN SPARK PROCESSED SILICON

This chapter is dedicated to the study of the paramagnetic centers present in spark processed silicon and how they are related to the observe quasiferromagnetism.

4.1 Model Concerning the Distribution of Paramagnetic Centers

In order to explain the magnetic hysteresis and the high Curie temperature in sp-Si we propose that some paramagnetic centers, found in spark processed silicon, interact such that the exchange integral is positive. First, to observe exchange interaction between electron spins, the distance³⁸ between them has to be smaller than 2 nm. It will be shown in a last section of this chapter that the calculated average paramagnetic centers density in spark processed silicon is about $2 \times 10^{19} \text{ cm}^{-3}$. Assuming that the paramagnetic centers are equally spaced from one another, this would put an upper limit of 3.7 nm between them. We propose therefore that the inter-spin distance is not homogeneous in sp-Si. That is, some paramagnetic centers could be less than 2 nm apart thus allowing exchange interaction between them. Figure 4-1 schematically depicts this proposed distribution of paramagnetic centers in spark-processed silicon. Some spins are assumed to form clusters (small inter-spin distance) and others are isolated (large inter-spin distance) such that they do not participate in exchange interaction. Our results presented in the previous chapter support such a model since the independent spins lead to paramagnetism which we found to be present and the interacting spins within a cluster lead to a hysteresis which we also found in sp-Si. In addition, to support our model we characterize the paramagnetic centers using electron paramagnetic resonance. But first, we need to explain a few concepts using this technique.

Note: we use spin or paramagnetic center interchangeably throughout this chapter.

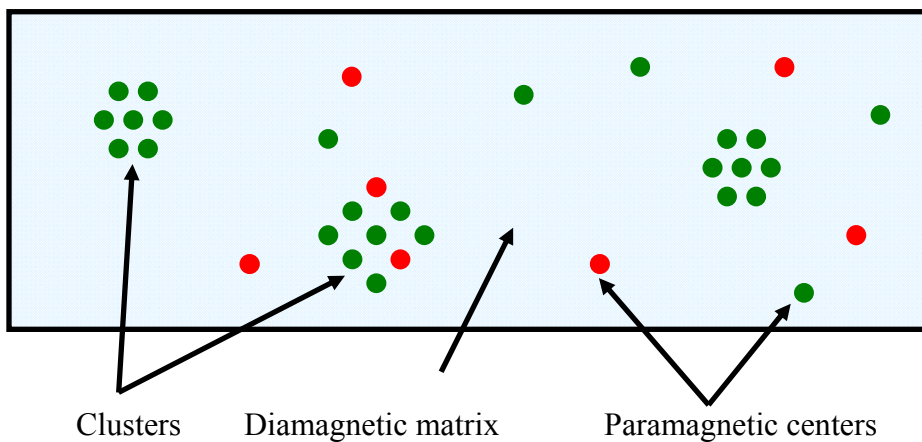


Figure 4-1. Proposed paramagnetic centers distribution.

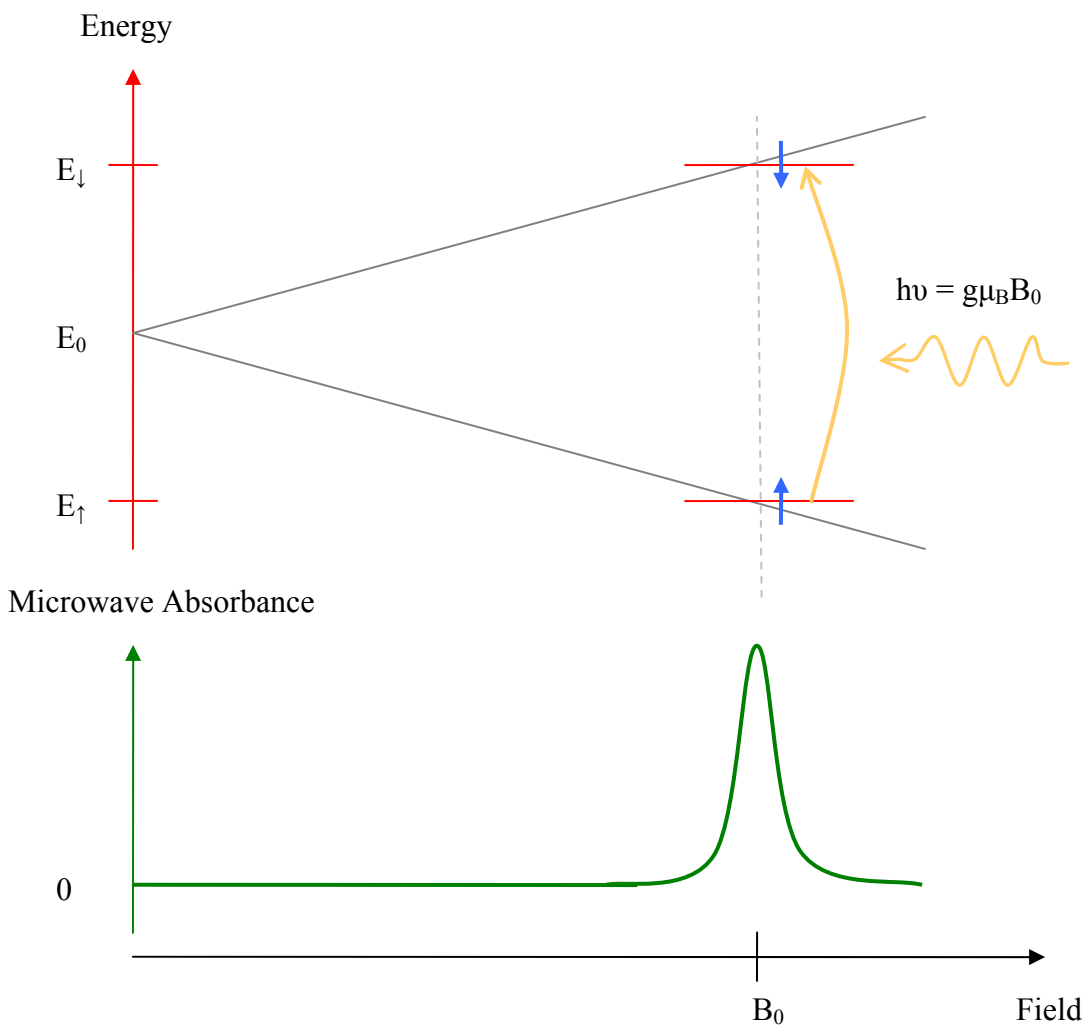


Figure 4-2. Energy levels of an electron at the resonance field.

4.2 Electron Paramagnetic Resonance (EPR) Concepts

To perform an electron paramagnetic resonance experiment, we place a sample containing unpaired spins in a resonant cavity which itself sits in the center of a large electromagnet. In addition to being exposed to a magnetic field, microwaves are directed towards the sample inside the cavity (Figure E-1 in Appendix E). The microwaves have a very specific frequency of 9.75GHz for X-band EPR while the field is swept around 3.5 kG. The field splits the electron energy in two, $E_{\downarrow} = +\frac{1}{2} g \mu_B B_0$ and $E_{\uparrow} = -\frac{1}{2} g \mu_B B_0$, where g is the Lande factor, μ_B is a constant called the Bohr magneton, and B_0 the magnetic field. When the magnetic field is such that the difference between the two energy levels is equal to the microwave energy we have resonance, i.e. the electron absorbs the microwave photon. The resonance condition leads to the following equation, $\Delta E = E_{\downarrow} - E_{\uparrow} = g\mu_B B_0 = h\nu$, where h is the Planck constant and ν is the microwave frequency. The absorption is maximal at the resonant condition, $B_0 = h\nu/g\mu_B$. Since, μ_B , h and ν are constants; the resonant field depends on the g -factor. This factor depends on the environment of the paramagnetic center studied. It is used as an identifier for a particular type of magnetic center. Figure 4-2 shows the resonance conditions.

In practice, modern EPR instruments use field modulation to record a spectrum. Field modulation adds a small alternating field to the large static field. This small field is about 1 Gauss in our case while the large field is in the 3000 to 4000 Gauss range. The modulation allows better sensitivity by using lock-in amplification. In addition, instead of directly observing the absorption we measure its first derivative.

In the next section we explain how spectra are decomposed into independent factors which are then analyzed individually to characterize the studied material.

4.3 Characterization of Continuous Wave Electron Paramagnetic Resonance Spectra

The EPR spectrum of spark-processed silicon is complex. It contains several features which need to be separated before each individual component is studied. To study sp-Si EPR spectra we use a mathematical function to model the absorption. But first, we need to explain the mathematical function. Figure 4-3 schematically depicts our deconvolution scheme.

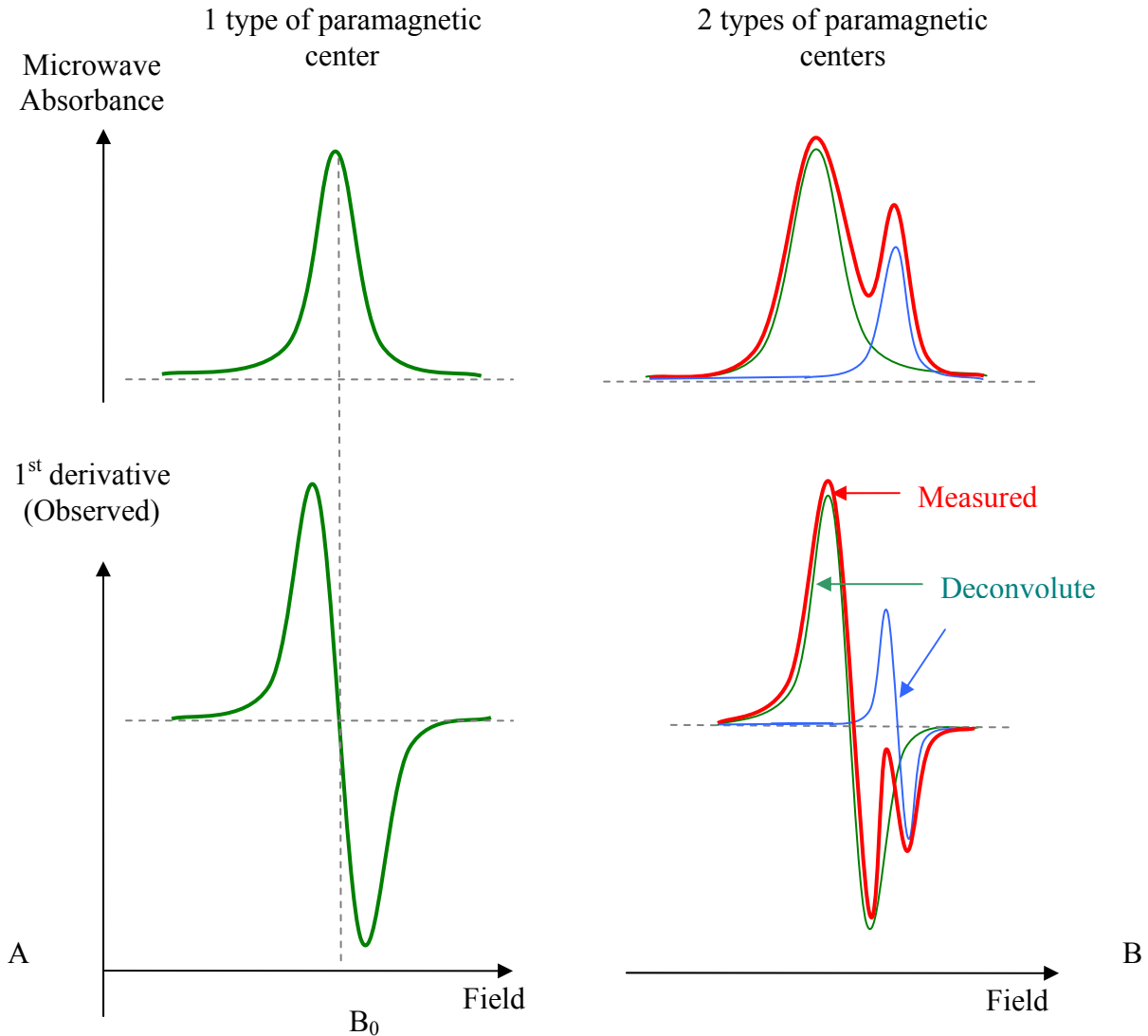


Figure 4-3. Lorentzian distribution and 1st derivative of electron microwave absorbance as a function of the magnetic field. A) one type of paramagnetic center. B) two different types of paramagnetic centers (red curves) and their deconvolution (blue and green curves).

When only one type of paramagnetic center is observed the model is simply the first derivative of a single line. The term line refers to a very sharp peak characteristic of one paramagnetic center. In addition, when two or more types of paramagnetic centers are observed simultaneously, the model will be the sum of the first derivatives of two or more lines which is due to the independent physical origin of the electron resonance for each type of center. Each line is characterized by a mathematical function. In the case of sp-Si we use a Lorentzian distribution but other functions are also commonly used such as Gaussian or Dysonian distributions. The type of distribution is characteristic of the excited spins. For example highly oriented pyrolytic graphite displays a Dysonian behavior, which is discussed in the next chapter.

The equation for a normalized Lorentzian distribution is: $f_{x_0, \Gamma}(x) = \frac{1}{\pi} \frac{\frac{\Gamma}{2}}{(x-x_0)^2 + (\frac{\Gamma}{2})^2}$ where Γ is

the full width at half maximum, and x_0 is the center of the line. This distribution is normalized using the following condition: $\int_{-\infty}^{+\infty} f_{x_0, \Gamma}(x) dx = 1$. Our model for one line is $y=A \times f(x)$, where A is the area under the curve. We call it the amplitude. Under specific conditions, it is proportional to the number of paramagnetic centers. The first derivative of the Lorentzian distribution is defined

as: $f'_{x_0, \Gamma}(x) = \frac{1}{\pi} \frac{\Gamma(x-x_0)}{\left[(x-x_0)^2 + (\frac{\Gamma}{2})^2 \right]^2}$. In spark processed silicon we observe two types of

paramagnetic centers and therefore our full mathematical model for the absorption is:

$y = A_1 f'_{x_1, \Gamma_1}(x) + A_2 f'_{x_2, \Gamma_2}(x)$ where x is the magnetic field. Each type of paramagnetic center is characterized by an amplitude (A), a center field (x_0) and a line width (Γ). We call our model

“two-Lorentzian”. Figure 4-4 displays an EPR spectrum for spark processed silicon measured at room temperature and a two-Lorentzian model. We found a very good agreement between the

model and the experimental data, where the coefficient of correlation is better than 0.98. The full justification of our model will be discussed later in this chapter. First we need to identify each of the paramagnetic centers observed in the spectrum. This is done by calculating the g-factor from the Lorentzian model and comparing it with literature data. For a precise identification, a known standard, DPPH (2,2-Diphenyl-1-picrylhydrazyl), is used as a reference point for the center field. The standard and a sp-Si sample were measured at the same time in the EPR system thus virtually eliminating instrumental errors.

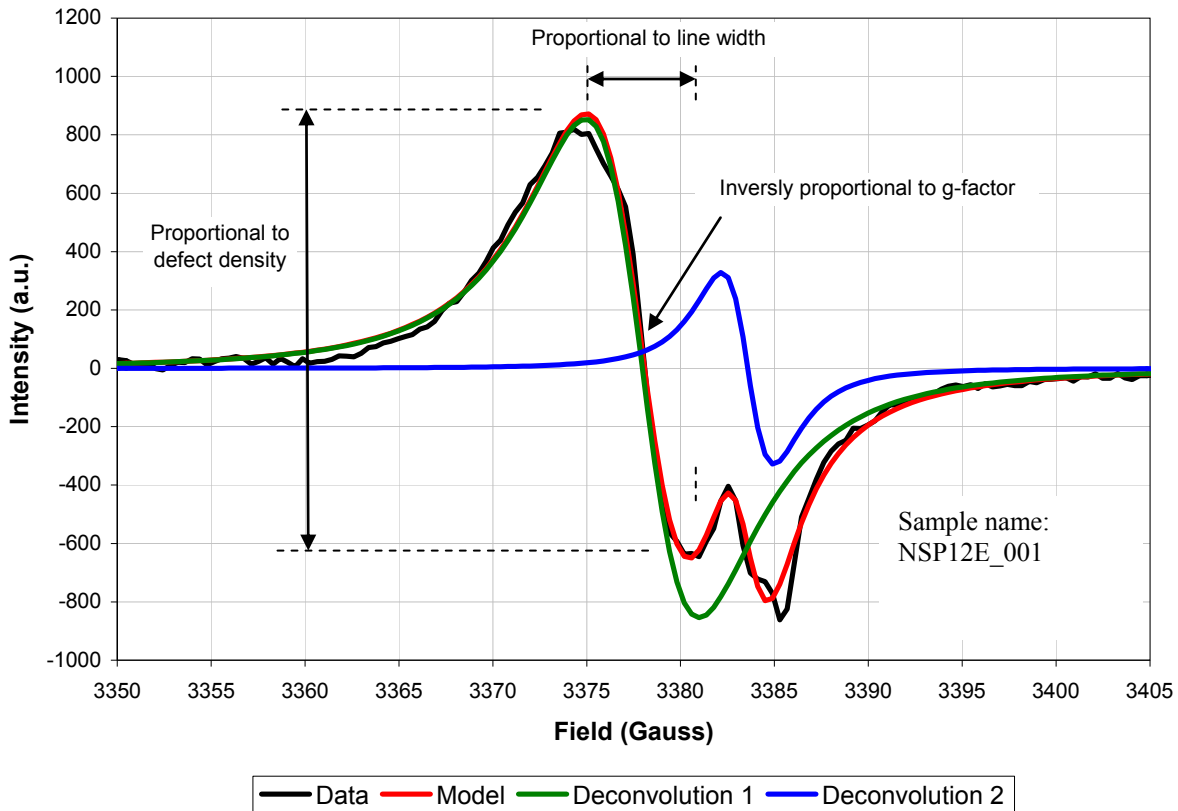


Figure 4-4. Electron paramagnetic resonance spectrum of spark-processed silicon (back line) at room temperature with its double Lorentzian 1st derivative model (red). For clarity the deconvoluted curves are plotted in green and blue. Experimental parameters, power = 0.6331 mW, power attenuation = 25 dB, modulation field = 1 G, time constant = 10 ms, detector gain = 60 dB, temperature = 300 K.

Figure 4-5 displays the spectrum of sp-Si along with the DPPH standard. Using a three-Lorentzian model (correlation coefficient = 0.986) we obtain three resonant fields, two from sp-Si and one from DPPH. The published g-factor³⁹ for our standard is 2.0036. From the resonant condition equation presented in the previous section ($g\mu_B B_0 = h\nu$), we calculate the microwave frequency to be $\nu_{\text{cal}} = 9.75044\text{GHz}$. Then, using the same resonance condition equation with the calculated frequency and the resonant field found for spark processed silicon from our Lorentzian model we calculate two g-factors, $g_1 = 2.0050$ and $g_2 = 2.0013$.

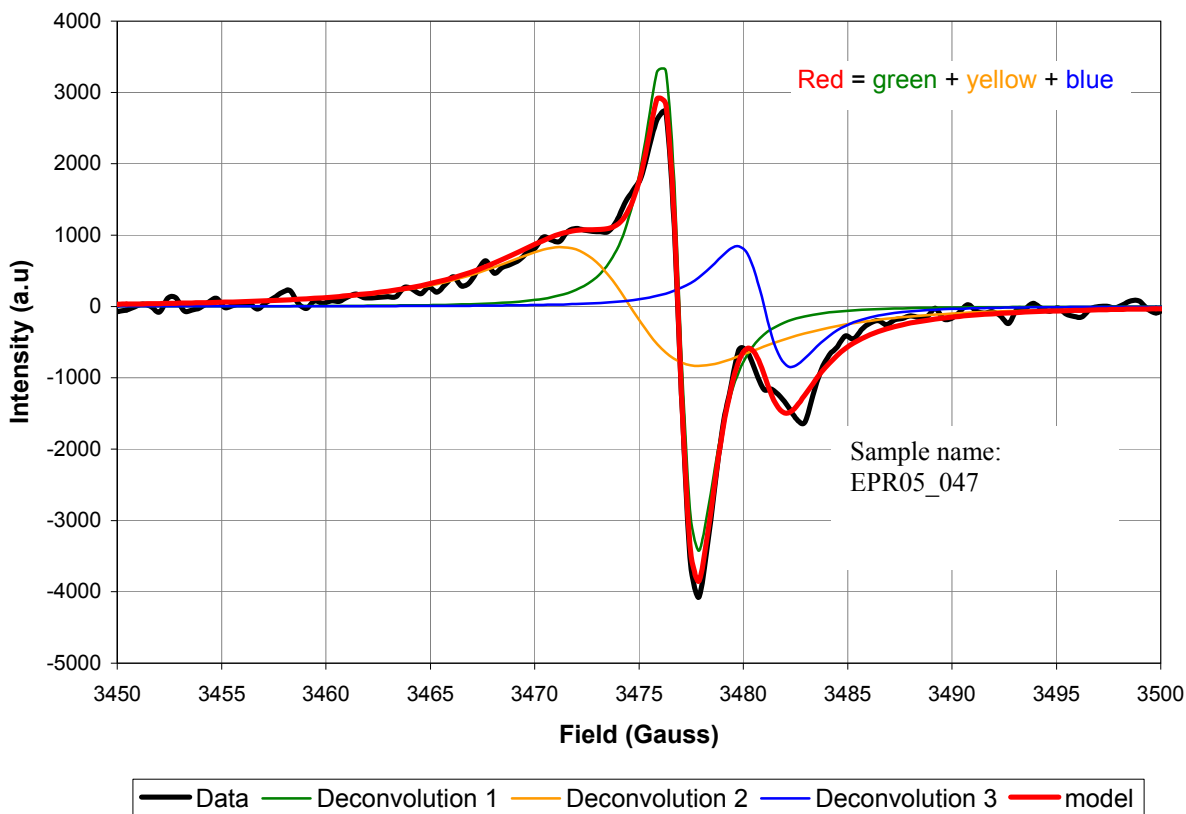


Figure 4-5. Electron paramagnetic spectra of spark-processed silicon along with DPPH reference standard (black line). Its model plotted in red is deconvoluted in three sub-models (green, yellow and blue curves). Experimental parameters, power = 0.6331 mW, power attenuation = 25 dB, modulation field = 1 G, time constant = 40 ms, detector gain = 70 dB, temperature = 300 K.

Using the extensive literature⁴⁰⁻⁴⁷ on paramagnetic centers in silicon-based material, we identify the first paramagnetic center with a g value of 2.0050 to stem from silicon unpaired bond, backboned by three silicon atoms as schematically represented in Figure 4-6; it is called D center. From literature⁴¹⁻⁴⁶ the D center g-value varies between 2.0050 and 2.0055. In addition the paramagnetic center with a g-value of 2.0013 is attributed to a silicon unpaired bond, backboned by three oxygen atoms; it is called E' center. The E' center has many variations⁴⁰ stemming from different precursors in SiO₂ based material, but they all have g values between 2.0000 and 2.0018. Spark processed silicon is a nonstoichiometric silicon dioxide doped with nitrogen²⁸ (SiO_x:N) and therefore finding E' and D center is acceptable.

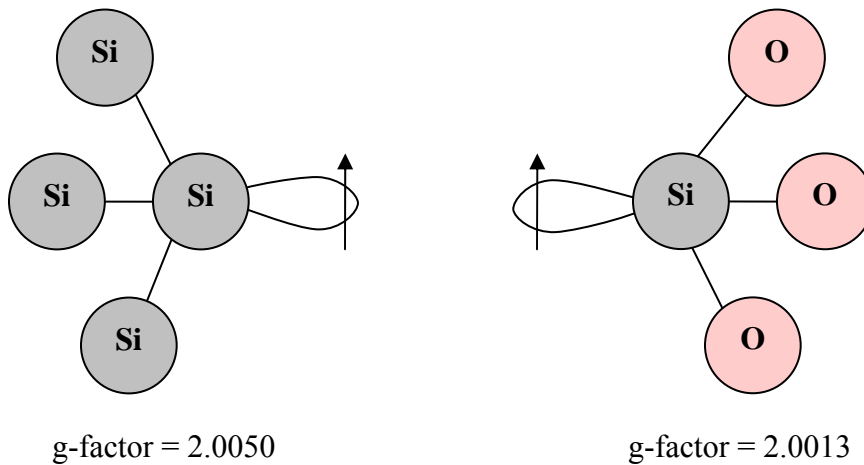


Figure 4-6. Nature of spark-processed silicon paramagnetic centers.

It is to be noted that any impurities such as iron, nickel, or cobalt, which could cause a magnetic hysteresis may absorb microwaves as well and therefore may be identified using the same method as in the identification of paramagnetic centers in sp-Si. They would possess, however, different g-values than those found here. No characteristic absorption from these elements was found in spark processed silicon.

The resonant field has helped us to identify the paramagnetic centers but we have not justified yet why our model is correct. To verify that the different types of paramagnetic centers are truly independent from one another in sp-Si, we conducted a power saturation experiment. The amplitude, as defined previously, is linearly dependent on the square root of the microwave power⁴⁴. This relationship is valid for small power values. When the power gets high enough the amplitude saturates. Figure 4-7 displays the amplitude of the D centers versus the microwave power.

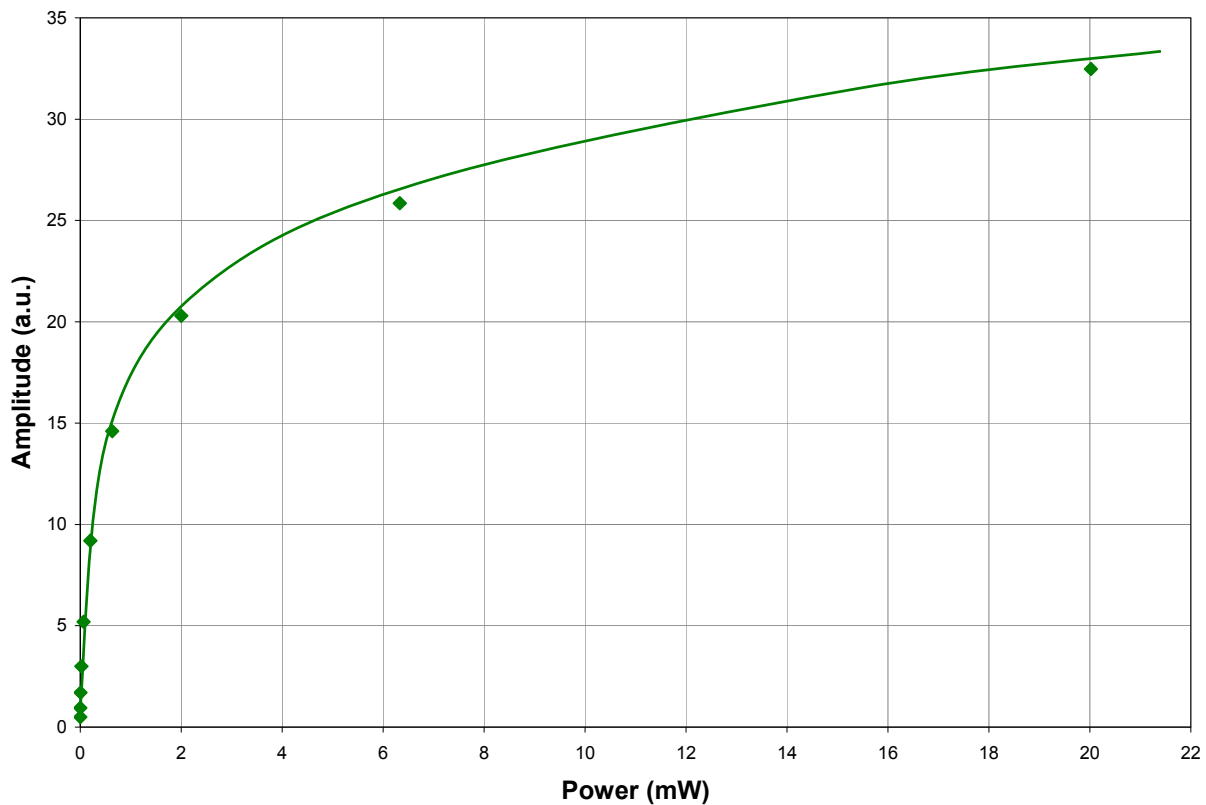


Figure 4-7. Amplitude of D paramagnetic centers as a function of microwave power.

In order to find the saturation point we first plot the amplitude as a function of the square root of the input power, Figure 4-8. The point at which the amplitude is deviating from a linear trend, defines the saturation point. In the case of the D centers a power greater than 0.2 mW (30

dB attenuation in our spectrometer) is enough to saturate the paramagnetic centers. Above the saturation point, the amplitude is no longer proportional to the number of spins.

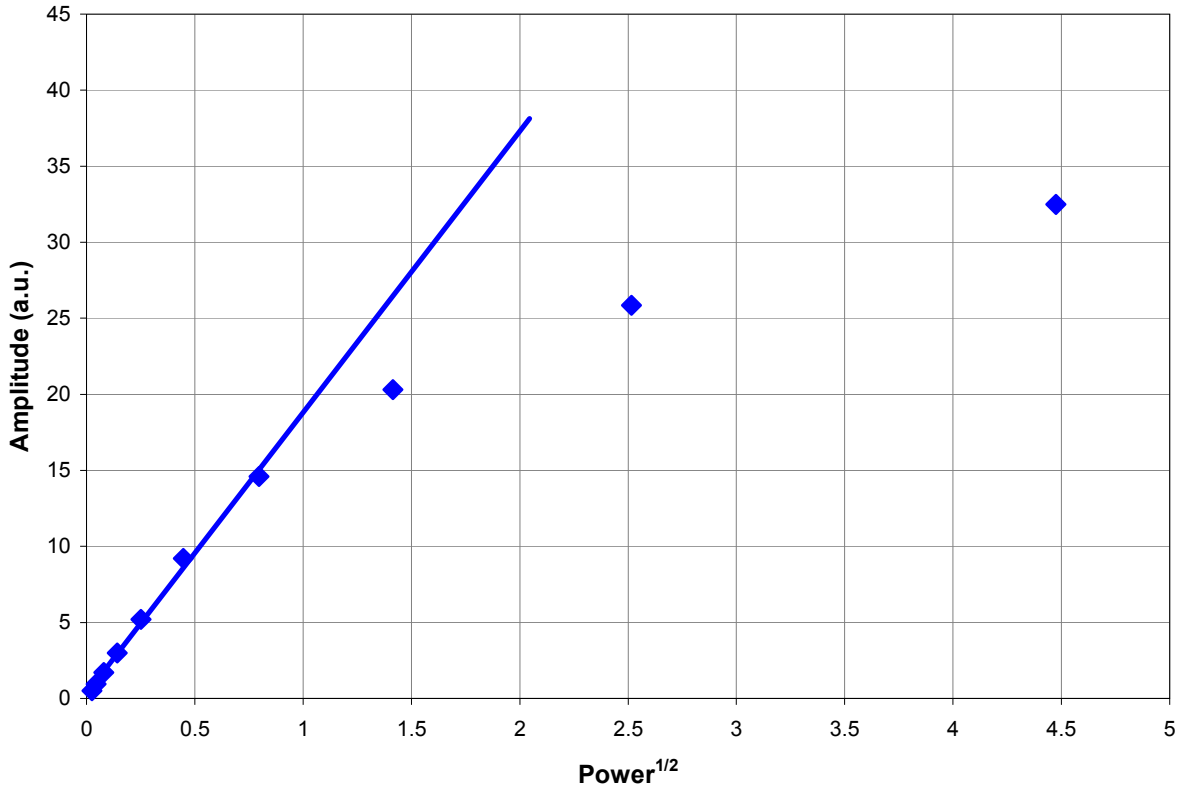


Figure 4-8. Amplitude of D paramagnetic centers as a function of the square root of the microwave power (dots). A linear trend is fitted for the lowest power data points ($R^2=0.995$).

We conducted a similar study for the E' centers as depicted in Figures 4-9 and 4-10. A saturation power of 0.06 mW (35 dB attenuation in our spectrometer) was found. Knowing the saturation point is not only important for comparing samples or spectra from the same sample at different temperatures, it is also important to justify our two-Lorentzian model. Since the saturation points are different for each of the observed features in a sp-Si spectrum, they are not stemming from the same physical origin and therefore are independent. This independence justifies that our model uses the sum of two independent lines. Figure 4-11 shows schematically

how the amplitudes of the D center and the E' center responded differently to the microwave power.

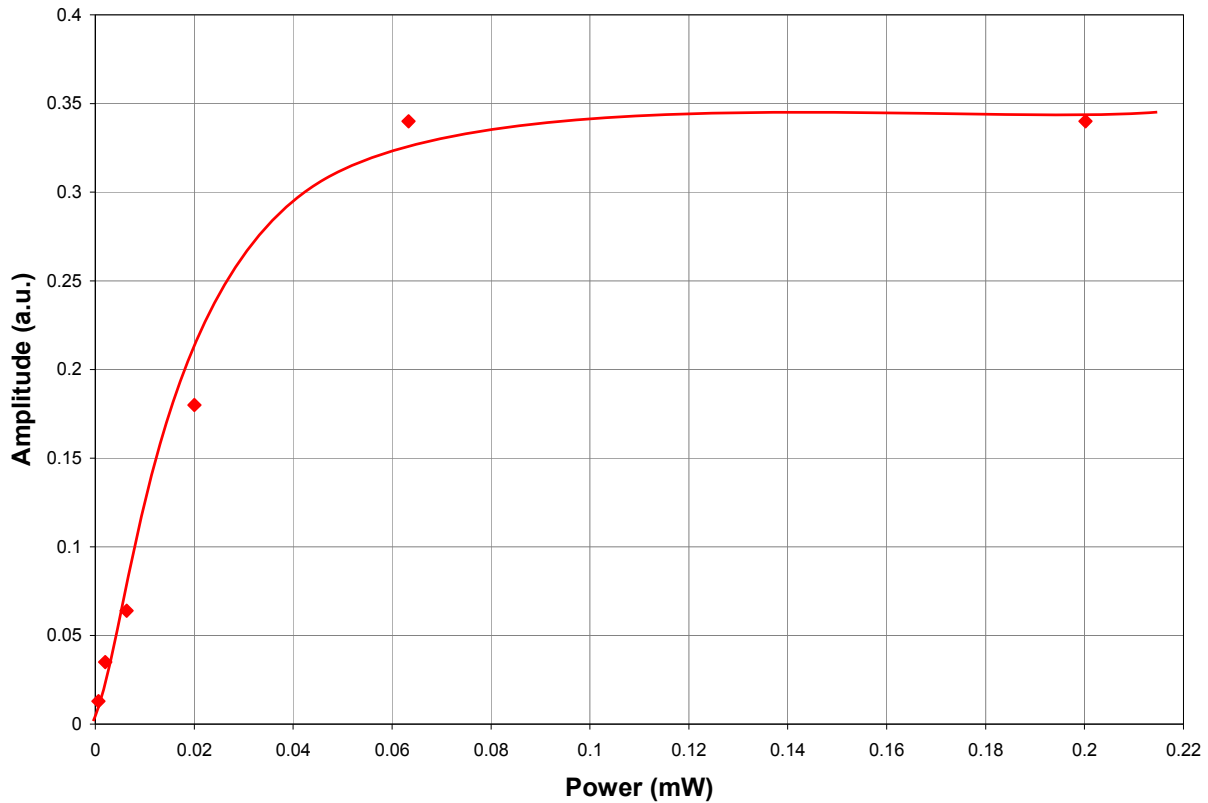


Figure 4-9. Amplitude of E' paramagnetic centers as a function of microwave power.

In addition, the line width of each of the two observed features do not have the same behavior with respect to the microwave power as seen in Figure 4-12. The D centers' line width does not vary with microwave power, while the E' centers' line width is linearly dependent on the log of the power which is explained in the next paragraph. The different behaviors of the E' and D center are characteristic of their independent physical origin and justifies our two-Lorentzian model.

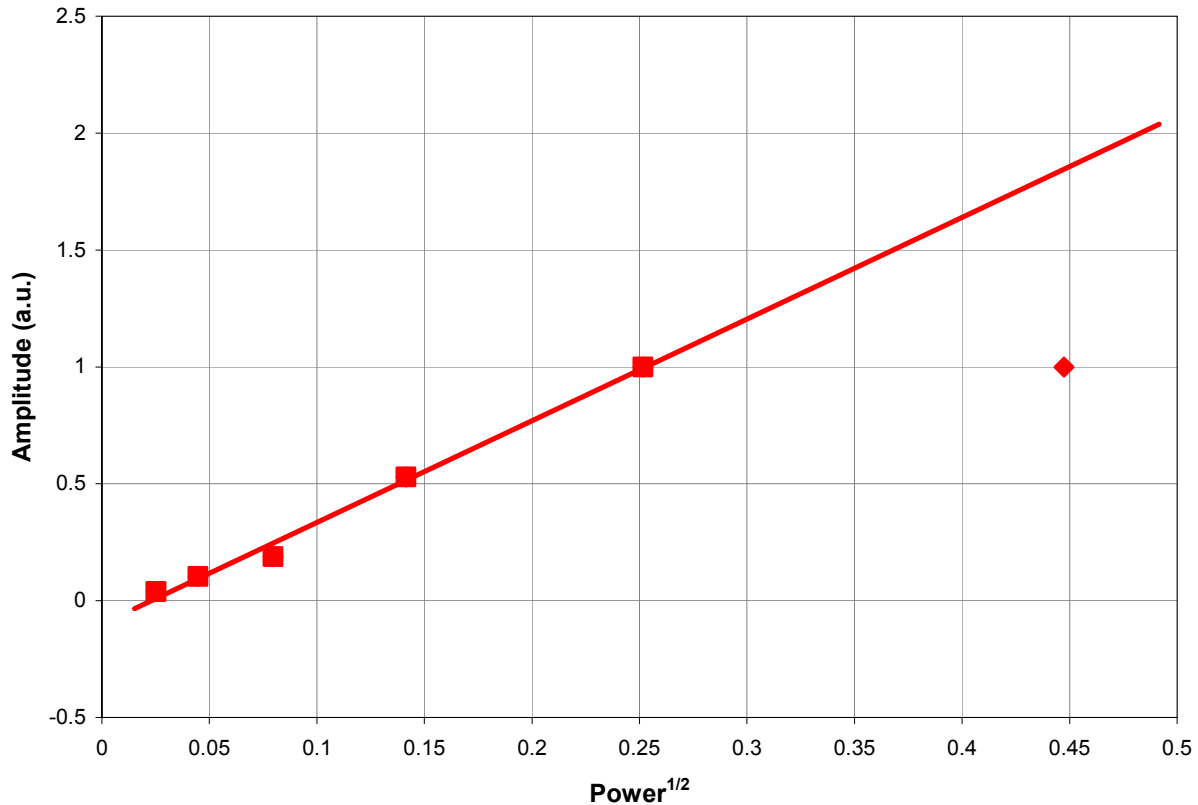


Figure 4-10. Amplitude of E' paramagnetic center as function of the square root of the microwave power (dots). A linear trend is fitted for the lowest power data points ($R^2=0.995$).

Eaton and Eaton⁴⁸ have developed a power saturation model which we apply to sp-Si. The saturation model⁴⁸ is defined as: $amplitude = \frac{a \times P^{1/2}}{(c + P)^{b/2}}$ where P is the microwave power, a is a proportionality constant, c is a constant related to the power at half saturation and b is an exponent which depends on the homogeneity of the line. The exponent constant b is an important factor. In the extreme cases when $b = 1$ we are in the inhomogeneous limit and when $b = 3$ we are in the homogeneous limit. In the case of sp-Si we plot and compare the models ($b = 1$ and $b = 3$) for each of the paramagnetic centers in Figure 4-13 and 4-14. In the case of the D centers, the data is

very well describe ($R^2=0.998$) by the inhomogeneous case while for the E' centers the model matches the data well for the homogeneous case.

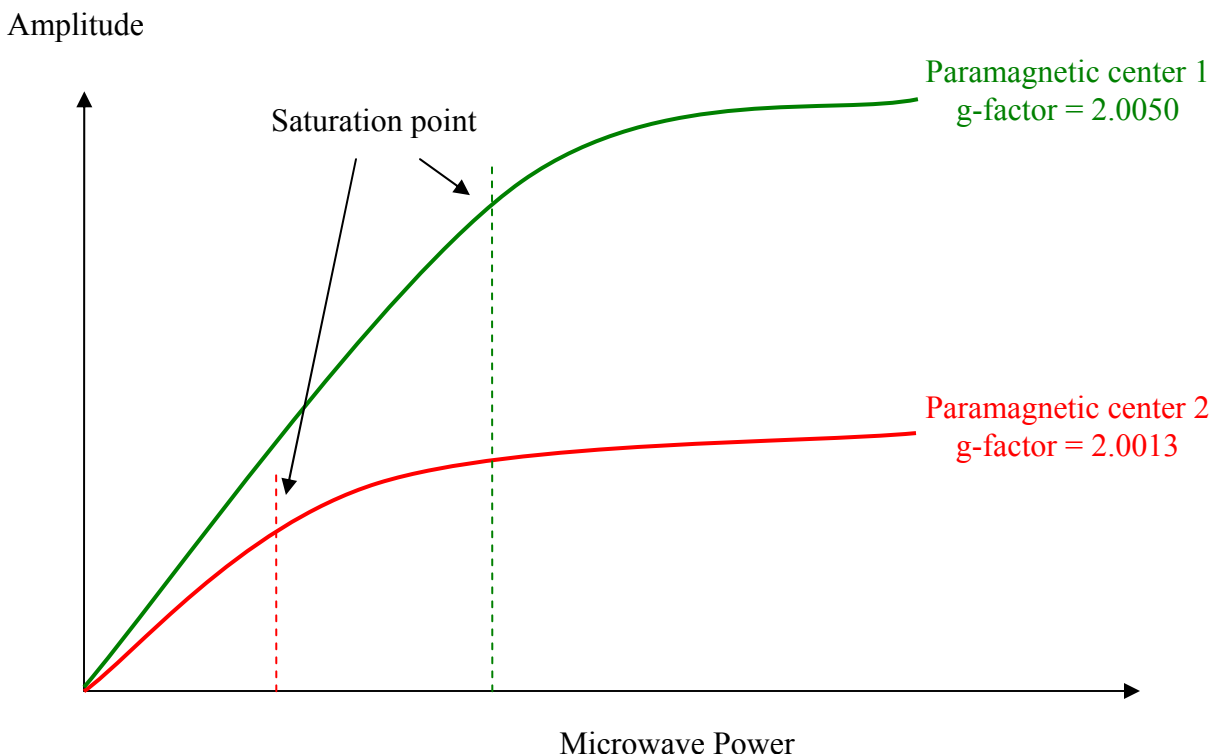


Figure 4-11. Saturation effect observed for the two paramagnetic centers in spark-processed silicon.

For comparison purposes we also plotted the other models on each of the graphs to visually convince ourselves which model (i.e. which b value) works best. It can be added that this conclusion is further confirmation that both EPR lines come from different paramagnetic centers.

Finally, the next figure is dedicated to confirm that the Lorentzian equation is the best choice for modeling sp-Si EPR spectra. Figure 4-15 displays the comparison between sp-Si data and two models best fit, Gaussian and Lorentzian. Both models were best fitted using the software OriginPro 7.5.

In conclusion, we have presented several validation points to confirm the Lorentzian model of sp-Si EPR lines and using this model we have identified the paramagnetic centers present.

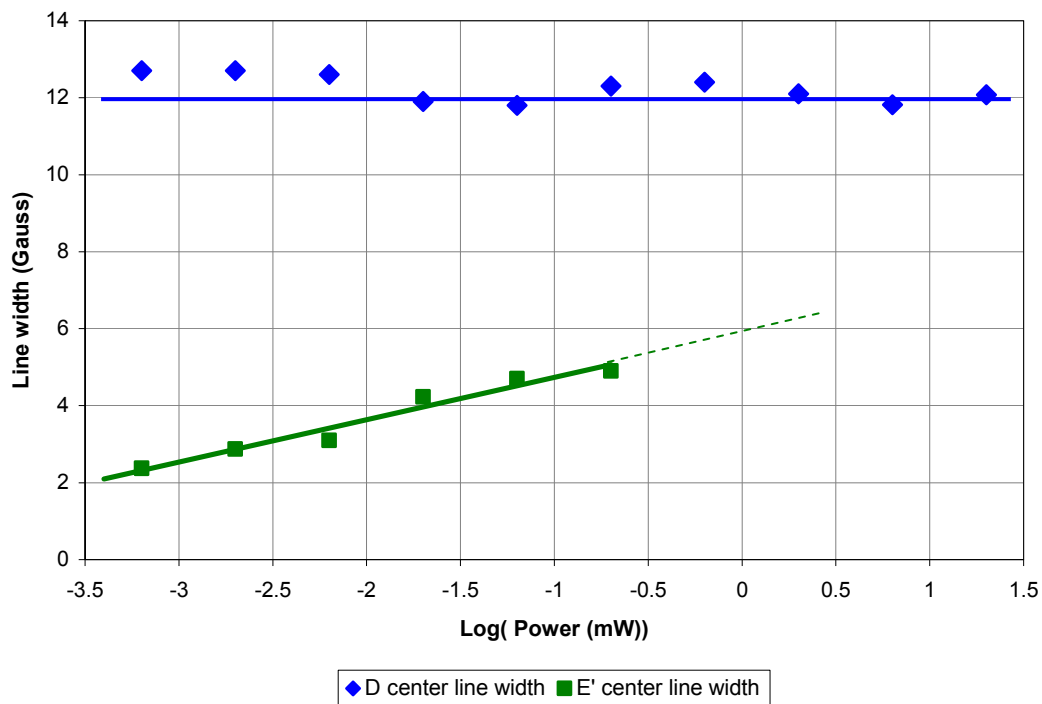


Figure 4-12. Line width as a function of Log (power) for spark-processed silicon.

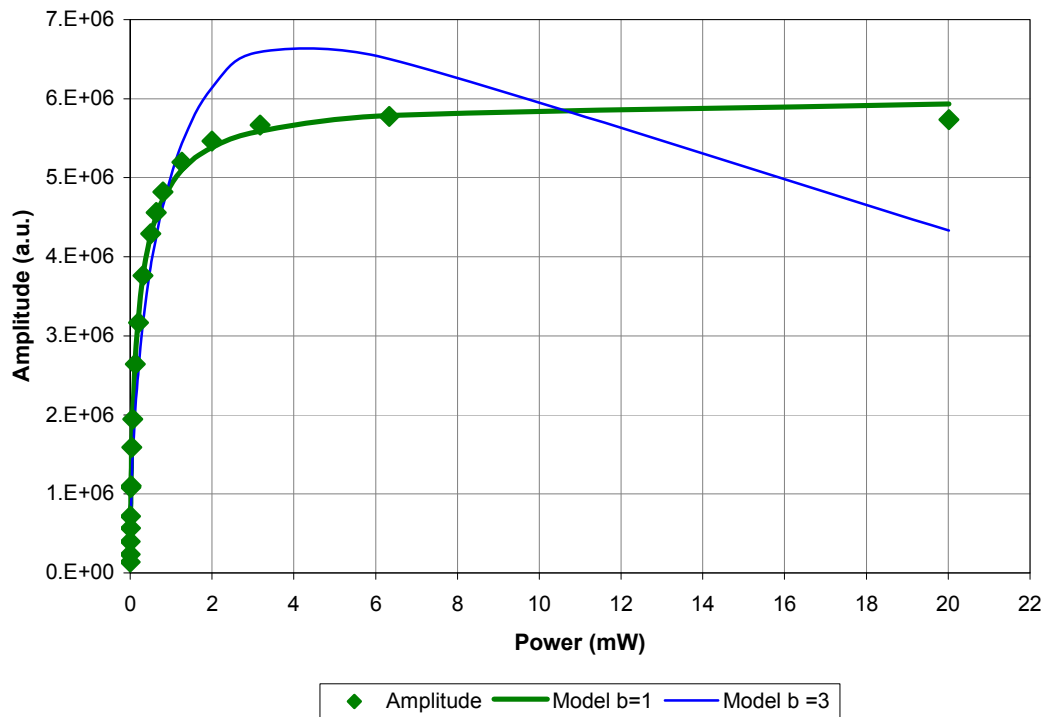


Figure 4-13. Amplitude of D paramagnetic centers as a function of microwave power (dots). Two saturation models are fitted to the data (solid lines).

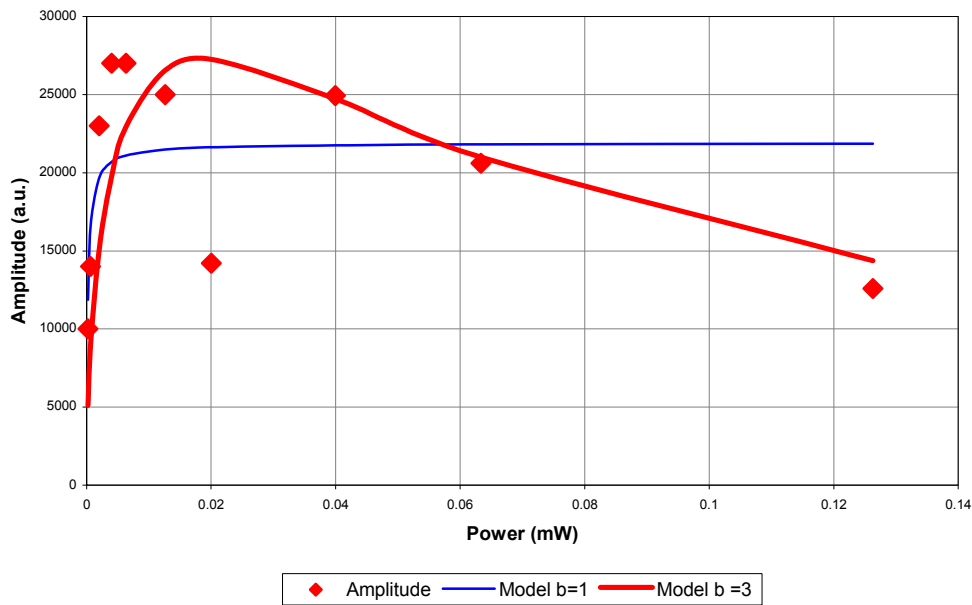


Figure 4-14. Amplitude of E' paramagnetic centers as a function of microwave power for sp-Si (dots). Two saturation models have been fitted to the data (solid lines).

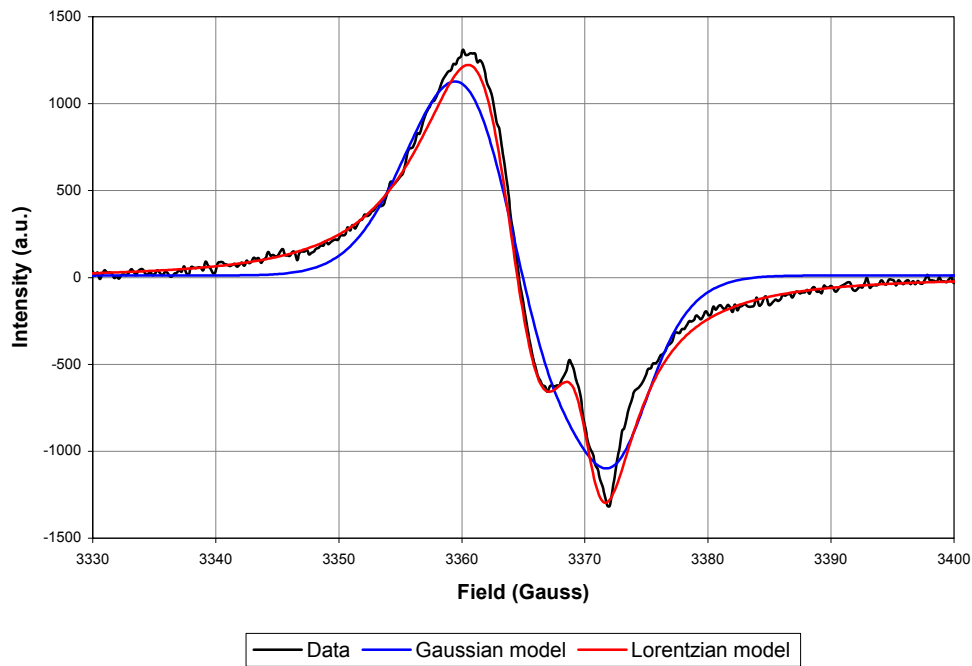


Figure 4-15. Electron paramagnetic resonance spectra of spark-processed silicon at 4.2K (black line) and two possible models: Gaussian based (blue line) and Lorentzian based (red line). Experimental parameters, power = 0.002 mW, power attenuation = 50 dB, modulation field = 1 G, time constant = 20 ms, detector gain = 70 dB, temperature = 4.2 K.

We can now concentrate on characterizing the paramagnetic centers, compare the results with the magnetization obtained from our SQUID and validate our quasiferromagnetic model.

4.4 Electron Paramagnetic Resonance Parameter versus Temperature

The temperature dependence of the sp-Si EPR spectra is very useful. First, the amplitude of the EPR lines is proportional to the number of spins, as long as we are not saturating the signal.

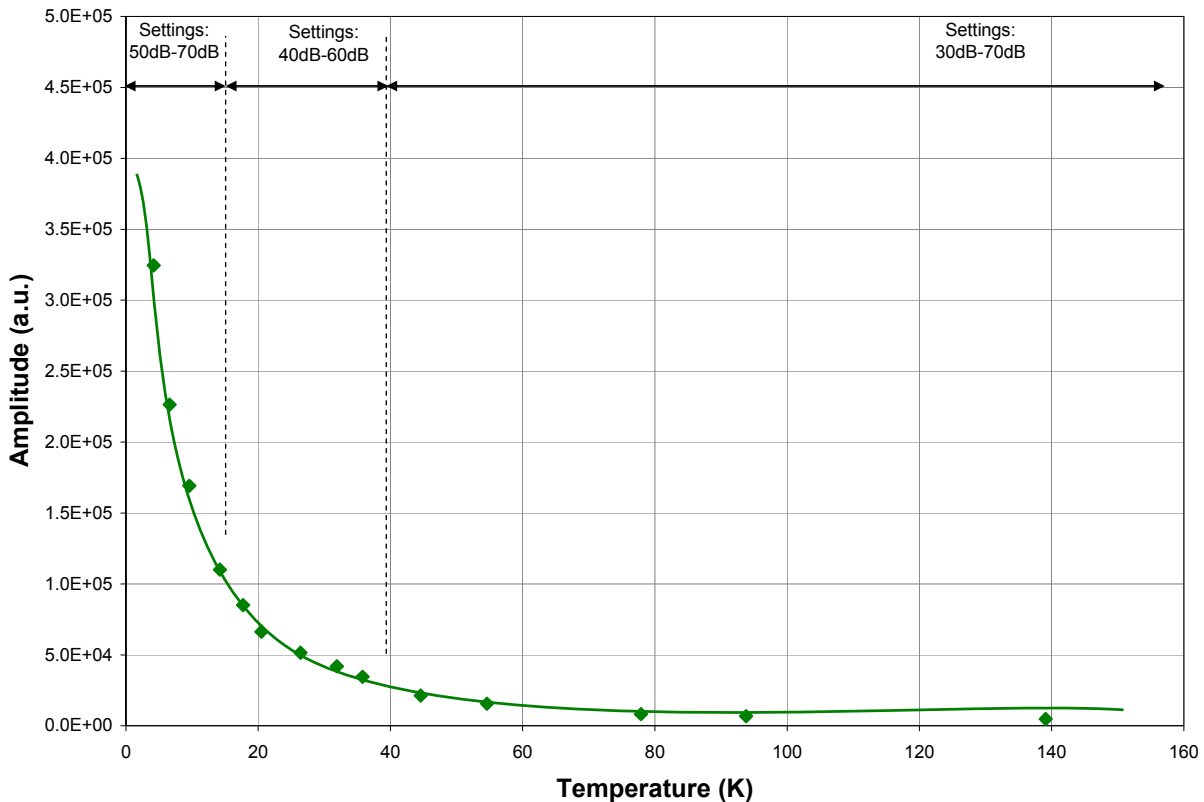


Figure 4-16. Amplitude of D centers versus temperature. The data points above 40K have been divided by 10 to account for the change in gain setting. The gain is changed to keep the signal in the linear regime.

Since we have performed a saturation experiment we now know in which power range we have to measure our data. Also, the magnetization of independent spins is proportional to the number of spins. Thus, the amplitude of the EPR absorption line is proportional to the magnetization as long as these two assumptions are met. In addition, the temperature dependence

of the line width will be useful for comparison with pulsed EPR experiments, which will be presented in a later section. We present, now, the temperature dependence of the amplitude, line width and g-factor all together of the D and E' centers present in sp-Si at low temperature and then high temperature.

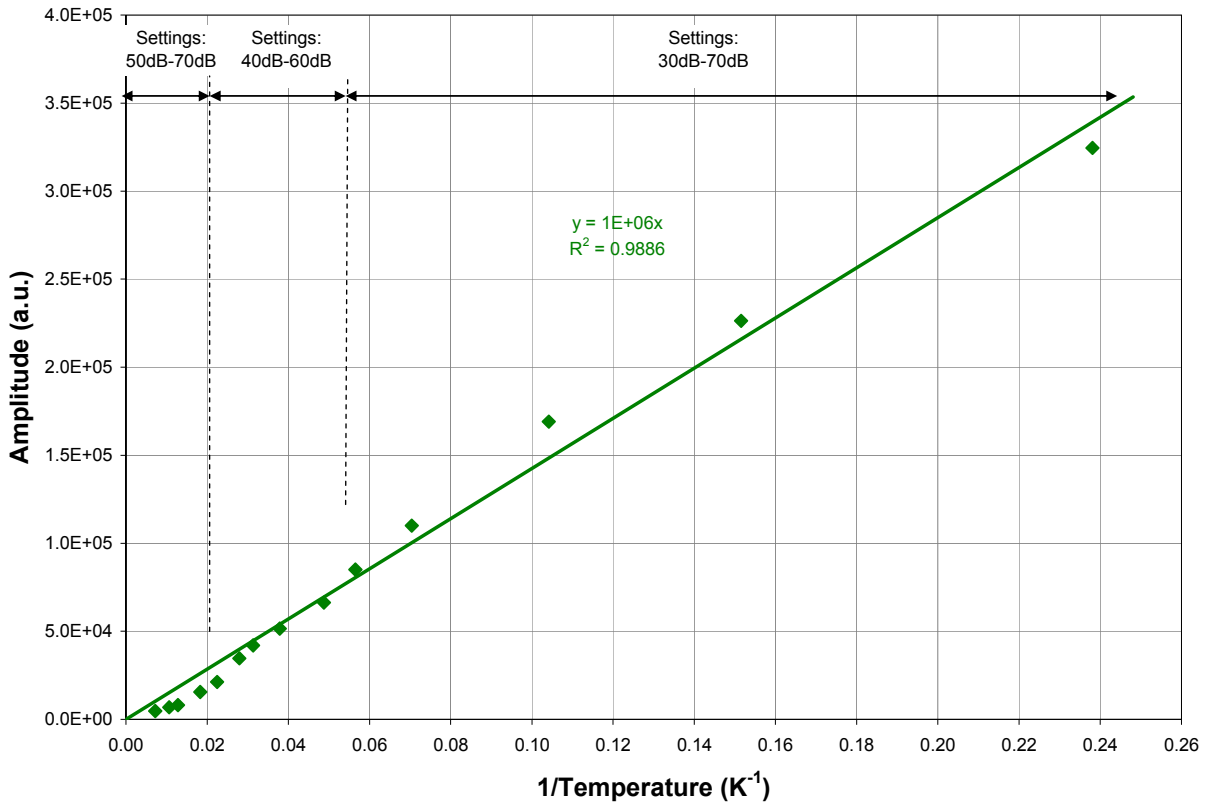


Figure 4-17. Amplitude of D centers versus inverse temperature (dots). The data points below 0.025K^{-1} have been divided by 10 to account for the increased gain. A linear trend is fitted to the data (solid line).

4.4.1 Low Temperature 5 to 300K

In order to study each paramagnetic center type we continue to use our two-Lorentzian model and apply it at each temperature. Then the modeled amplitude, line width and g-factor can be plotted as a function of temperature.

The amplitude versus temperature is plotted in Figure 4-16 for the D centers. One can observe that the amplitude increase as the temperature decrease. In order to prevent saturation,

the microwave power was decreased and the detector gain increased. Three different settings were used and the amplitude was multiplied by the proper coefficient to account for mismatches between the microwave power and the signal gain scales. Furthermore, the amplitude is plotted against the inverse temperature in Figure 4-17. A linear trend is fitted to the data with a correlation coefficient of 0.99.

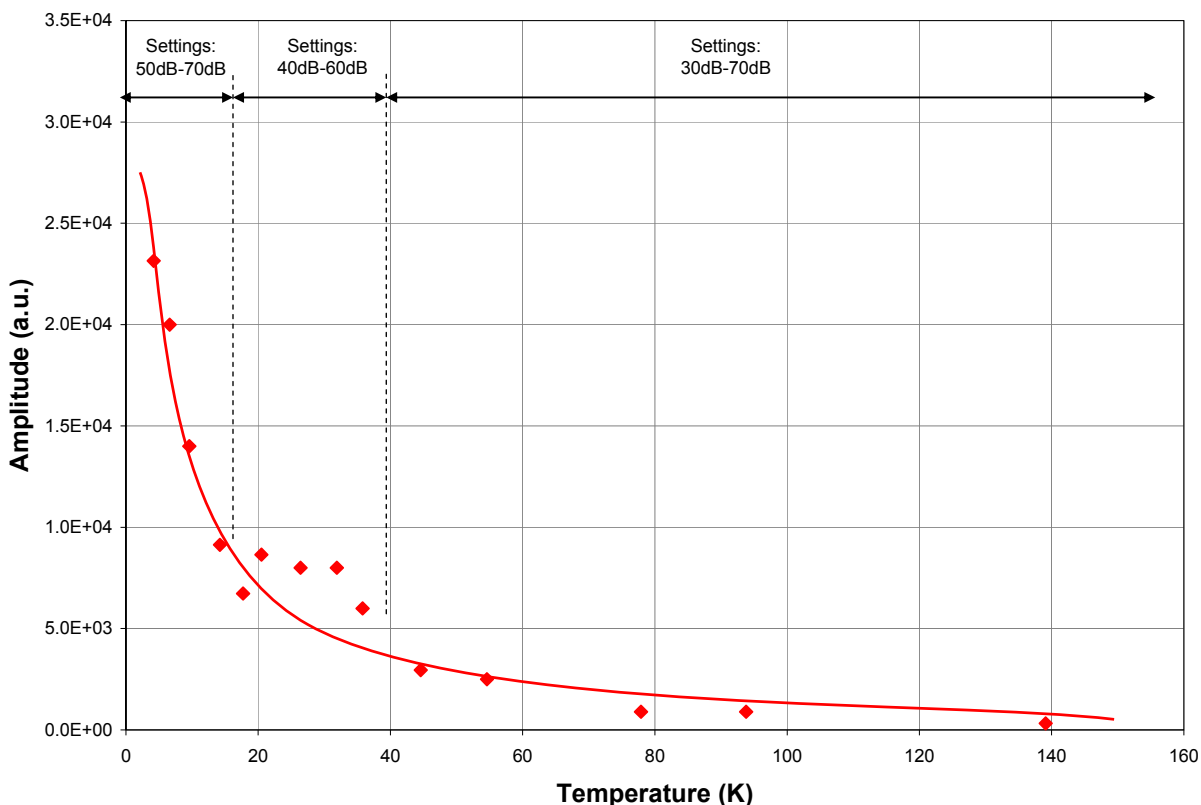


Figure 4-18. Amplitude of E' centers versus temperature. The data points above 40K have been divided by 10 to account for the increased gain.

In the case of independent spins, the magnetization is simply proportional to the measured amplitude and therefore inversely proportional to the temperature. The experimental results suggest that the EPR amplitude follows the Curie law. It could be argued that this relationship demonstrates the independence of the paramagnetic centers and therefore deny our cluster model. But, it has been calculated⁴⁹ that for a ratio of independent spins over spins within

clusters of 50%, the magnetic susceptibility is almost observed as coming from independent spins only. First, we believe that spins in sp-Si are mostly independent, as shown by the observed Curie law. In addition, we suggest that the magnetization coming from the clusters of spins is small in comparison to the magnetization from the independent spins. Similar conclusions are drawn for the E' centers. Figure 4-18 and 4-19 present the amplitude of the E' centers as a function of the temperature and inverse temperature, respectively.

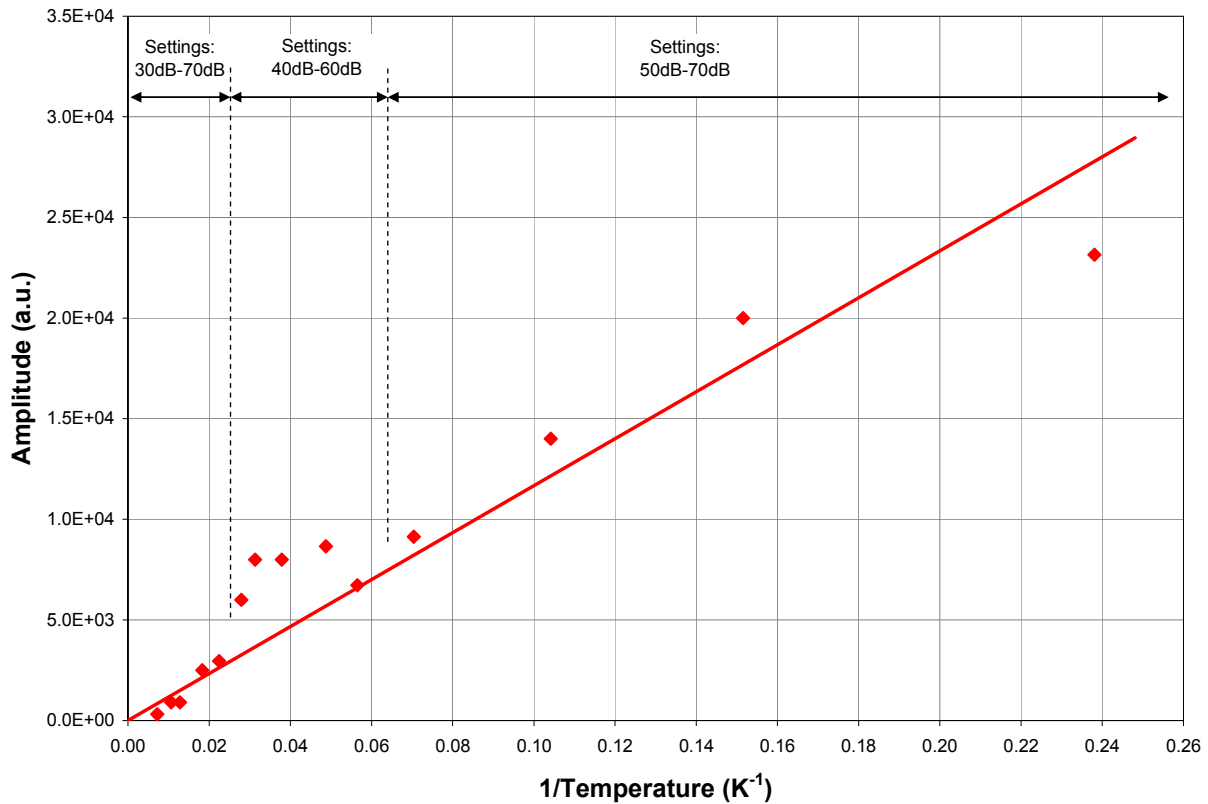


Figure 4-19. Amplitude of E' centers versus inverse temperature (dots). The data points below 0.025 K⁻¹ have been divided by 10 to account for the increased gain. A linear trend is fitted to the data (solid line).

Additionally, the line width for both centers is plotted versus the temperature in Figure 4-20. In both cases the line width is essentially temperature independent. The line width depends

on different relaxation mechanism and a full account of that dependence will be presented in the pulsed EPR section of this chapter.

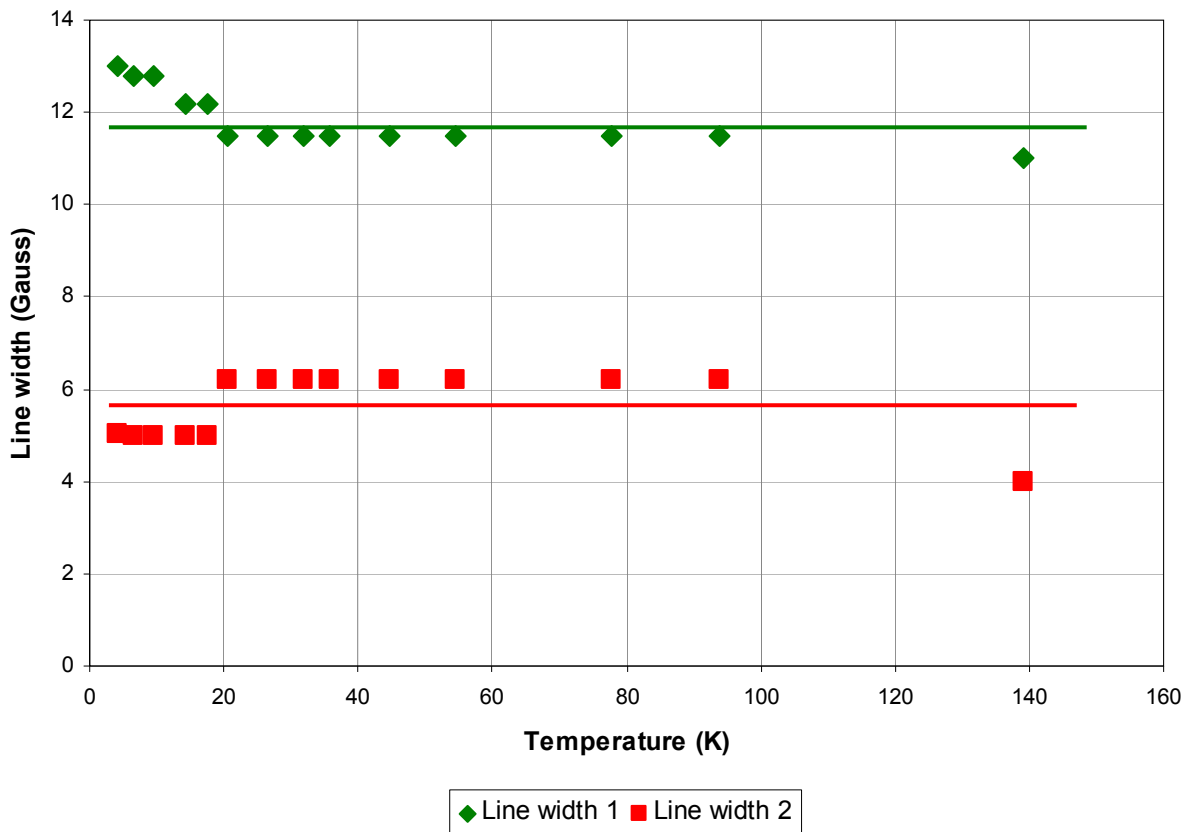


Figure 4-20. Line width of the two paramagnetic centers present in spark-processed silicon versus temperature in the low temperature range. Line width 1 corresponds to the D centers and line width 2 corresponds to the E' centers.

The characterization of the centers is completed with the temperature dependency of the g-factors. Figure 4-21 presents the g-factor for each center as a function of temperature. For the D centers the g-factor does not depend on the temperature while for the E' centers the g-factor has a small temperature dependency. We believe that the main reason which explains this small dependence is associated with the difficulty of fitting the Lorentzian equation. The signal from the E' centers is much smaller than the D centers and therefore modeling is a more difficult process since both signals are collected together and interfere with one another.

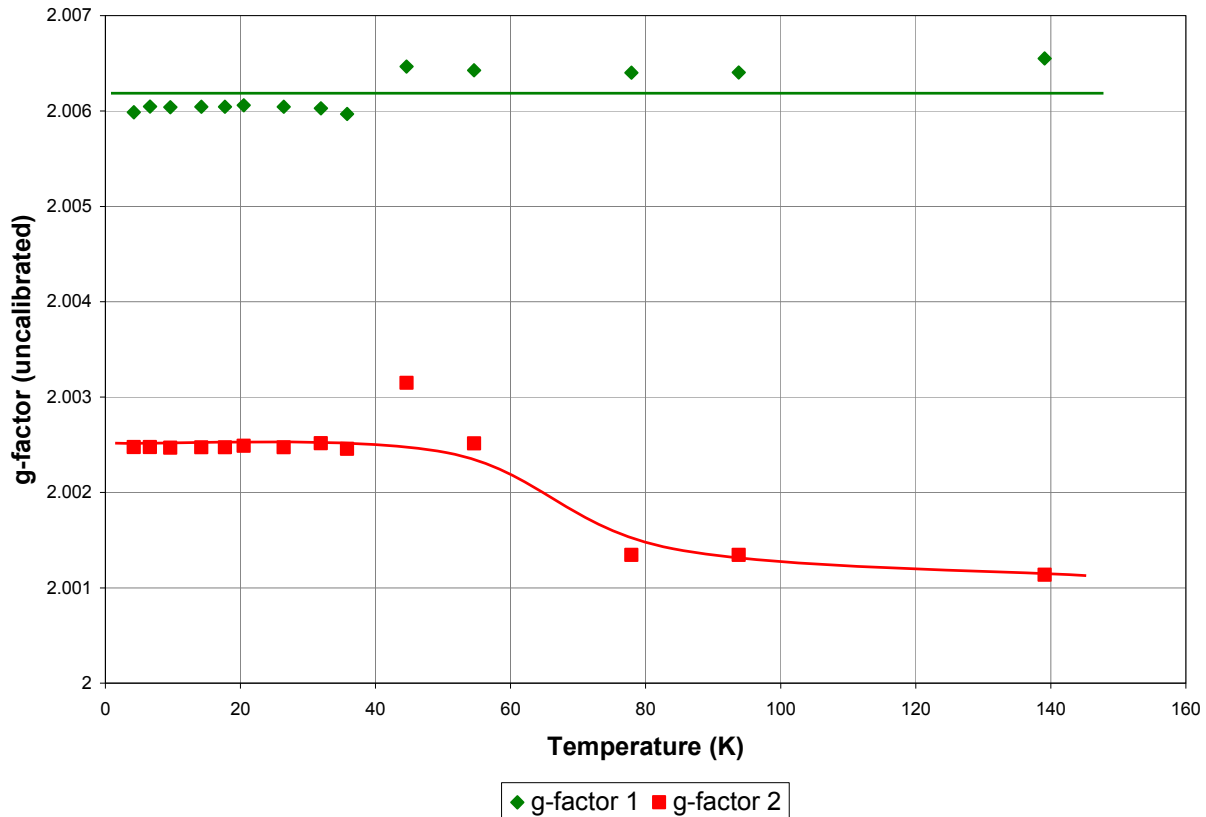


Figure 4-21. Spark-processed silicon paramagnetic centers g-factor (uncalibrated) versus temperature. The g-factor 1 corresponds to the D centers while the g-factor 2 corresponds to the E' centers.

4.4.2. High Temperature 300 to 800K

While the low temperature EPR equipment was readily available, we were not equipped at first for high temperature measurements. I designed and assembled a high temperature oven for the EPR spectrometer which allows stable temperature up to 600 K. The temperature can be pushed up to 700 K if precision is not essential. More details can be found in the Appendix B about the design and working condition of this oven. For the highest temperature measurements we collaborated with Dr. Causa from the Centro Atomico Bariloche in Argentina, who is equipped with a commercial high temperature EPR cavity.

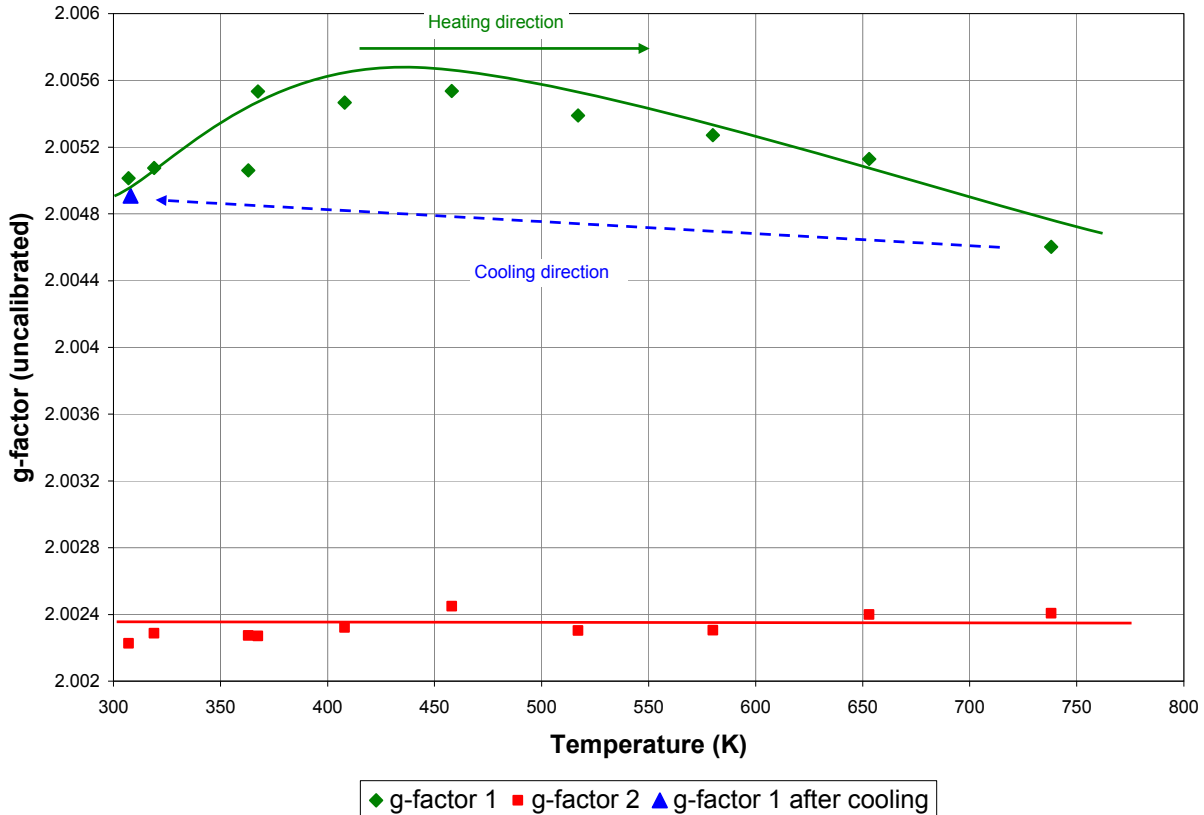


Figure 4-22. Spark-processed silicon paramagnetic centers g-factor versus temperature. The g-factor 1 corresponds to D centers while the g-factor 2 corresponds to E' centers. The g-factor 1 was measured again after cooling back to room temperature (blue triangle) and the same value was found as before the heating (green diamond).

The same analysis method for the high temperature EPR spectra as for the low temperature spectra of sp-Si was used, meaning that we continue to use a two-Lorentzian model.

First, we look at the g-factor temperature behavior. Figure 4-22 displays g-factors for both paramagnetic centers. The g-factor of the E' centers is temperature independent in this temperature region. On the other hand the g-factor of D centers is affected by the temperature. Both g-factors are deconvoluted from the same spectrum. If the temperature dependence was due to the deconvolution method we would observe both g-factors to have the same temperature dependency. But, it is not the case. The scatter around the average g-factor of the E' center give

an estimate of the error on the measurement. But a much larger variation of the D centers g-factor is observed. Therefore, we conclude that the g-factor of the D centers is temperature dependent. It should be noted that after cooling back to room temperature the g-factor of the D centers reverts to its original value and therefore the process is reversible. Also, it only affects the g-factor of D centers and not the g-factor of E' centers. We suggest that thermal expansion could be one of the effects responsible for the g-factor temperature dependence. Since the E' centers are related to oxygen rich defects we assume that they are located in the SiO₂ matrix. The D centers are only related to silicon atoms and therefore we suggest that they are likely to be located in or at the surface of silicon clusters within the SiO₂ matrix. Specifically, the thermal expansion coefficient of each of these materials, that is, SiO₂ and silicon are very different. The thermal expansion coefficient of SiO₂ is very small compared to the one of silicon². This could induce changes on the bond length between silicon atoms, therefore affecting the electron orbitals and consequently the g-factor of the D centers.

It should be noted in passing that the concept of silicon clusters imbedded in a SiO₂ matrix has been studied and documented by our group using comparison between optical properties and computer molecular modeling⁵⁰ as well as by direct transmission electronic microscopy observation of silicon nanocrystals⁵¹.

Secondly, the study of the line width as a function of the temperature does not show any influence as displayed in Figure 4-23. For both centers the line width is temperature independent.

Finally, the amplitude variation of the EPR line intensity for each defect as a function of the temperature is studied. Using our high temperature apparatus we observed a slight decrease of the D and E' centers amplitude as a function of temperature in the 300 – 600 K range (results not shown). Due to the strong decrease in sensitivity of our cavity at temperatures above 600 K

we felt like our data was not reliable above this temperature. This prompted the collaboration with Dr. Causa who has measured the EPR spectra of sp-Si for us. Her EPR system is designed to work at temperatures up to 1300K with no loss in sensitivity. Once the spectra were received, I used the same two-Lorentzian model analysis to calculate the amplitude of the E' and D paramagnetic centers.

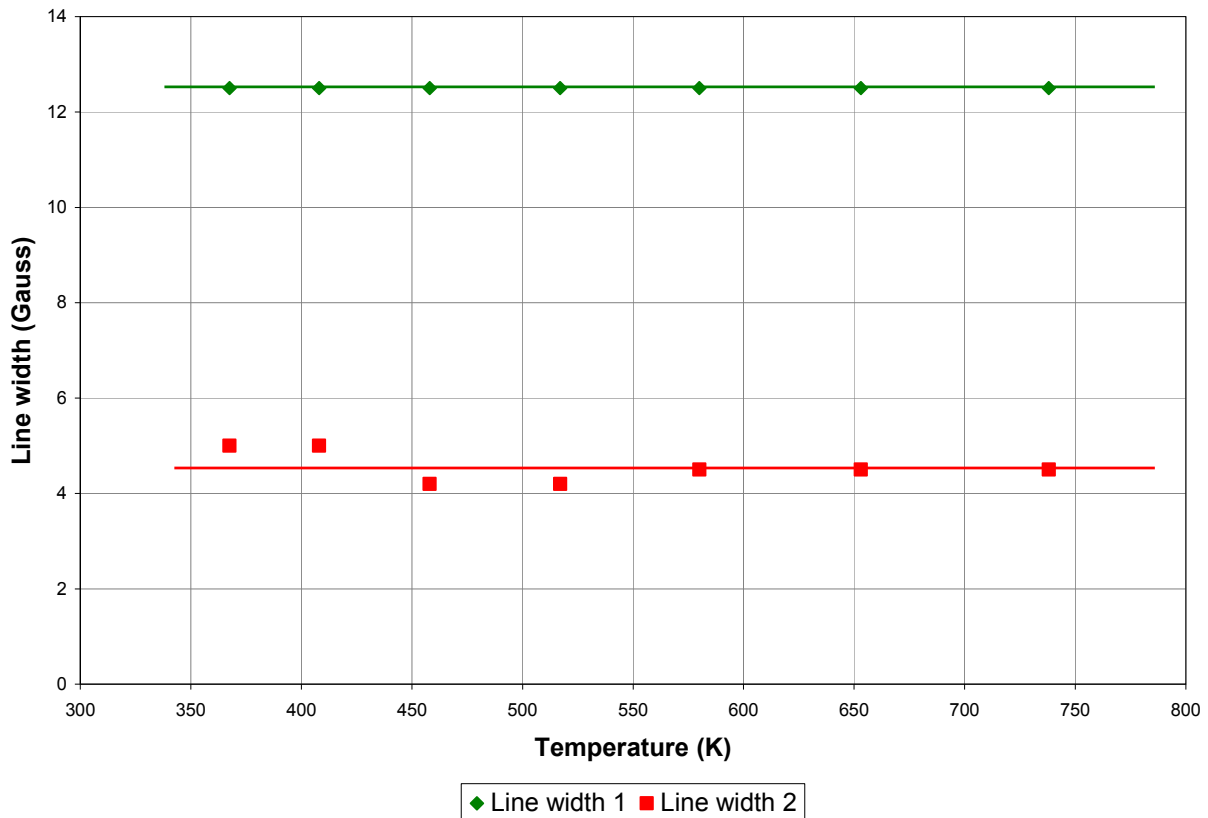


Figure 4-23. EPR line width of the two paramagnetic centers present in spark-processed silicon versus temperature in the high temperature range. The line width 1 corresponds to D centers while the line width 2 corresponds to E' centers.

Figure 4-24 displays the amplitude of the D and E' paramagnetic centers (that is the A factor in the Lorentzian model) as a function of the temperature. In the case of the D centers, the amplitude is steady up to 500 K and then decreases down to almost zero at 700 K. On the other hand, the E' paramagnetic centers amplitude is not affected by the temperature between 580 and

780 K. At temperatures below 580 K the deconvolution with the two-Lorentzian model is not possible because the E' center is too weak compared to the D centers amplitude.

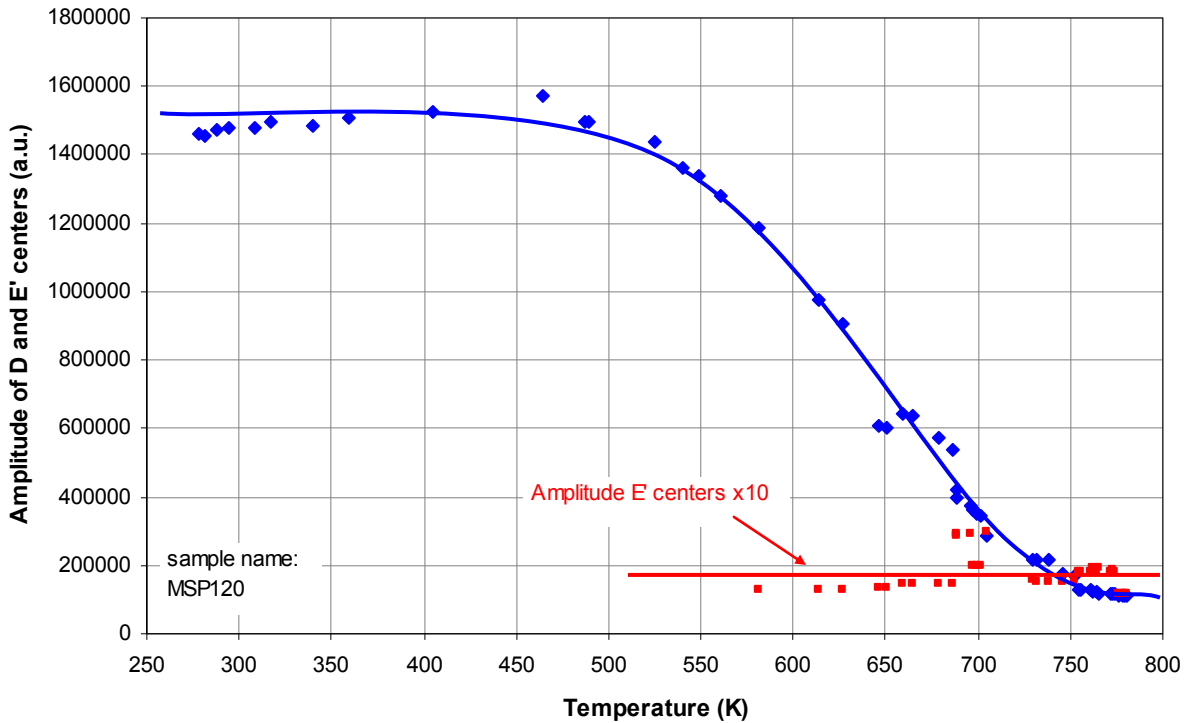


Figure 4-24. Amplitude of D (blue) and E' (red) centers versus temperature for spark-processed silicon in the high temperature range.

These results confirm our previous suggestion that the D and E' centers are not related to one another. In addition, we previously suggested that the E' centers are located in the SiO₂ amorphous matrix while the D centers are located in silicon nanocrystals or clusters. Therefore, we propose that these two types of centers are not close to one another, adding another argument to our theory of non-random distribution of paramagnetic centers.

At low temperature, we observed that the magnetization as well as the amplitude of the D and E' centers were characteristic of the Curie law. But, at high temperature (that is about 300 K) the measurements do not suggest a Curie law behavior but rather a behavior modeled with the Weiss equation. This is shown in Figure 4-24, where a Curie law model is plotted and one can

see that the data does not follow that law. We suggest that the deviation from the Curie law at high temperature can be explained by the decoupling of the interacting centers within clusters. When the temperature is near the Curie point, the thermal energy is large enough to overcome the exchange interaction between two spins. When this happen the two spins become individual spins and now behave like independent paramagnetic centers explaining the non-zero amplitude above the Curie point.

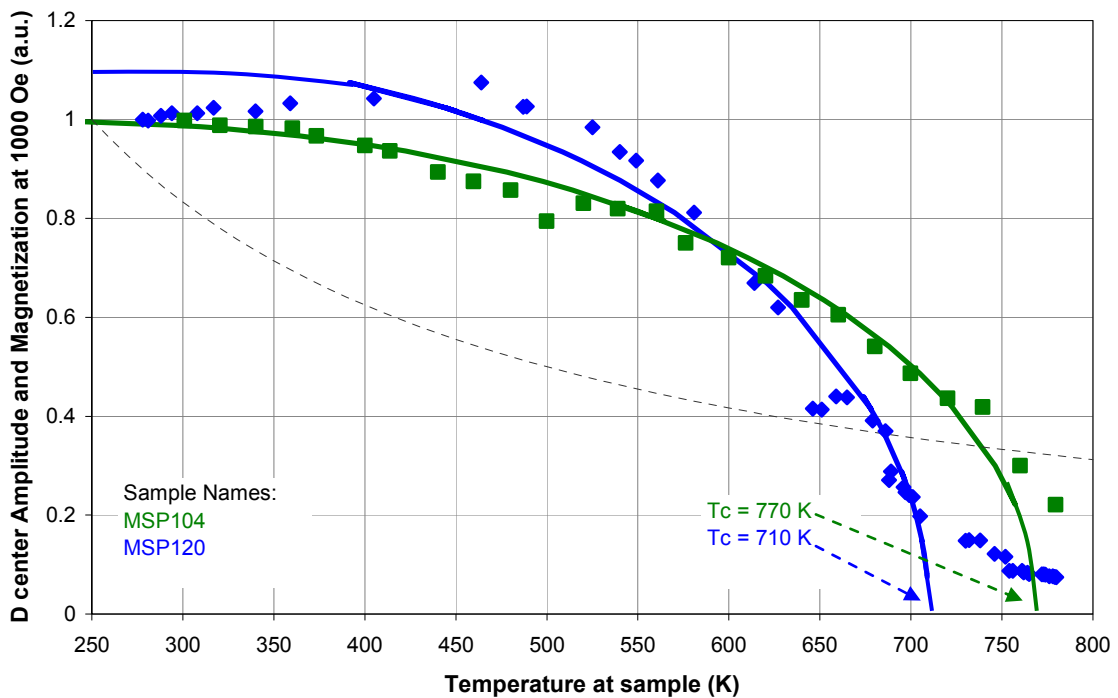


Figure 4-25. Amplitude of D centers (blue dots) and Magnetization at 1000 Oe (green dots) versus temperature for spark-processed silicon in the high temperature range. A Weiss equation is fitted through both data sets (solid curves). For comparison a Curie law curve is plotted (black dash).

The amplitude data of the D centers was also compared to the Weiss equation to evaluate the Curie temperature. We followed the same method previously described in chapter 3 (section 3.2.3). A Curie temperature of 710 K was found. Figure 4-25 displays the D centers amplitude as a function of temperature along with its Weiss model curve. In addition, the magnetization of a

similar sp-Si sample as a function of temperature is plotted on the same graph along with its Weiss model curve (previously presented in section 3.2.3). The comparison between the two sets of data suggests that the D centers are at the origin of the magnetization behavior of sp-Si for temperature above 300 K.

It could be argued that the Curie temperature evaluated from the Weiss model with the magnetization data is too different from the one found with the data stemming from EPR, but, we could attribute the differences to the type of instrument, which inevitably lead to some discrepancies, and to the samples being prepared in a similar manner but not being exactly the same. For example, the EPR technique is not sensitive to diamagnetism and species with an integer total spins while the SQUID magnetometer is.

It should be noted in passing that the data obtained from Dr. Causa and our data obtained with our own laboratory made equipment are consistent with one another for temperatures up to 600 K. Above that temperature our data on amplitudes of the E' and D centers is no longer reliable.

In conclusion, the continuous wave EPR has allowed the identification and separation of two paramagnetic centers. Also, the EPR spectral analysis and the comparison with the magnetization of sp-Si at high temperature are consistent with our paramagnetic center distribution model.

Continuous wave EPR allows the indirect measurement of the density of the paramagnetic centers, but the direct method by pulsed EPR is preferred. The main reason for not using cw-EPR is the need for a precise measurement of the sample volume, which turns out to be extremely difficult for sp-Si. Pulsed EPR is a better technique for measuring the density which leads to the distance between paramagnetic centers. But it requires the characterization of the observed

signals which is more complex, as this technique is more complex than cw-EPR. The next section focuses on that method.

4.5 Characterization of Pulsed Electron Paramagnetic Resonance

Our goal in using pulsed EPR is to calculate the density of the paramagnetic centers at the local level and therefore calculate the maximum separation distance between spins. This will then be used to complement the model proposed to explain quasiferromagnetism. We separate this part of the chapter into several sections to facilitate its understanding. In the first section, we present the relaxation rates measured on sp-Si and information extracted from them. In a subsequent section we propose to separate the centers by relaxation rates. Then, we measure the relaxation rates leading to the local density of spins.

4.6 Relaxation Rates

In the pulsed EPR world there are many ways of acquiring a signal. In our case, we are very much interested in the basic spin-lattice and spin-spin relaxation rates of sp-Si paramagnetic centers.

4.6.1 Spin-Lattice Relaxation Rate

The spin-lattice relaxation rate is also known as T_1 and longitudinal relaxation. In Figure 4-26 we present the spectrum from which we measure T_1 . The detected intensity is plotted as a function of time. In such experiments the intensity is expected to decay exponentially with time at a rate of $1/T_1$. But, in the case of sp-Si bi-exponential decay functions are necessary for a good match to our data, as seen in Figure 4-26. We called the exponential decay times T_1 and T_1' . The model equation used is: $Intensity(t) = A_1 e^{-t/T_1} + A_1' e^{-t/T_1'}$, where A_1 and A_1' are the exponential amplitudes of each of the decays.

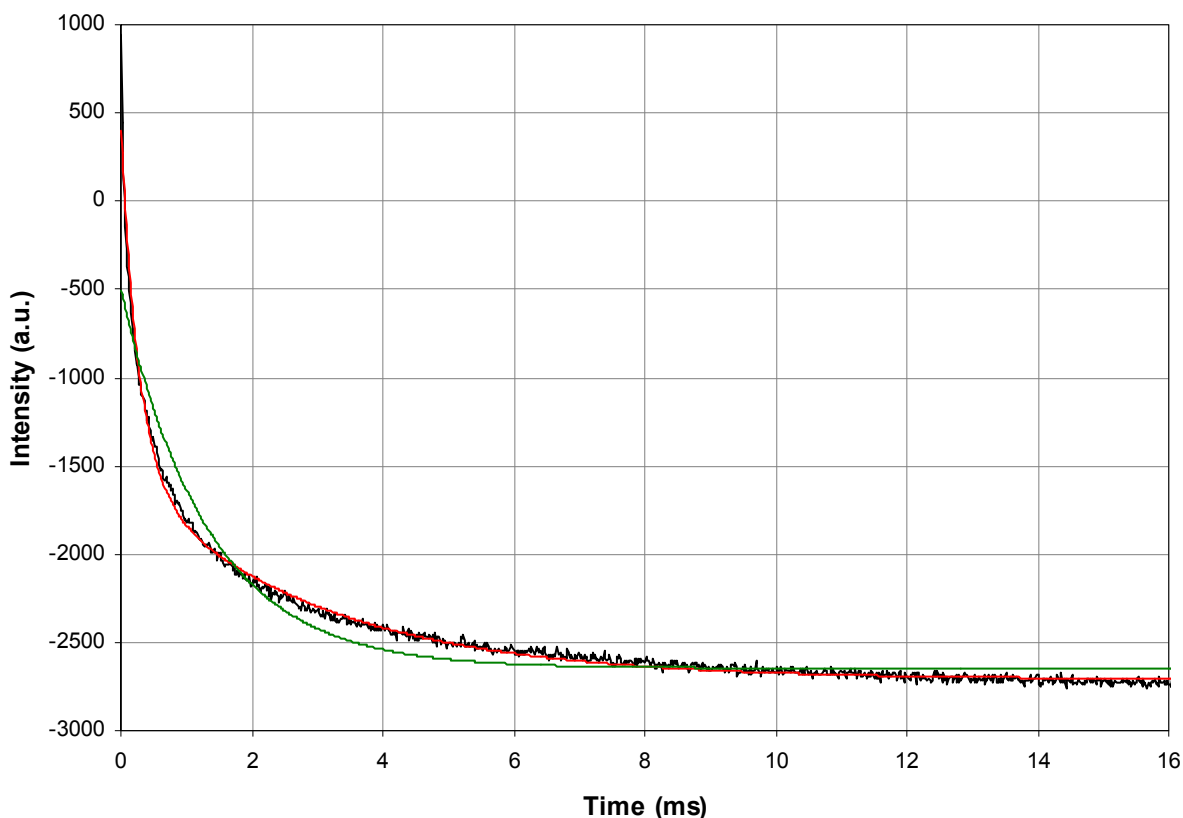


Figure 4-26. Intensity versus time for a spin-lattice relaxation rate experiment of spark-processed silicon (black line), one-exponential decay model (green line) and bi-exponential decays (red line). Experimental parameters (inversion recovery), center field = 3455.5 Gauss, shot repetition time = 408 ms, shot loop = 1, pulse length = 16 ns and step is 16 ms.

In a subsequent experiment we measure T_1 and T_1' as a function of temperature. The results are presented in Figure 4-27. In both cases the relaxation rate follows a direct process up to 60 K. A direct process is characterized by the proportionality between T_1 and the temperature⁵². In addition above 60 K and according to the same authors, T_1 and T_1' follow a hopping process. We are mostly interested in the T_1 processes to help understand the physical origin of the line width in the cw-EPR. It must be added in passing that the line width in cw-EPR can have several origins and knowing the behavior of the spin-lattice relaxation rate as a function of the temperature is necessary to meet this goal.

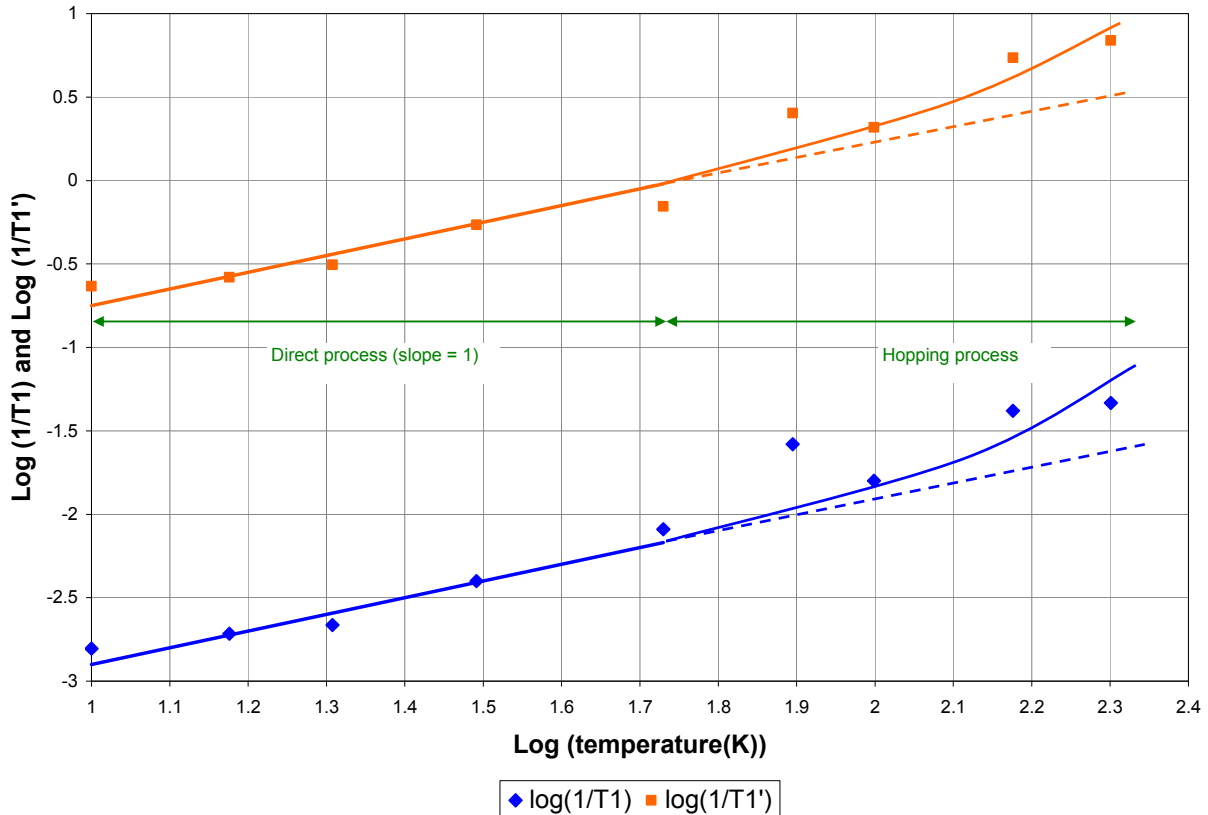


Figure 4-27. Spin-lattice relaxation rates versus temperature for spark-processed silicon.

4.6.2 Spin-Spin Relaxation Rate

The spin-spin relaxation rate is very important to us as it is the first step towards measuring the density of defects. This relaxation rate is also called T_2 or transverse relaxation rate. But T_2 is obtained indirectly from the phase memory time (T_m). By running an echo decay pulse EPR experiment⁵³ we obtain intensity versus time curves. The exponential decay constant is T_m . The relationship between T_m and T_2 is given by the following equation:

$$\frac{1}{T_m} = \frac{1}{T_2} + f(\text{Power, concentration})$$

where concentration is the density of spins in a given sample

and where the function of power and concentration is a constant for a given sample at a given power. In this section, it is the case, that is, we use the same sample and use the same input power setting for all measurements throughout this section, therefore the relationship becomes

simply: $\frac{1}{T_m} = \frac{1}{T_2} + \text{constant}$. Figure 4-28 displays the intensity as function of time of sp-Si. Once

again, the data can only be fitted with bi-exponential decays.

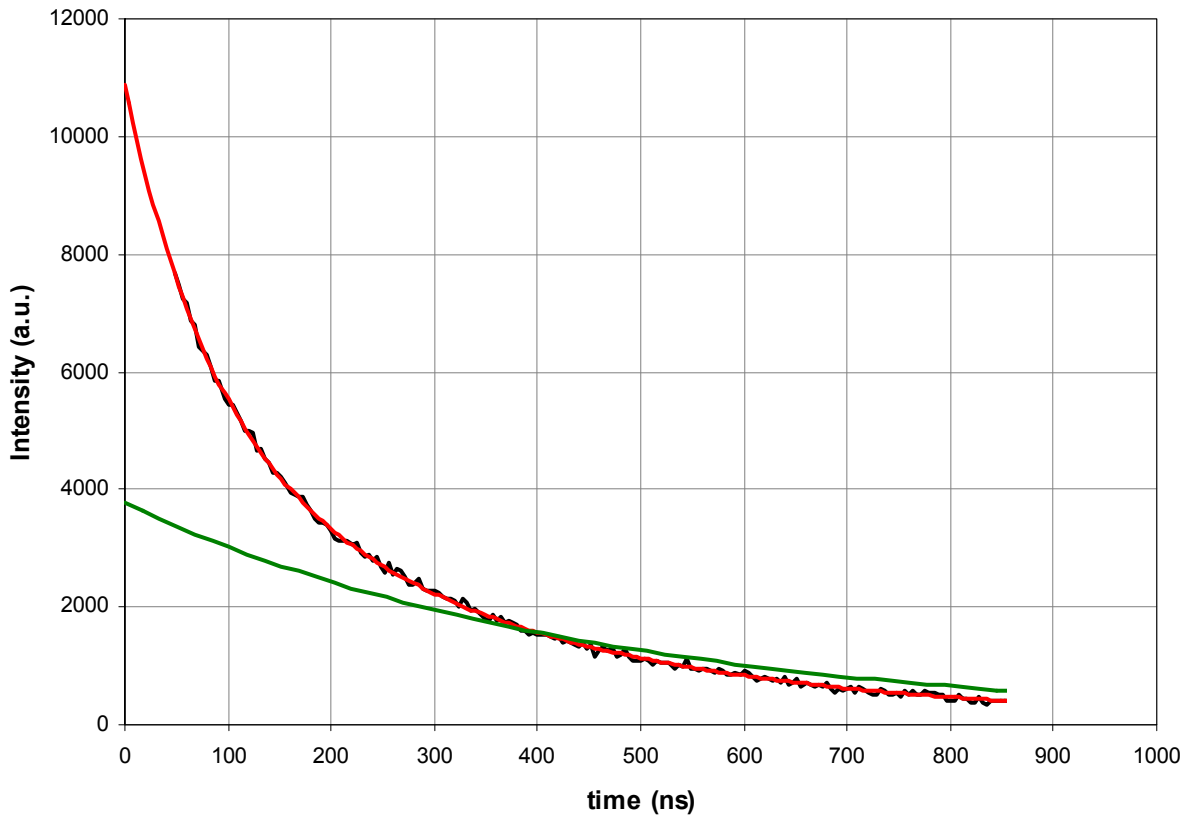


Figure 4-28. Intensity versus time for a spin-spin relaxation rate experiment on spark-processed silicon (black line), one-exponential decay model (green line) and bi-exponential decays (red line). Experimental parameters for the 2 pulses echo decay, center field = 3467 Gauss, shot repetition time = 51 ms, shot loop = 2, pulse length = 16 ns and step = 4ns.

For information, the model equation used is: $Intensity(t) = A_2 e^{-t/T_m} + A_2' e^{-t/T_m'}$ where A_2 and A_2' are the exponential amplitudes of each of the decays. If we use only one exponential decay the fit is poor as can be visually observed in the graph.

In the next experiment, we measured T_m and T_m' as a function of temperature. The results show essentially no temperature dependence, as seen in Figure 4-29. According to Eaton and

Eaton⁵⁴ the line width can be calculated from the following equation:

$$\Delta H^2 = A \left(\frac{1}{\gamma^2 T_2^2} + B_1^2 \frac{T_1}{T_2} \right)$$

where A is a proportionality factor, B₁ is the microwave magnetic field

and γ the electron gyromagnetic ratio. In the case of sp-Si the second term is much smaller than the first one and therefore the line width depends only on T₂. Since T₂ is directly related to T_m, the line width depends on T_m only. This is confirmed experimentally since the line width and T_m have the same temperature dependency.

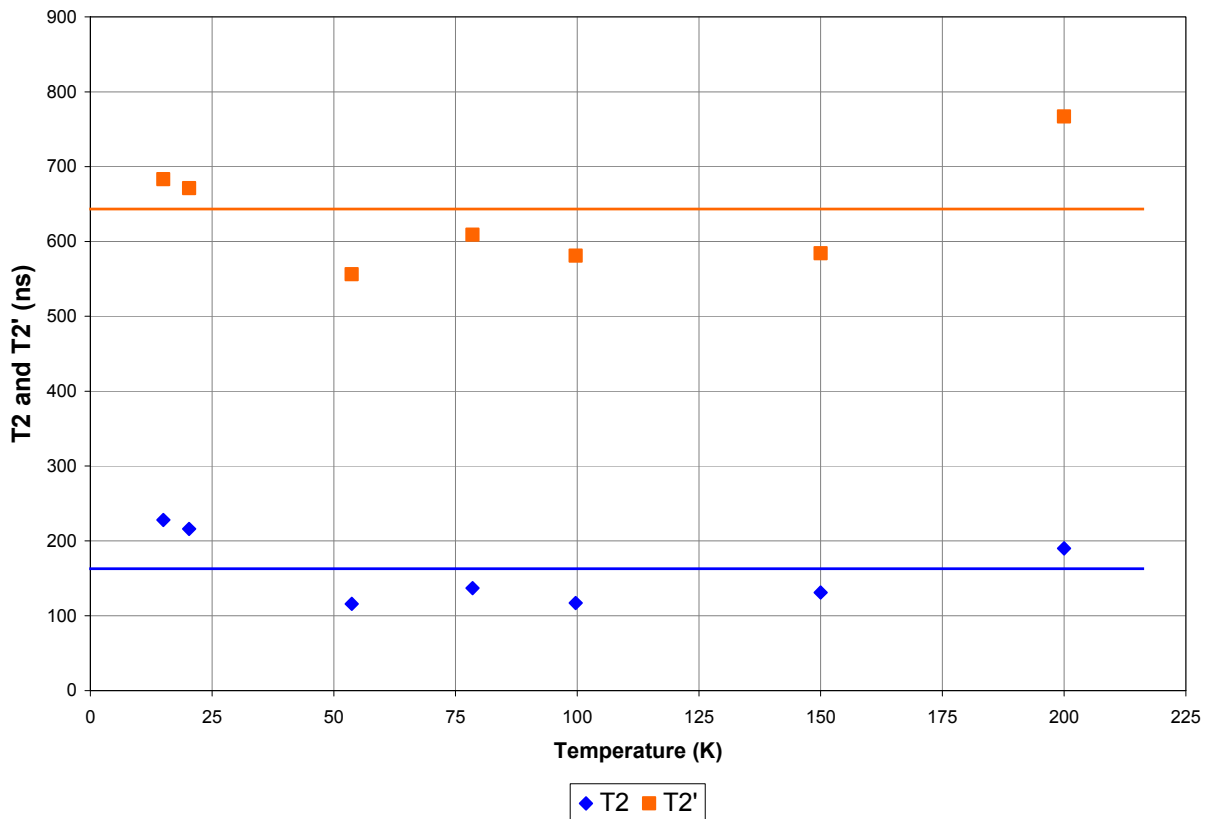


Figure 4-29. Spin-spin relaxation rates versus temperature for spark-processed silicon.

In brief, we have found two spin-lattice relaxation rates as well as two spin-spin relaxation rates. It is of great interest to figure out which rate is related to the D centers and which one is related to the E' centers. This is of major importance since this will allow us to perform the separate measurement of the density for each type of centers.

4.7 Separation of Rates to Identify Paramagnetic Centers

The processes involved in the relaxation of the spins after being excited by microwaves are strongly dependent on the pulse length and pulse power. Therefore, in order to assign the two defects observed with cw-EPR according to their own relaxation rates, we use several experiments. First we measured an echo detected field sweep pulse spectrum. The data for sp-Si is presented Figure 4-30. This is similar in principle to the concept presented at the beginning of this chapter in Figure 4-3. A double Lorentzian line model is used to deconvolute the data, showing again that two paramagnetic centers are present in the EPR signal. The characteristic values (center field, line width) are presented in Table 4-1.

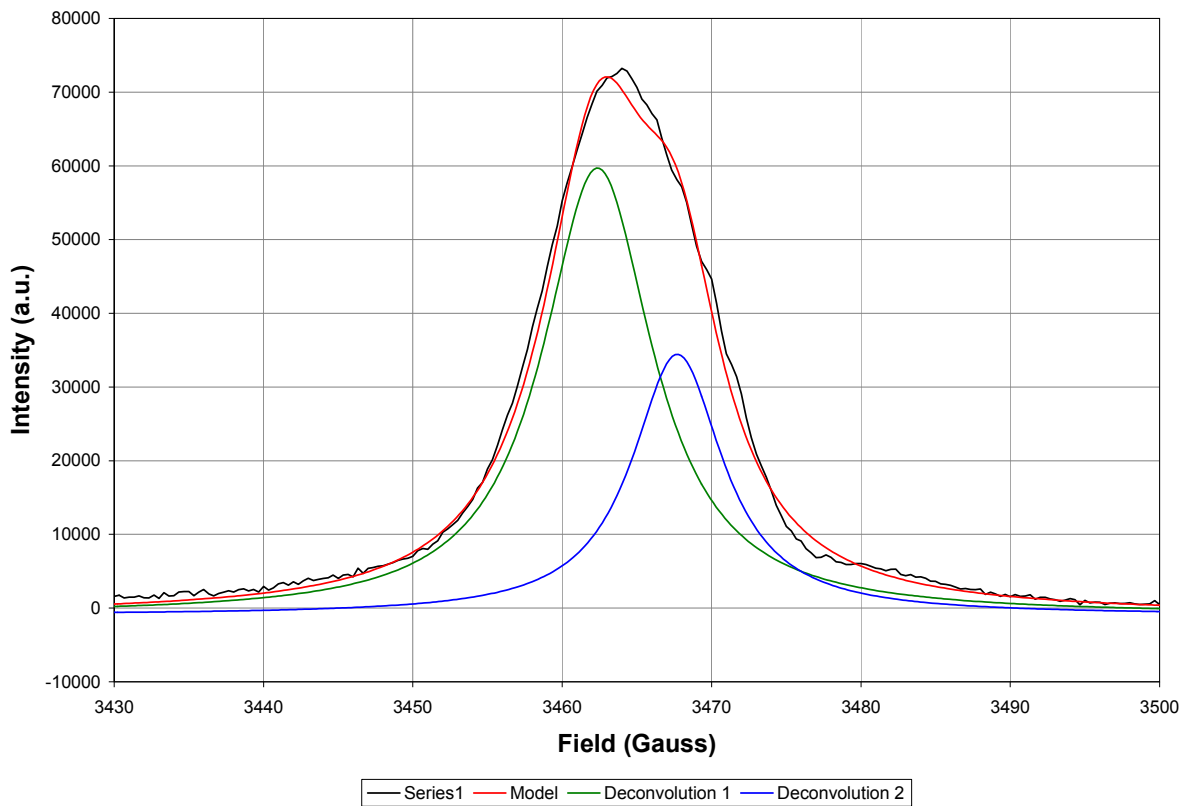


Figure 4-30. Field sweep pulsed electron paramagnetic resonance of spark-processed silicon (black curve). A two-Lorentzian model is fitted to the data (red curve) and each of its individual components (green and blue curves). Experimental parameters, power attenuation = 10 dB, shot repetition time = 20 ms, shot loop = 30, pulse length = 30 ns.

On the other hand, when fitting the bi-exponential decay model to the phase memory time experiment we are capable of extracting the exponential proportionality parameters (A_2 and A_2'). Since these parameters are related to the relaxation rates and we want to assign them, we measured these parameters as a function of the magnetic field in order to compare them with the field sweep curve obtain previously (Figure 4-30).

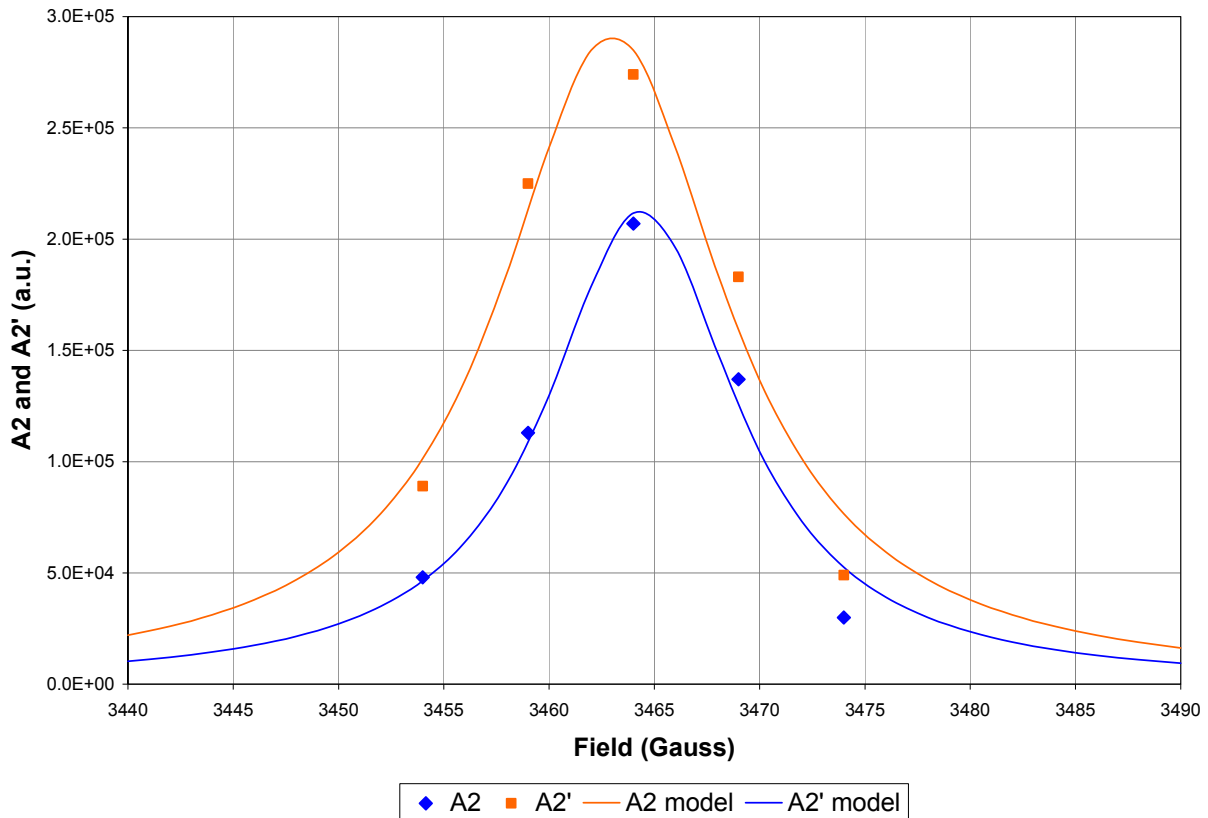


Figure 4-31. Amplitude of exponential decays in spin-spin relaxation rate experiments versus field for spark-processed silicon (dots). Lorentzian distribution models have been fitted to the data (solid lines) with long pulse (200 ns equivalent to 1.8 Gauss).

Figure 4-31 displays A_2 and A_2' as a function of the external magnetic field. Lorentzian line models are fitted to validate the data. Their characteristic values are summarized in the Table 4-1. If we compare them with the field sweep experiment we are able to assign the A_2 with the D centers and A_2' with the E' centers.

Table 4-1. Characteristic values of echo detected field sweep and amplitude of exponential decay as a function of magnetic field.

Con stan ts	Echo detected field sweep	Exponential decay amplitude
H_0^D [Gauss]	3462	3463
ΔH^D [Gauss]	10	12.5
$H_0^{E'}$ [Gauss]	3467	3465
$\Delta H^{E'}$ [Gauss]	9	11

Note: H_0 is the center field and ΔH is the line width.

In conclusion, we are able to separate the paramagnetic centers using pulsed EPR which allows the calculation of the density of centers for each type of defects (D and E') as described in the next section.

4.8 Spin Density

The concept used to calculate the spin concentration was presented by Eaton and Eaton⁵⁴ and was applied to γ -irradiated SiO₂, a very close cousin of sp-Si (composition and structure wise). We have found this method to be more reliable than other methods such as the “comparative technique” using cw-EPR for example. The comparative technique has been found to be a lot less accurate than the method applied by us due to great difficulties in measuring the volume of the sp-Si material.

The calculation of the concentration is based on the following relationship⁵⁴:

$$\frac{1}{T_m} = \frac{1}{T_2} + \frac{4\pi^2 \gamma g \mu_B C}{9\sqrt{3}} \sin^2 \left(\frac{\pi}{2} \left(\frac{\text{Power}}{\text{Power}_0} \right)^{1/2} \right)$$

where the only constant which has not been

presented yet is C, the density of spins. Figure 4-32 shows $\frac{1}{T_m}$ and $\frac{1}{T_m'}$ as function of the power

and Figure 4-33 displays $\frac{1}{T_m'}$ versus $\sin^2 \left(\frac{\pi}{2} \left(\frac{\text{Power}}{\text{Power}_0} \right)^{1/2} \right)$. The slope of the curve is proportional

to the concentration of defects and the y-intercept is the inverse of T_2 . In the case of sp-Si, we found the concentration of D centers to be $1.4 \times 10^{19} \text{ cm}^{-3}$ and the concentration of the E' centers to be $0.5 \times 10^{19} \text{ cm}^{-3}$. The total density of paramagnetic centers is therefore $1.9 \times 10^{19} \text{ cm}^{-3}$.

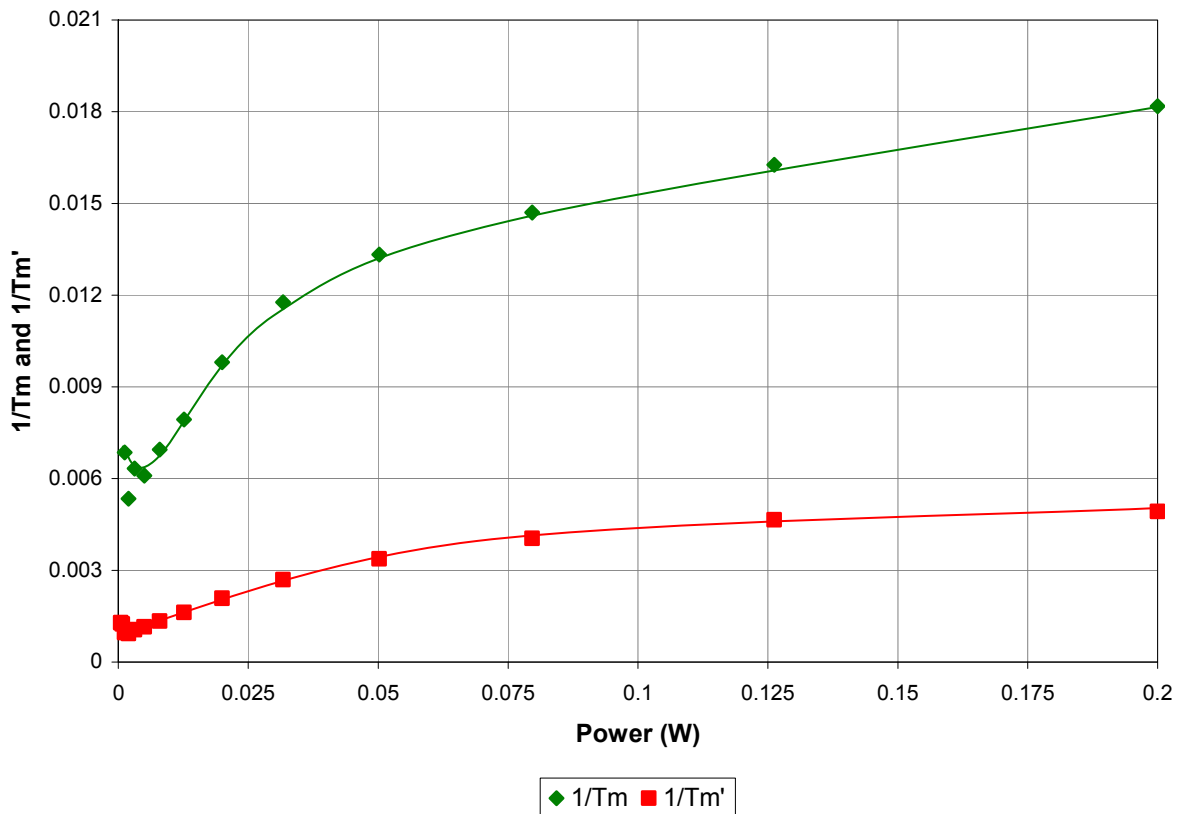


Figure 4-32. Phase memory time for each paramagnetic center measured as a function of the input power of spark-processed silicon.

We have measured this density on different samples to investigate the repeatability and we found all these values to be within 20% of the average (Figure 4-34). The D center average density is $1.6 \times 10^{19} \text{ cm}^{-3}$ while the E' center average density is $0.5 \times 10^{19} \text{ cm}^{-3}$, leading to an average total density of $2.1 \times 10^{19} \text{ cm}^{-3}$.

It should be noted that in Chapter 3 we reported that the magnetization was dependent on the spark frequency (Figure 3-6). Because we only measured an average density of paramagnetic centers, no link can be drawn between the magnetization and the density. Only the knowledge of the distribution would allow a comparison between the magnetization and the density of spins.

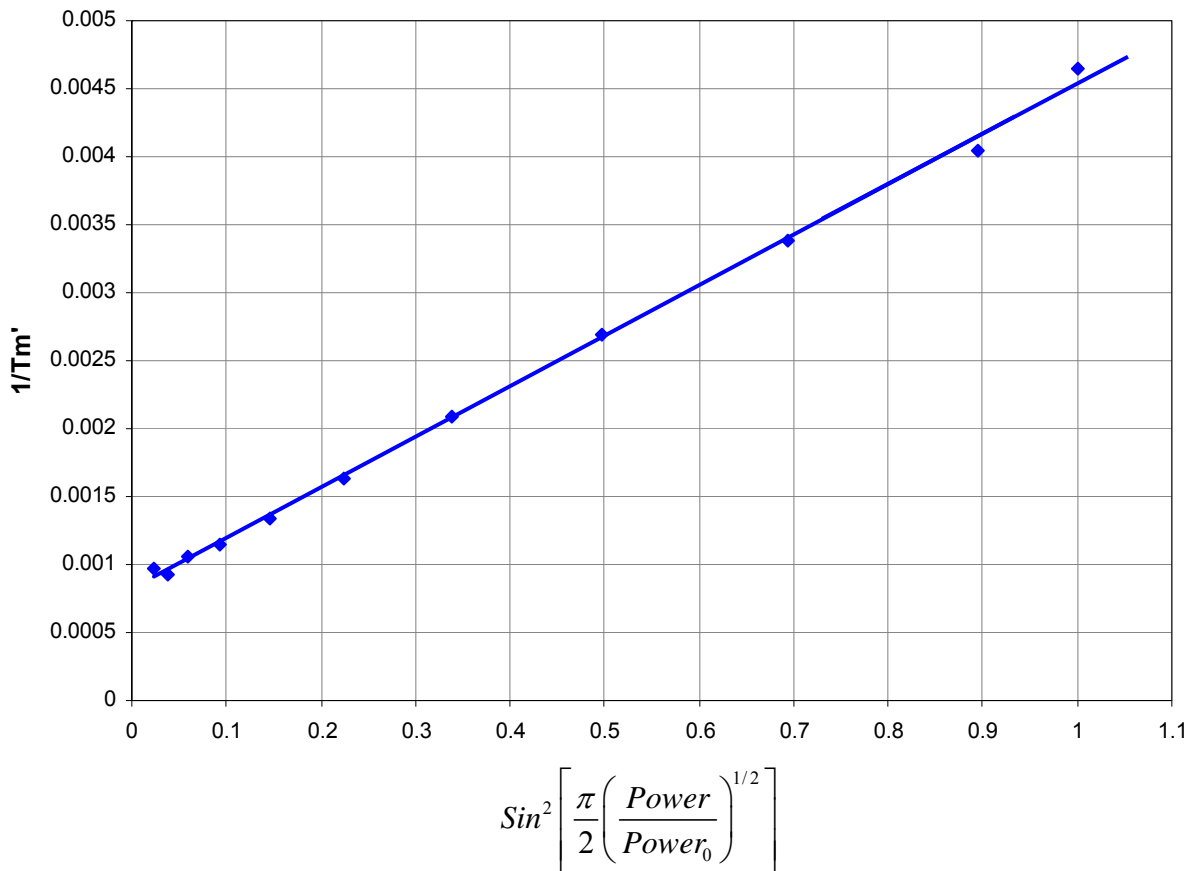


Figure 4-33. Inverse phase memory time ($1/T_m'$) versus $\sin^2(\pi/2 \times (\text{power}/\text{power}_0)^{1/2})$ of spark-processed silicon (dots). A trend line is run through the data with a correlation coefficient of 0.998.

If we assume that all the paramagnetic centers are equidistant from one another, then the inter-spin distance is equal to the cubic root of the inverse of the total density. This way, we found a maximum inter-spin distance of 3.7 nm (or 3.6 nm if we use the average density calculated from Figure 4-34). This result is very much within the range of values reported by Eaton and Eaton on γ -irradiated quartz⁵⁴. As mentioned in the first section, it is usually assumed that the maximum distance between spins which allows exchange interactions is 2 nm. But, it has been shown⁵² that sp-Si is composed of silicon nanocrystals embedded in the SiO₂ matrix. Therefore, we suggest at first, that the distribution of paramagnetic centers is not homogeneous which is also suggested by the heterogeneous structure. Secondly, we suggest that the D centers are located on the border or inside the silicon nanocrystals. These nanocrystals observed by Shepherd⁵¹ have sizes ranging from a few to tens of nanometers. If the paramagnetic centers are located in or around such nanocrystals it is possible for their inter-spin distance to be less than 2 nm and therefore exhibit exchange interaction leading to the observed magnetic hysteresis.

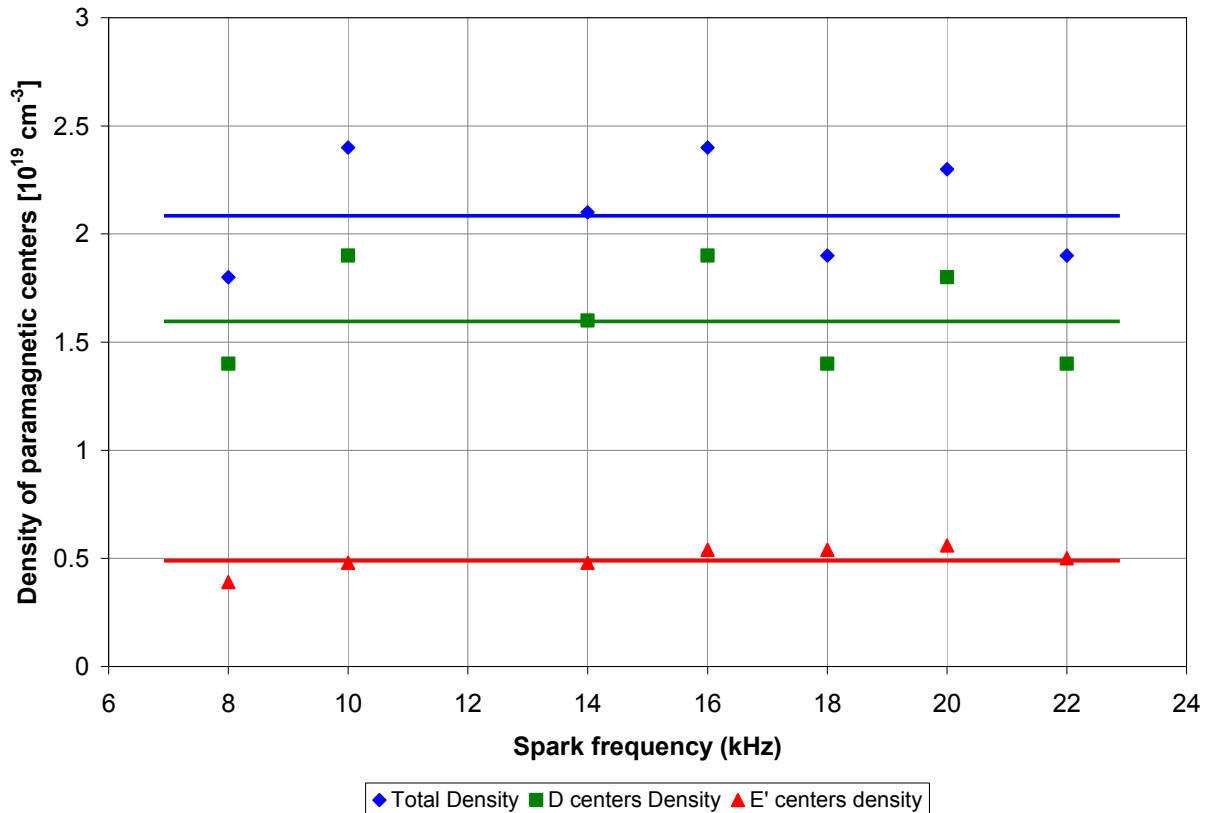


Figure 4-34. Density of paramagnetic centers as a function of the spark frequency for spark-processed silicon. The density of D centers is represented by squares while the density of E' centers is represented by triangles. The total density is represented by diamonds.

It should be added in passing that a technique known as double quantum coherence EPR which allows the measurement of the spatial distribution of paramagnetic centers developed by Freed⁴⁸ was tried on sp-Si but we were unsuccessful due to limitation of the technique itself. Still, it may be possible in the future, once the EPR sensitivity has been improved, to measure the distribution of centers.

It should be noted in passing that hydrofluoric acid etching (49% pure) for several minutes did not change the EPR signal shape or amplitude. We concluded that the measured paramagnetic centers are not surface related.

4.9 Summary

In this chapter we successfully identified two paramagnetic centers believed to be present in sp-Si, namely the E' centers and the D centers (Figure 4-6). Also, we successfully measured the densities of each of the two centers to be $1.4 \times 10^{19} \text{ cm}^{-3}$ for the D centers and $0.5 \times 10^{19} \text{ cm}^{-3}$ for the E' centers. In addition, we have measured a Curie temperature of 710 K from the amplitude of the D centers to be compared with a Curie temperature of 765 K measured from the magnetization at 1000 Oe (Chapter 3). Finally, we presented a cluster model consistent with the magnetization results and the paramagnetic centers distribution (Figure 4-1). Our arguments can be summarized as followed:

- Sp-Si is not homogeneous, it is composed of Si nanocrystals embedded in the SiO₂ matrix,
- D paramagnetic centers are likely to be located in or around silicon nanocrystalline regions,
- E' paramagnetic centers are likely to be located in the SiO₂ matrix,
- The structure suggests an inhomogeneous distribution of inter-spin distances,
- Paramagnetic centers are less than 3.7 nm apart but they could be less than 2 nm apart,
- Exchange interaction is possible between paramagnetic centers if they are closer than 2 nm,
- The paramagnetic centers are not surface related,
- Positive exchange interaction explains the observed magnetic hysteresis in sp-Si.
- The magnetic response at high and low temperatures of the D centers and the magnetization at 1000 Oe (Chapter 3) have a very similar behavior. They both follow the same laws.

In the next chapter we expand our model to other materials and therefore describe a full class of materials as quasiferromagnets.

CHAPTER 5 FURTHER CONSIDERATIONS

While the two previous chapters deal with spark processed silicon magnetic properties and its model, this chapter extends this model to other materials. Quasiferromagnetism was first studied using spark processed silicon. Later, we found that other materials had similar magnetic properties and therefore, we classified them as quasiferromagnets.

In this chapter we first present the work of Hack³ on the annealing effect of the magnetic properties of spark processed silicon which further confirms the magnetic model proposed in the previous chapter. Then, we discuss and present some of the magnetic properties of other materials as well as why we classified them as quasiferromagnets. These materials include ion implanted silicon into silicon, argon implanted into silicon; neutron irradiated silicon and highly oriented pyrolytic graphite (HOPG).

5.1 Annealing of Spark Processed Silicon

In this section we report on the annealing effect of the magnetization as well as the annealing effect of the electron paramagnetic resonance spectrum of spark processed silicon. This work was performed by Jonathan Hack during his masters' thesis at UF. It was published³ in 1997. This work proposed to link the magnetic hysteresis to paramagnetic centers.

Hack measured the magnetization of sp-Si at 0 and 1000 Oe as function of cumulative annealing. First, he measured the magnetization of sp-Si as processed, and then after annealing at 500 K for 30 min in a nitrogen atmosphere and subsequently, at higher temperatures, up to 1300 K. The results are normalized to the as prepared samples (Figure 5-1). The magnetization decreases as the cumulative annealing increases. Furthermore, the decrease is more pronounced around 700 K. Finally, in the high temperature range (i.e. above 900 K) the remanence magnetization decreases to zero at 0 Oe and the saturation magnetization (at field of 1000 Oe)

also decreases down to the diamagnetic value of the substrate. The hysteresis is destroyed (non-reversible process) at the cumulative annealing temperature of 900 K while a small but not negligible paramagnetic magnetization remains at 1000 Oe.

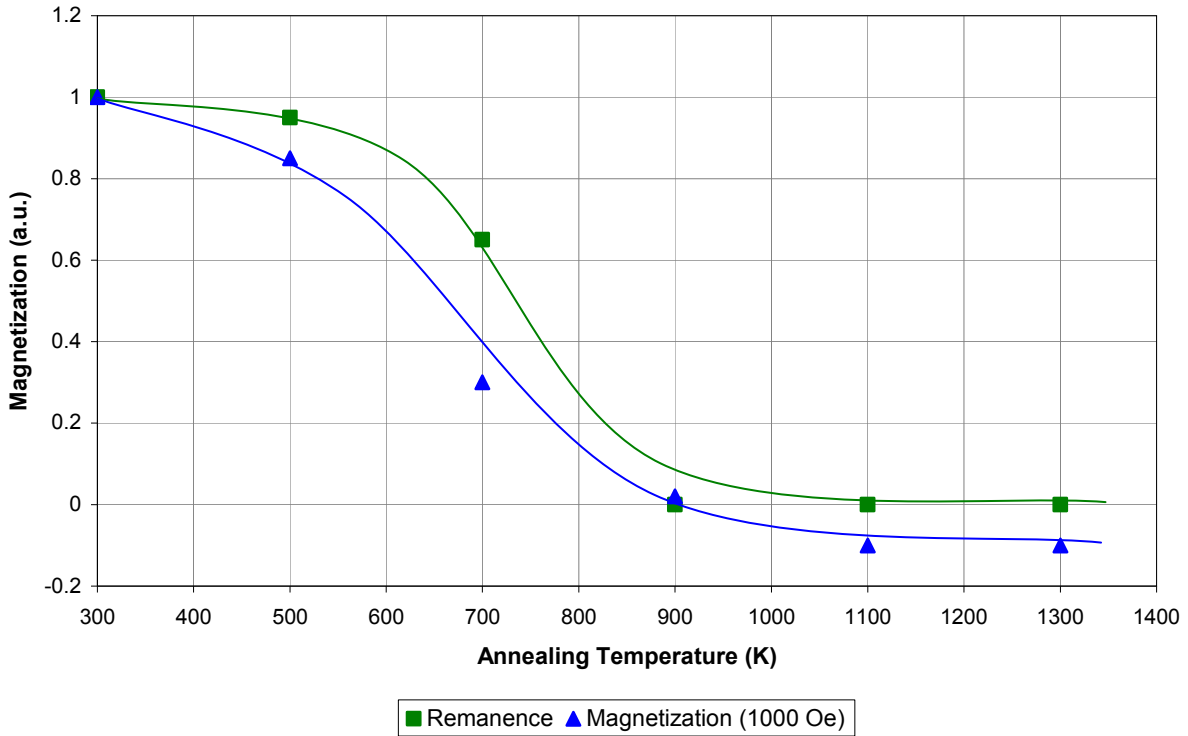


Figure 5-1. Magnetization at 0 and 1000 Oe of spark processed silicon as a function of cumulative isochronal (30 min) annealing temperature.

In addition, he measured the electron paramagnetic resonance spectrum at each annealing temperatures and extracted the peak to peak amplitude of the main line. The results are shown Figure 5-2. The peak to peak amplitude is proportional to the number of defects present in the sample as long as we are in none saturated regime as explained in the Section 4.3. The normalized amplitude decreases as the temperature is increased in a similar manner as the magnetization. In addition, the largest slope (strongest relative decrease) is found at 700 K as for the magnetization. Finally, the EPR peak to peak amplitude decrease almost to zero at the highest temperature as does the magnetization.

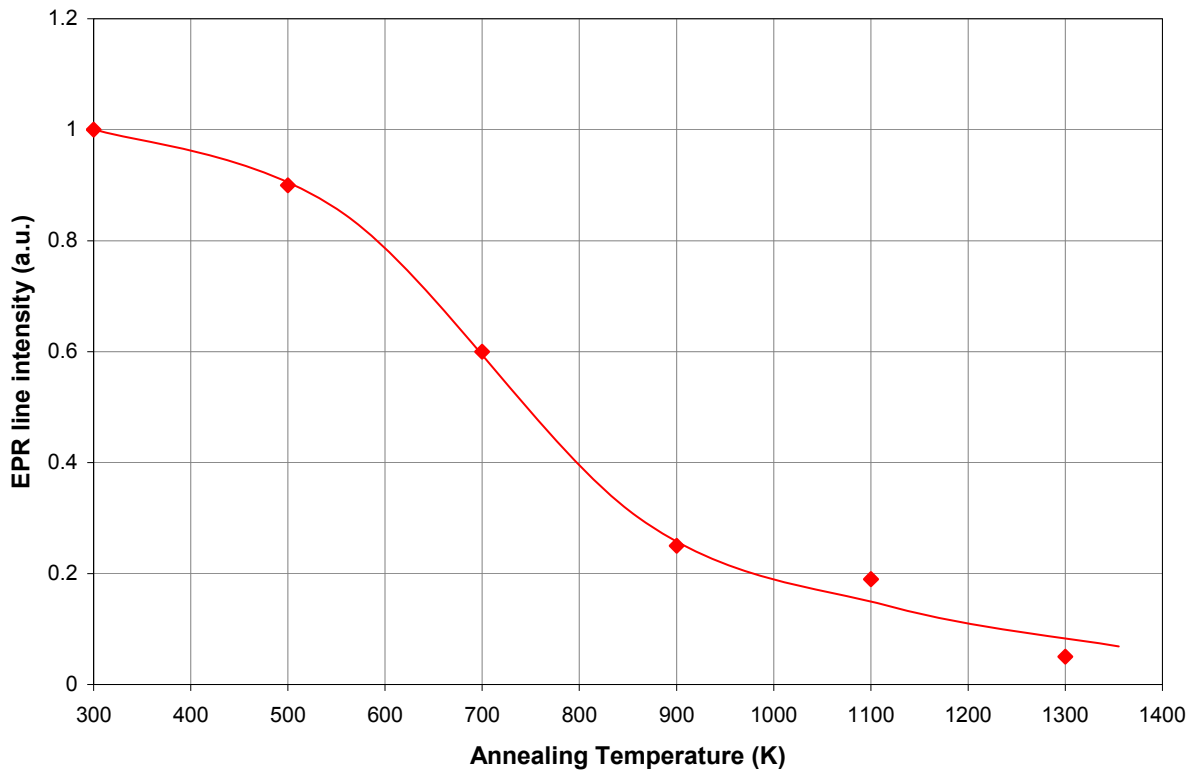


Figure 5-2. Electron paramagnetic resonance peak to peak spectra line of spark processed silicon as a function of cumulative isochronal (30 min) annealing temperature.

Hack concluded that the paramagnetic centers were at the origin of the observed magnetic hysteresis of sp-Si. The pioneering work of Hack is the origin of this dissertation.

In my quasiferromagnetic model, I suggest that some paramagnetic centers are clustered and thus, have a positive exchange interaction. If one anneals sp-Si, thus removing paramagnetic centers, the clusters would decrease in size and therefore the magnetization would decrease as a result. Eventually, their number would approach zero, and the clusters would disappear (leading to a vanishing of the hysteresis).

We conclude that the observations of Hack are in general agreement with our proposed quasiferromagnetism model.

5.2 Ion Implanted Silicon

Ion implantation is a very common process used in the semiconductor industry. In the seventies Khokhlov¹⁹ studied the EPR spectra of paramagnetic defects produced by the ion implantation process. Since, some others have continued to study the EPR spectra of ion implanted silicon but the magnetization itself has been left out. I have published³⁵ for the first time on the magnetic hysteresis at room temperature of silicon implanted into silicon and argon-implanted silicon. We will review in this section the most relevant results from this publication.

The samples were prepared using a very low implantation current density (less than $10\mu\text{A}/\text{cm}^2$) as well as high doses (greater than $\Phi=10^{16}$ ions/ cm^2) while the silicon substrate were kept at room temperature by water cooling the stage. We believe that such processing conditions favor a large defect density (preventing self-annealing during implantation). We suggest that ion implantation would be an interesting area for further investigations, for example, to produce quasiferromagnetic silicon and allow potential application of this material in the spintronics area.

It should be re-emphasized that SIMS spectra were performed on each type of the processed samples. No ferromagnetic elements (Fe, Ni, Co, Mn...) could be found³⁵.

Below, we present the magnetization response and then the EPR spectra of this material.

5.2.1 Magnetic Response of Ion Implanted Silicon

The magnetization as function of the field was measured for argon-implanted silicon. The results are shown Figure 5-3. Two magnetic hysteresis curves are presented, one for the sample implanted at a dose of 2×10^{16} cm^{-2} and one for implantation at a dose of 2×10^{17} cm^{-2} . Both hysteresis are observed at room temperature. In addition a silicon wafer was implanted using silicon ions with a dose of 5×10^{16} cm^{-2} . Again a hysteresis was observed at room temperature as shown in Figure 5-4. These results are not expected from the classical theory of magnetism. Once again, a new concept is needed: quasiferromagnetism.

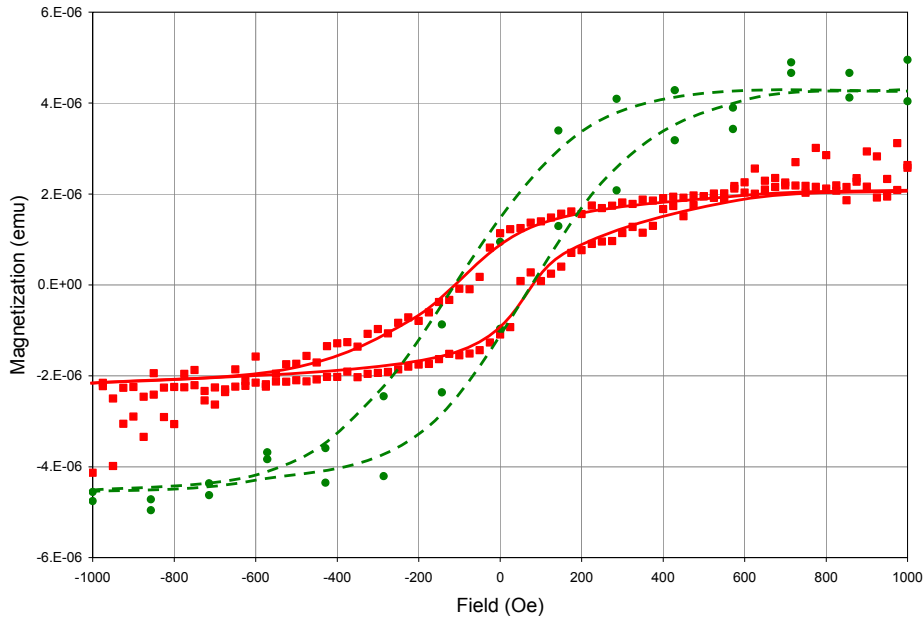


Figure 5-3. Magnetization as a function of the magnetic field strength at 300 K for silicon implanted with argon ions. The solid red curve corresponds to an argon dose of $2 \times 10^{16} \text{ cm}^{-2}$ and the dash green curve to a dose of $2 \times 10^{17} \text{ cm}^{-2}$. The magnetization has been adjusted for the diamagnetism of the substrate.

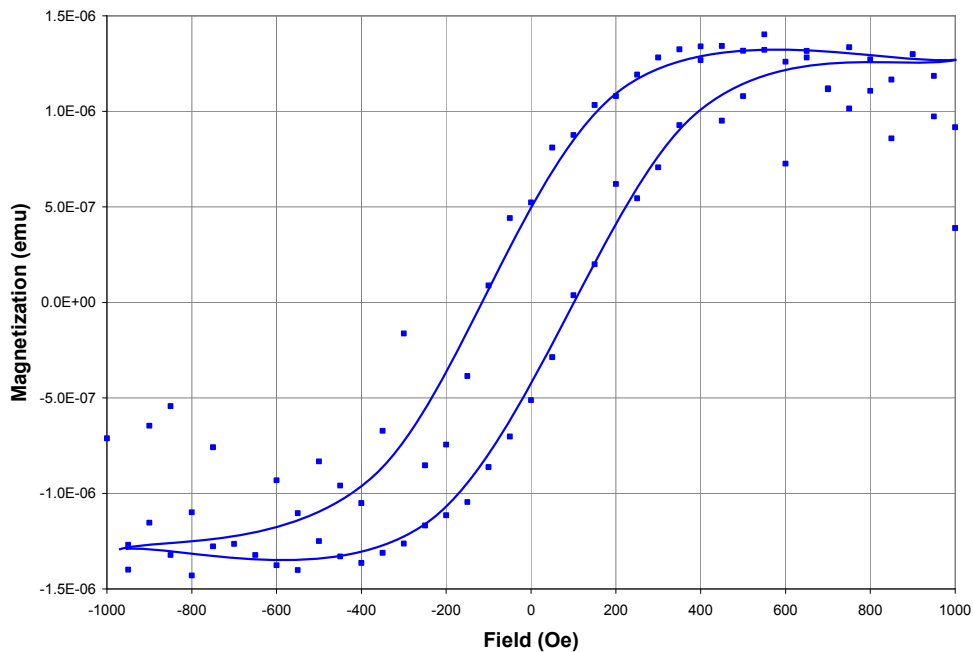


Figure 5-4. Magnetization as a function of magnetic field strength at 300 K for silicon implanted with silicon ions. The dose was $5 \times 10^{16} \text{ cm}^{-2}$. The magnetization has been adjusted for the diamagnetism of the substrate.

5.2.2 Electron Paramagnetic Resonance of Ion Implanted Silicon

The electron paramagnetic resonance spectrum of argon-implanted silicon at $2 \times 10^{16} \text{ cm}^{-2}$ is displayed Figure 5-5.

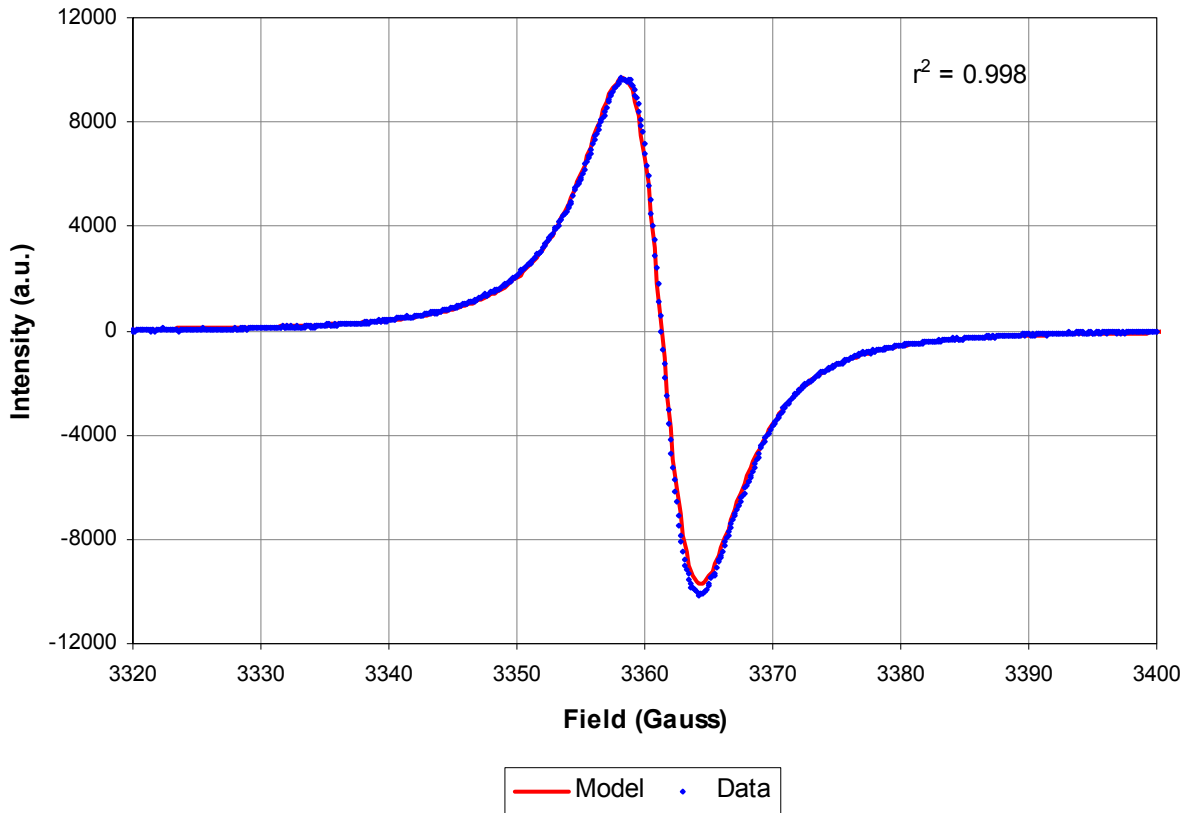


Figure 5-5. Electron paramagnetic resonance spectra of argon implanted into silicon at a dose of $2 \times 10^{16} \text{ cm}^{-2}$ (blue squares) and its Lorentzian model (solid red). Experimental parameters, power = 2 mW, power attenuation = 20 dB, modulation field = 1 G, time constant = 80 ms, detector gain = 55 dB, temperature = 5 K.

The measurements were taken at 5 K to reduce thermal noise. A Lorentzian line is used to model the data. We found a very good fit between the model and the experiment (correlation coefficient is 0.998). Since one line was enough to model the data we conclude that there is only one type of defect in this material. According to Khokhlov¹⁹ and Gerasimenko⁵⁵ the pertinent paramagnetic defects are “VV centers” (silicon dangling bonds around voids). Similarly the electron paramagnetic resonance spectrum of silicon-implanted silicon with a dose of 10^{16} cm^{-2} at

5 K was measured and analyzed (Figure 5-6). In this case a two-Lorentzian model was necessary to match the data. The g-factors are 2.0054 and 2.0023 respectively.

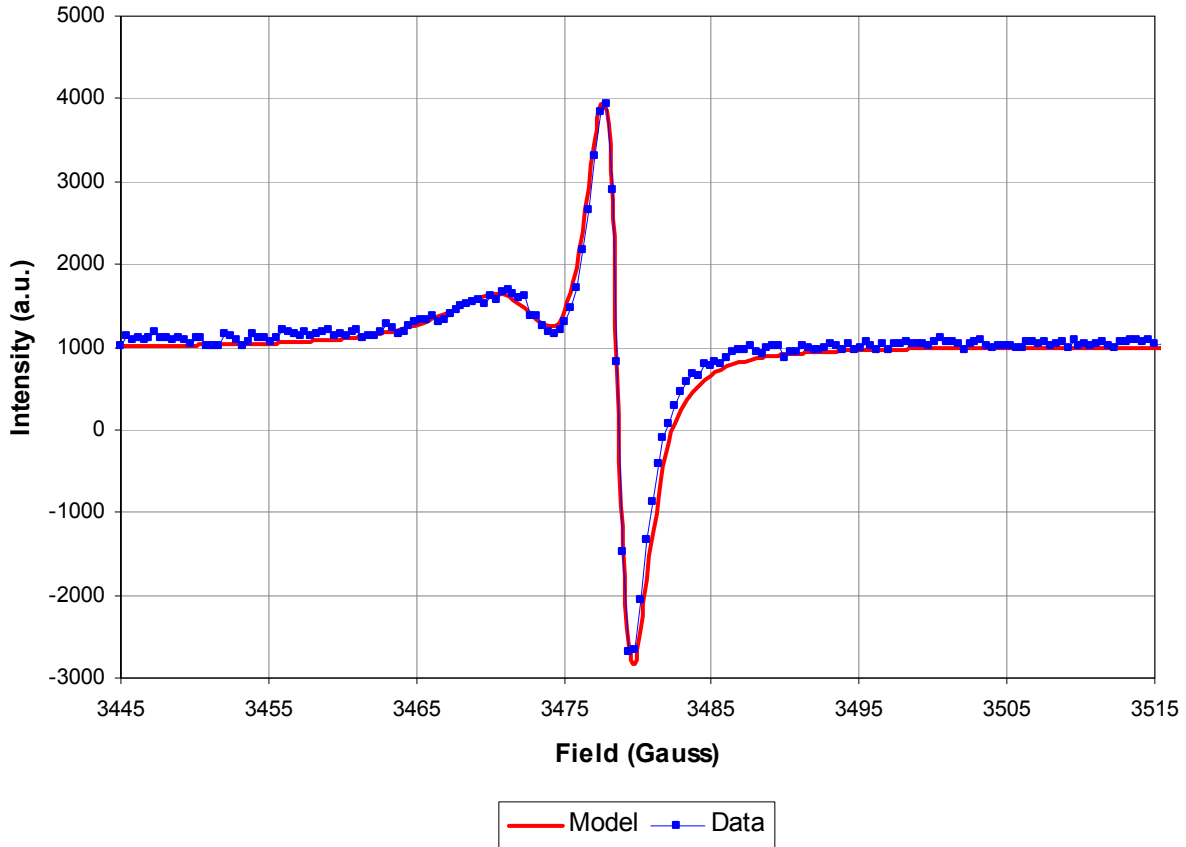


Figure 5-6. Electron paramagnetic resonance spectra of silicon implanted into silicon at a dose of 10^{16} cm^{-2} (blue squares) and its two-Lorentzian model (solid red). Experimental parameters, power = 50 mW, power attenuation = 6 dB, modulation field = 1 G, time constant = 80 ms, detector gain = 60 dB, temperature = 5 K.

They allow the identification of the paramagnetic defects to be silicon dangling bonds⁴⁰ (D centers) and E' centers⁴⁴ respectively. We believe that the E' centers are located on the surface of the substrate in the oxide layer. On a silicon wafer there is a natural silicon oxide layer forming as long as the substrate is left in an ambient atmosphere. In addition, Tomozeiu⁴⁴ has shown that the g-factor of E' centers is slightly dependent of the thickness of the silicon oxide layer. In our case, the thickness corresponds to the natural oxide formed at the surface.

The ion implanted silicon samples which we characterized have similar magnetic characteristic as sp-Si, that is, a magnetic hysteresis loop at room temperature and paramagnetic centers. Once again, these samples do not contain elements with d or f shell electrons and therefore fits well within the quasiferromagnetic materials point of view. Overall, we suggest that ion-implanted silicon materials seem to have the same magnetic behavior as sp-Si and therefore can be explained by the same quasiferromagnetic model.

5.3 Neutron Irradiated Silicon

Neutron irradiated silicon samples were prepared following the same general ideas as ion implanted silicon. We tried to manufacture the material with the largest possible density of paramagnetic defects hoping that they would form interacting clusters. In this section we present magnetization curve of neutron irradiated silicon. I have already published⁴ this work in 2006. Thus, only a brief summary will be given here.

A piece of silicon wafer was exposed to thermal neutrons in the University of Florida nuclear reactor for 12 hours. A 12-hour exposure equate to a dose of $4 \times 10^{16} \text{ cm}^{-2}$. The magnetization curve was measured at 10K, to reduce large noise, see Figure 5-7.

According to Jung and Newell⁵⁶ weak magnetic interaction are observed between closely spaced dangling bonds in neutron irradiated silicon. Jung measured a distance of 0.5 nm between two particular types of dangling bonds in neutron irradiated silicon using an electron paramagnetic resonance technique.

Magnetic hysteresis and weak magnetic interaction between paramagnetic centers contribute to classify neutron irradiated silicon as a quasiferromagnet. Similarly to ion implanted silicon, neutron irradiated silicon has the same magnetic characteristic as sp-Si and therefore should be in the same magnetic class.

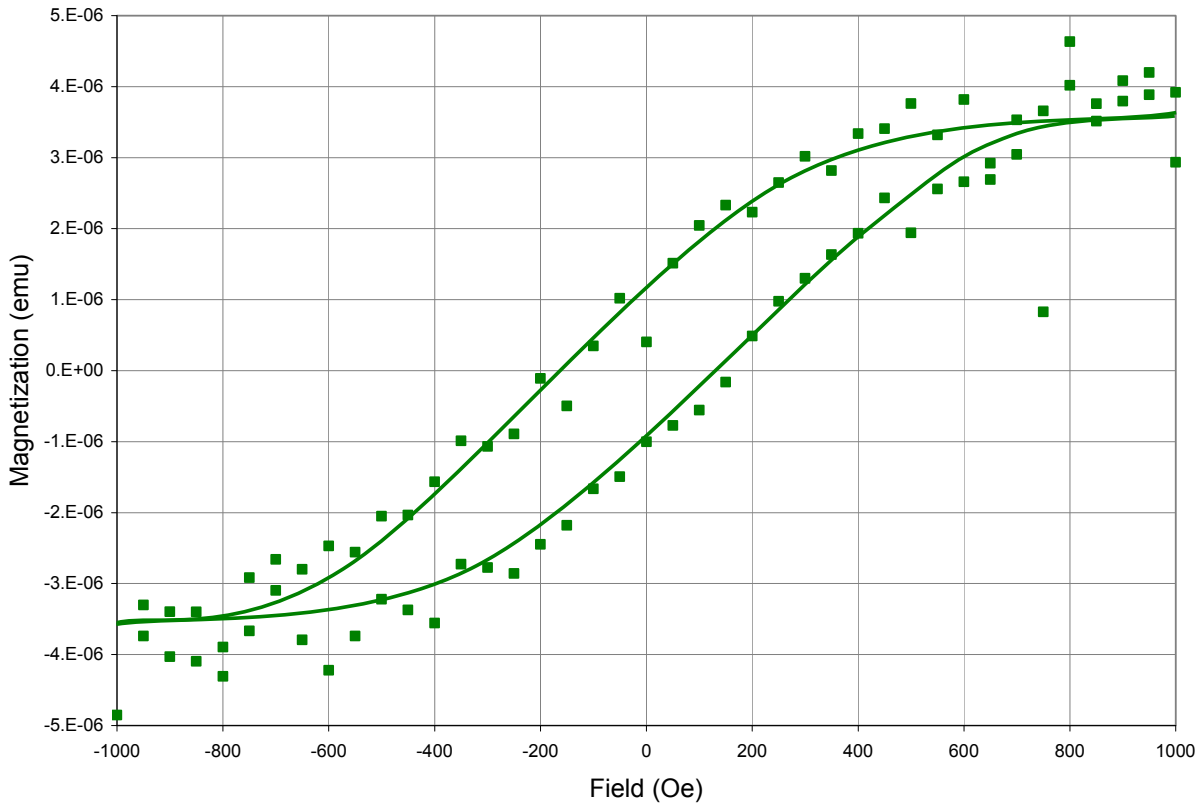


Figure 5-7. Magnetization versus magnetic field strength of neutron irradiated silicon at a dose of $4 \times 10^{16} \text{ cm}^{-2}$. The magnetization is adjusted for the diamagnetism of the substrate. The measurement temperature was 10 K.

Once again, SIMS spectra were taken on a neutron irradiated sample and no magnetic elements (such as Fe, Ni, Co...) were found.

5.4 Highly Oriented Pyrolytic Graphite

In this section we present another material which we classify as quasiferromagnet. This material is not based on silicon. Highly oriented pyrolytic graphite (HOPG), an allotrope form of carbon, was purchased from Mikromash⁵⁷. This material is processed from pure graphite at temperatures of 3,000°C under pressure. This material was previously known for its unusual magnetic properties which triggered our interest. In this respect, we present the magnetization measurements as well as electron paramagnetic resonance data which relate this material to quasiferromagnetism.

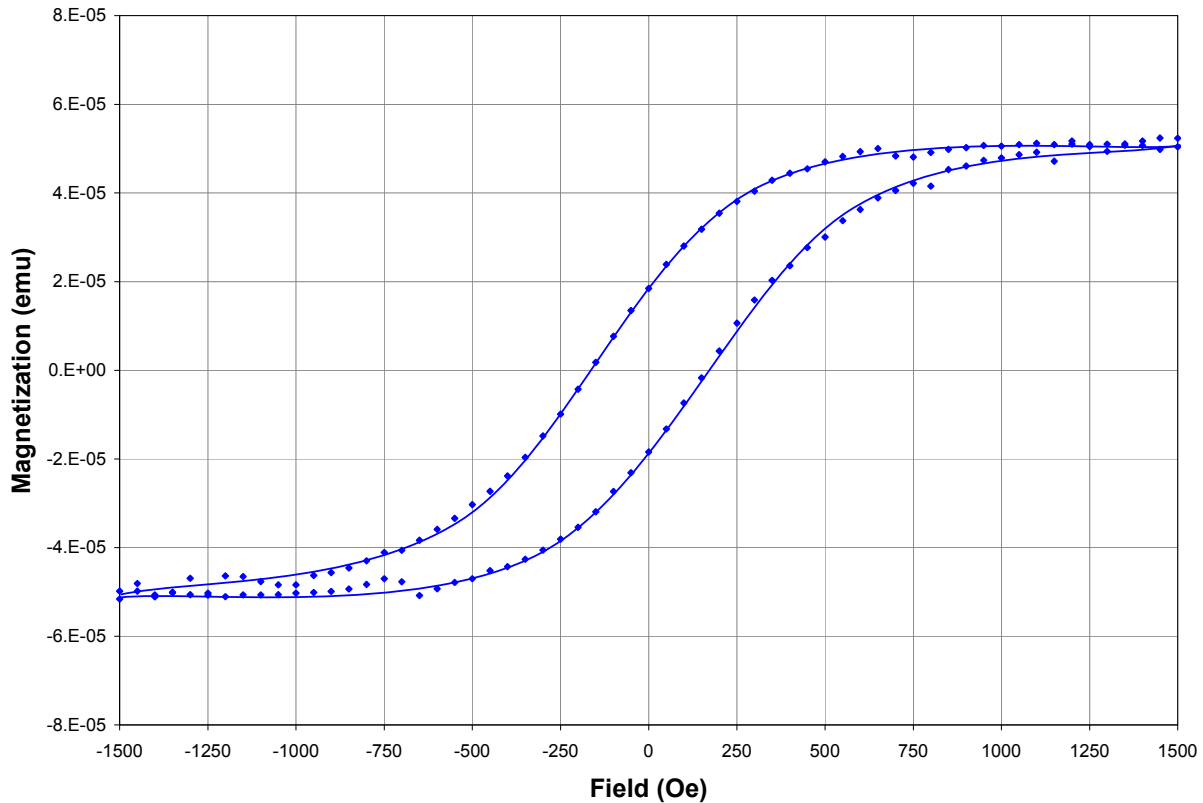


Figure 5-8. Magnetization as a function of magnetic field strength of HOPG graphite. The magnetization is adjusted for the diamagnetism of the sample. The measurement temperature was 300 K.

5.4.1 Magnetization Response of Highly Oriented Pyrolytic Graphite

The as-purchased material was measured with our SQUID magnetometer at room temperature. A wide hysteresis is observed. Since the sample also exhibits strong diamagnetism, its contribution was subtracted, see Figure 5-8. The coercive field is about 200 Oe, which is much larger than in the case of silicon based quasiferromagnets. For example, sp-Si has a coercive field of about 50 Oe and ion implanted silicon one of about 100 Oe.

5.4.2 Electron Paramagnetic Response of Highly Oriented Pyrolytic Graphite

The electron paramagnetic resonance of HOPG graphite is more involved than in the case of silicon-based materials. HOPG is a conductor and therefore the EPR line do follow a rather complex model call Dysonian lines named after Dyson^{58,59} who theoretically studied the EPR of

conductors and in particular of metals back in 1955. However, in the case of HOPG the EPR intensity line can be reduced to an asymmetric Lorentzian line (only the first term of the

Dysonian line) with the following equation: $\frac{dP}{dH} = A \frac{-\Gamma^2 (H - H_0)^2 - 2(H - H_0) + 1}{[1 + \Gamma^2 (H - H_0)^2]^2}$ where

$\frac{dP}{dH}$ is the EPR intensity, A the amplitude, H the field, H_0 the center field and Γ the full width.

Figure 5-9 displays the comparison between the EPR data and Dysonian line model for HOPG graphite at room temperature.

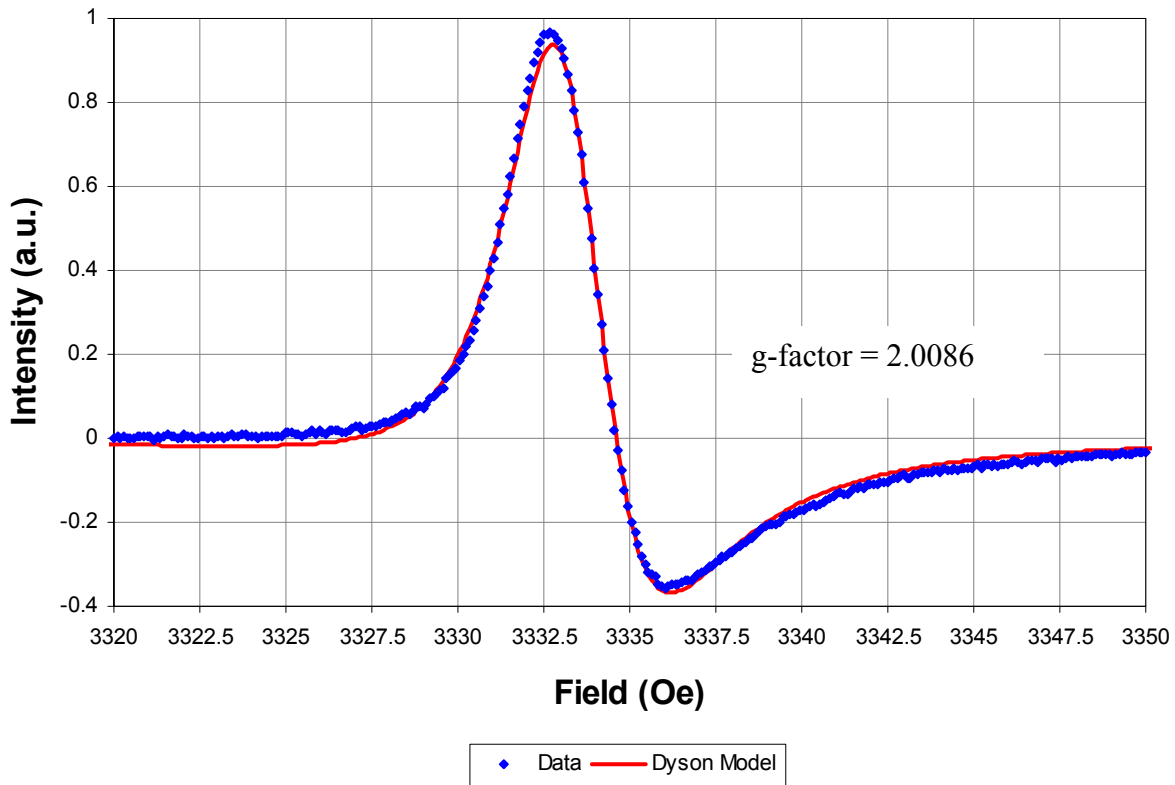


Figure 5-9. Electron paramagnetic resonance spectra of HOPG graphite (blue squares) and its Dysonian line model (solid red). The coefficient of correlation is 0.99. Experimental parameters, power = 0.6315 mW, power attenuation = 25 dB, modulation field = 1 G, time constant = 5 ms, detector gain = 60 dB, temperature = 300 K.

A correlation coefficient of 0.98 is found between the data and model. This is a quite reasonable match considering that we approximated the Dysonian line using only one term. (The

reader is referred to the original paper written by Dyson⁵⁸ to see the complete equation). In addition, according to Feher⁵⁹ who confirmed the work of Dyson on different conductive materials, any materials modeled with the equation used to model HOPG, contains paramagnetic impurities distributed throughout the volume of the metal.

Once again, we found a material with paramagnetic impurities and a magnetic hysteresis at room temperature. These characteristics are similar to the ones of sp-Si and to ion and neutron irradiated silicon. Even if HOPG graphite is different from silicon-based material due to its conductive nature, we suggest that it should also be classified as a quasiferromagnetic material.

5.5 Summary

In this chapter we looked at several different materials from the quasiferromagnetism point of view. In brief:

- The original work started by Jonathan Hack is in line with our suggested quasiferromagnetic model, that is, the paramagnetic centers observed by EPR are at the origin of the observed magnetic hysteresis at room temperature.
- Ion-implanted silicon with either argon or silicon and neutron irradiated silicon contains paramagnetic centers and display magnetic hysteresis at room temperature. Similarly to sp-Si, we suggest that the macroscopic behavior is explained by the interaction of the paramagnetic centers.
- HOPG graphite exhibits a magnetic hysteresis at room temperature in addition to a Dysonian shaped EPR spectrum, characteristic of paramagnetic centers in conducting materials. When compared with sp-Si, strong similarities suggest a quasiferromagnetic behavior.

CHAPTER 6 CONCLUSION

The present investigations have been conducted to study in detail unknown magnetic properties of non-magnetic materials. Because of their uniqueness we term them “quasiferromagnetics”. The experimental results and interpretations which have been observed during this study are summarized below.

6.1 Macroscopic Magnetic Behavior of Spark-Processed Silicon

It has been confirmed that spark-processed silicon displays a magnetic hysteresis quite analogous as Fe, Co, Ni and rare-earth metals. Once again, sp-Si does not contain magnetic impurities at levels which would explain the magnetic hysteresis at room temperature.

The magnetization (remanent and at 1000 Oe) of sp-Si decreases as the temperature increase. Applying the Weiss equation to the magnetization data, we evaluated a Curie temperature of 765 K for sp-Si. It should be noted in passing that at such temperatures the annealing effect is quite small but still noticeable. A new technique was developed to measure the magnetization at such high temperatures.

On the other hand, at low temperatures (below 100 K), the magnetization at 1000 Oe of sp-Si follows the Curie-Weiss law, characteristic of paramagnetic materials.

6.2 Electron Paramagnetic Resonance of Spark-Processed Silicon

The electron paramagnetic resonance of sp-Si allowed the identification and characterization of paramagnetic centers within the material. Two type of centers were identified namely, the D centers, (silicon dangling bond back-boned by three other silicon atom) and the E' centers, (silicon dangling bond back-boned by three oxygen atoms.) The D centers amplitude decrease as function of the temperature in a similar manner as the magnetization measured with the SQUID magnetometer. Applying the Weiss equation to the EPR data, we evaluated a Curie

temperature of 710 K for the sp-Si D centers. In contrast, the E' centers amplitude is essentially independent of temperature in the range 300 to 800 K. A new heating system was built for the EPR system in the process leading to these results (Appendix E).

At low temperatures, both the D and E' center amplitudes follow the Curie-Weiss law, characteristic of paramagnetic materials. This is a similar behavior as the magnetization measured with the SQUID magnetometer.

In addition, the pulse EPR technique allowed the measurement of the local average spin concentration. We measured a concentration of $1.4 \times 10^{19} \text{ cm}^{-3}$ for the D centers and $0.5 \times 10^{19} \text{ cm}^{-3}$ for the E' centers. This translates into a maximum spin to spin distance of 3.7 nm.

6.3 Quasiferromagnetic Model for Spark-Processed Silicon

In order to explain the origin of the magnetic hysteresis loop observed at room temperature in sp-Si we have developed a model based on our experimental results. Figure 4-1 illustrates the most important assumption, that is, the distribution of paramagnetic centers (D and E') is not homogeneous. Using this assumption leads to the possibility of having spin-spin distances of less than 2 nm which is the commonly accepted upper limit for exchange interaction to occur between spins.

It has been shown from previously published^{50,51} work from our group that sp-Si does not have a homogeneous structure. Furthermore, sp-Si was also shown to have nanocrystals of silicon embedded into an amorphous SiO₂ matrix. Due to the physical nature of the D centers (that is, containing only silicon atoms) they can only be located in silicon rich domains while the physical nature of the E' centers (that is, containing both silicon and oxygen atoms) they can only be located in the SiO₂ matrix. Therefore, we suggests that D centers are forming clusters in or around silicon nanocrystals leading to a high local density of spins and subsequently leading to possible exchange interactions between them.

In addition to the distribution model, our experimental data suggest that D centers are responsible for the observed magnetic hysteresis. Using two different techniques (SQUID magnetometry and EPR) we found that the magnetization of the D centers (i.e. amplitude) and the macroscopic magnetization have close Curie temperatures (765 K and 710 K respectively) in addition to a similar temperature response. At low temperatures, they both follow the Curie-Weiss law and at higher temperatures they both follow the Weiss equation.

6.4 Other Quasiferromagnetic Materials

In addition to sp-Si, we have found several other materials which we classified as quasiferromagnetic materials. We classified them as such because similarly to sp-Si they display a magnetic hysteresis at room temperature and contain paramagnetic defects. These materials are:

- Ion implanted silicon with silicon at a dose of $5 \times 10^{16} \text{cm}^{-3}$,
- Ion implanted silicon with argon at a dose of $2 \times 10^{16} \text{cm}^{-3}$,
- Neutron irradiated silicon at a dose of $4 \times 10^{16} \text{cm}^{-3}$,
- HOPG graphite.

Similarly to sp-Si, we suggest that the macroscopic magnetic behavior is explained by the interaction of the paramagnetic centers.

6.5 Future Work

We presented experimental work done on ion-implanted silicon; neutron irradiated silicon and highly oriented pyrolytic graphite and how they are related to sp-Si and quasiferromagnets. We suggest that all material with a high density of interacting paramagnetic centers with a magnetic hysteresis and no magnetic elements (atoms containing d-shell and/or f-shell electrons) should be called a quasiferromagnet.

First, we believe that there are many other techniques (such as plasma processing, evaporation, sputtering...) which under specific condition could create materials with unpaired

bonds, which could contain magnetically interacting paramagnetic centers. This presents a great area of engineering research where new material could be discovered and where such materials could lead to application such as spintronics transistors.

In addition, the materials presented in this study should be investigated further. For example a more complete EPR study could be done and in particular pulse-EPR studies. Such a study would allow the confirmation or distinction between these materials and sp-Si. We think that conductors such as HOPG and semiconductor-based quasiferromagnets are slight variations of one another and we should classify them as type 1 and type 2 quasiferromagnets according to their conductivity. More research should be done toward understanding the link between the conductivity and the magnetic properties as these are the bases for building future spintronics devices.

Finally, even if the materials which we presented in this dissertation could not be used directly for the manufacturing of devices it should be noted that the fundamental understanding of local magnetism (cluster of spins) is necessary to further the engineering of new spintronic devices.

Magnetism is an exciting research topic as evidenced by the recent Nobel Prize. This dissertation has led me to grow and learn basic research principles which I will use throughout my life. In the mean-time, working on this topic has allowed us to advance it through the discovery of quasiferromagnetism.

Before we invented the concept of quasiferromagnetism and before we started to study consistently the magnetic properties of spark-processed silicon very little was known on the magnetization of materials containing large amounts of paramagnetic centers. In addition, only a

restricted amount of information was known about the characteristic of such materials at the electron level.

I believe that this work is the first step in the direction of understanding magnetism not stemming from d or f-shell magnetism. It should be pursued further.

APPENDIX A SPARK PROCESS POWER SUPPLY

I designed and fabricated a power supply which was used for the fabrication of spark-processed silicon. In this Appendix, I describe how the power supply works and needs to be operated.

A.1 Power Supply Principles of Operation

First, we describe how the power supply circuit works. Its schematic is plotted in Figure A-1. The 110V AC coming from the wall outlet is transformed into 24V DC. Then the voltage is again decreased to 12V DC corresponding to the pink subsection of the circuit only. This subcircuit creates a pulsed DC waveform with a low current (typically 2 mA). The pulsed signal is obtained by charging a capacitor (C_1, C_2, C_3 or C_4) through a resistor (R_1+F) for the high state ($V = 12V$) and discharging the same capacitor through another resistor (R_2+G) for the low state ($V = 0V$). A NAND gate is used to square the signal. Then, the output of this gate is inversed and amplified (3 times) by feeding the signal through three other NAND gates. The output of the pink subcircuit can be visualized on an oscilloscope using the outlet labeled E. Figure A-2 displays schematically what is seen on the oscilloscope. The length of the low and high states can be calculated from the product of the capacitor by each of the respective resistors. Since we use variable resistors (F and G) we can vary the duty cycle and the frequency. The frequency is equal to the inverse of the sum of the low and high state ($frequency = \frac{1}{(G+F)C_i}$). The duty cycle is equal to: $\frac{P_1}{P_2} = \frac{R_1+F}{R_2+G}$. The frequency and duty cycle range which are limited by the capacitor C_i can be expanded by using a selection of four capacitors (C_1, C_2, C_3 and C_4).

The second subcircuit, in green on the schematic, uses a BJT transistor (T_1) to pre-amplify the pulsed DC signal from a 2 mA to 200mA.

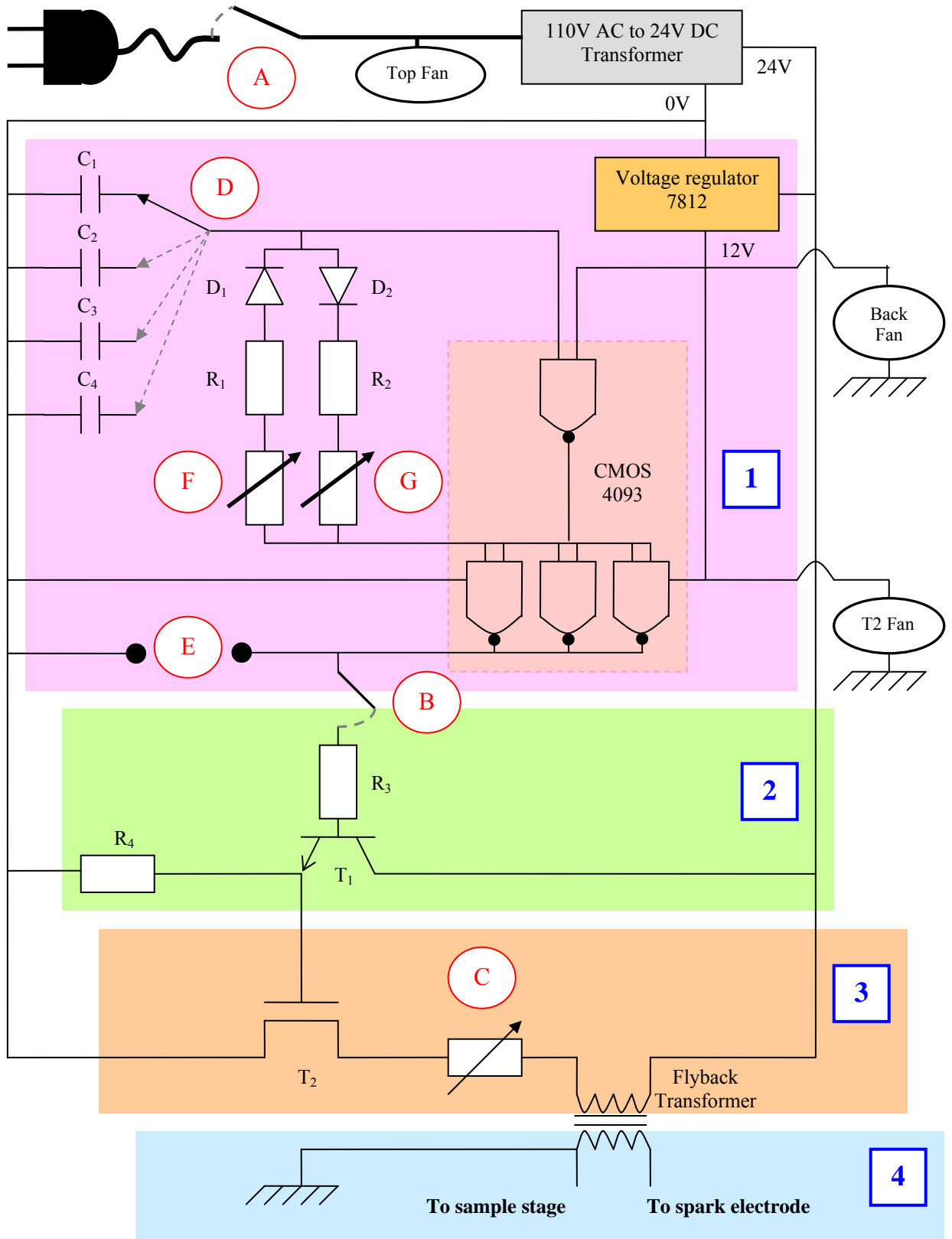


Figure A-1. Power supply schematic.

Then, the signal is amplified even more using a power MOSFET transistor (T_2). The current flowing through the orange subcircuit is about 2 Amps. Finally, the high current (2 Amps) low voltage (24V) pulsed DC signal is transformed into a high voltage (several kV) low current (few mA) pulsed signal through the flyback transformer. The spark tip is connected to the high voltage output of the flyback transformer while the stage is connected to the ground. In addition, a variable resistor is placed in series with the flyback transformer to increase or decrease the output high voltage.

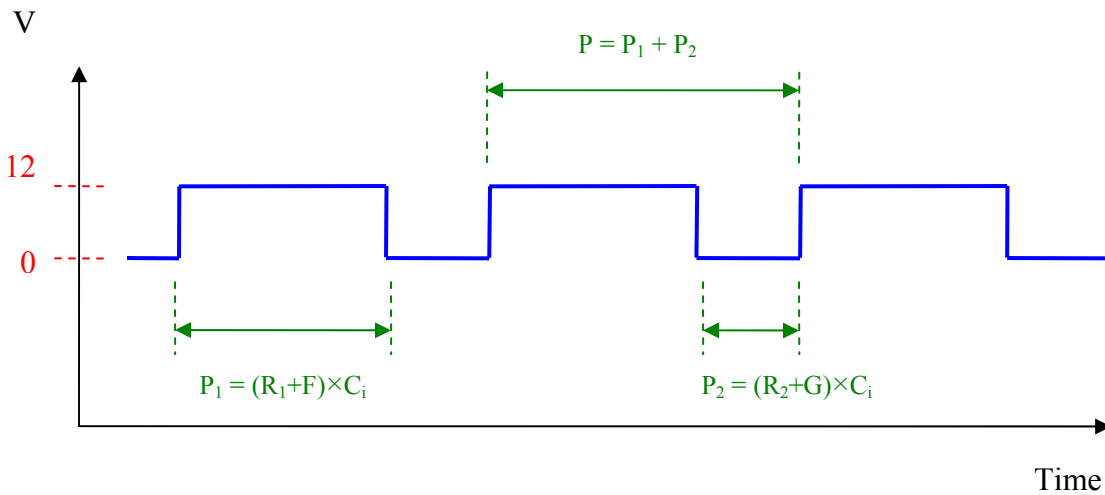


Figure A-2. Typical waveform observed at the read out (E) on the screen of an oscilloscope.

A.2 Power Supply Inner Components

Practically, several cooling devices were added. Heat sinks were used to cool down the voltage regulator and the high power transistor (T_2). In addition to the heat sink, the high power transistor (T_2) was cooled by a large fan. Two other fans were positioned at the back of the power supply to cool down the flyback transformer and one on the top of the box to cool down the entire circuit. A previous bad experience with an uncooled circuit taught me to be on the safe side by adding more fans than probably needed. Figure A-3 displays a picture of the built circuit as described.

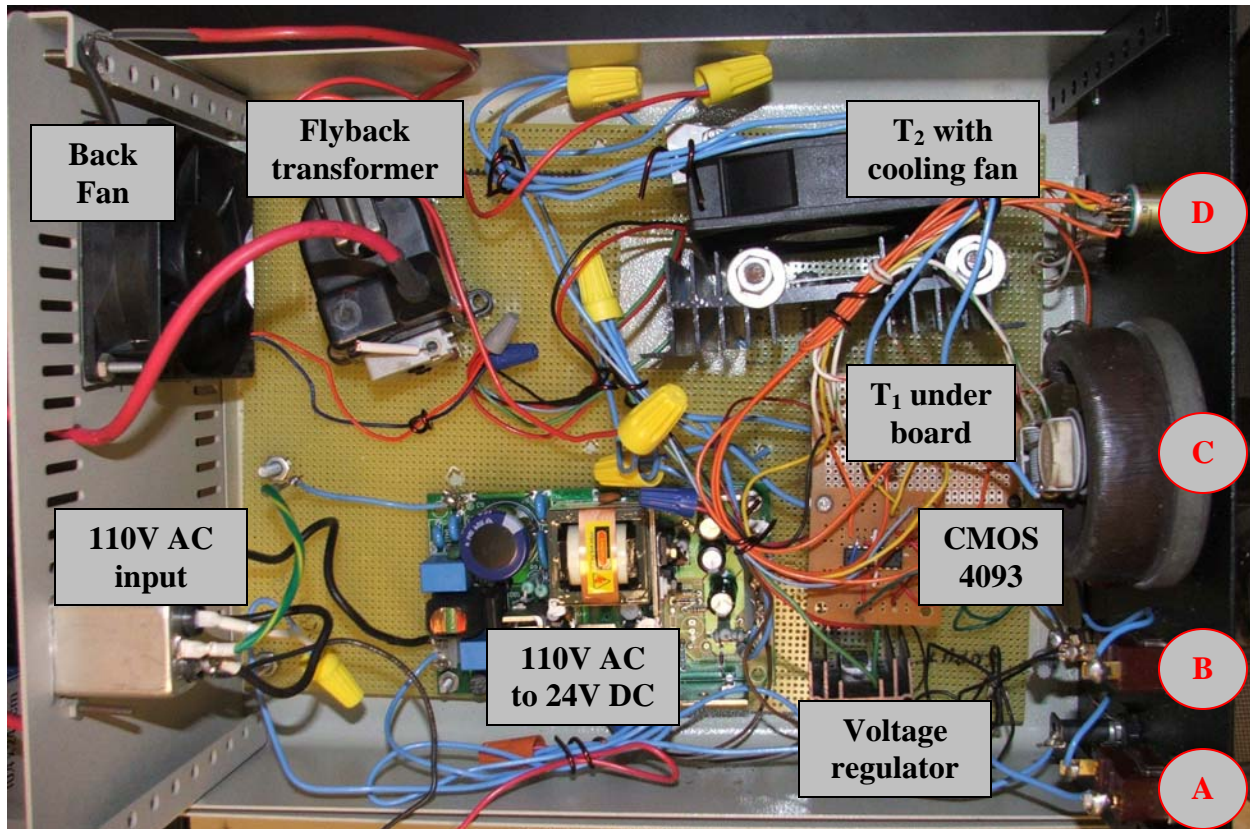


Figure A-3. Power supply without its top cover.

To complete the description of the power supply, a picture of the front panel is included in Figure A-4. The front panel allows the variation of the controls A – G. Below is the list of the controls with their meaning and labels:

- A, main switch
- B, high voltage switch
- C, high voltage power control (variable resistance 0 to 300 Ω)
- D, frequency range selector
- E, waveform read out
- F and G, frequency and duty cycle fine adjustment (variable resistance 0 to 75k Ω).

A list of component is included for a full description:

- $C_1 = 10 \text{ nF}$ (1.6 – 12kHz)
- $C_2 = 3.5 \text{ nF}$ (5 – 40kHz)
- $C_3 = 1 \text{ nF}$ (12 – 100kHz)
- $C_4 = 0.6 \text{ nF}$ (25 – 125Hz)
- D_1 , 1N4148 diode

- D_2 , 1N4148 diode
- $R_1 = 10k\Omega$
- $R_2 = 10k\Omega$
- $R_3 = 1k\Omega$
- $R_4 = 1k\Omega$
- CMOS 4093, quad 2 input NAND
- Voltage regulator 7812, $V_{out} = 12V$ DC
- T_1 , 2N2222 NPN BJT transistor
- T_2 , IRFPS43N50K HEXFET power MOSFET transistor
- Flyback transformer from high voltage circuit of television set
- Fuse 110V, 0.75Amp.



Figure A-4. Front side of the spark machine. The labels A – G designate the same control as in the schematic (Figure A-1).

Finally, it is to be noted that the sparks do not occur under all conditions. The power supply will only create a spark when specific conditions of frequency, power, duty cycle and sparking gap are met.

APPENDIX B
HgCo(SCN)₄ MAGNETIC REFERENCE

B.1 SQUID Magnetometer Verification

This reference material is used to verify that the SQUID magnetometer is properly functioning. Several references can be used to validate magnetization measurements with the SQUID magnetometer at very low temperature (2-100K). The cobalt mercury cyanide is a widely used reference for this range and was readily available to us. This material comes in a powder form and special handling is required due to its toxicity and potential to contaminate the magnetometer. A special sample holder was designed to prevent loss or scattering of the material during the measurement process. We are describing the sample holder here at first.

The measurement process in the SQUID magnetometer is done in a helium atmosphere, thus requiring pumping the chamber to a vacuum and then backfilling with helium. Since pumping down could move HgCo(SCN)₄ particles outside the holder, into the pump system and onto the detector, we prepared a quartz ampoule under argon gas. The quartz ampoule is made of a 5 mm outside diameter (4 mm inside diameter) quartz tube closed on each end. The ampoule was back filled with argon just below one atmosphere before it was closed. In order for the reference material to be positioned in the center of a symmetric holder, it was placed inside a plastic straw, normally used as a sample holder, but seating on another piece of quartz tube such that the ampoule seats in the middle of the straw. This not only places the sample properly but also virtually eliminates the magnetization from the quartz ampoule. The SQUID magnetometer is a differential technique and as such, makes differential measurements between the area above the sample, the sample itself, and the area below the sample. The design of our holder, placing quartz above, at the sample and below by adding a support tube underneath, creates a net

difference of zero. Therefore the quartz holder does not appear as a component of the observed magnetization. Only the magnetization from the sample is observed.

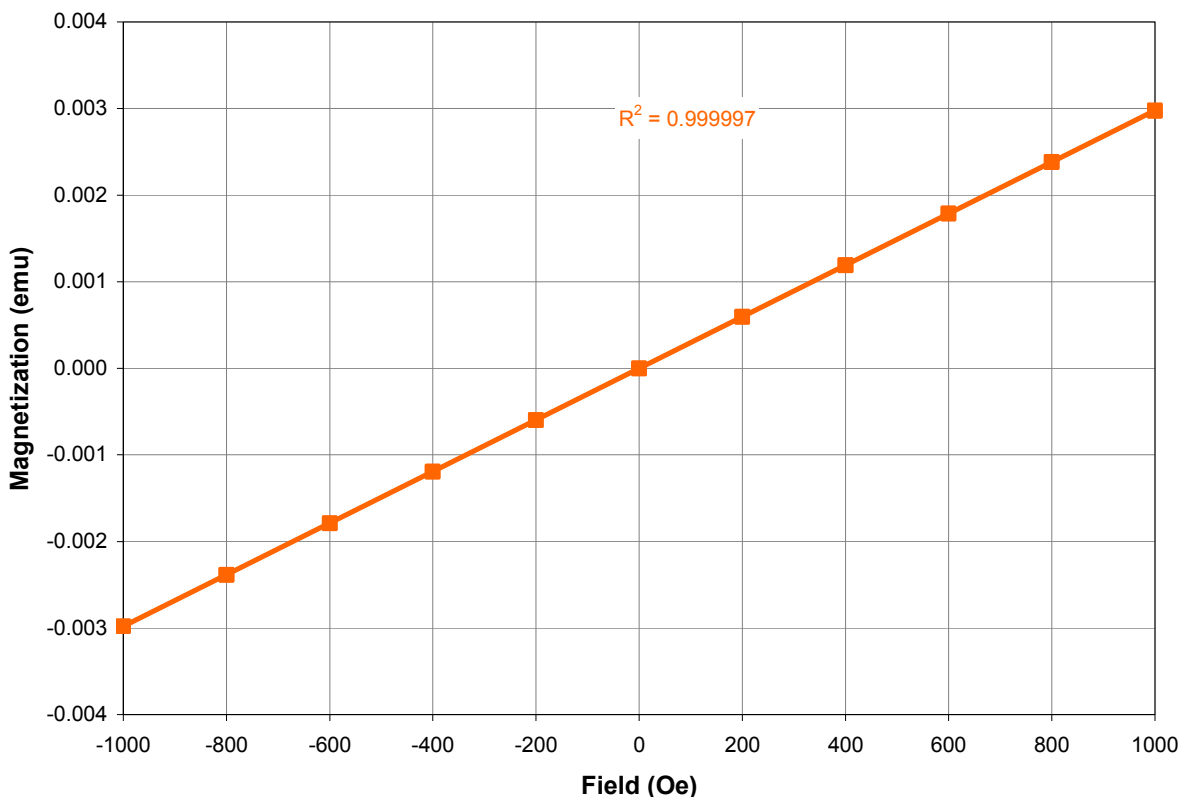


Figure B-1. Magnetization versus field at room temperature for HgCo(SNC)_4 (square). A linear curve has been fitted to the data points (solid line).

The magnetization as a function of magnetic field at room temperature for HgCo(SNC)_4 prepared as described is displayed in Figure B-1. The typical positive linear trend is observed between the magnetization and the field as it is expected for a paramagnetic material. A very good correlation is found between the data and the linear fit ($R^2 = 0.999997$). The sample mass is calculated from the accepted magnetic susceptibility³¹ measured at 20°C. A magnetization of 0.003162 emu at 1000 Oe and 20°C (293K) leads to a calculated mass of 191 mg. This calculated mass is useful for comparing the susceptibility constants in the gram unit system.

The magnetization versus temperature of HgCo(SNC)_4 is plotted in figure B-2.

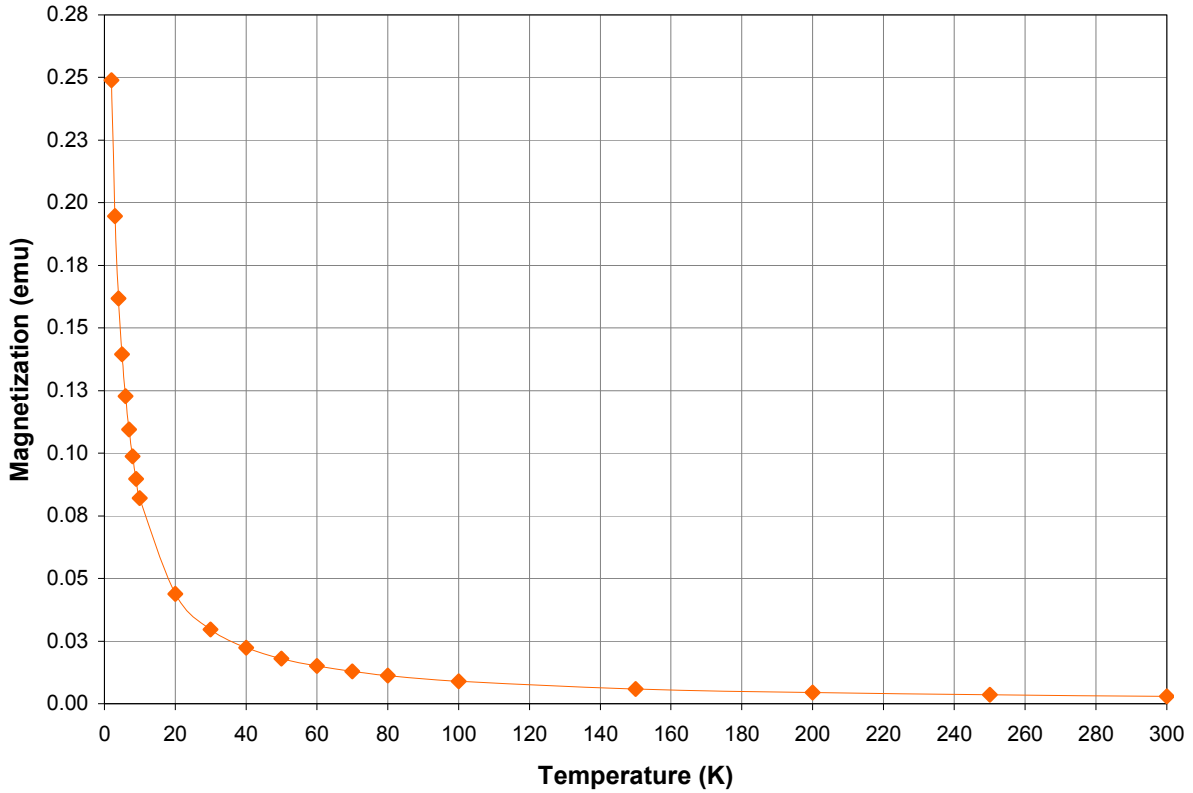


Figure B-2. Magnetization versus temperature at 1000Oe for HgCo(SNC)₄.

The magnetization increase as the temperature is decreased. The magnetization is modeled using the sum of three terms define as: $\chi(T) = \chi_{dia} + \chi_{para}^0 + \chi_{para}(T)$ where

$$\chi(T) = \frac{\text{Magnetization}}{\text{Field}}, \chi_{dia} \text{ is the diamagnetic susceptibility independent of temperature,}$$

χ_{para}^0 is the temperature independent paramagnetic susceptibility and $\chi_{para}(T)$ is the temperature dependent paramagnetic susceptibility, which is also called the Langevin paramagnetic

susceptibility and is a function of the temperature as follows: $\chi_{para}(T) = \frac{C}{T - \theta}$ where C is the

Curie constant, and θ is temperature constant.

We apply the Curie-Weiss law to our data set; the fitting constants are presented in Table B 1. To visualize the good correlation between our measured data and the Curie-Weiss law, we plot

the temperature dependent part of the magnetization as function of inverse temperature minus theta. The temperature dependent part of the magnetization is proportional $C/(T-\theta)$ and is presented Figure B-3.

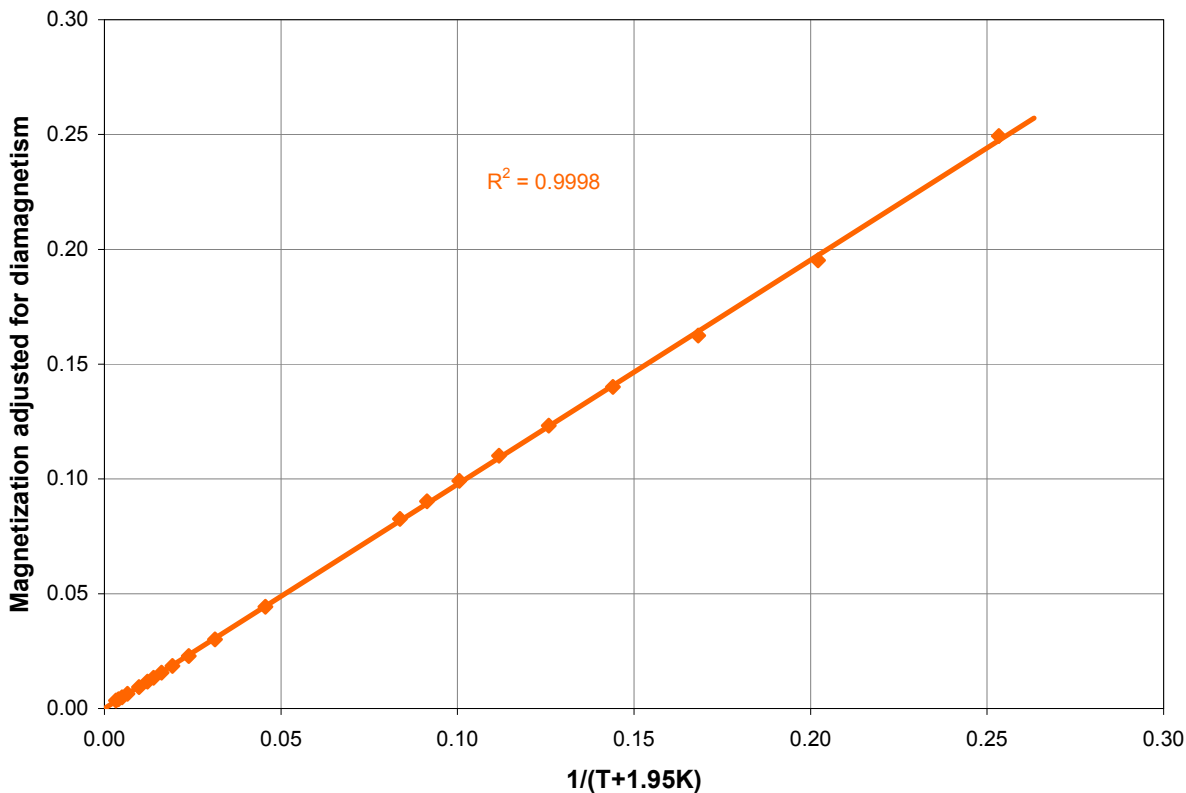


Figure B-3. Magnetization adjusted for diamagnetism as a function of the inverse temperature (squares). The temperature is shifted by 1.95K. A linear trend is fitted to the data (solid line).

Using these equations I modeled my measurements and the one of O'Connor³² using their published data. The values are presented in Table B-1. The analysis of O'Connor contains errors and a detailed treatment of the magnetic susceptibility of $\text{HgCo}(\text{SNC})_4$ is the following sections. Nevertheless, the measurement of the data by O'Connor is considered to be excellent³³.

Table B-1. Constants from susceptibility model.

	$\chi_{dia} + \chi_{para}^0 [10^{-6} \text{ g}^{-1}]$	$C [10^{-6} \text{ g}^{-1}]$	$\theta [\text{K}]$
This work	-3.05	5056	1.95
O'Connor ³²	-7.82	5433	1.98

A good agreement between our measurements and the one from O'Connor is observed. If we compare directly our modeled constants to the ones of O'Connor, it does not seem that we have a very good match. But if we look at the correlation between the susceptibility as function of temperature, which we are ultimately interested in, we find an excellent match with a correlation coefficient of 0.9999. This coefficient was calculated using the data of Table B-2, which displays the susceptibility values calculated from our measurement and the susceptibility values from O'Connor.

We conclude that $\text{HgCo}(\text{SNC})_4$ is a good reference for very low temperature magnetic measurements and that our SQUID magnetometer is working properly in the 2 to 100K range since we had a very good correlation between our data and previously published ones.

$\text{HgCo}(\text{SCN})_4$ is commonly used as a magnetic reference thanks to its ease of preparation and stability³¹⁻³⁴. In the following sections, we present several issues encountered during the magnetic properties review of $\text{HgCo}(\text{SCN})_4$. First, we take a look at why some discrepancies can be found between a proposed model (for example Curie-Weiss law) and measured data. Then, we will review the models proposed to explain the magnetic properties of this standard and discuss their validity.

B.2 Model Weighting

The Curie-Weiss model is widely used to model paramagnets. But as computer modeling evolved the method employed to compare a set of data to a model changed. We show here that using a classical technique leads to slightly different fitting parameters than using a more direct approach. Let's use the Curie-Weiss law as an example for our purpose of showing these differences. We will use the following equation to represent the Curie-Weiss law: $M = \frac{C}{T + \theta}$,

where T is the temperature and M the magnetic susceptibility, C and θ are fitting parameters.

Table B-2. Magnetic susceptibility [10^{-6} g^{-1}] as function of temperature of $\text{HgCo}(\text{SNC})_4$ of our data set and O'Connor's data set.

T[K]	O'Connor ³²	This work
102.6	46.4	45.4
96.85	49.9	48.1
91	53.5	51.2
82.85	57.9	56.3
75.72	62.8	62.0
68.88	69.7	68.5
61.66	78.0	76
53.76	89.8	88
45.64	105	103
37.58	128	124
31.43	153	148
27.87	170	166
25.77	185	179
24.72	193	187
23.66	202	195
22.83	209	201
22.21	214	207
21.56	220	213
20.91	227	219
20.27	235	225
19.62	241	232
18.89	251	241
18.06	262	251
17.26	273	262
16.5	285	273
15.64	300	287
14.2	329	314
13.15	353	336
11.92	386	367
10.56	430	408
9.23	484	456
8.02	544	511
6.91	613	573
5.91	691	642
5.21	758	702
4.5	838	775
4.202	862	815
3.911	904	853
3.611	954	898
3.226	1025	966
2.9	1093	1033
2.39	1232	1165
1.99	1379	1299

The classical fitting method would be to plot $\frac{1}{M}$ as function of T. The equation is rewritten as: $\frac{1}{M} = \frac{1}{C}T + \frac{\theta}{C}$. In this case we expect the data to have a linear trend with a slope of $\frac{1}{C}$ and a y-intercept equal to $\frac{\theta}{C}$. This classical method can be done quickly without computer help. On the other hand, the more direct method of fitting the equation requires a computer's help. To illustrate our point we plot the data according to each method in Figure B-4. The A graph illustrates the direct method while the B graph illustrates the classical one. In addition the data used for these two graphs are shown in table B-3.

Table B-3. Data example.

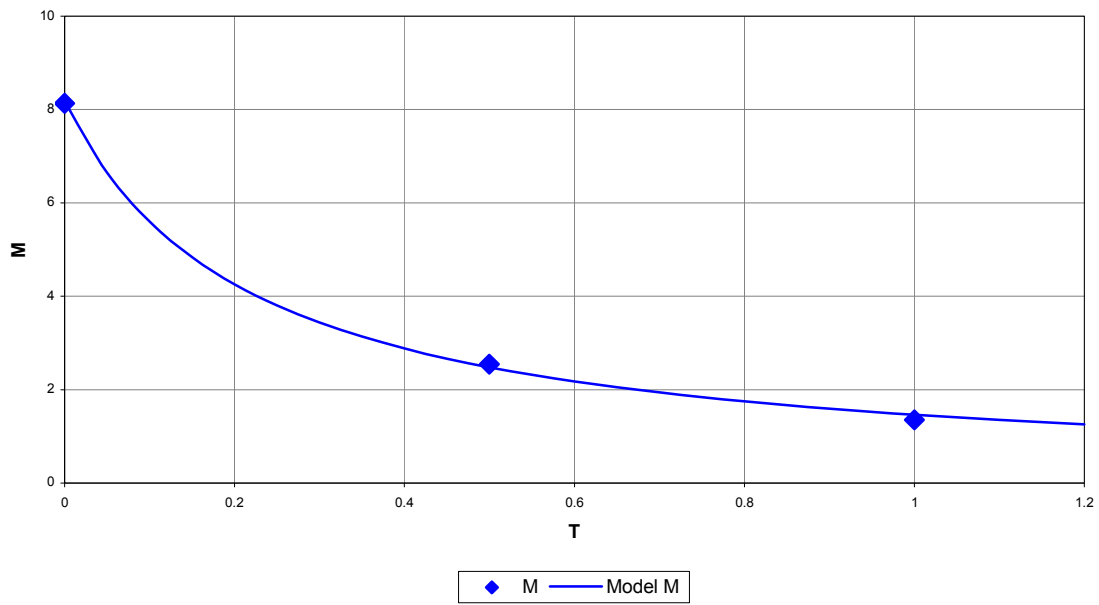
T	M	$\frac{1}{M}$
0	8.131	0.123
0.5	2.544	0.393
1	1.352	0.739

Both models lead to excellent correlation coefficient of 0.999 with the direct method and 0.995 with the classic one. Even with very good correlation coefficient, the fitting parameters can have large discrepancies up to 18% in our case as show in table B-4.

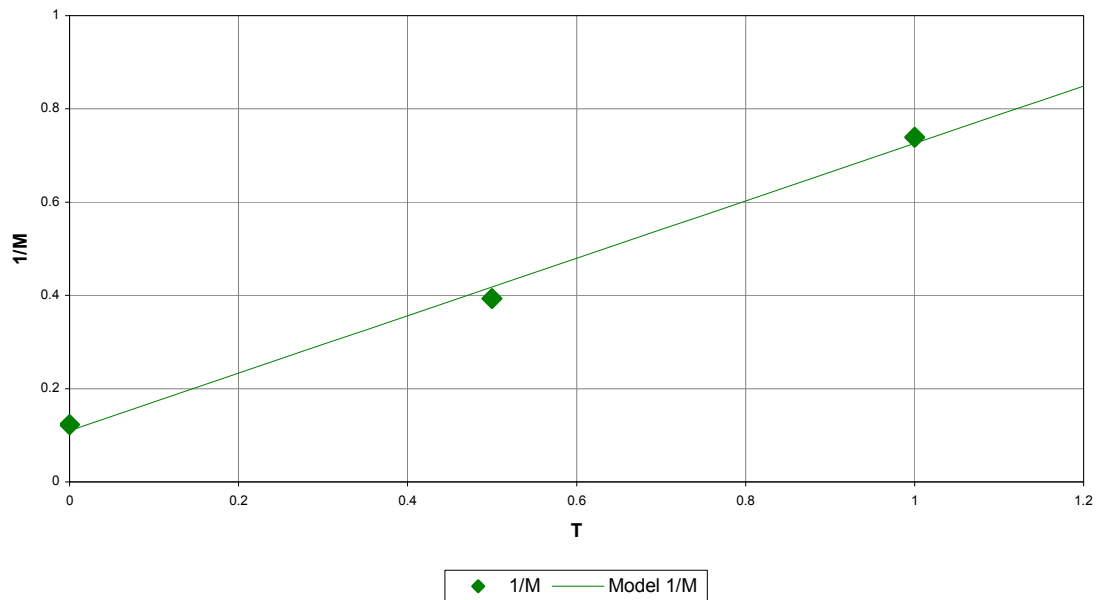
Table B-4. Fitting parameters.

Constants	Direct Method	Classic Method	Discrepancy
C	1.780	1.620	9%
Θ	0.218	0.178	18%

We use the same data, the same equation but the fitting parameters were evaluated differently leading to large discrepancies! Our quantification of “large” is due to the fact that we expected very small differences in our fitting parameters since the correlation coefficients are so high. Therefore, one must be careful when using the coefficient correlation alone as a judging factor for a good model fit.



A



B

Figure B-4. Example of the Curie law model. A) M-T plot and its model. B) M-1/T plot and its model.

The discrepancies in fitting parameters between the classic and direct method comes from the weighting of the data points. The direct method will weight each data point equally where the classic method will decrease the weight of the data point with high M values and increase the

weight of the data point with low M values. In physics terms: the direct method considers each data point to have the same precision while the classic method assumes that the large M data point have less precision and should account for less. In the case where we know which data point have more precision we can weight the model accordingly. But in the case of the classic method the weighting is, in most cases, unrelated to the precision of the data and therefore does not account properly for it.

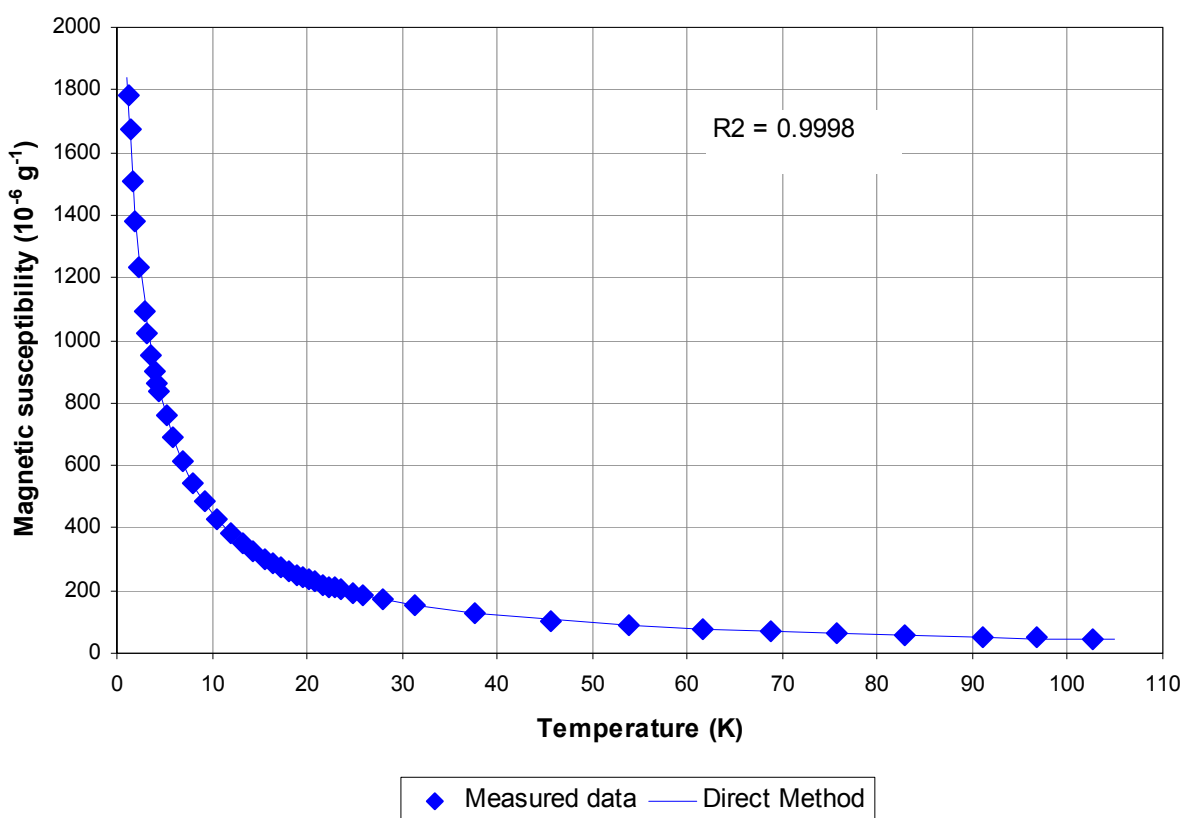


Figure B-5. Magnetic susceptibility of HgCo(SNC)_4 and its model using the direct method.

On the other hand the direct method (as presented here) does not account for the precision either but concedes the data point to be equal. If no information is known about the precision, one should use the direct method and not the classic one. If one knows the precision of each data point, it is possible to take this information into account in the direct method and obtain more

trustworthy fitting parameters. Historically, the classical method has been used because computers were not available. When high resolution is not required the classical method can be used but since computers are so widely used nowadays we believe that the direct method should always be used.

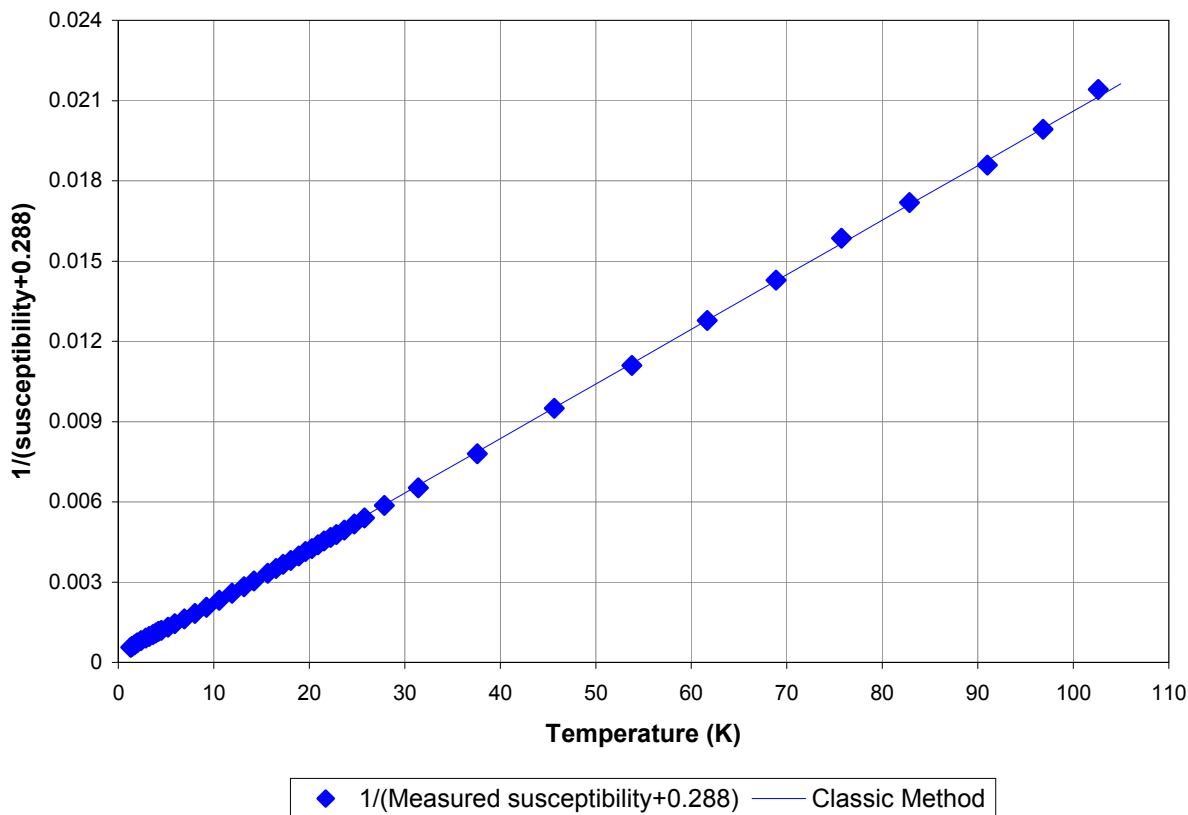


Figure B-6. Inverse magnetic susceptibility of HgCo(SNC)_4 adjusted for diamagnetism versus temperature and its model using the classic method.

Now we compare the direct and classic method on physical data. For our purpose we use the magnetic susceptibility data provided by O'Connor³² and the model

equation: $\chi = \chi_0 + \frac{C}{T - \theta}$ for the direct method and $\frac{1}{\chi - \chi_0} = \frac{1}{C}(T - \theta)$ for the classic method. The

data with its model using the direct method is plotted Figure B-5. In addition, the inverse susceptibility adjusted for diamagnetism (using a value proposed by O'Connor³²) and its model

using the classical method is plotted Figure B-6. In both cases the model and data match very well (correlation coefficients better than 0.999). But the fitting parameters do not match that well as we discuss now.

The diamagnetic susceptibility (χ_0) must be set to use the classic method. First, we use the value found using the direct method. This allows observing only the effect of weighting on the model and not the effect of choosing a set value. The fitting parameters are presented in Table B-5 for comparison. A large discrepancy is found for the value of theta between the methods and a moderate discrepancy is found for the Curie constant. Applying these two methods on physical data reveals that weighting the data can be an important issue. Once again, since we do not know the precision, we can only assume that all measurements have the same precision and therefore we must weight equally our data points when applying the model. Now let's see what happens to the fitting parameters when the diamagnetic susceptibility is changed.

Table B-5. Comparison of the direct and classic method of O'Connor data set. For both methods the diamagnetic constant is set and equal to the value found through the direct method.

Constants	Direct Method	Classic Method	Discrepancy
$\chi_0 [10^{-6} \text{ g}^{-1}]$	-7.86	-7.86	0%
C [10^{-6} g^{-1}]	5389	5621	4.3%
θ [K]	-1.82	-2.62	44%
r^2	0.9998	0.9991	N/A

O'Connor used an empirically calculated value³² for the diamagnetic susceptibility of $\text{HgCo}(\text{SNC})_4$. If we use that value we obtain the fitting parameters in Table B-6. When comparing the direct and classic method we obtain large discrepancies. In particular the diamagnetic susceptibility is twenty times larger when using the direct method than when we use the proposed value by O'Connor. In addition the discrepancies for the other fitting parameters are larger than when we use the same diamagnetic constant. We conclude that setting the

diamagnetic constant in the classic method leads to additional variation in the fitting parameters.

This is another reason why one should use the direct method rather than the classic one.

Table B-6. Comparison of the direct and classic method with O'Connor data set. For the classic method the diamagnetic constant is set and equal to the value proposed by O'Connor.

Constants	Direct Method	Classic Method	Discrepancy
$\chi_0 [10^{-6} \text{ g}^{-1}]$	-7.86	-0.288	96%
C [10 ⁻⁶ g ⁻¹]	5389	4902	9%
θ [K]	-1.82	-1.02	44%
r^2	0.9998	0.9997	N/A

B.3 Temperature Independent Susceptibility

The previous section led us to see that the diamagnetic constant is an important factor in the model of the magnetic susceptibility of HgCo(SNC)₄. In this section we will discuss what has been previously done regarding temperature independent susceptibility. It includes the diamagnetic constant and the paramagnetic temperature independent constant, also sometimes called Van Vleck magnetism^{38,60}. The Van Vleck susceptibility is given by:

$$\chi_0 = \frac{N}{V} \left(2\mu_B^2 \sum_n \frac{|\langle 0 | (L_z + g \cdot S_z) | n \rangle|^2}{E_n - E_0} - \frac{e^2 \mu_0}{6m_e} \sum_{i=1}^Z \langle r_i^2 \rangle \right) \text{ where } \frac{N}{V} \text{ is the spin density,}$$

$$2\mu_B^2 \sum_n \frac{|\langle 0 | (L_z + g \cdot S_z) | n \rangle|^2}{E_n - E_0} \text{ is the temperature independent paramagnetic term and}$$

$$-\frac{e^2 \mu_0}{6m_e} \sum_{i=1}^Z \langle r_i^2 \rangle \text{ is the diamagnetic term. In the first term, } L_z \text{ is the orbital angular momentum}$$

operator projected on the z-axis, S_z is the total spin angular momentum projected on the z-axis, g

is the Lande factor, E is the energy, n designates the electron number and μ_B is the Bohr

magneton. In the second term, e is the electron's electric charge, μ_0 is the vacuum magnetic

permeability, m_e is the electron mass, r is the electron radius and Z is the total number of

electrons. In practice, the full calculation has only been performed on monoatomic gases and

small molecules with high symmetry due to complexity of electron orbital's. In a large molecule like $\text{HgCo}(\text{SNC})_4$, the simplest approach is to use a linear combination of individually calculated temperature independent susceptibilities for an atom or small group of atoms. Selwood⁶¹ and Pascal⁶² proposed values presented in Table B-7 for the diamagnetic term. From the stoichiometric composition we found $\chi_{dia}^0 = -37 - 12 - 4 \times 35 = -189 \times 10^{-6} \text{ mol}^{-1}$ according to Selwood and $\chi_{dia}^0 = 4 \times (-33.26 - 4.85 - 10.3) - 12 - 32.31 = -238 \times 10^{-6} \text{ mol}^{-1}$ according to Pascal's method. It must be added in passing that Selwood [61] recognized that these diamagnetic corrections are not to be taken as absolute values.

Table B-7. Diamagnetic correction per mol.

Species	Selwood ⁶¹ χ_{dia}^0 [10^{-6} mol^{-1}]	Pascal ⁶² χ_{dia}^0 [10^{-6} mol^{-1}]
CNS^-	-35	-33.26
C-N	0	-4.85
C-S	0	-10.3
Co^{2+}	-12	-12*
Hg^{2+}	-37	-32.31
$\text{HgCo}(\text{SNC})_4$	-189	-238

* Pascal's value was not available therefore it was taken to be equal to Selwood's.

In addition to the diamagnetic correction a temperature independent paramagnetic correction may be required. According to Nelson⁶³ Co^{2+} has a non-zero paramagnetic susceptibility of $\chi_{para}^0 = 430 \times 10^{-6} \text{ mol}^{-1}$. This value is similar to the calculation of Cotton⁶⁴ based on optical measurements. But according to Selwood, Cobalt-cyanide salts, $[\text{Co}(\text{CN})_x]^{-y}$, do not have a temperature independent paramagnetic susceptibility if they are coupled with a non-magnetic element such as Hg. Therefore no temperature independent susceptibility should be added in our model.

Nelson's method includes, first, measuring the magnetic susceptibility from 40 to 300 K. This is done in order to avoid the low temperature effect which will be discussed in the next

section. Then modeling the data using the equation: $\chi = \chi_0 + \frac{C}{T - \theta}$ where $\chi_0 = \chi_{para}^0 + \chi_{dia}^0$. In addition, Nelson calculates the temperature independent susceptibility (χ_{para}^0) from the previous equation. Using this method on my data I obtained $\chi_{para}^0 = 270 \times 10^{-6} \text{ mol}^{-1}$ and $\chi_{para}^0 = 302 \times 10^{-6} \text{ mol}^{-1}$ using O'Connor's data. This is far from what Nelson found ($\chi_{para}^0 = 430 \times 10^{-6} \text{ mol}^{-1}$).

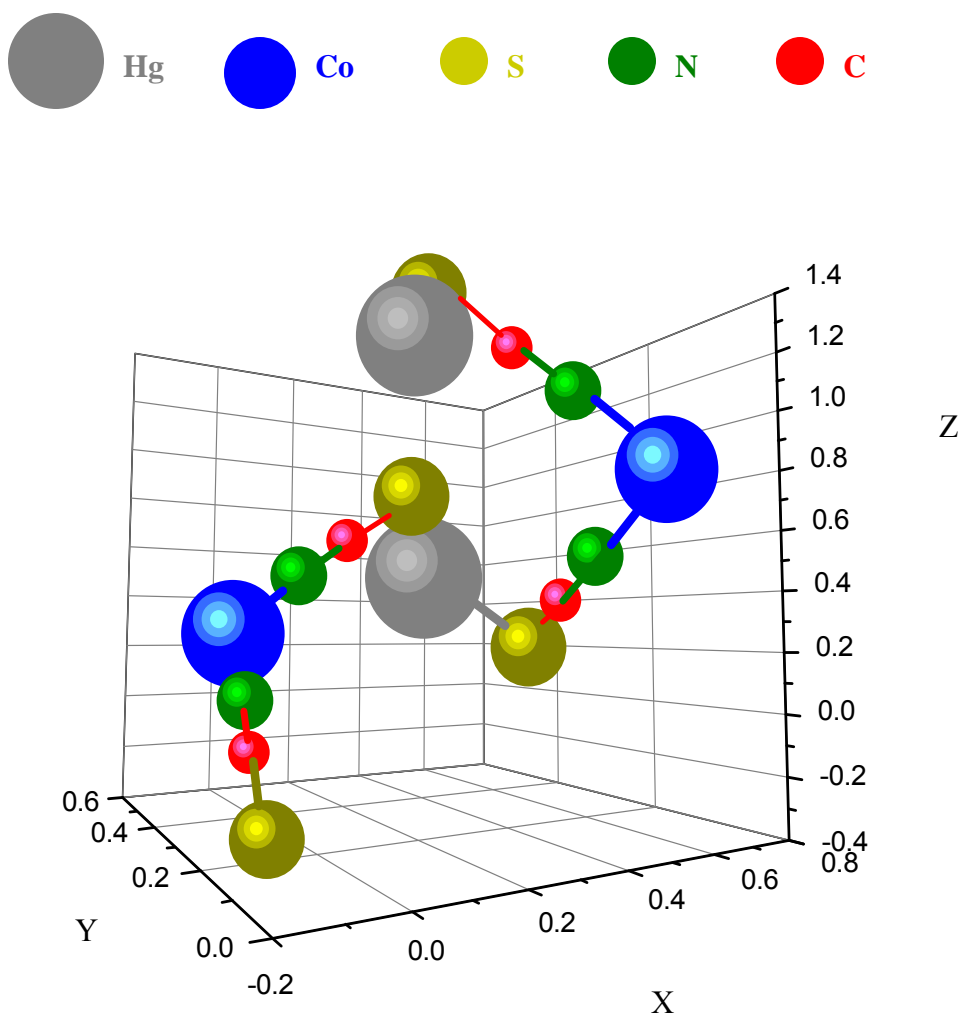


Figure B-7. Three dimensional representation of HgCo(SNC)₄. X,Y,Z are the fractional coordinates.

Finally, according to Selwood, the higher the symmetry of a molecule the better the correction agree with experiment. In the case of $\text{HgCo}(\text{SNC})_4$ the molecule has a complex symmetry⁶⁵ and therefore the temperature independent corrections are not accurate. A three-dimensional plot of a section of $\text{HgCo}(\text{SNC})_4$ is presented in Figure B-7.

In conclusion, the suggested values for the $\text{HgCo}(\text{SNC})_4$ temperature-independent susceptibility corrections need to be taken with a grain of salt. We found many publications on this topic but there were lots of inaccuracies or contradictory explanations and therefore we suggest that the full calculation of the temperature independent susceptibility using electron orbital's be performed before an improved analysis is proposed.

B.4 Zero Field Splitting and Exchange Interaction

I would like to finish this appendix with effects seen at very low temperature in the case of this standard material, namely zero field splitting and exchange interaction. Nelson⁶³, O'Connor³² and Hatfield⁶⁶ all agree that below 20 K both zero field splitting and exchange interaction must be taken into account to properly model the magnetic susceptibility of this cobalt salt. But none of them agree on the model. Hatfield⁶⁶ seems to have the most accurate model for zero field splitting as he uses both measurements as a function of temperature and field to validate his equation. He proposes the following set of equations:

$$\chi = \chi_0 + \frac{(\chi_{\parallel} + 2\chi_{\perp})}{3}$$

$$\chi_{\parallel} = \frac{N\mu_B g^2}{4k_B T} \left[\frac{\frac{\sinh\left(\frac{y}{2}\right)}{\frac{y}{2}} + 9e^{-x} \frac{\sinh\left(\frac{3y}{2}\right)}{\frac{3y}{2}}}{\cosh\left(\frac{y}{2}\right) + e^{-x} \cosh\left(\frac{3y}{2}\right)} \right]$$

$$\chi_{\perp} = \frac{N\mu_B g^2}{k_B T} \left[\frac{\frac{\sinh(y)}{y} + \frac{3}{2x} \cosh(y)e^z - \frac{3}{2x} e^{-z}e^{-x}}{e^z \cosh(y) + e^{-x}e^{-z}} \right]$$

$$x = \frac{D}{k_B T}, \quad y = \frac{g\mu_B H}{k_B T} \quad \text{and} \quad z = \frac{3y^2}{4x}.$$

The constants are defined as follows: D is the zero field splitting constant, k_B the Boltzman constant, T the temperature, g the Landé factor, H the magnetic field and μ_B the Bohr magneton.

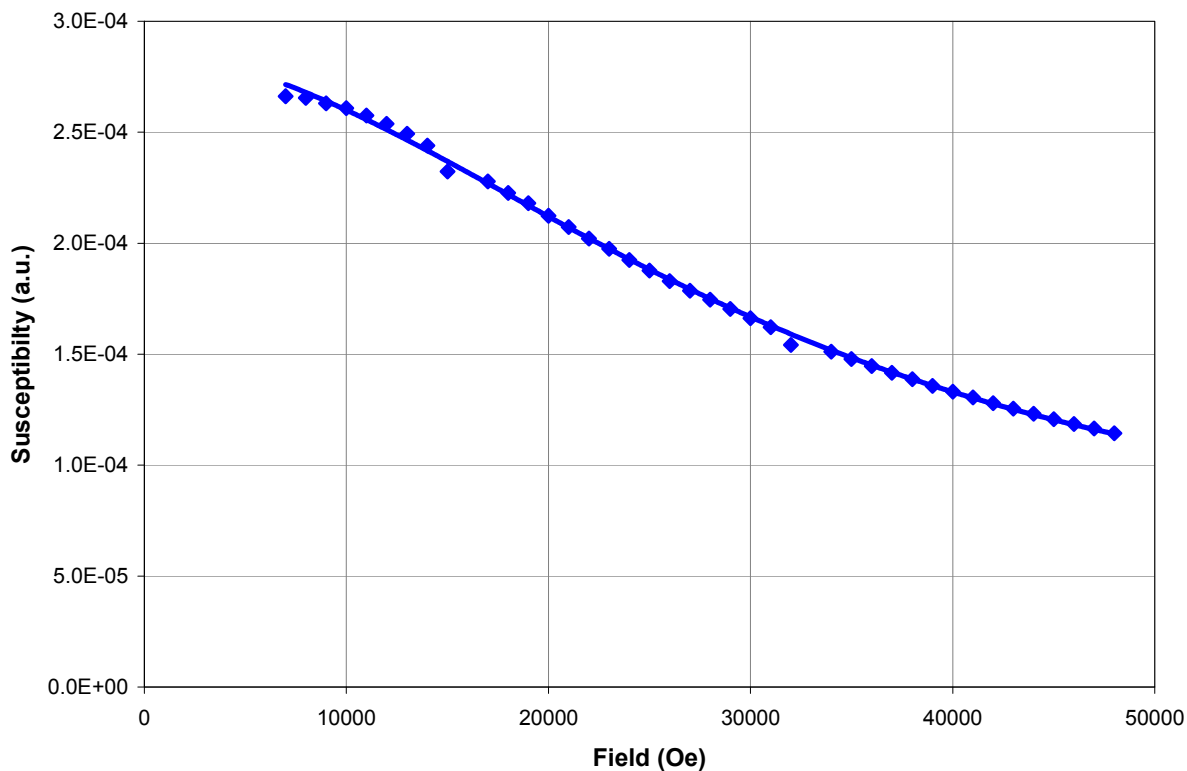


Figure B-8. Magnetic susceptibility of HgCo(SNC)_4 as function of magnetic field at 2 K (square) and its model (solid line).

Using Hatfield's equations applied to the susceptibility versus field measurements at 2 K we found a zero field splitting constant of 7 cm^{-1} (Figure B-8). This value is at the same order of

magnitude to the one calculated by Hatfield (19 cm^{-1}). In addition Hatfield⁶⁶ recognize that he did not have a precise value for the zero-field splitting.

The zero-field splitting effect has been shown before and we successfully reproduced the measurement and modeling technique used. This confirms that our SQUID magnetometer is properly calibrated.

Finally the model proposed for the exchange interaction occurring at very low temperature can be reviewed in the work by Nelson on $\text{HgCo}(\text{SNC})_4$ crystals. The measurement of the exchange interaction in this material is well beyond the scope of this work and a good presentation of this effect and model is presented⁶³ on a $\text{HgCo}(\text{SNC})_4$ crystal.

B.5 Conclusions

This appendix was aimed at showing several issues which have occurred during the study of magnetism. First, it is a complicated topic as shown by the contradictory experiments and models proposed by several leading authors in this field on a “standard” material. Secondly, we were able to reproduce accurately the results produced by others. It demonstrates that our methods and equipment are in good working conditions. Also, we wanted to raise awareness on the difficulty of modeling as different authors use different techniques which add confusion to an already difficult topic. Finally, we suggest that this material be studied further using optical absorption measurements for example, to compare with zero field splitting value from magnetic measurements or that its temperature independent susceptibility be fully modeled using quantum theoretical calculation.

APPENDIX C
ALUMINUM MAGNETIC REFERENCE FOR TEMPERATURE RANGE 50 – 300 K

Aluminum has been well studied in the 50-300K temperature range and is a well suited magnetic reference in that range due to its large temperature dependence. This Appendix details the results and conclusions presented in section 3.3.2.

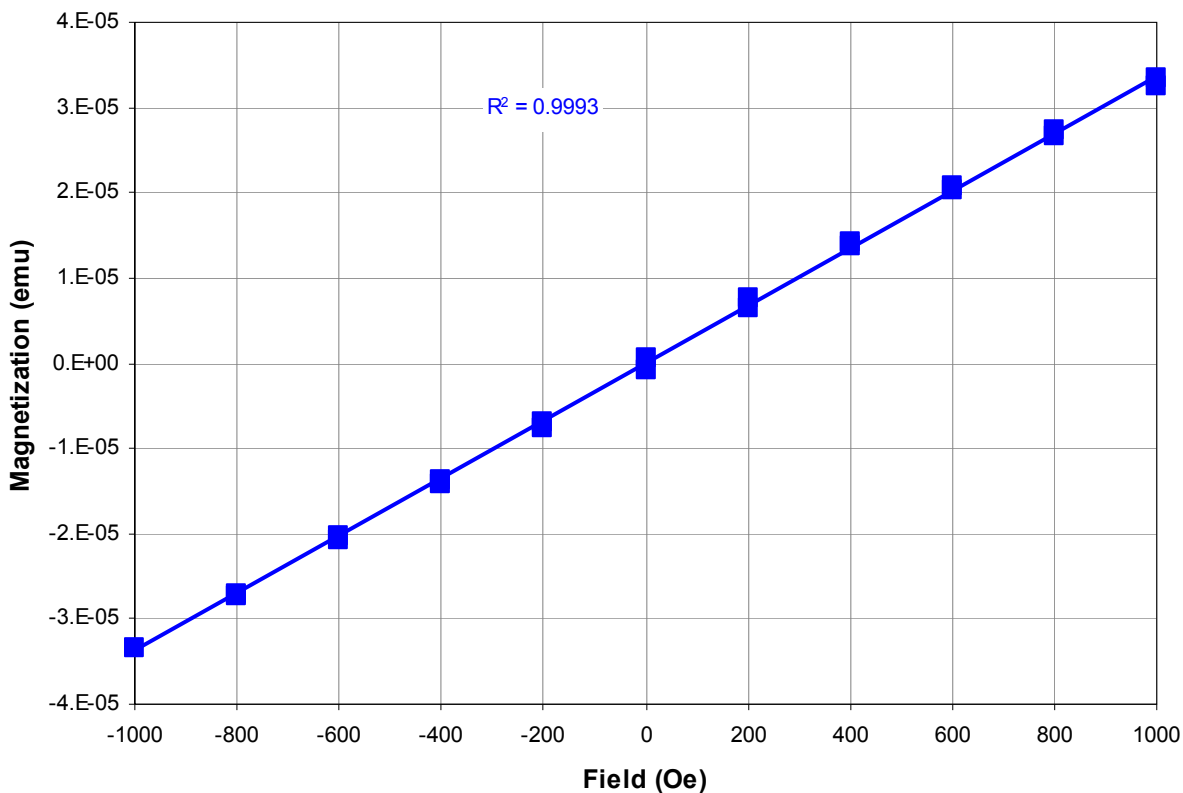


Figure C-1. Magnetization versus field at room temperature of 99.999% pure aluminum (squares). A linear curve is fitted to the data (solid line).

First, we measured the magnetization of an aluminum piece as function of magnetic field at room temperature to evaluate the magnetic susceptibility. The data are plotted in Figure C-1. The magnetization is linearly proportional to the field as expected for a paramagnet. The measured magnetic susceptibility at room temperature is 3.377×10^{-8} emu for the aluminum sample. Using the measured weight of the sample (53.4 ± 0.1 mg) we calculated a sample volume

of $0.0198 \pm 0.00004 \text{ cm}^{-3}$ leading to a volume susceptibility of $1.70 \pm 0.03 \times 10^{-6} \text{ cm}^{-3}$. This value is very close to the published² value of $1.65 \times 10^{-6} \text{ cm}^{-3}$.

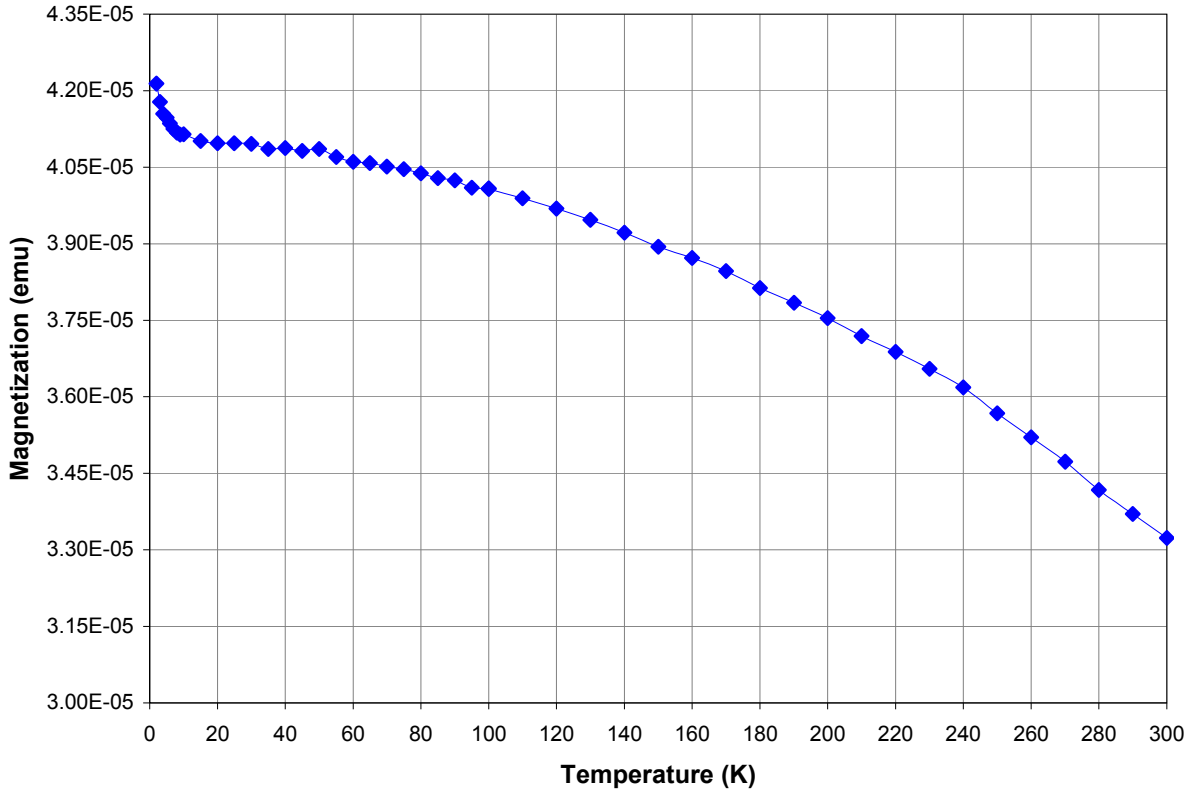


Figure C-2. Magnetization versus temperature at 1000 Oe for 99.999% pure aluminum.

Next, we measured the magnetization as function of temperature at 1000 Oe. The data are plotted in Figure C-2. The magnetization decreases as the temperature increases but not like the Curie law. Rather, aluminum magnetization is linearly dependant on the square of temperature according to Hedgcock³⁴. A linear trend is fitted through our magnetization measurement versus temperature square as seen in Figure C-3.

Table C-1. Comparison of model constants for aluminum.

	$\chi_{dia} + \chi_{para}^0 [10^{-6} \text{ cm}^{-3}]$	B [$10^{-12} \text{ K}^{-2} \text{ cm}^{-3}$]
This work	18.8	-3.96
Hedgcock ³⁴	19.2	-3.70

Using the calculated volume of our sample we obtained fitting parameters displayed in Table C-1 in cm^{-3} units for direct comparison with Hedgcock's work³⁴. For modeling our data we use the following equation: $\chi = \chi_{dia} + \chi_{para}^0 + B \times T^2$. We found a correlation coefficient of 0.997 between our data and the model.

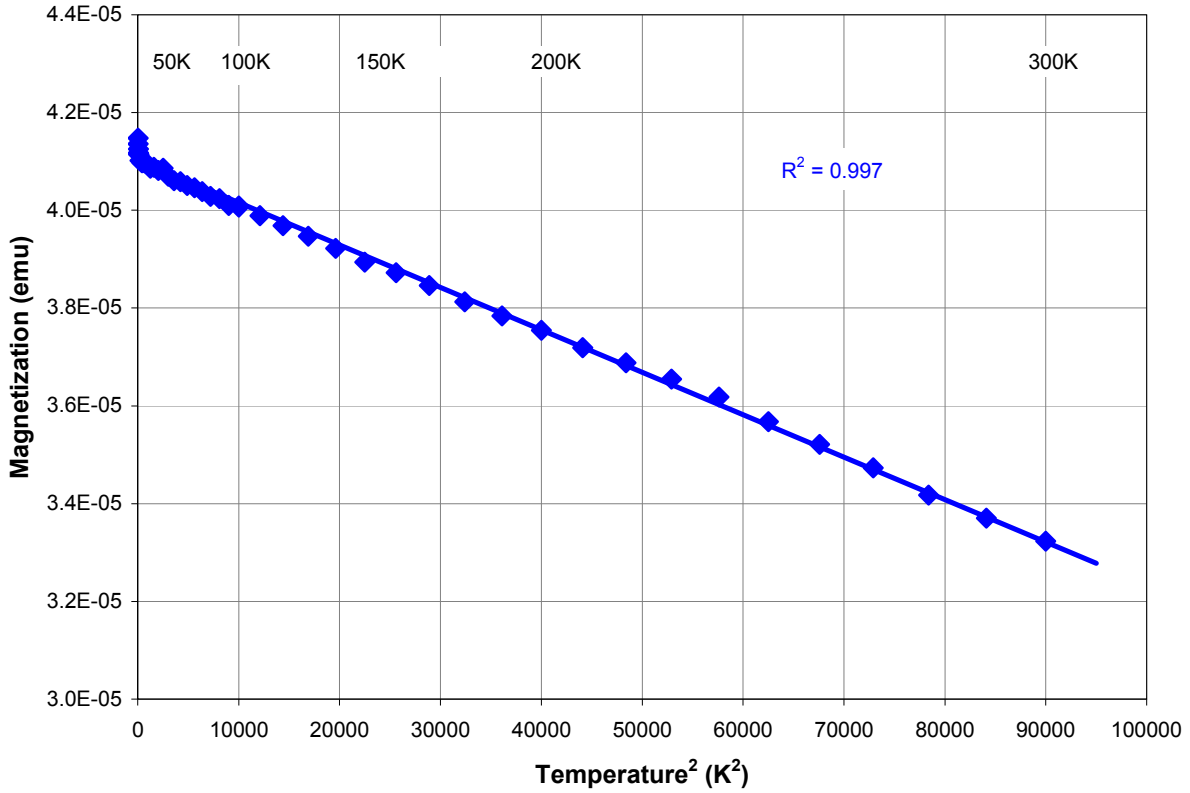


Figure C-3. Magnetization as function of temperature square at 1000Oe for 99.999% pure aluminum (diamonds). A linear trend is fitted to the data (solid line).

The results from $\text{HgCo}(\text{SNC})_4$ and Aluminum reference lead us to conclude that our SQUID is properly calibrated from 50 to 300 K.

APPENDIX D
OXYGEN CONTAMINATION AT LOW TEMPERATURES

This Appendix is aimed at giving all the details necessary to visualize the oxygen contamination problem.

As stated in section 3.3.3 oxygen is paramagnetic in its gas and liquid phases, becomes antiferromagnetic when solid below 54.3 K, and changes its crystal structure³⁶ (β to γ at 43.8 K). The magnetic transitions of oxygen at 54.3 K and 43.8 K generate a noticeable change in the measured magnetic susceptibility of a sample while some gaseous oxygen is left in the sample chamber. For example Figure D-1 displays the magnetization of a piece of plastic straw as a function of temperature at 500 Oe. A very large peak around 50 K is observed above a broad flat magnetization (equal to the diamagnetic susceptibility of the piece of straw).

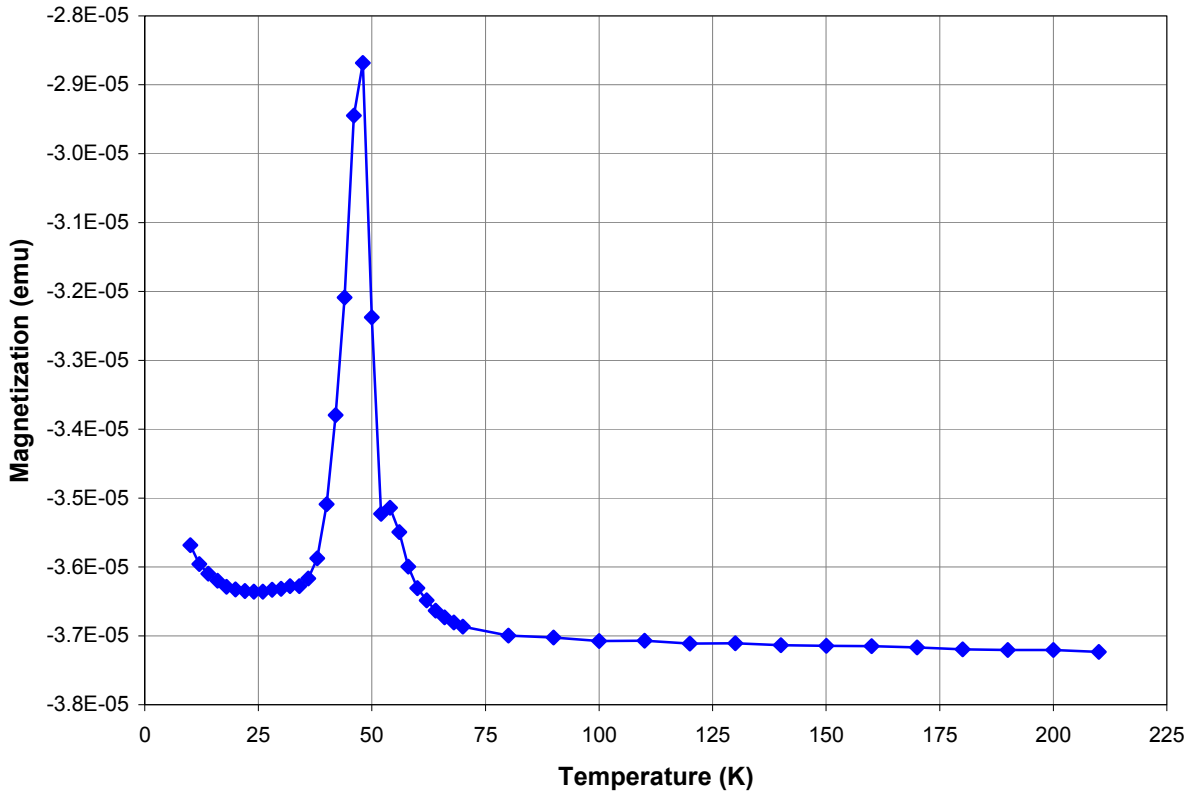


Figure D-1. Magnetization versus temperature for a piece of plastic straw at 500Oe.

In our SQUID magnetometer, a sample is normally measured in a Helium gas atmosphere. Following the sample loading, the load lock (or the entire chamber) is purged with Helium gas. But due to pumping and Helium quality there is still oxygen left in the chamber. To find out what was the oxygen residual limit, we measured the magnetization versus temperature of another piece of straw for several different numbers of purges. The data is presented in Figure D-2.

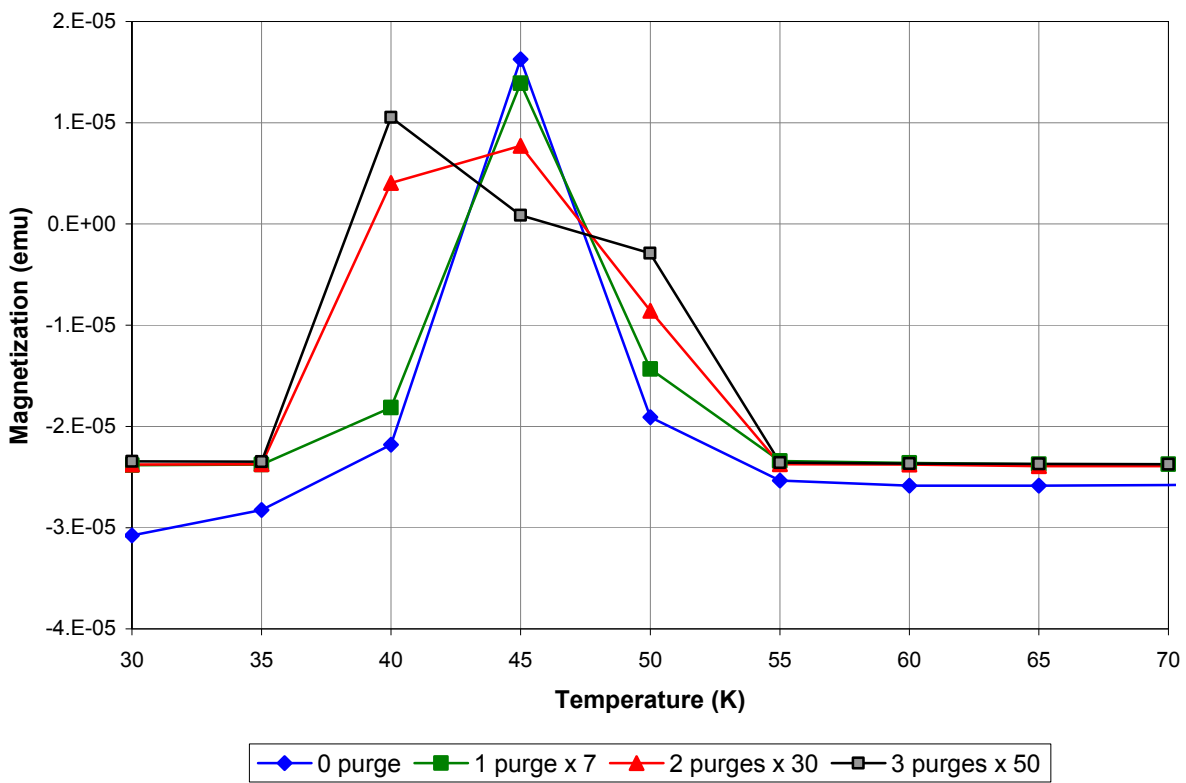


Figure D-2. Magnetization at 1000 Oe of a piece of straw as a function of temperature for several different purges. The 0 purge magnetization has been shifted by -15K. The 1,2 and 3 purge magnetization has been multiplied by 7, 30 and 50 at 40, 45 and 50K.

For better visibility the magnetization at and around the oxygen peak has been multiplied by a scalar listed in the Figure D-2 legend. When no purge is performed a large peak is observed as expected since we leave a large amount of oxygen gas from air in the chamber. But, even when we purged 3 times the oxygen peak is still visible. Plotting the oxygen peak height as a

function of the number of purges done during the loading of the sample helps us better visualize the decrease of oxygen amount present in the SQUID magnetometer chamber. Figure D-3 displays such a graph.

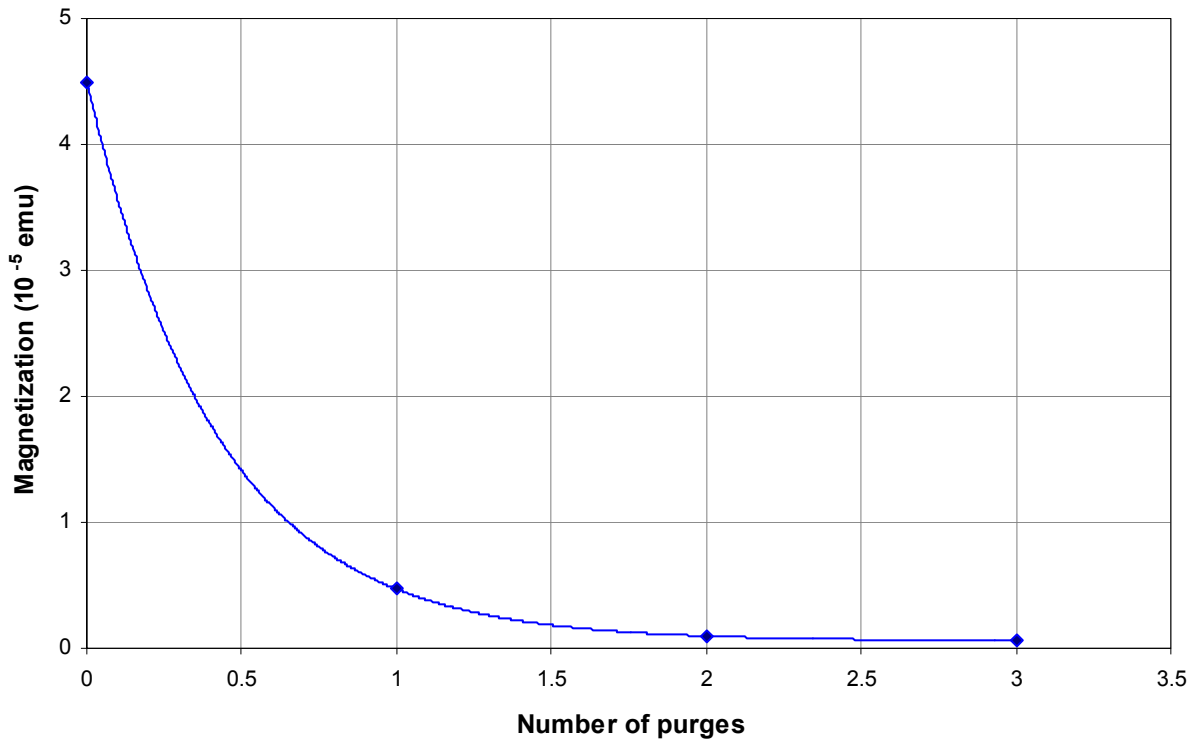


Figure D-3. Oxygen magnetization peak height versus number of purges (diamonds). An exponential decay model is fitted to the data in solid.

An exponential decay model is used to model the decrease of oxygen amount as function of the number of purge. The model has the following form: $M = M_0 + A \times e^{-n/n_0}$, where M_0 is the residual magnetization due to oxygen, A is the exponential amplitude and n_0 is the exponential decay constant. Applying this model to our data, we found $M_0 = 0.059 \times 10^{-5}$ emu, $A = 4.44 \times 10^{-5}$ emu and $n_0 = 0.42$. We found that a small but visible residual amount of oxygen is present and further purging would not decrease it. This small trace of oxygen could be explained by the

limiting pumping capability of the mechanical pump and the presence of trace oxygen within the helium gas use to cool down the sample.

It is to be noted that the magnetic oxygen peak position depends on the rate at which the temperature is changed³⁷. For example, this is observed on our zero purge experiment, and this is why we shifted our curve accordingly to better visualize the peak height as function of the number of purges.

Finally, this “oxygen” effect is only visible in samples with magnetization in the 10^{-5} - 10^{-6} emu range. Therefore we recommend, in addition to multi-purging, using samples as large as possible to decrease the relative effect due to oxygen magnetic transition.

APPENDIX E ELECTRON PARAMAGNETIC RESONANCE SYSTEM OVEN APPARATUS

The design and construction of an oven was required for above room temperature measurements of electron paramagnetic resonance. In this appendix we will describe how it is designed and how it works.

To simplify the explanations, Figure E-1 is presented. In this figure, the left side is a picture of the oven apparatus including the resonant cavity and the waveguide, while on the right side a schematic representation of the cross cut is plotted.

First, at the bottom of the oven apparatus, room temperature nitrogen gas is introduced into the hot quartz ampoule. Nitrogen was used because of its wide availability, none corrosive nature and its zero background signal in the EPR cavity. The temperature range of the ampoule can be varied from 20°C to 1000°C by adjusting the current in the heating element with a Variac. An E-type thermocouple is built in the outside of the ampoule to monitor the quartz temperature. The nitrogen is slowed down in the ampoule due to the increase in cross section and small quartz piece making the molecular path length longer. Another thermocouple can also be inserted at the output to monitor the temperature of the nitrogen. Typically high temperatures of near 600°C have been utilized.

Since we only want to heat the sample and not the cavity, we used an insulating double wall quartz tube to prevent heat from warming up the cavity and thus affect the measurements. The insulation in the quartz tube is obtained by pumping the space between the walls down to 10^{-5} torr with a turbo-pump. The stainless steel metal casing was designed with an inner groove to accommodate two viton o-rings. These o-rings are very critical for high vacuum quality. To prevent fast degradation as the temperature rise in the column, only viton o-rings, specially designed for high temperature were used.

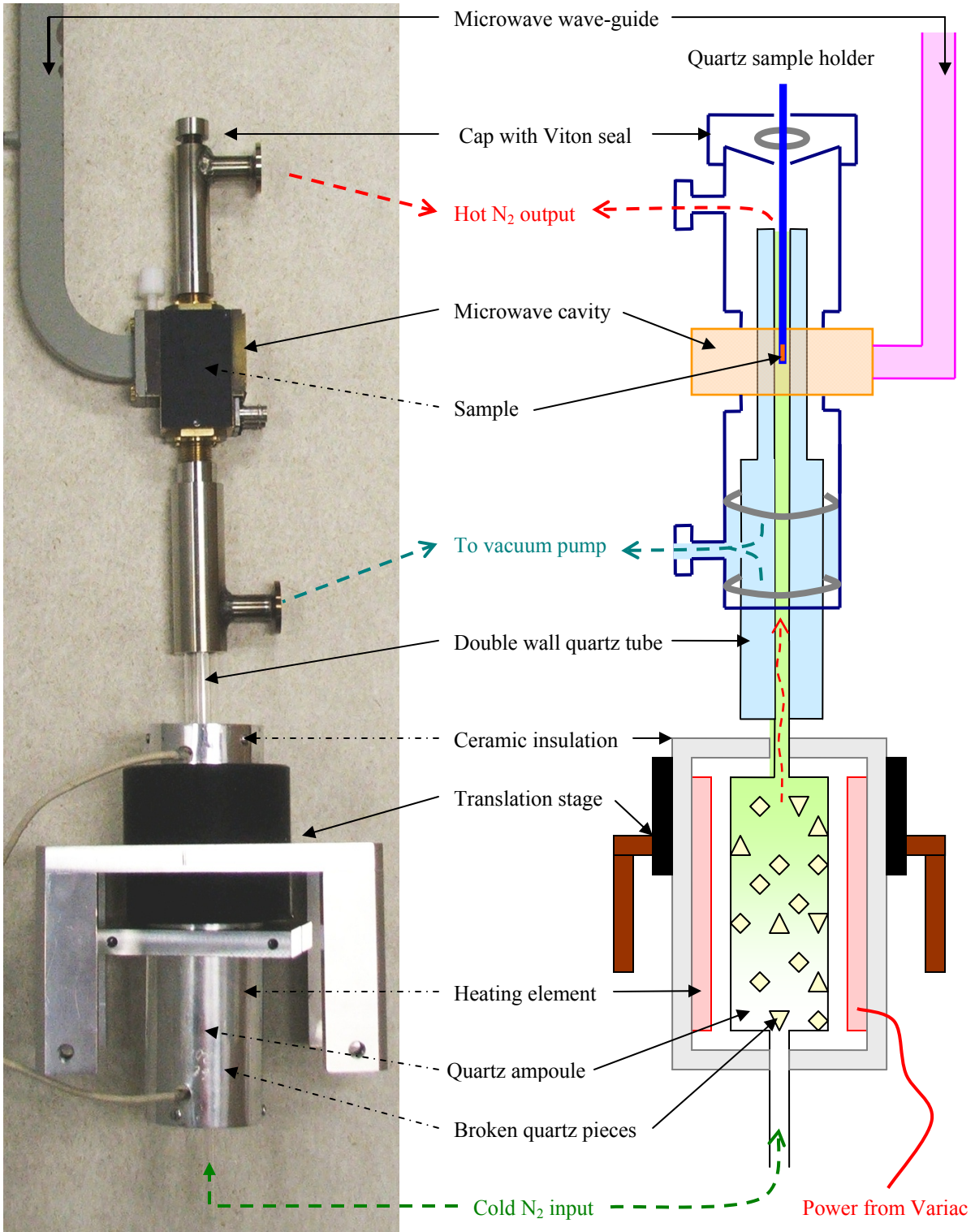


Figure E-1. Picture and schematic cross section of the oven apparatus for the electron paramagnetic resonance system.

The hot nitrogen gas flows through the cavity warming up the quartz sample holder and is then released in the air through the exit port. Once in the air, the gas cools down very rapidly.

The design of the top part allows the variation of the viton o-ring inner diameter by screwing in or out the cap (squeezing or releasing the o-ring). Since the sample holder passes through the o-ring, simply screwing in the cap will lock the holder in place. The sample position can be adjusted by sliding the sample holder through the o-ring when the cap is unscrewed. To accommodate various sizes of quartz holder diameters, three inserts have been manufactured. This allows the use of 3, 4 and 5 mm quartz tubes.

A thermocouple can be inserted in the quartz holder and positioned a few millimeters away from the sample without perturbation of the spectrum acquisition. This method allows a very accurate sample's temperature measurement.

In addition, a translation stage is used to adjust the waveguide and cavity position in the center of the magnet. For practical reasons, the moving part of the stage is made of plastic. It will melt if the experiment is conducted for too long (more than 2 hours).

Finally, the sample temperature is controlled by varying the power to the heating element and the flow of nitrogen. At temperatures below 300°C at the sample, the cavity stays at room temperature which allows a high quality resonance. But, when high temperatures are reached (500°C) the cavity warms up just enough to modify to resonance condition and affect the observed spectrum. To properly acquire EPR spectra at elevated temperature, a water cooling system would be necessary to maintain the cavity at room temperature. But, such modifications are beyond our capabilities. Bruker, the manufacturer of the EPR system which we use sell a high temperature (up to 1300 K) cavity for \$50,000. I manufactured our system for less than \$1,300.

LIST OF REFERENCES

- ¹B. D. Cullity, Introduction to Magnetic Materials, Addison-Wesley Publishing Company, Reading, Massachusetts, USA, 1972.
- ²R. E. Hummel, Electronic Properties of Materials, third edition, Springer, New York, New York, USA, 2001.
- ³J. Hack, M.H. Ludwig, W. Geerts, and R.E. Hummel, Mat. Res. Soc. Symp. Proc. **452**, 147 (1997).
- ⁴T. Dubroca, J. Hack, and R.E. Hummel, Appl. Phys. Lett. **88**, 182504 (2006).
- ⁵P. Esquinazi, A. Setzer, R. Höhne, and C. Semmelhack, Phys. Rev. B **66**, 024429 (2002).
- ⁶P. Esquinazi, and R. Höhne, J. Magn. Magn. Mater. **20**, 290 (2005).
- ⁷D. Spemann, K. Schindler, P. Esquinazi, M. Diaconu, H. Schmidt, R. Höhne, A. Setzer, and T. Butz, Nucl. Intr. And Meth. B **250**, 303 (2006).
- ⁸P. Reichart, D. Spemann, A. Hauptner, A. Bergmaier, V. Hable, R. Hertenberger, C. Greubel, A. Setzer, G. Dollinger, D.N. Jamieson, T. Butz, and P. Esquinazi, Nucl. Intr. And Meth. B **249**, 286 (2006).
- ⁹Y. Kopelevich, P. Esquinazi, J. Torres, and S. Moehlecke, J. Low Temp. Phys. **119**, 691 (2000).
- ¹⁰P. Esquinazi, A. Setzer, R. Höhne, C. Semmelhack, Y. Höhne, D. Spemann, T. Butz, B. Kohlstrunk, and M. Lösche, Phys. Rev. B **66**, 024429 (2002).
- ¹¹D. Spemann, K.-H. Han, P. Esquinazi, R. Höhne, and T. Butz, Nucl. Intr. And Meth. B **219**, 886 (2004).
- ¹²P. Esquinazi, R. Höhne, K.-H. Han, A. Setzer, D. Spemann, and T. Butz, Adv. Mat. **15**, 1719 (2003).
- ¹³A.V. Rode, E.G. Gamaly, A.G. Christy, J.G. Fitz Gerald, S.T. Hyde, R.G. Elliman, B. Luther-Davies, A.I. Veinger, J. Androulakis, and J. Giapintzakis, Phys. Rev. B **70**, 054407 (2004).
- ¹⁴A.V. Rode, E.G. Gamaly, A.G. Christy, J.G. Fitz Gerald, S.T. Hyde, R.G. Elliman, B. Luther-Davies, A.I. Veinger, J. Androulakis, and J. Giapintzakis, J. Magn. Magn. Mater. **290**, 298 (2005).
- ¹⁵A.V. Rode, A.G. Christy, N.R. Madsen, E.G. Gamaly, S.T. Hyde, and B. Luther-Davies, Cur. Appl. Phys. **6**, 549 (2006).
- ¹⁶W. Orellana, and P. Fuentealba, Surf. Science **600**, 4305 (2006).
- ¹⁷N. Park, M. Yoon, S. Berber, J. Ihm, E. Osawa, and D. Tomanek, Phys. Rev. Lett. **91**, 23 (2003).

- ¹⁸R. Laiho, E. Lahderanta, L. Vlasenko, and M. Afanasiev, *J. Lumin.* **57**, 197 (1993).
- ¹⁹A.F. Khokhlov, and P.V. Pavlov, *Pi'ma Zh. Eksp. Teor. Fiz.*, **24**, 238 (1976).
- ²⁰M. Bolduc, C. Awo-Affouda, A. Stollenwerk, M.B. Huang, F. Ramos, and V.P. LaBella, *Nuc. Intr. Meth. Phys. Res. B* **242**, 367 (2006).
- ²¹S.E. Lofland, B. Seaman, K.V. Ramanujachary, N. Hur, and S.W. Cheong, *Phys. Rev. B* **67**, 020410 (2003).
- ²²J.M.D. Coey, *Sol. Stat. Sci.* **7**, 660 (2005).
- ²³P. Stamenov, and J.M.D. Coey, *J. Magn. Magn. Mater.* **290**, 279 (2005).
- ²⁴J.M.D. Coey, *Current Opinion in Sol. Stat. Sci.* **10**, 83 (2006).
- ²⁵R.E. Hummel, and S.-S. Chang, *Appl. Phys. Lett.* **61**, 1965 (1992).
- ²⁶R.E. Hummel, S.-S. Chang, M. Ludwig, and A. Morrone, *Mater. Res. Soc. Symp. Proc.* **283**, 45 (1993).
- ²⁷J. G. Polihronov, T. Dubroca, M. Manuel and R. E. Hummel, *Mat. Sci. Eng. B* **107**, 124 (2004).
- ²⁸M.E. Stora, and R.E. Hummel, *J. Phys. Chem. Sol.* **63**, 1655 (2002).
- ²⁹L.H. Lewis, and K.M. Bussmann, *Rev. Sci. Instrum.* **67**, 10 (1996).
- ³⁰MPMS Application note 1014-822, Quantum Design Inc., San Diego, California, USA, (2001).
- ³¹B.N. Figgis, and R.S. Nyholm, *J. Chem. Soc.*, 4190 (1958).
- ³²C.J. O'Connor, and E. Sinn, *Inorg. Chim. Act.* **32**, 29 (1979).
- ³³J.-C. Bunzli, *Inorg. Chim. Act.* **36**, L413 (1979).
- ³⁴F.T. Hedgcock, and P.L. Li, *Phys. Rev. B* **2**, 1342 (1970).
- ³⁵T. Dubroca, J. Hack, and R. Hummel, *Phys. Rev. B* **74**, 026403 (2006).
- ³⁶J.A. Cowan, R.C. Kemp, and W.R.G. Kemp, *Metrologica* **12**, 87 (1976).
- ³⁷A. Jezowski, Z. Litwicki, V.V. Sumarokov, and P. Stachowiak, *Low Temp. Phys.* **32**, 1082 (2006).
- ³⁸S. Blundell, *Magnetism in Condensed Matter*, Oxford University Press, Oxford, England, 2001.
- ³⁹S.-S. Gouk, N. M. Kocherginsky, Y. Y. Kostetski, H. O. Moser, P. Yang, T.-M. Lim, and W. Q. Sun, *Radia. Research* **163**, 535 (2005).

- ⁴⁰W.L. Warren, E.H. Pointdexter, M. Offenber, and W. Muller-Warmuth, *J. Electrochem. Soc.* **139**, 870 part I (1992).
- ⁴¹W.L. Warren, J. Kanicki, F.C. Rong, and E.H. Pointdexter, *J. Electrochem. Soc.* **139**, 880 part II (1992).
- ⁴²C.J. Nicklaw, M.P. Pagey, S.T. Pantelides, D.M. Fleetwood, R.D. Schrimpf, K.F. Galloway, J.E. Wittig, B.M. Howard, E. Taw, W.H. McNeil, and J.F. Jr. Conley, *IEEE Trans. Nucl. Sci.*, **47**, No 6 (2000).
- ⁴³V.Y. Bratus, M.Y. Valakh, I.P. Vorona, T.T. Petrenko, V.A. Yukhimchuk, P.L.F. Hemment, and T. Komoda, *J. Lumin.* **80**, 269 (1999).
- ⁴⁴N. Tomozeiu, E.E. Van Faassen, W.M. Arnoldbik, A.M. Vredenberg, and F.H.P.M. Habraken, *Thin Sol. Films* **420**, 382 (2002).
- ⁴⁵K.G. Shaw, and R.K. MacCrone, *J. non-Cryst. Sol.* **159**, 253 (1993).
- ⁴⁶B. Rakvin, and B. Pivac, *J. Appl. Phys.* **81**, 3453 (1997).
- ⁴⁷P.A. Thomas, M.H. Brodsky, D. Kaplan, and D. Lepine, *Phys. Rev. B* **18**, 3059 (1978).
- ⁴⁸L.J. Berliner, G.R. Eaton, and S.S. Eaton, *Biological Magnetic Resonance* vol. 19, Plenum Publishers, New York, New York, USA, 2001.
- ⁴⁹S.J. Hudgens, *Phys. Rev. B* **14**, 1547 (1976).
- ⁵⁰J.G. Polihronov, R.E. Hummel, and H.-P. Cheng, *J. Lumin.* **101**, 55 (2003).
- ⁵¹Shepherd N.D., University of Florida dissertation, Visible electro-luminescence in spark-processed silicon, 2001.
- ⁵²J.C. Gourdon, P. Fretier, and J. Pescia, *J. Physique Lettres* **42**, L-21 (1981).
- ⁵³A. Schweiger, and G. Jeschke, *Principles of Pulse Electron Paramagnetic Resonance*, Oxford University Press, Oxford, England, 2001.
- ⁵⁴S.S. Eaton, and G.R. Eaton, *J. Mag. Res.* **102**, 254 (1993).
- ⁵⁵N.N. Gerasimenko, A.V. Dvurechenskii, A.I. Mashin, and A.F. Khokhlov, *Fiz. Tekh. Poluprovodn.* **11**, 190 (1977).
- ⁵⁶W. Jung, and G.S. Newell, *Phys. Rev.* **132**, 648 (1963).
- ⁵⁷MikroMash USA, 9755 SW Commerce Cir, Suite B-1 Wilsonville, OR 97070.
- ⁵⁸F.J. Dyson, *Phys. Rev.* **98**, 349 (1955).
- ⁵⁹G. Feher, and A.F. Kip, *Phys. Rev.* **98**, 337 (1955).

- ⁶⁰J.H. Van Vleck, *The Theory of Electric and Magnetic Susceptibilities*, Lowe and Brydone Printers Ltd, Oxford, England, 1932.
- ⁶¹P.W. Selwood, *Magnetochemistry*, Interscience Publishers Inc., New York, New York, USA, 1956.
- ⁶²L.N. Mulay, and E.A. Boudreaux, *Theory and Applications of Molecular Diamagnetism*, Wiley-Interscience Publication, New York, New York, USA, 1976.
- ⁶³D. Nelson, and L.W. Haar, *Inorg. Chem.* **32**, 182 (1993).
- ⁶⁴F.A. Cotton, D.M.L. Goodgame, M. Goodgame, and A. Sacco, *J. Am. Chem. Soc.* **83**, 4157 (1961).
- ⁶⁵J.W. Jeffery, and K.M. Rose, *Acta Cryst.* **B24**, 653 (1968).
- ⁶⁶D.B. Brown, V.H. Crawford, J.W. Hall, and W.E. Hatfield, *J. Phys. Chem.* **81**, 1303 (1977)

BIOGRAPHICAL SKETCH

Thierry Dubroca was born in France in 1977. He attended Notre Dame high school at Fontenay-le-Compte where he graduated with honors in 1995. After attending competitive classes in mathematics and physics for three years at the preparatory school St. Joseph in La Roche-sur-Yon, he was successfully admitted to the National School of Engineering Physics in Grenoble, France. He graduated with honors in June 2001 with an engineering degree in applied physics and a minor in entrepreneurship. Thierry concurrently earned a master's degree in semiconductor physics from University Joseph Fourier and the Grenoble National Polytechnic Institute in September 2001.

In 2000, while completing his engineering degree in France, Thierry moved to Gainesville, FL where he was an exchange student at the University of Florida. He continued on and earned a master's degree in material science and engineering in 2002.

He started as a teaching assistant for Dr. John Ambrose and the Major Analytical Instrumentation Center. During the fall 2001, he joined Prof. Rolf Hummel's group where he worked as a research assistant on infrared spectrometry. Thereafter, while he began his doctoral research on magnetic properties of materials, he studied management, and, in 2004, received a Master of Science in management from the Warrington College of Business and Administration at the University of Florida. Thierry finishes his education earning a Ph.D. in material science and engineering from the University of Florida while still being under the supervision of Professor Rolf Hummel. That same year, he won the Rugby South conference championship with the Gainesville Hogs.